



# Coupling Eulerian interface capturing and Lagrangian particle methods for atomization simulation

Victor Cheron

## ► To cite this version:

Victor Cheron. Coupling Eulerian interface capturing and Lagrangian particle methods for atomization simulation. Fluid Dynamics [physics.flu-dyn]. Normandie Université, 2020. English. NNT : 2020NORMR097 . tel-03193155

**HAL Id: tel-03193155**

**<https://theses.hal.science/tel-03193155>**

Submitted on 8 Apr 2021

**HAL** is a multi-disciplinary open access archive for the deposit and dissemination of scientific research documents, whether they are published or not. The documents may come from teaching and research institutions in France or abroad, or from public or private research centers.

L'archive ouverte pluridisciplinaire **HAL**, est destinée au dépôt et à la diffusion de documents scientifiques de niveau recherche, publiés ou non, émanant des établissements d'enseignement et de recherche français ou étrangers, des laboratoires publics ou privés.



Normandie Université

# THÈSE

Pour obtenir le diplôme de doctorat

Spécialité Mécanique des fluides, énergétique, thermique, combustion, acoustique

Préparée au sein de l'Université de Rouen Normandie

## Coupling Eulerian interface capturing and Lagrangian particle methods for atomization simulation

Présentée et soutenue par  
**Victor CHÉRON**

Thèse soutenue publiquement le 16 décembre 2020  
devant le jury composé de

Stéphane Vincent	Professeur MSME, Université Gustave Eiffel – Marne-la-Vallée	Rapporteur
Jean-Luc Estivalèzes	Ingénieur de Recherches ONERA – Toulouse	Rapporteur
Frédéric Risso	Directeur de recherches IMFT, CNRS – Toulouse	Examineur
Thibaut Ménard	Maître de Conférences CORIA, Université de Rouen Normandie – Rouen	Examineur
Alain Berlemont	Directeur de recherches CORIA, CNRS – Rouen	Directeur de thèse
Jorge César Brändle de Motta	Maître de Conférences CORIA, Université de Rouen Normandie – Rouen	Co-encadrant de thèse

Thèse dirigée par Alain BERLEMONT et co-encadrée par Jorge César BRÄNDLE DE MOTTA,  
laboratoire CORIA (UMR 6614)





---

# Remerciements

---

Je remercie Madame Armelle Cessou, directrice de l'unité Mixte de recherche 6614 CORIA, pour m'avoir accueilli au sein du laboratoire CORIA.

Pour avoir accepté de prendre part à l'évaluation de ce travail de thèse, je tiens à remercier Messieurs:

**Stéphane Vincent**, Professeur à l'Université Gustave Eiffel, au sein du laboratoire MSME,  
**Jean-Luc Estivalèzes**, Ingénieur de Recherches à l'ONERA de Toulouse,

rapporteurs, et

**Frédéric Risso**, Directeur de recherches au CNRS, au sein du laboratoire IMFT, Toulouse,  
**Thibaut Ménard**, Maître de Conférences à l'Université de Rouen Normandie, au sein du laboratoire CORIA,

**Alain Berlemont**, Directeur de recherches au CNRS, au sein du laboratoire CORIA,  
**Jorge César Brändle de Motta**, Maître de Conférences à l'Université de Rouen Normandie, au sein du laboratoire CORIA,

**Lian-Ping Wang**, Professeur au sein de University of Delaware, Newark, USA et Southern University of Science and Technology, Shenzhen, CHINA,

d'avoir accepté de juger ce travail.

Durant ces années au sein du laboratoire, j'ai eu la chance d'être *co-encadré* par **Jorge César Brändle de Motta**, que je tiens particulièrement à remercier pour son enthousiasme sans faille. Il a su m'apporter sa science du détail, sa patience pour m'expliquer ses attentes durant cette étude tout en me laissant expérimenter mes propres idées, et, souvent, me tromper pour apprendre. Sur le plan humain également, j'ai pu beaucoup partager avec lui. **Jorge César Brändle de Motta** a été d'une très grande aide et compréhension pour mener à bien ce projet et tranquiliser les angoisses non nécessaires. Je pense que ses futurs doctorants auront une chance certaine de travailler dans cet environnement de confiance.

Je tiens à remercier *le chef*, **Alain Berlemont**, qui a dirigé cette thèse en apportant son expérience, sa vision et son aide. Grâce à lui, j'espère un jour maîtriser l'écriture à la Russe.

Ayant développé nos études au sein du code de calcul *Archer*, j'ai pu compter sur le soutien de l'architecte, **Thibaut Ménard**, qui m'a permis de voir plus clair au sein de ces nombreuses lignes **F90**. Je le remercie pour son temps et ses nombreuses discussions qui m'ont permis de prendre du recul sur l'étude numérique des jets liquides, se terminant souvent par : *mais je l'ai déjà développé, attends, fais voir ton code*.

Lorsque je suis arrivée au sein du laboratoire, j'ai été prévenu que je passerai beaucoup de temps en sa compagnie pour mener à bien cette étude. Mon encadrant n'a pas menti, j'ai eu la chance de compter sur l'apport de **Alexandre Poux**, toujours intéressé et moteur au sein de la recherche. Je le remercie pour le temps qu'il a dédié à s'intéresser à notre projet, le nombre d'interactions que j'ai pu avoir avec lui, et, ses énigmes.

Je tiens à remercier l'ensemble de l'équipe *Numerical Team Meeting*, qui m'a permis d'améliorer la qualité de mon travail et de perfectionner sa mise en forme. Plus particulièrement Messieurs

**Francois-Xavier Demoulin** et **Julien Réveillon** qui m'ont fait en confiance en me permettant d'obtenir une première expérience d'enseignement. De plus, les conseils de **Francois-Xavier Demoulin** m'ont permis d'effectuer un projet de recherche au sein du laboratoire *Centro Motores Termicos* durant mes études de Master, ce qui fut déterminant pour la suite de mon parcours. Egalement, ils m'ont permis de gérer mon timing durant ces trois années de thèse, qui peuvent, défiler à la vitesse d'un jet atomisé.

Durant cette étude, j'ai eu la chance d'être responsable de l'étude de stage de **Hayet Salmi** dans le cadre de la validation de son cycle de Licence. Je la remercie d'avoir eu confiance en moi pour mener à bien cette première mission d'encadrement. Je tiens particulièrement à remercier **Marie-Charlotte Renoult**, **Saïd Idlahcen**, **Jean-Bernard Blaisot**, **Thierry Muller** et **Bruno Mille**, pour le prêt d'espace, de matériel et de savoir faire durant cette étude expérimentale.

Cette connection avec les salles obscures du laboratoire m'a permis d'initier une étude jointe avec **Jean-Bernard Blaisot** que je tiens à remercier pour le temps qu'il a consacré à me présenter ses techniques d'étude de l'atomisation tout en m'introduisant à ses techniques expérimentales.

Je tiens à remercier l'ensemble des services communs du laboratoire, **Cedric Chambrelan**, **Alexis Boulet**, **Guillaume Edouard**, **Christophe Letailleur**, **Florence Fradet**, **Valérie Thieury**, **Nathalie Delahaye** pour leur aide.

Durant ce temps passé au sein du laboratoire, j'ai eu la chance d'en sortir. Cela m'a donné l'opportunité d'intéragir avec des scientifiques passionnés, que cela soit au sein du comité de suivi de thèse, conférences ou autre événement scientifique. Je tiens donc à remercier **Vincent Moureau**, **Davide Zuzio**, **Fabien Evrard**, **Fabian Denner**, **Wim-Paul Breugem**, **Markus Uhlmann**, **Wojciech Aniszewski**, **Daniel Fuster**, **Marco Cialesi Esposito**, **Sagar Pal**, **Gianluca Lavallo** et assurément d'autres personnes m'ayant inspirés durant les nombreuses présentations de qualité auxquelles j'ai pu assister.

Au compte de mes sorties, j'ai eu la chance d'être accueilli au sein du group de recherche de **Lian-Ping Wang**, au sein de l'université de SUSTech. Je tiens à le remercier pour son accueil au sein de son laboratoire durant cet échange m'ayant permis d'avoir une nouvelle vision de la recherche, et également son équipe de recherche ayant facilité mon intégration. Notamment **Chen Tao**, qui a partagé avec moi le challenge d'une comparaison de code en un temps restreint.

Je tiens à remercier **Andres Amell** pour m'avoir accueilli au sein de son laboratoire, et à toute son équipe de recherche. Plus particulièrement Julian Obando et ses proches qui m'ont permis considéré tel qu'un membre de leur famille durant mon séjour. Cela n'aurait pas été possible sans l'aide de **Gilles Cabot**, que je tiens à remercier pour m'avoir permis de réaliser ce projet. Grâce à lui, j'ai également pu entrer en contact durant mon cycle de Licence avec un doctorant du CORIA, **Manuel Marin**, dans le but de perfectionner mon espagnol. Plutôt que les langues étrangères, c'est un intérêt pour la recherche qu'il a éveillé en moi et je l'en remercie pour cela.

A travers lui, j'ai pu écouter les lamentations de thésards, ce qui ne m'a pas étrangement pas freiner, et je tiens donc à remercier cette *première génération*, **Andres Valencia Correa**, **Antonio Ficuciello**, **Felix Dabonneville**, **Lila Ouldarbi**, **Frédéric Berthillier**, **Erwan Salaün**.

Durant trois années, j'ai partagé un bureau avec **Anirudh Asuri Mukundan**, et bien plus. Je tiens à le remercier pour tous ces moments passés, ces *late nights working until starving*, et toutes ces discussions sur le sens de nos études. Je tiens également à remercier **Nelson Valdez**, **Alberto Remigi** et **Jean-Baptiste Charpentier** pour avoir réussi à créer une atmosphère digne d'un PMU au sein de notre bureau grâce à ces discussions allant du traitement de l'interface au sein de Navier-Stokes à la date du mariage d'Anirudh.

Je tiens également à remercier ceux qui font la vie du laboratoire, que ce soit au sein du football du Vendredi, de *l'A2Doc*, ou tous les bons moments passés en leur compagnie : **Eliot Schuhler**, **Cléante Langrée**, **Niccolo Tonicello**, **Hassan Tofaili**, **Diego Ferrando**, **Hector Valdez**, **Teddy Tawk**, **José Moran**, **Jérôme Yon**, **Aurélien Perrier**, **Romain Janodet**, **Rafael Herrera**, **Angel Martinez**, **Leandro Martinez**, **Pahola Acevedo**, **Benjamin Duret**, **Pradip Xavier**, **Thomas Godin**, **Corine Lacour**, **Petra Daher**, **Geoffroy Vaudor**, **Edouard Rouet**, **Clément Brunet**, **Claude Rozé**, **Rezki Becheker**, **Javier Anez**, **Aqeel Ahmed**, **Lorenzo Palanti**, **Francesco Gava**, **Hakim Hamdani**, **Javier Marreo Santiago**,

**Clément Patat, Gilles Godard, Jean-Charles Sautet, Béatrice Patte-Rouland, Fabien Thiesset** et bien d'autres.

Il est indéniable que ces remerciements doivent se terminer par un énorme **merci** à ma famille, et plus particulièrement à mes parents, **Delphine** et **Thierry Chéron**, qui m'ont supporté tout au long de ces longues années d'études, à je l'imagine, se demander quand est ce que ces longues semaines de travail s'arrêteraient. Il semblerait que maintenant, ce soit la fin, ou le début, selon ma grand-mère.



Quand la science inspire l'art... Photo : Victor Chéron.



---

# Contents

---

<b>I</b>	<b>State of the art</b>	<b>19</b>
I.1	Introduction to jet analysis . . . . .	20
I.1.1	Application to a combustion chamber . . . . .	21
I.1.2	Primary atomization . . . . .	27
I.1.3	Breakup limit . . . . .	30
I.1.4	Numerical investigation on droplet stability . . . . .	35
I.2	Numerical methods . . . . .	36
I.2.1	Navier-Stokes framework . . . . .	37
I.2.2	Navier-Stokes numerical implementation . . . . .	37
I.3	Interface Capturing Method (ICM) . . . . .	38
I.3.1	Introduction to interface numerical treatment . . . . .	38
I.3.2	Interface Capturing Method in DNS . . . . .	39
I.4	<i>Archer</i> . . . . .	43
I.4.1	Treatment of the interface in <i>Archer</i> . . . . .	43
I.4.2	Navier-Stokes coupling . . . . .	44
I.4.3	Block decomposition . . . . .	47
I.4.4	Summary . . . . .	48
I.5	Limits of atomisation . . . . .	48
I.5.1	Under resolved treatment of interface . . . . .	48
I.5.2	<i>Archer</i> volume restriction . . . . .	49
<b>II</b>	<b>Implementation of Lagrangian Tracking Method</b>	<b>51</b>
II.1	Particles Lagrangian Modelling . . . . .	52
II.1.1	One-way coupling . . . . .	52
II.1.2	Two-way coupling . . . . .	54
II.1.3	Full Resolved Particles (FRP) approach . . . . .	57
II.1.4	Collision modelling . . . . .	61
II.1.5	Summary . . . . .	62
II.2	Implementation of the Lagrangian solver . . . . .	62
II.2.1	Storage per processor . . . . .	62
II.2.2	Multi processors strategy . . . . .	67
II.2.3	Temporal scheme description . . . . .	68
II.3	Validation of the Lagrangian tracking . . . . .	68
II.3.1	Description of the test cases . . . . .	70
II.3.2	One-way Lagrangian model in <i>Archer</i> . . . . .	72
II.3.3	Two way method validation . . . . .	73
II.3.4	Temporal scheme analysis . . . . .	79
II.3.5	Full Resolved Particles results . . . . .	85
II.3.6	Summary . . . . .	91
II.4	Comparison of methods . . . . .	92
II.4.1	Physical results . . . . .	92
II.4.2	Summary . . . . .	94

<b>III Implementation of Hybrid Method</b>	<b>95</b>
III.1 State of the Art . . . . .	96
III.2 Detection of structure . . . . .	97
III.2.1 Algorithm . . . . .	97
III.2.2 Parallel efficiency . . . . .	101
III.2.3 Summary . . . . .	102
III.3 Distance to interface criteria . . . . .	103
III.3.1 Resolved droplet to Lagrangian particle . . . . .	104
III.3.2 Particle to resolved droplet . . . . .	104
III.4 Sphericity criteria . . . . .	105
III.4.1 Introduction . . . . .	106
III.4.2 Numerical Methods . . . . .	106
III.4.3 Droplet to particle transformation criteria . . . . .	109
III.4.4 Lamb oscillation . . . . .	110
III.4.5 Immersed Droplet in a HIT . . . . .	111
III.4.6 Airblast atomizer . . . . .	113
III.5 Reconstruction of the interface . . . . .	115
III.5.1 ICM to Particle . . . . .	115
III.5.2 Particle to ICM . . . . .	116
III.6 Reconstruction of the velocity field . . . . .	118
III.6.1 Velocity field reconstruction . . . . .	120
III.6.2 Configuration . . . . .	122
III.6.3 Results . . . . .	122
III.7 Treatment of collisions in Hybrid coupling . . . . .	124
III.7.1 Strategy for particles interactions . . . . .	125
III.7.2 Head-on collision . . . . .	126
<b>IV Enhancement of transformation criteria</b>	<b>129</b>
IV.1 2D and 3D droplet's splash . . . . .	131
IV.1.1 Splash configuration . . . . .	131
IV.1.2 Numerical configuration . . . . .	133
IV.1.3 2D Results . . . . .	136
IV.1.4 3D Results . . . . .	144
IV.1.5 Summary . . . . .	148
IV.2 Plateau-Rayleigh instability of a round liquid jet . . . . .	150
IV.2.1 Plateau-Rayleigh configuration . . . . .	150
IV.2.2 Numerical configuration . . . . .	151
IV.2.3 Results . . . . .	152
IV.2.4 Summary . . . . .	166
IV.3 Decaying Homogeneous Isotropic Turbulence . . . . .	167
IV.3.1 Decaying Homogeneous Isotropic Turbulence configuration . . . . .	167
IV.3.2 Results . . . . .	168
IV.3.3 Summary . . . . .	173
<b>V Study of Jet in crossflow atomization</b>	<b>176</b>
V.1 Configuration setup . . . . .	177
V.2 Physical results . . . . .	179
V.2.1 ICM results . . . . .	179
V.2.2 Hybrid approach . . . . .	185
V.2.3 Configuration comparisons . . . . .	201
V.3 Computational cost of simulation . . . . .	204
<b>Appendix</b>	<b>210</b>

<b>List of Figures</b>	<b>211</b>
<b>List of Tables</b>	<b>215</b>
<b>Bibliography</b>	<b>217</b>





---

# Nomenclature

---

## Roman letters

### Symbol Description

$\cdot_d$	Physical quantity representing a droplet [-]
$\cdot_g$	Physical quantity representing the gas phase [-]
$\cdot_l$	Physical quantity representing the liquid phase [-]
$\cdot_p$	Physical quantity representing a particle [-]
$\dot{m}$	Flow rate [ $kg.s^{-1}$ ]
$\vec{a}$	acceleration vector [ $m.s^{-2}$ ]
$\vec{f}$	forces [ $kg.m^{-1}.s^{-2}$ ]
$\vec{n}$	Normal [-]
$\vec{u}$	velocity vector [ $m.s^{-1}$ ]
$\vec{x}$	position vector [ $m$ ]
$A_0$	Area of the injector [ $m^2$ ]
$A_a$	Area of the aire core [ $m^2$ ]
$A_p$	Area of the inlets ports [ $m^2$ ]
$A_s$	Area of the swirl atomizer chamber [ $m^2$ ]
$b_\delta$	Impact distance for droplets binary collision [-]
$C_1$	Empirical constant used to compute $\beta$ [-]
$C_{Dis}$	Discharge coefficient [-]
$C_D$	Drag coefficient [-]
$d$	Diameter [ $m$ ]
$D_{32}$	Sauter Mean Diameter [ $m$ ]
$d_{Hinze}$	Hinze diameter of stability based on dissipation analysis [ $m$ ]
$E_{bu}$	Breakup up energy, assimilated to droplets [-]
$g$	Gravitational constant [ $m.s^{-2}$ ]
$k$	Turbulent kinetic energy [ $m^2.s^{-2}$ ]

$L_c$	Characteristic length [m]
$m$	Mass [kg]
$R$	Radius [m]
$R_p^*$	Reconstructed radius for particle transformation [m]
$Vol$	Volume [ $m^3$ ]

### Greek letters

#### Symbol Description

$\alpha$	Volume of Fluid within a cell [-]
$\beta$	Batchelor constant in turbulent breakup [-]
$\cdot_T$	Physical quantity at the interface [-]
$\Delta x$	Mesh size [m]
$\delta$	Area of redistribution for Two-way method [m]
$\delta_{a,b}$	Collision distance overlap in soft sphere model [m]
$\delta_h$	Dirac function in IBM framework
$\dot{\gamma}$	Shear rate at interface [ $m^{-1}$ ]
$\epsilon$	Turbulent dissipation [ $m^2.s^{-3}$ ]
$\eta$	Drag correction applied in sedimented environment [-]
$\eta_K$	Kolmogorov length scale [m]
$\kappa$	Curvature [ $m^{-1}$ ]
$\Lambda$	Taylor length scale [m]
$\lambda$	Area of interpolation for Two-way method [m]
$\mu$	Dynamic viscosity [ $kg.m^{-1}.s^{-1}$ ]
$\nu$	Kinematic viscosity [ $m^2.s^{-1}$ ]
$\Omega$	Volume of integration [ $m^3$ ]
$\phi$	Level set function
$\rho$	Density [ $kg.m^{-3}$ ]
$\sigma$	Surface tension [ $kg.s^{-2}$ ], also used for standard deviation.
$\tau$	Stress tensor Navier Stokes [-]
$\tau_p$	Characteristic time of particle [-]
$\tau_s$	Restoring stress [-]
$\tau_v$	Viscous shear stress [-]

### Abbreviations

#### Symbol Description

1W One way method

2W Two way method

[.] Jump condition

*Archer* Numerical inhouse solver

*CLSVoF* Coupled *Level-set* Volume of Fluid method

*DNS* Direct Numerical Simulation

*DPS* Disperse Particle Simulation

*Eul.* Eulerian

*FRP* Full Resolved Particle

*GFM* Ghost Fluid Method

*IBM* Immersed Boundary Method

*ICM* Interface Capturing Method

*Lag.* Lagrangian

*LES* Large Eddy Simulation

*LPP* Lagrangian Point Particle

*S.&N.* Schiller and Naumann correction

*VoF* Volume of Fluid

*NS* Navier-Stokes equations

*Sto.* Stokes

## Mathematical operators

### Symbol Description

$\nabla \cdot$  Divergence operator

$\nabla$  Gradient operator

$\otimes$  Tensorial product

$\partial$  Partial derivative

$D$  Lagrangian derivative

## Dimensionless numbers

### Symbol Description

$\mu^*$  Viscous ratio  $\mu^* = \frac{\mu_l}{\mu_g}$

$\rho^*$  Density ratio  $\rho^* = \frac{\rho_l}{\rho_g}$

$At$  Atwood number  $At = \frac{\rho_l - \rho_g}{\rho_l + \rho_g}$

$C_D$  Discharge coefficient  $C_D = \dot{m}_l [A_o (2\rho_l \Delta P_l)^{0.5}]^{-1}$

## NOMENCLATURE

---

$Ca$  Capillary number  $Ca = \frac{\mu V}{\sigma}$

$M$  Momentum ratio  $M = \frac{\rho_l V_l^2}{\rho_g V_g^2}$

$Oh$  Ohnesorge number  $Oh = \frac{\mu}{\sqrt{\rho \sigma L_c}}$

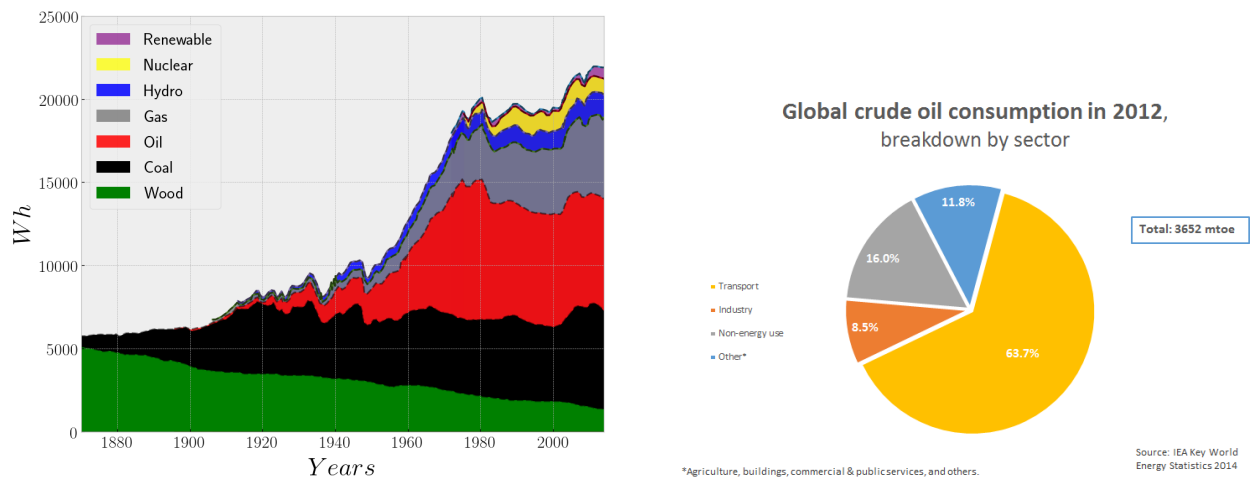
$Re$  Reynolds number  $Re = \frac{\rho V L_c}{\mu}$

$We$  Weber number  $We = \frac{\rho V^2 L_c}{\sigma}$

# Foreground

For decades, goods and people transport grew exponentially causing to several modifications in our daily lives. Major changes appeared during the industrial revolution era, 1840, with the development of the railway industry. From the train driver loading engines with coal through the recent developments of fuel cell cars, a common factor is required to produce a motion: Energy.

Along the years, energy has been obtained from several ressources such as wood, coal, oil or gases [figure 1a], leading to an evolution of the energy used per inhabitant from 10kWh to 20kWh today, in less than 50 years. Nowadays, approximately 60% of those ressources are used to transport goods and people [figure 1b], leading to major issues.



(a) Average energy consumed per inhabitant on earth, Data extracted from BP statistics.

(b) World oil crude consumption per sector, 2014, from IAE KeyWorld statistics.

Figure 1

The first challenge is that these resources consumption exceeds the production capacity. In the long run, this will cause an inflation of the price of access to these resources changing our lifestyle. Indeed, Research and Development has been encouraged to find substitutes. A serious alternative to the diesel consumption has been developed at the end of the 19th century, it was a biodiesel made of arachide oil and exposed at the 1900 *Exposition Universelle de Paris* under the name of the peanut engine [Hendrickson, J.]. This substitute was developed by Rudolf Diesel himself and became a milestone to enhance biodiesel research, he then perspicaciously declared in 1912 during a speech:

*The use of vegetable oils for engine fuels may seem insignificant today but such oils may become, in the course of time, as important as petroleum and the coal-tar products of the present time.*

Being a finite resource is a constraint for oil consumption that does not harm people, its side effects are more dangerous: pollutant emission production. They are quantified through equivalent  $\text{CO}_2$ , in kilograms, emissions. All gases are scaled by the reference pollutant emission  $\text{CO}_2$ , showing for example that methane is 21 times more pollutant than  $\text{CO}_2$ , it will then create 21 kg of  $\text{CO}_{2eq}$ . The direct effect of pollutant emissions is a decrease of air quality, yielding to an increase of deaths through

respiratory disease [figure 2]. A known example is  $NO_x$  reaction with ammonia that creates acid nitric, harming respiratory systems.

It appears that the more populated is the country, the worst is the air quality, however, atmosphere contamination has a worldwide impact, called global warming. It is a long term rise in the average temperature which has been scientifically demonstrated by long term measurements leading to significant climate change. Those world modifications include ice-melting raising the sea level, spreading of the desert.

Number of deaths from outdoor air pollution, 2016

Absolute number of premature deaths by country attributed to ambient (outdoor) air pollution of particulate matter (PM) and ozone ( $O_3$ ).

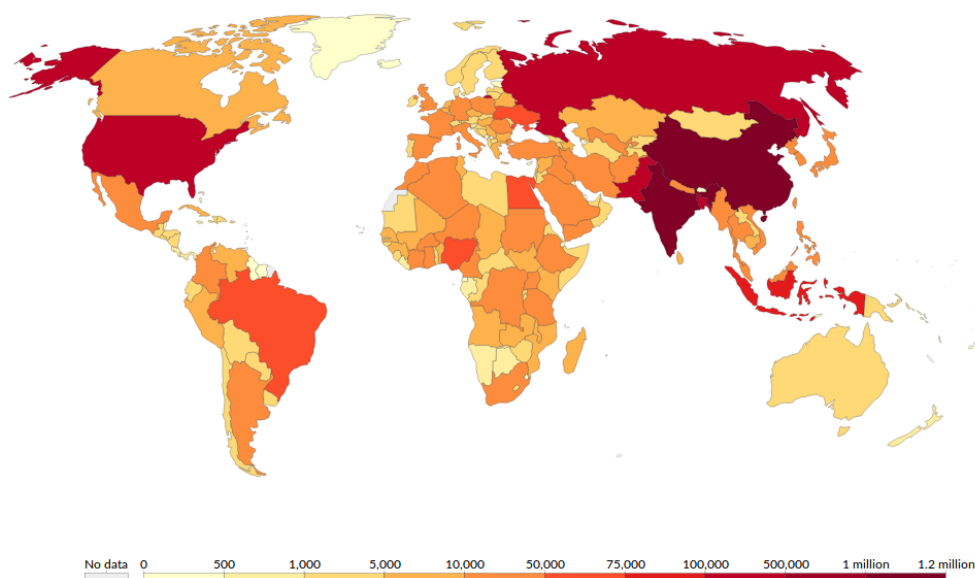


Figure 2: Number of death from outdoor air pollution from *Our world in data*.

Finally, due to the space of oil in our lives and its side effects, it became the major challenge of the 21st century. Now, energy is at the center of international agreements, as seen during the COP 25 Madrid, where more than 195 countries agreed on the importance of acting against global warming with the reduction of  $CO_2$  production in order to maintain global warming under  $2^\circ C$  toward 2100 which passes through improving transport of goods and people.

In a near future, it is impossible to shift from fossil energies to others, and Europe enhanced research and development on oil combustion to a better understanding. The main objectives are to reduce greenhouse gases and improve fuel efficiency, inducing a smoother transition to bio fuel. In France, government enhanced Research and Investigation dividing the country into *pôles d'investigations*. Haute-Normandie became the center of investigation on transportation and companies such as *Renault*, *Revima* or *Safran* have been implemented near national research center.

The Complexe de Recherche Interprofessionnel en Aérothermochimie, CORIA, a laboratory belonging to Normandie Université, based in Rouen, is part of this program, naturally following national impulse. Along the years, experimental and numerical expertises have been developed to deepen knowledge on combustion inside engines, and, more especially on the patterns that follows injected fuel in combustion chamber before evaporation [figure 3].

On this experimental snapshot, a dense liquid jet is injected into a combustion chamber. The liquid shape evolves downstream to the jet and breaks into several smaller structures. The distribution of these structures is determinant to improve combustion efficiency and reduce pollutant emissions. The complexity is that engine design is in constant evolution because of new law requirements.

Modelling liquid jet evolution through computationnal fluid dynamic is an ideal strategy to analyze several configurations. It has been first developed to study weather condition, a century ago [Richardson, 2007], until recent studies over diesel jet injection analysis using several processors [Shinjo and Umemura, 2010]. The combination of computer science and fluid mechanics provides

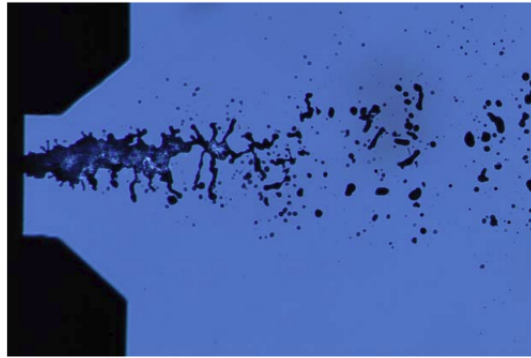


Figure 3: Atomization of a liquid jet in a combustion chamber [Dumouchel and Grout, 2009].

access to reliable tools, validated thoroughly on analytical and experimental studies permitting their usage on realistic application.

Although the advances brought by numerical simulation to the study of the propagation of a liquid jet are significant, there are still areas of shadows. Diameter of the smallest droplets can be 100 times smaller than liquid injection diameter, yielding to a multiscale issue that complexify their studies.

In numerical simulation, several solutions are developed to solve this issue. The purpose of this PhD is to be able to obtain information from these structures, and to develop a numerical method to improve their treatment in typical two-phase flow atomization. This method is based on the assumptions that small droplets, transported with Eulerian model, are considered spherical and can be transported with a Lagrangian model. The methodology is detailed in this manuscript, following its description, implementation and use.

This investigation has been granted by the Région Normandie, France, hosted by the CORIA Laboratory and the Université of Normandie - Rouen.



## Outline

The first chapter of this manuscript focuses on the description of the physics behind the destabilization of the liquid bulk to understand the creation of small droplets. The numerical solver *Archer*, used to study liquid jet atomization, is presented. Finally, drawbacks of the methods are highlighted, showing the motivations of our implementation.

In the second chapter, the numerical solver that we developed to treat small droplets is presented. Several methods have been implemented and are compared to the already implemented one in *Archer*.

The third chapter describes the implementation of a Hybrid approach between Eulerian and Lagrangian solvers. Some general steps have to be respected when passing from a solver to another one, such as conservation of some quantities or validation of hypotheses ensuring that the model can be used. Since hypotheses have to be validated, criteria have been implemented and are described in the third section, the fourth section focuses on the influence of these criteria on simulations' results.

A comparison between solvers is done on academical applications in the fourth chapter enabling a full application of the Hybrid approach. The advantages of these tests are to reproduce two-phase flow atomization conditions phenomena under controlled conditions.

The last chapter is devoted to the use of the Hybrid approach on crossflow atomization application. Our choice here is to apply the method at low numerical resolution in order to perform a wide series of simulations. Experimental and numerical set up are first introduced and a comparison between the existing solver and the Hybrid approach is done through a droplets' dispersion study.

## Plan de thèse

Le premier chapitre de ce manuscrit décrit la physique de la déstabilisation d'un jet liquide dans le but d'appréhender la création de gouttes dans un jet atomisé. Le code de calcul *Archer*, utilisé pour l'étude de la propagation des jets atomisés, est présenté en se concentrant sur la modélisation du transport de l'interface. Notant les limites potentielles du code de calcul, nous présentons la méthode qui est développée dans ce manuscrit.

Dans le second chapitre, le développement d'une extension du code de calcul *Archer* permettant de transporter les petites échelles d'un jet liquide atomisé est détaillé. Plusieurs méthodes ont été implémentées dans le code de calcul, elles sont décrites puis comparées à la méthode de transport d'interface existante.

Le troisième chapitre présente le couplage entre l'extension Lagrangienne et le code de calcul *Archer*, basé sur un transport Eulérien, la méthode Hybride. Des étapes doivent être respectées pour assurer la conservation de la masse et de la quantité de mouvement lors de changement de méthode de résolution numérique. Pour assurer une transition physique, des critères de transformation sont implémentés.

Une comparaison est menée entre le code numérique *Archer* et la méthode Hybride sur des applications académiques. Ces dernières sont choisies car elles permettent de reproduire des conditions représentatives de l'atomisation tout en laissant un contrôle relatif des phénomènes observés.

Le dernier chapitre de ce manuscrit présente une étude comparative de la méthode Hybride appliquée à un jet atomisé dans un *crossflow*. Cette étude fut menée dans un domaine sous résolue dans le but de pouvoir exécuter plusieurs simulations en variant les paramètres de transformation. La première partie de ce chapitre se concentre sur la description expérimentale et numérique du cas ciblé, puis la comparaison des résultats Eulérien à notre référence. Dans un second temps, la comparaison Hybride/*Archer* est proposée dans le but de résumer les apports de la méthode développée durant cette thèse.

## State of the art

*In this chapter we briefly introduce the phenomenon of liquid jet atomization and its shape modification. Its modeling is described through the introduction of mass and momentum equations conservation. Special care is hold on the description of the interface treatment, giving the opportunity to introduce the numerical solver Archer used in our study. Finally, the limits of the solver are shown to justify the implementation of our method.*

### Contents

I.1	Introduction to jet analysis . . . . .	20
I.1.1	Application to a combustion chamber . . . . .	21
I.1.2	Primary atomization . . . . .	27
I.1.3	Breakup limit . . . . .	30
I.1.4	Numerical investigation on droplet stability . . . . .	35
I.2	Numerical methods . . . . .	36
I.2.1	Navier-Stokes framework . . . . .	37
I.2.2	Navier-Stokes numerical implementation . . . . .	37
I.3	Interface Capturing Method (ICM) . . . . .	38
I.3.1	Introduction to interface numerical treatment . . . . .	38
I.3.2	Interface Capturing Method in DNS . . . . .	39
I.4	Archer . . . . .	43
I.4.1	Treatment of the interface in Archer . . . . .	43
I.4.2	Navier-Stokes coupling . . . . .	44
I.4.3	Block decomposition . . . . .	47
I.4.4	Summary . . . . .	48
I.5	Limits of atomisation . . . . .	48
I.5.1	Under resolved treatment of interface . . . . .	48
I.5.2	Archer volume restriction . . . . .	49

## I.1 Introduction to jet analysis

Two-phase flow atomization is a process of breaking bulk liquids into small droplets. These droplets are often called dispersed phase, that represents the liquid phase. As it will be seen later in this section, small droplets can be considered perfectly spherical. The surrounding gaseous phase is called the carrier phase. The final size of the droplets depends on various forces, one of the most important is the aerodynamic force.

This phenomenon can be observed around us. For example, when walking near a powerful waterfall, [figure I.1a], it is possible to feel small droplets hitting the skin. Another natural example is shown on figure I.1b that represents an atomizing ocean wave, where a lot of sea droplets are ejected from the main liquid core, the white regions on the top of the wave. Even if the water is colorless, the lip transports sediments that change the absorption/scattering coefficient which explains the white color. The transfer of droplets to the carrier phase creates aerosols and impact on the climate. This natural phenomenon is studied to understand its influence on local climate scale [Deike et al., 2016]. More generally, the breaking wave process is also studied in industrial applications to understand wave/dyke interactions [Duran, 2015].



(a) Natural atomization of a waterfall.



(b) Natural atomization on a breaking wave process from [Trontin, 2009].

Figure I.1

This thesis focuses on the treatment of small droplets created by industrial atomization. Several industrial applications exist, see the detailed review of [Nasr et al., 2002]. Three examples of different applications that involve sprays are presented below to show the importance of atomization in different industrial applications: jet for firefighter and jet in sprinklers. Then, it is linked to our goal, the treatment of droplets in combustion chamber.

Firefighters use fire hose in order to reduce the propagation of wildfires. To be efficiently used, they have to control the amount of water that interacts with the flames. They can increase their range of action through the pressure rate, for their application it is important to diminish pressure drop along the pipe since it gives a larger distance from the danger zone. It shows that to understand atomization, we have to study the liquid injection conditions.

In jet sprinklers application they focus on droplets' diameter evolution at several distances from the injector because their goal is to create mono-dispersed spray: all droplets have the same size [Lawson et al., 1988, Grant et al., 2000]. Since droplets are spherical, we express their size in radius. The droplet size distribution is an important parameter to study atomization, and it is evaluated in most of its applications [Hansen, 2013].

In this introductory chapter, we present industrial and physical analysis of the atomization. A first subsection is on characterization of jet and sprays. The second describes the phenomena that generates the first droplets from liquid core. A third section explains how these droplets break in smaller ones.

### I.1.1 Application to a combustion chamber

The spray requirements in combustion chambers evolve with respect to the engine characteristics since they give the atomization conditions. We give a brief description of the atomizer, from the simple shape toward much more complex design. Next, the flow within the atomizer is described and physical properties are briefly studied through a dimensional analysis. This general description permits to introduce some classical analyses used to study sprays: spray angle, breakup length and the droplet size distribution.

#### Industrial atomizers design

A.H. Lefebvre in his book *Atomization and Sprays* [Lefebvre and McDonell, 2017] gives a definition of an ideal atomizer. It must have: a good atomization over wide flow rates, fast response to liquid flow rate change, free of flow instabilities, low power requirements, design flexibility, low cost, light weight, easy maintenance, low susceptibility to damage during manufacture and installation. The balance between those criteria is somehow tight. For example, we can consider the simplest atomizer made of a cylindrical pipe with a diameter reduction at the nozzle, used in old diesel car engine devices. These atomizers some respect ideal requirements such as cheap manufacture, light weight and simple design but face some limits: it is not possible to provide several flow rates.

Moreover, new technological requirements complicate the design of the atomizer, such as in aeronautic where they must be developed following the DGAC (JAR-E) certification which implies a weigh restriction with less pollutant emission. It yields to innovative atomizers development, for example assisted atomizer with air flow that shorten the breakup length, but have higher cost in manufacture design and energy requirements. It shows that knowing the target application and the spray distribution requirements are of first importance to design an atomizer. Sometimes, a simple atomizer satisfies the requirements and good knowledge on its design help to determine it. Following [Lefebvre and McDonell, 2017], the atomizers are divided in three kinds providing a different atomization range.

The first one are the pressure driven atomizers. In this kind of atomizers the destabilization of the liquid bulk is done with the control of the discharge coefficient and the geometry of the atomizer. The discharge coefficient,  $C_{Dis}$ , is defined by:

$$C_{Dis} = \dot{m}_l [A_o (2\rho_l \Delta P_l)^{0.5}]^{-1}, \quad (I.1)$$

where  $\dot{m}_l$  is the injected flow rate,  $\Delta P_l$  is the discharge pressure that represents the pressure loss in the nozzle flow and  $A_o$  the final orifice area. Increasing the discharge pressure increases the liquid velocity input,  $V_{inj}$  and then increases the injection Reynolds number based on the liquid density and kinematic viscosity (respectively  $\rho_l$  [ $kg.m^{-3}$ ] and  $\mu_l$  [ $m^2.s^{-1}$ ]), and the injection velocity,

$$Re_{inj} = \frac{\rho_l V_{inj} L_c}{\mu_l} \quad (I.2)$$

where  $L_c$  is the characteristic length of injection, usually the diameter of the nozzle. For these atomizers, increasing the discharge pressure diminishes droplets' size and increases spray angle [figure I.2].

On figure I.3a a sketch of a simplex injector is given. The design of this atomizer is made of a pipe that drives the flow until the metering orifice where the diameter is reduced to achieve the desired performances. The liquid is ejected from the atomizer at the end of the cup. The manufacture is quite straightforward, which gives the name simplex atomizer. The shape deformation of the liquid bulk for this design is related to the Kelvin-Helmholtz instability [Jiang et al., 2010], described in subsection I.1.2. The typical spray angle is in the range  $5^\circ$ - $15^\circ$  degrees.

The simplest simplex atomizer ejects the liquid phase in quiescent air. In more complex configuration, simplex atomizer are assisted by an air injection around the liquid jet which belongs to the second family of atomizers. This air injection modifies the spray. When the atomization is air assisted, more energy is required for the atomization process. This kind of atomizer introduces a new dimensionless number, the momentum ratio,  $M$ :

$$M = \frac{\rho_l V_l^2}{\rho_g V_g^2}, \quad (I.3)$$

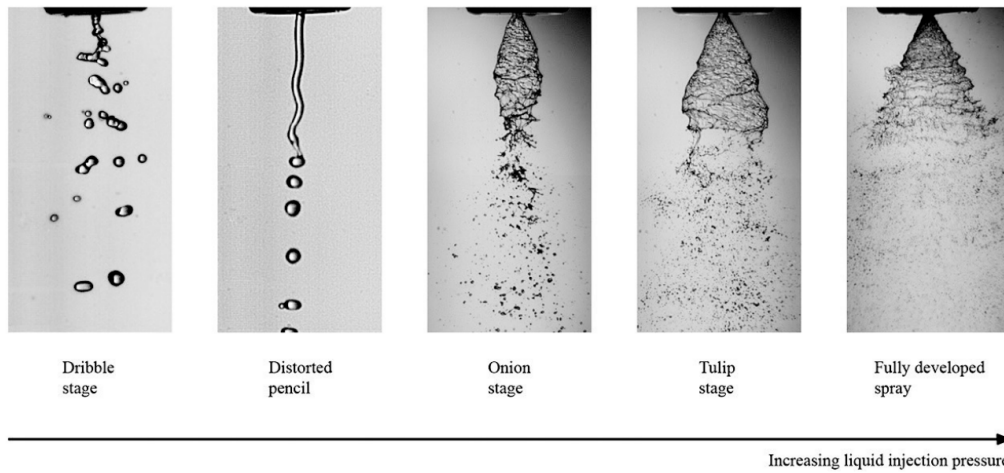
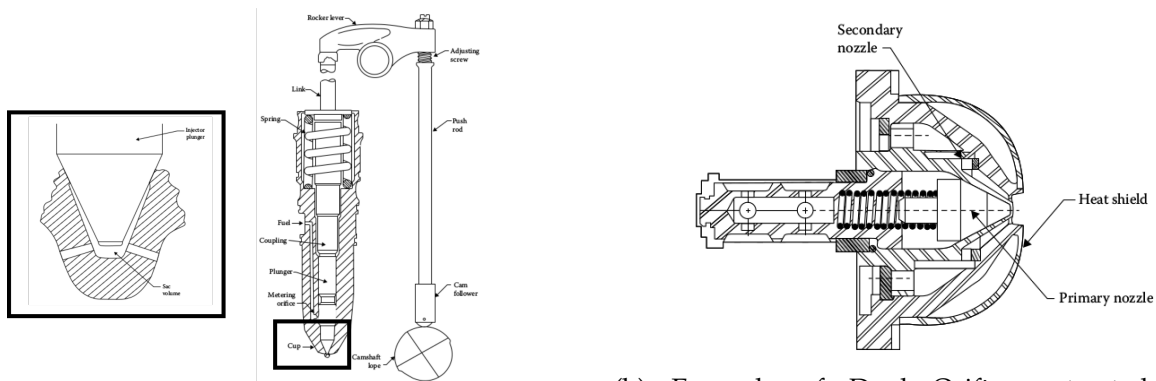


Figure I.2: Influence of the discharge coefficient on liquid instability from [Lefebvre and McDonnell, 2017].

depending on the momentum ratio, different phenomena can occur and the atomization process can be completely different.

An example of air assisted atomizer is displayed on figure I.3b. The primary nozzle injects the liquid within the combustion chamber and the secondary nozzle injects the carrier phase. Compared with simplex atomizer [figure I.3a], the geometry is more complex. Such atomizers are used when it is necessary to increase the energy to destabilize the liquid phase. They are found in applications that require a short breakup length such as aircraft gas turbine. These injectors can have several configurations. For example pre-filming air assisted atomizer that can be encountered in [Mukundan et al., 2019a] where the carrier phase breaks a liquid sheet and transports the liquid parcel. Other configurations are found such as crossflow, the carrier phase is injected perpendicularly to the direction of injection of the liquid [Brown and McDonnell, 2006]. As seen for the pressure atomizer family, the complexity of the atomizer can be enhanced in order to satisfy a specific atomization regime and coupling different technologies.



(a) Diesel Injection from Cummins Engine Company.

(b) Example of Dual Orifice extracted from [Lefebvre and McDonnell, 2017].

Figure I.3

The last family of atomizers use centrifugal force and are called rotary atomizers. The strategy is to add a mechanical rotation induced by an additional surface in the atomizer geometry. For example, it can improve the efficiency of a simplex atomizer. The added material can be a flat disk, a cup, or other surface that permits creating rotary motion. The mechanical rotation of the surface is transferred to the liquid by an injection onto the rotating surface. The higher the motion is, the faster is the primary breakup to happen. Then, the faster occurs the secondary atomization where the primary ejected liquid structures break into small droplets. In short lapse of time, a single rim of liquid is ejected from

the rotating surface and then breaks into several ligaments. The advantage of this fast uniform process is the creation of relatively uniform droplets' size distribution. Indeed, the disk surface plays a key role and influences the results, the smoother and the less friction are, better is the atomization.

Obviously, the shape of the atomizer has a key role in the propagation of interface instabilities leading to breakup, but, as seen in [Payri et al., 2019], injection velocity profiles of both phases greatly influences atomization.

### State of the flow at injection

The physics of the flow within an atomizer before to go through the nozzle and be released within the combustion chamber is an important parameter for atomization. Turbulence's influence on atomization has been studied in atomizer, when possible pipe flow laws can be implemented to recover the characteristics of the atomization, with more or less satisfaction on the results [Payri et al., 2019]. Another more reliable method is to simulate the flow inside the injection and use the results as inlet conditions.

Flow rate can be perturb by other physical phenomenon, the cavitation which involves quick pressure evolution, leading to the creation of vapor bubbles inside the injector. It can have a strong effect on spray evolution and on the final droplets' distribution.

### Dimensionless analysis of the jet

We commented that spray evolution is influenced by the choice of atomizer. Others parameters such as liquid and carrier properties are also important to characterize the flow. This was observed in [Crua et al., 2015] for kerosene/air and diesel/air atomization where the liquid jet breakup was modified by the change of fluids. To study the influence of liquid and gas properties, dimensionless numbers are defined. We propose to review the dimensionless numbers involving the density, viscosity, surface tension and momentum of both phases. All those dimensionless numbers give information on the jet spreading and they are often coupled to provide more knowledge on the spray.

The viscous ratio,  $\mu^*$ , is a dimensionless number that compares the dynamic viscosity of the liquid phase and the carrier phase:

$$\mu^* = \frac{\mu_l}{\mu_g}. \quad (\text{I.4})$$

In general, a large liquid viscosity implies a higher resistance to deformation.

The density ratio,  $\rho^*$ , is a dimensionless number based on the density of each phase:

$$\rho^* = \frac{\rho_l}{\rho_g}. \quad (\text{I.5})$$

In atomization, the density ratio evolves when the pressure changes, and it is important to quantify its influence on atomization. For example, if the density ratio is increased at constant injection's velocity, the inertial force is increased.

An example of its outcome on the spray dispersion is represented on figure I.4 from a numerical simulation [Herrmann, 2010b]. The configuration is a turbulent liquid round jet atomized by an air crossflow that provokes its bending. All physical and geometrical parameters are kept constant to study the influence of the density ratio. On left image, the density ratio is set to  $\rho^* = 10$ , ten times smaller than the density ratio of the right image. It results in a smaller jet penetration that influences the droplet size and spatial distribution. It is observed by the size of the liquid core: the left jet shows a bigger liquid core than the right image.

Viscous and density effects are coupled in the dimensionless Reynolds number,  $Re$  [equation I.2]. Reynolds number can be defined based on injector geometry to determine injection regime, laminar or turbulent. The transition between the two states is found in the range  $Re = 2000 \sim 5000$ , a transitory Reynolds number can be defined to discriminate both regimes, based on the injector geometry. Laminar flow are found in liquid jet with small deformations, they are observed when the liquid leaves a tap with small motion. Turbulent flow are chaotic, they are observed in most of the

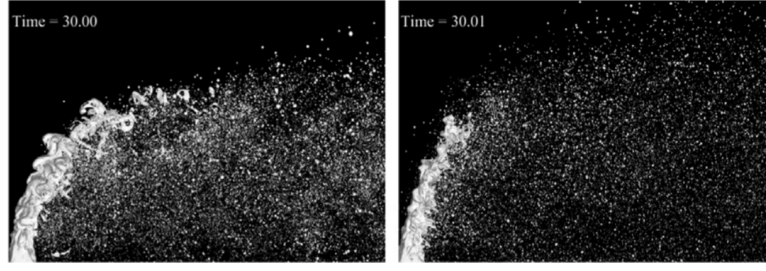


Figure I.4: Jet in crossflow for two density ratio, left:  $\rho^* = 10$ , right:  $\rho^* = 100$ , from [Herrmann, 2010b].

combustion chamber application. This thesis focuses on jet at high Reynolds number that leads to wide dispersion of droplets of small size.

The Reynolds number is often coupled to the Weber number to define parameters of atomization. This dimensionless number compares the inertial force to the surface tension force which is the force that maintains the equilibrium of a shape, i.e. that maintains droplets spherical. This number is defined by:

$$We = \frac{\rho_g V_{inj}^2 L_c}{\sigma}. \quad (I.6)$$

Due to the wideness of fluid mechanics applications and the interest in inertial vs surface tension forces, the Weber number has a lot of expressions, changing the velocity and characteristic length. For example the Weber number quantifying atomization range uses  $L_c$  to represent the diameter of injection and injection velocity, and the higher it is the more small droplets are created. These dimensions are modified to evaluate droplets' breakup, the characteristic length becomes droplets' diameter and the velocity is the slip velocity between the droplet and the carrier phase. Using the slip velocity to characterize the droplets' Weber number is an assumption open to discussion [subsection I.1.4].

From Weber number and Reynolds numbers, the dimensionless capillary number,  $Ca$ , can be derived. It quantifies the viscous effects to the surface tension ones. Again, with the presence of the stabilizing forces on the denominator, the higher is the capillary number, the smaller are the droplets.

$$Ca = \frac{We}{Re} = \frac{\rho_l V_{inj}^2 L_c}{\sigma} \times \frac{\mu_l}{\rho_l V_{inj} L_c} = \frac{\mu_l V_{inj}}{\sigma} \quad (I.7)$$

In the definition of Reynolds, Capillary and Weber numbers, the main forces acting on the shape deformation of the liquid bulk are present: viscous, inertial and surface tension forces. Those dimensionless numbers depend on the flow velocity. In some configuration, it is interesting to remove the velocity in the dimensionless number conserving the physical properties of the both phases, for example the Ohnesorge number,  $Oh$ . It is the ratio between the squared root of Weber number and Reynolds number:

$$Oh = \frac{\sqrt{We}}{Re} = \frac{\mu}{\sqrt{\rho \sigma L_c}}. \quad (I.8)$$

It depends on the surface tension, viscosity, density and the characteristic length. The surface tension and inertial forces are together at the denominator, opposed to the viscous effects. The Ohnesorge number quantifies viscous force influence in liquid jet deformation. It is also often used to study the droplets' stability.

Several dimensionless numbers, among many others, have been introduced to characterize fluid properties influence on the spray behavior. Now we focus on the spray analysis and the characteristics that can help to describe it.

### Spray characteristics

According to the application, the atomization spreading varies. It is then necessary to determine the characteristics of the spray that can differentiate them. We define three common parameters: the

spray angle, the breakup length and the droplet size distribution.

### Spray angle

The spray angle is the angle formed by two straight lines drawn from the atomizer's nozzle orifice on the edge of the liquid cone. It gives a spatial representation of the jet. In the earliest studies, spray angle measurements were obtained with tubes displayed circularly in a  $r - \theta$  axis. After a given atomization time, the quantity of atomized liquid in each tube provides information on the liquid volume fraction at various spray angles. It gives a spray angle representation with a spatial volume fraction evolution, at the distance of choice of the atomizer. This representation is showed on figure I.5 where the spray is showed on the left figure and its volume fraction evolution along  $\theta$  on the right figure.

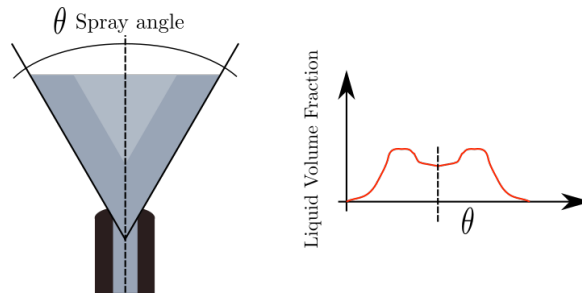


Figure I.5: Representation of a spray with angle measurements.

At constant fluid properties, the spray angle is influenced by the nozzle geometry and dimensions and the discharge coefficient. At constant flow rates, a relation to determine the spray angle is given in [Lefebvre and McDonell, 2017] that shows geometrical design influence and fluid properties' independence in spray angle measurements. We list this equation below expressed in terms of combustion chamber's dimensions:

$$\tan \theta = \frac{\frac{\pi}{4}(1 - A_a/A_0) \times K_\theta}{B} \text{ where } B = \frac{A_p}{D_m d_o} \left[ \frac{D_m}{d_o} \right]^{1-n_\theta}, \quad (\text{I.9})$$

with  $A_a [m^2]$  the aire core area,  $A_p [m^2]$  the inlet ports area,  $D_m [m]$  the diametric distance between centerlines of inlet ports and  $d_o [m]$  the orifice diameter. Parameters  $K_\theta$  and  $n_\theta$  are defined empirically:

$$n_\theta = 28A_o^{0.14176} \times \frac{A_p^{0.27033}}{A_s^{0.17634}} \text{ and } K_\theta = 0.0831 \times \frac{A_p^{0.34873}}{A_o^{0.26326} A_s^{0.32742}} \quad (\text{I.10})$$

with  $A_s [m^2]$  the area of the swirl atomizer chamber.

This result is evaluated for non-viscous flow using simplex atomizer [Babu et al., 1990]. Considering viscosity influences spray angle due to frictions inside the atomizer, it reduces the tangential velocity. It is characterized by a boundary layer at the wall, it increases with the viscosity ratio. Then, it is observed for simplex atomizer that the higher is the viscosity the more limited is the spray angle [Chen et al., 1992b]. Nevertheless, the main variation between experiments and inviscid theory remained below 10%. Other models consider the influence of the surface tension and the density in their determination of the spray angle.

### Breakup length

The breakup length is a metric information, it is the distance from the atomizer where the liquid bulk breaks. It represents the beginning of the area called primary atomization composed of droplets, ligaments and other liquid structures with complex interactions. As for the spray angle, it is expected to reduce breakup length in order to avoid waste of fuel on combustion chamber's wall or poorly atomized fuel. A method to determine the breakup length is to inject a laser light through the nozzle



to illuminate the liquid jet. The main advantage of this technique is that the laser light follows the bending of the jet [Charalampous et al., 2009]. When the liquid breaks, the laser induced fluorescence stops giving liquid core breakup length.

### Droplet size distribution

As priorly introduced, droplet size distribution is used to determine the efficiency of atomization. The size considered is their radius, the small droplets are supposed spherical and no longer candidate to breakup or deformation because the action of the surface tension overcomes the action of the aerodynamic forces. For ligaments and larger droplets, an equivalent radius can be obtained based on different assumptions, for example perimeter or surface area. In experimental studies, several intrusive and non-intrusive strategies exist to determine the size of the droplets. They can involve X-Ray, laser, images or even holography. Some of them are more reliable for the droplets' size measurements while other are more relevant for large scale analysis.

First, we describe the rainbow pattern analysis of isolated droplets. A specific interaction is created between a droplet and laser light [van Beeck and Riethmuller, 1996]. This interference gives a rainbow pattern, from this pattern, it is possible to determine the droplet's diameter, velocity and temperature. The drawback of this method is that the rainbow pattern is obtained only for the spherical droplets and is mainly used to study the dispersed area.

Another strategy to recover information on droplets is the Phase Doppler Particle Analysis (PDPA), that is based on Phase Doppler Interferometers (PDI) [Bachalo and Houser, 1984]. A laser light scatter detection is used to measure the spherical droplet size/velocity. It consists in the analysis of the interference between two laser beams and the droplet. Then, the phase of the signal is analyzed with the Lorenz-Mie theory to recover droplets' characteristics. The advantage of this method is that it is non-intrusive [Schober et al., 2002].

Other methods provide an entire 2D atomization description, for example shadowscopy, using series of images to provide the statistical evolution of the flow. The method depends on the quality of the camera: the higher is the number of pixels in a droplet, the better they are described. The drawback of this technique is that the droplets can be out of the focus of the camera, it creates a loss of information, this issue is improved in [Yon and Blaisot, 2004]. Finally, the surface of the droplet is obtained through image processing from which droplet radius is deduced.

X-rays analysis are a novel method in the jet description. The advantage of X-rays is that they are able to penetrate dense liquid region, providing a scalar information on jet thickness [Bothell et al., 2020]. Another advantage is that the refraction and diffraction at the interface is lower for X-rays. The images obtained from this analysis quantify the droplets' size distribution. However, the development of these methods remains costly and require protected installation.

The acquisition of droplet diameter allows to generate an histogram. The bins are expressed in terms of diameter interval  $\Delta D$ . The normalized histogram provides the probability distribution function. This distribution can be fitted with different laws, such as the log-normal distribution. In figure I.6b an example is given.

The dispersion of the jet can be quantified by its standard deviation,  $\mu$ . In [Kolev, 2015], a definition of poly-dispersion is given based on this standard deviation. When its value exceeds 10% of the mean diameter, the distribution is no longer mono dispersed. The distributions given in figure I.6b have a single mode that is characterized by the diameter  $D_{peak}$ . A bi-modal distribution, which is characterized by two local maximum on the distribution, indicates the presence of two distinct atomization process. Droplet distribution with more than one mode can be observed in twin-fluid atomizers [Li et al., 2013].

On figure I.6b, other information are displayed. They are expressed in subscript diameter and provide various information on the spray and some of them are described below.

In atomization, a quantity is often used, the ratio between the averaged volume of droplets and the averaged surface area, it is the Sauter mean diameter or SMD on figure I.6b. Its definition is set in equation I.11, where a and b represents the metric considered. For the Sauter mean diameter,  $D_{32}$ , the

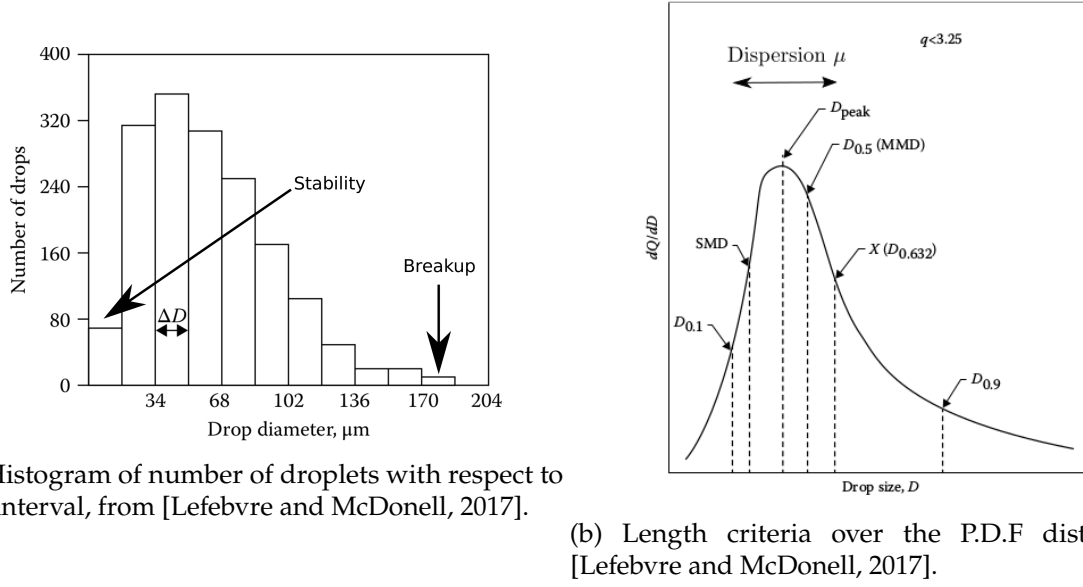


Figure I.6

equivalent volume [ $m^3$ ] and surface [ $m^2$ ] are considered, giving  $a = 3$  and  $b = 2$ .

$$D_{ab} = \left[ \frac{\sum N_i D_i^a}{\sum N_i D_i^b} \right]^{1/(a-b)} \quad (\text{I.11})$$

Due to the variety of atomizers and regimes, it is not possible to determine an empirical law providing a universal size distribution function. Some empirical correlations exist for specific applications. They can be simple or include a lot of parameters to provide a good fitting with the studied distribution. An example of empirical law is the one to determine the Sauter Mean Diameter [Merrington and Richardson, 1947] and more of them are detailed in [Sirignano, 2010]. From those results, an approximation of droplet distribution can be obtained, for example with the use of the Rosin-Rammler distribution which can be sufficient in some studies.

The aim of our study is to improve the description of the jet with the conservation of all scales of atomization. The primary atomization is described in the next section with a focus on the main shape deformation that occurs in such applications. It provides insight on the breakup length and size of the bigger droplets in this area. Then, the dispersed area is described with a focus on the stability of small droplets in jet.

### I.1.2 Primary atomization

The liquid bulk shape deformation at injection is due to the action of forces that overcome the surface tension force. They have been characterized in dimensionless numbers such as Weber, Reynolds or Ohnesorge numbers giving a general description of the atomization evolution.

For meticulous description of the jet, it is important to determine how the shape deformation evolves, resulting in the creation of the primary atomization area. Some simplified interface phenomena allow us to understand the atomization. Three of them are briefly introduced in the next section, usually called surface instabilities. The conditions needed to see these instabilities grow during atomization and their locations are given.

#### Plateau-Rayleigh

The condition to observe the development of the Plateau-Rayleigh instability are: a cylindrical liquid shape and an initial deformation at its surface. This instability is purely geometrical and is initialized by inertia. In other words, it can be reproduced without any initial velocity. The deformation

can be initialized on the surface of the cylinder with a bending or produced by a velocity modulation or jet vibration. With time the deformation increases until the cylinder breaks. Thus, under the action of the surface tension, the liquid ejected from the jet evolves until a spherical shape. An example of this instability is given on figure I.7 from *Archer* simulation where the instability is produced through the velocity profile inside the liquid cylinder. A pinch off is observed and a droplet is created. Then, droplets evolve under a prolate-oblate morphology.

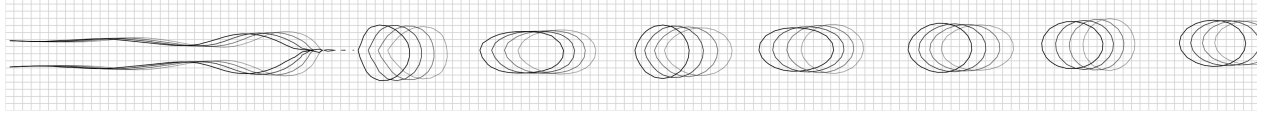


Figure I.7: Plateau-Rayleigh Instability on a cylindrical atomized liquid jet in quiescent air [Chapter IV].

The result of the Plateau-Rayleigh instability is the creation of a main droplet and, under some conditions, smaller satellite droplets.

A mathematical analysis of the growth rate at the interface permits to determine the number of ejected droplets for inviscid regime [Lord, 1900]. The conditions are a specific wavelength,  $k$  that is of the order of  $kR_0 \approx 0.697$  with  $R_0$  the initial radius of the cylindrical jet. Under these conditions, several parameters are determined. The example is given for atomized cylindrical jet with an initial liquid velocity  $U_0$  in quiescent air, which is more representative of our application. The radius of the ejected droplet,  $R_d$ , the breakup length,  $L_b$ , and the time of breakup,  $t_b$ , are obtained from equation I.12 where  $q$  represents the growth rate of the initial disturbance  $\eta_0$ . For numerical study, this instability can be used to determine exactly if the physic is well reproduced by models or simulations against the theory.

$$R_d = 1.89R_0, \quad L_b = U_0 t_b = \frac{U_0 \ln(1/\eta_0)}{q} \quad (\text{I.12})$$

The atomization driven by this instability is found for example in simplex atomizer at low discharge coefficient. Indeed, this phenomenon can occur in more complex atomization that creates several size of droplets. This instability is observed also for the ligaments' breakup in the secondary atomization. The breakup of ligaments under the influence of Plateau-Rayleigh instability creates various droplets. It has been observed in some experimental results that the viscosity influence the number of droplets' [Marmottant and Villermaux, 2004a]. The more viscous the more extended is the ligament and the smaller are the droplets. This specific event is called an erosive breakup and it can be observed for ligaments. A simple representation is given on figure I.8. The spherical droplet is first flattened, then, it has a prolate shape and under the action of external forces, the tip of the droplet is reduced and the erosive breakup appear. More detail on this specific event are given in the subsection I.1.3.

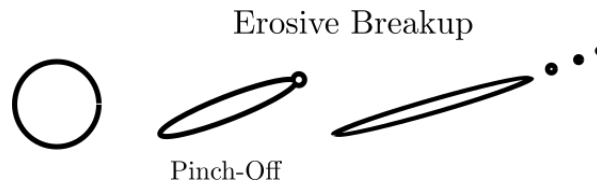


Figure I.8: Ligament erosive breakup illustration.

## Rayleigh Taylor

The Rayleigh Taylor instability [Lord, 1900] is the result of a heavy fluid penetrating a lighter one. It requires an initial perturbation at the interface, then, the heavy fluid penetrates the lighter one until it takes the position of the lighter one. This instability is often characterized by the mushroom shape of the penetrating phase. It is naturally observed on volcanic eruptions where a mushroom cloud is formed or under the action of gravity for water above oil. For industrial atomization, the

Rayleigh-Taylor instability can be observed in diesel jet atomization for example, where the action of the gravity is replaced by the acceleration of one fluid into another. The difference of densities between the two phases determines the evolution of the instability. A dimensionless number based on it is defined: the Atwood number:

$$At = \frac{\rho_l - \rho_g}{\rho_l + \rho_g}. \quad (I.13)$$

### Kelvin-Helmholtz

This instability is generated by a difference of velocity gradient at the interface. It is driven by aerodynamic force. The modification of the surface is represented by the development of vortices near the interface. These vortices roll the surface and create waves or ligaments. The droplets are tears off the main liquid structure, it can be assimilated to an erosive breakup. The development of this instability is widely observed in natural flows, clouds for example [figure I.9a]. In industrial atomization, this instability is often encountered in air blast atomizer because of the velocity difference between the two phases. At high momentum ratio we can observe the vortices motion at the interface developing in two dimensions. The size of the resulting ligaments is related to the wave evolution and can modify the droplet size distribution. An example of liquid sheet atomization is given in figure I.9b from [Crapper et al., 1975] where the creation of vortex is observed, leading to wave breakup.



(a) <https://tempojaopessoa.jimdo.com/nuvens> (b) Snapshot of liquid sheet atomization with Kelvin-Helmholtz induced wave breakup [Crapper et al., 1975].

Figure I.9

### Summary

The brief review of those three main instabilities found in liquid phase shape deformation is important to understand the physics behind the primary breakup. In complex atomization, those instabilities, induced by the slip velocity, ratio of density and capillary motion are encountered and act to overcome the action of the surface tension. It is then not surprising that in some primary breakup study [Marmottant and Villermaux, 2004b], using a coaxial jet configuration, they identified the action of the Kelvin-Helmholtz instability to initialize a small perturbation induced by velocity difference at jet interface. Then, this perturbation evolves and density ratio plays a role since we observe the development of a Rayleigh Taylor like instability. Oscillating waves are then transformed into a cylindrical mushroom headed structure [figure I.10]. Finally, the liquid is detached from the liquid core with oscillation shape deformation growth, which is due to Plateau-Rayleigh instability.

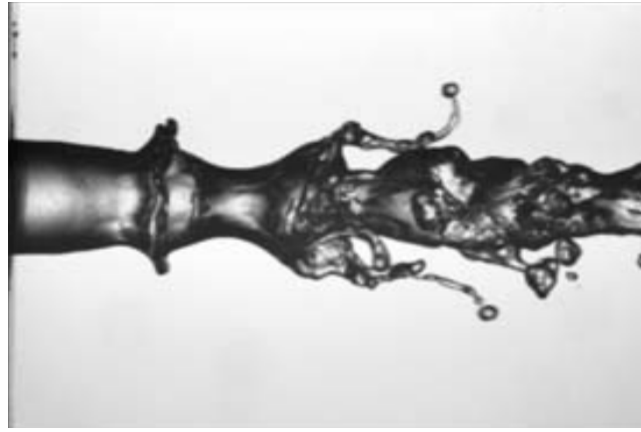


Figure I.10: Coaxial atomization from [Marmottant and Villermaux, 2004b].

In this section we have seen that instabilities are the reason why the liquid jet breaks. They can be modified by the flow motion, the combustion chamber's geometry or fluid properties. Due to the wideness of parameters, it is complex to analytically describe the evolution of the jet. Experimental studies are used to understand the primary atomization area [Dumouchel, 2008]. Some conclusions from primary atomization studies are extrapolated to the study of the dispersed phase. Since structures in this area are smaller and more dispersed, breakup phenomena are different. Some conclusions obtained on the analysis of the breakup are presented in the next section.

### I.1.3 Breakup limit

The purpose of this section is to determine the diameter below the which spherical droplets no longer break. This diameter can be different depending on the application and the physical properties of the fluids, it is not the same in high turbulent jet or in high viscous jets. The goal of this section is to introduce different families of stability analysis.

To compare them, some characteristic numbers of droplet stability are provided such as the averaged breakup time,  $t_b$ , and the critical droplet's diameter  $d_{crit}$ . The breakup time is the averaged lifetime of droplets of a given size before breaking into smaller droplets. This time should be compared to the other times such as the evaporation time or the traveling time in the combustion chamber to determinet the relevant characteristic time. The critical diameter is the diameter below the one droplets no longer break. Due to the variety of forces in two-phase flow, this critical diameter can be defined at for several stages of atomization process, for example when aerodynamic force is dominant [Janssen and Meijer, 1993], or when the turbulent motion is dominant [Hinze, 1955]. It is different from the smallest diameter because in chaotic sprays, size dispersion is often very wide. The reason why several breakup analyses are proposed is due to the complexity to consider various phenomena [Guildenbecher et al., 2009, Wierzba, 1990]. First models were following four main assumptions on droplet breakup mechanism [Lasheras et al., 2002, Liao and Lucas, 2009, Solsvik et al., 2016]. They are the following one:

- Viscous shear stress
- Turbulent motion of the jet
- Shear off
- Instabilities

This section is specially focused on viscous breakup and turbulent breakup. The shear off breakage can be assimilated to viscous breakup and is not described. The instabilities considered for the droplet breakup are described in subsection I.1.2 and are not described neither. Next, we focus on viscous and turbulent breakup. To conclude, an introduction on complex models considering several destabilizing forces is given.

## Viscous shear breakup

The viscosity influences the droplet breakup evolution. It creates a gradient of velocity on its interface that elongates the droplet through a ligament shape. The viscous force has been studied in experiments [Grace et al., 1978] where a shape evolution analysis of a droplet for several range of capillary number and viscous ratio has been done. In his experiments, the droplet was immersed in a pipe at constant flow rate. A modification on the capillary number defined in subsection I.1.1 is defined at droplet scale. The modification replaces the velocity of the flow by the shear flow at the interface of the droplet,  $\dot{\gamma}$ , with droplet diameter  $d_d$  [equation I.1.3].

$$Ca = \frac{\tau_v}{\tau_s} = \frac{\mu^* d_d \dot{\gamma}}{2\sigma} \quad (\text{I.14})$$

From equation I.1.3 we can obtain a diameter of stability for a critical capillary number:

$$d_{d,crit} = \frac{2\sigma Ca_{crit}}{\mu^* \dot{\gamma}}, \quad (\text{I.15})$$

from the which it is possible to determine a breakup time from empirical function [Liao and Lucas, 2009, Wierzbna, 1990] depending on the viscous ratio  $\mu^*$ .

From their experiments done in shear flow [Grace et al., 1978, Janssen and Meijer, 1993], it is possible to draw a map of droplets' morphological evolution [figure I.11]. Two regimes are drawn: stable and unstable. The lower is the capillary number the more stable is the droplet. However, in their definition, stability does not imply that the droplet remain spherical, see for example the influence of the viscous ratio on the elongation of the droplet. From their respective work, we can provide an estimation of the shape deformation from the shear at the interface and the viscous ratio. Moreover, a quantity that is often used in breakup model, the number of resulting droplets from a breakup can be estimated.

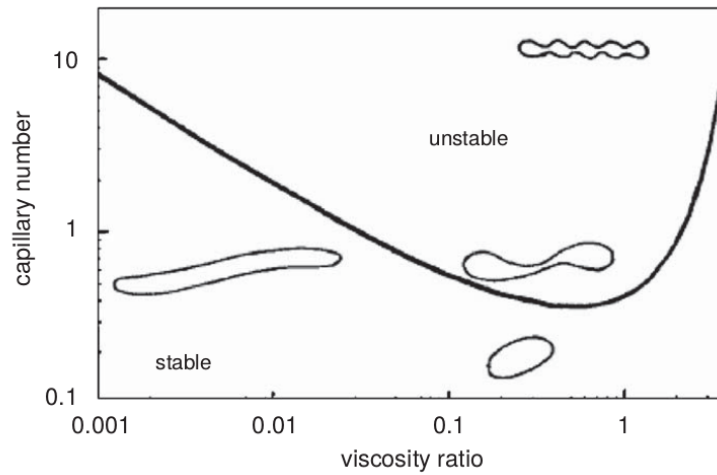


Figure I.11: Breakup regimes map with capillary number against viscous ratio [Janssen and Meijer, 1993].

## Turbulent breakage

The pioneer work of [Hinze, 1955] highlighted the influence of turbulence on droplets breakup using analytical study of [Batchelor, 2019] and experimental results of [Clay, 1940]. The theoretical work of [Batchelor, 2019] is on the fluctuation of velocity induced by turbulence to determine a critical breakup Weber number. The definition of this critical Weber number is showed in equation I.16.

The characteristic velocity is the velocity fluctuation of the carrier flow,  $\bar{u}^2 [m.s^{-1}]$ . The experiments used were done for water/air droplets' emulsion in turbulent flow at carrier phase Reynolds number of the order 5,000 to 50,000.

$$We = \frac{\rho_l \bar{u}^2 d_d}{\sigma} \quad (\text{I.16})$$

In Batchelor's theory [Batchelor, 2019], the fluctuation of velocity is linked to the dissipation  $\epsilon$  [ $m^2.s^{-3}$ ] within the system for large scales of turbulence  $L$ . To apply its theory, an empirical constant  $\beta$  is used, the Batchelor constant:

$$\bar{u}^2 \Big|_L = \beta (\epsilon d_d)^{2/3}. \quad (\text{I.17})$$

Equation I.17 is coupled with equation I.16 to express a critical Weber number:

$$We = 2 \frac{\rho_g}{\sigma} \epsilon^{2/3} d_{d,crit}^{5/3}. \quad (\text{I.18})$$

From this equation, one can extract the critical diameter, also called the Hinze diameter:

$$d_{d,crit} = C_1 \left( \frac{\sigma}{\rho_g} \right)^{3/5} \epsilon^{-2/5}. \quad (\text{I.19})$$

Hinze diameter involves a lot of assumptions because it does not include the density and viscous ratio influence. It requires an empirical constant  $C_1$ , set to  $C_1 = 0.725$ , and it provides an empirical critical Weber number but the lack of experiments makes it uncertain. Nevertheless, it is known that the dissipation is stronger at the interface due to energy transfer [Dodd and Ferrante, 2016], including the dissipation into the breakup analysis is then highly relevant.

To diminish Hinze hypotheses influence, other turbulent flows have been studied to describe the critical droplet size. In [Sleicher Jr., 1962], the turbulent flow is initialized in a pipe where the droplets are immersed. He studied the influence of the turbulence and the shear at the interface with a variation of the mean carrier velocity. First, he focused on the turbulence intensity influence's on the breakup. The results showed the influence of the viscosity and density ratio, showing that they should be considered in breakup study. A relation between the turbulent motion and the morphological evolution of the droplet until rupture called a vibrational breakup is then introduced. Second, he analyzed the influence of the turbulent shear on the breakup. He observed that this experimental setup was not a good candidate to explain the breakup of droplets because the shear can be influenced by the non homogeneity of the turbulence. The issue is that this definition is obtained for the pipe flow motion and it is not extended to other configurations which limits its observations.

A result of this study is the importance of considering the density and viscosity of both phases to improve secondary breakup model. The relevant parameters to turbulent breakup can be resumed in a function:  $F(\mu^*, \rho^*, \bar{u}^2, \sigma)$ . They are used to redefine the equation of the fluctuation of velocity with the results obtained in [Sleicher Jr., 1962]. It gives a critical Weber number, [equation IV.3], based on the Taylor length scale. In this equation, the energy spectra length scale is used which is determinant for future turbulent breakup models.

$$We = \frac{\rho_l \bar{u}^2 \Big|_L d_d}{\sigma} \quad with \quad \bar{u}^2 \Big|_L = C_1 (\epsilon \lambda)^{2/3} \quad (\text{I.20})$$

More recent work have been trying to couple the interactions between the morphological evolution of the droplets and the energy transfered by the turbulent motion of the carrier phase. Several theories are observed in the literature, some considering that the energy of the eddies is the dominant factor, others considering that it is the droplets' stabilizing energy. We classify them as follows:

- turbulent kinetic energy greater than an arbitrary defined critical value of Energy,  $E_{bu,d}$  [Chen et al., 1998, Bałdyga et al., 2001, Aly et al., 2010],
- turbulent velocity fluctuation greater than  $E_{bu,d}$  [Zaccone et al., 2007, Maaß et al., 2012],
- eddy energy greater than  $E_{bu,d}$  [Karimi and Andersson, 2018],

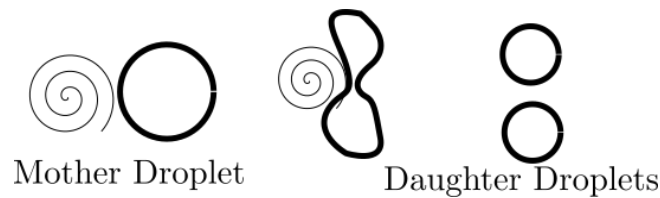


Figure I.12: Mother droplet breakup scheme.

- eddy turbulent inertial stress greater than daughter restoring stress [Solsvik et al., 2016, Håkansson et al., 2009] [figure I.12].

The difference between these models is that they do not require the same information. For example some require the turbulence magnitude while others require the droplets' daughter diameter, created by the breakup of the initial droplet, called the mother droplet [figure I.12]. These information are complex to couple since they are individually complicated to recover, for example the number of daughter droplets. An assumption is that a mother droplet always break into two droplets of equal size: a binary breakup. This breakup mechanism has been studied in the experiments [Walter and Blanch, 1986] where they identified three stages for the binary breakup. First: an oscillatory regime induced by the eddy-droplet interactions. To recall, it was observed in the morphological analysis of droplet-eddy interaction [Sleicher Jr., 1962]. Second, a stretching of the droplet which results into the last stage: pinch off of the surface yielding to a breakup. An open conclusion of their work is that various turbulent scales interact with the droplet and transfer energy to break it.

The binary breakup assumption was also discussed in the work of [Martinez-Bazan et al., 1999]. They showed that at high Weber number, even for small droplets, the assumption of binary breakup is no longer relevant. Then, the higher is the Weber number, the more complex it is to determine the number and the size of the small droplets. This model becomes challenging to use to determine the stability of the droplets.

More studies have been done to characterize the binary breakup and involved parameters, other than Weber number. In the work of [Andersson and Andersson, 2006], the binary breakup is linked to the density ratio and the global dissipation of the system. The higher is the density ratio, the higher is the probability to obtain a binary breakup. The reason is that more energy is required to overcome surface tension effects and the inertia of breakage is higher. The dissipation influences the number of droplets that are created. The higher is the dissipation of energy, the higher is the probability to obtain a binary breakup. They also validated the hypothesis that the turbulence has a multi scale influence on droplet's breakup following prior observations [Walter and Blanch, 1986].

From the spectra of energy, they defined three scales that are all acting differently on the droplet deformation for a droplet in the inertial range:

- The micro scale: Kolmogorov scale,
- the meso scale: order of the droplet radius and below,
- the macro scale:  $\approx$  droplet diameter and above.

The micro scale influences the droplet interface with the creation of small velocity fluctuations. These fluctuations create ripples that evolve at the interface. The amplitude of these ripples does not drastically grow because they do not have enough energy to break or flatten the droplet. The meso scale propagates oscillations on the entire droplet. They observed a flattening of the droplet of  $\approx 30\%$  of its initial shape. It is not sufficient to break it but induces the surface deformation. After some time, the surface tension acts to recover the equilibrium spherical droplet's shape and oscillations vanish. The macro scale transfers enough energy to the interface to break it, these eddies are located through the inertial range. They also commented in their study that the bigger eddies in the system do not influence the breakage mechanism but they only transport the droplets. From this experiment, we can resume the interaction between eddies and droplets through the scheme I.13 inspired from [Han et al., 2011].



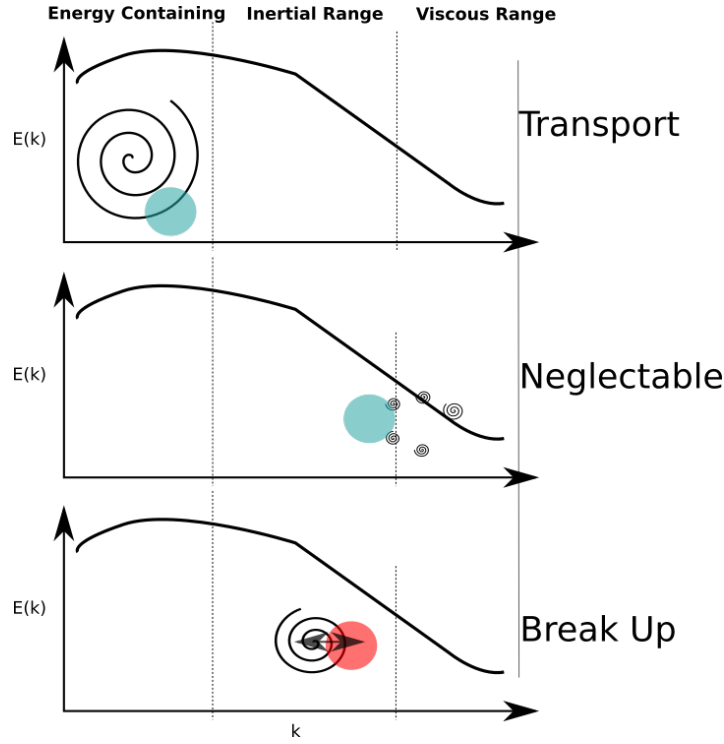


Figure I.13: Droplet-Eddy interaction scheme.

In [Andersson and Andersson, 2006], they also studied the breakup time evolution. They linked it to the average time that an interaction between macro scale eddies and droplets interact. It depends on the droplet diameter and the global turbulent dissipation. Then, if a droplet do not break after an equivalent breakup time, it means the eddy does not bring enough energy. The definition of the breakup time [equation I.21] where  $k$  [ $m^2.s^{-2}$ ] is the turbulent kinetic energy. This time must be compared to other characteristic times in combustion chamber.

$$t_b = \frac{2}{3} \frac{k}{\epsilon} \quad (I.21)$$

The small influence of the micro scale is an advantage in breakup modeling due to the numerical requirements to simulate them. However, recent works showed that this assumption is inaccurate [Karimi and Andersson, 2018]. The small scales are more relevant to the local dissipation near droplet. Improvements of these models could be done with the definition of local quantities, for example: the fluctuation of velocity at the interface. This quantity can vary around a droplet, and, numerical study of the flow near the droplet might provide key data to model turbulent breakup [Dodd and Ferrante, 2016].

### Coupled breakup model

In our application, aerodynamic, viscous and turbulence influence are the main parameters on breakup modeling. They are extensively investigated to determine the most accurate model. In specific atomization model, those effects can be found at different scales of the jet. Models that consider both of those forces are developed. For example, in the work of [Chen et al., 1998], their model is based on a relation between an energy ratio from eddy versus droplet's surface tension. They also include the damping effect that follow surface oscillations and the viscous effect on the breakup probability. It gives a complex model that tries to represent all the breaking factors.

In the experiments of [Galinat et al., 2007], they studied the behavior of an immersed droplet in inhomogeneous turbulence for several range of velocities. In their work they compared Kolmogorov-Hinze theory [Hinze, 1955], explained above, and Rayleigh-Lamb theory that focuses on droplet oscillations evolution. The droplet dynamic, represented by series of oscillations in the Rayleigh-Lamb approach, has been modeled with a frequency and a damping rate. The main idea of their work was to

point out that the breakup depends on the Weber number. At high Weber number the turbulence is responsible of breakup while at low Weber number, surface oscillations are responsible of breakup. To validate these results, a numerical model including the two theories has been developed where the evolution of the breakup criteria showed a different evolution on the same droplet. In their results they showed a strong dependency to the initial conditions of the simulation.

Since the computational power has been increasing, numerical studies are used to overcome the lack of experimental results in turbulent breakup studies. Since two models have been giving different results in the work of [Galinat et al., 2007], it is important to implement different numerical models [Aly et al., 2010]. In their work, they compared breakup probability under turbulence and aerodynamic forces for air assisted coaxial atomizer and showed the importance of coupling both models. The turbulent velocity fluctuation is based on the work of [Kocamustafaogullari and Ishii, 1995], [equation I.22], the characteristic length represents the inertial eddies diameter. This equation is of first interest for us because it is defined for high density ratio and represents our two-phase flow applications. The aerodynamic breakup is estimated on a critical Weber number computed from the slip velocity between both phases:

$$u^2 \Big|_L = \frac{\rho_l - \rho_g}{\rho_l} \rho^* \beta (\epsilon L_c)^{2/3}. \quad (I.22)$$

They showed that the breakup induced by aerodynamic force, calculated from [Kolev, 2015], appears near to the nozzle while turbulent breakup was dominant in the dispersed phase.

We note that dominant mechanisms are correlated with the primary and secondary breakup area of a jet. For primary atomization, the dominant forces are the aerodynamic and viscous forces. For the secondary atomization, the dominant phenomenon is the turbulent interaction with the droplet. To improve the treatment of the small droplets, we must consider the velocity fluctuation at the interface. One of the criteria to determine the numerical stability of a droplet must be related to the turbulent motion of the dispersed area. These Lagrangian statistics give relevant information on forces acting on small droplets. It must be helpful to improve the secondary breakup modeling, one of the objective of our investigation on the dispersed spray zone.

#### I.1.4 Numerical investigation on droplet stability

Numerical study is a delightful tool to study the droplet breakup. It permits to create the desired physical conditions to study droplet's breakup. The viscous force influence onto breakage has been widely investigated. Significant results have been obtained in the work of [Renardy, 2008]. She showed the influence of initial conditions on droplet breakup recovering the Grace curve [figure I.11]. She also showed that the angle of inclination of the droplet with respect to the stream flow is important in the droplet motion. The control of the angle between the droplet and the flow motion is the example of study that can be performed with numerical tools. It would be challenging to study its influence experimentally.

On the turbulent induced breakage, the Weber number based on Kolmogorov-Hinze theory coupled with the evolution of the surface to detect breakage of droplet in Homogeneous Isotropic Turbulence, (HIT), has been used [Perlekar et al., 2012], which was one of the first highly resolved simulation, on  $512^3$  cells. Following Hinze assumptions, they used a ratio of density and viscosity equal to 1. In their work, they directly calculated the fluctuation of the velocity without Batchelor assumption [Batchelor, 2019]. Then, they defined this relation as a ratio between the average droplet velocity and the maximal velocity at the surface of the droplet which allowed them to define a local weber number. The evolution of the surface was then a ratio between the total surface of the deformed droplet and its initial surface. Their results showed that the fluctuation based Weber number, [equation IV.3], increases with the surface deformation. When the droplet breaks, the Weber number is at its maximum. Their work showed the importance of considering local information instead of global information due to the proximity with the surface evolution.

Based on the importance of the local information, the two fluid Turbulent Kinetic Equation in a droplet laden decaying isotropic turbulence has been studied [Dodd and Ferrante, 2016], at an initial Reynolds number of  $Re_\lambda = 83$ . Droplets are initialized on the inertial range scale. In their extensive study, the influence of the density ratio, viscosity ratio, Weber number based on the root-mean-square

turbulence velocity and the volume fraction have been modified in order to characterize their influence onto energy budget, and, even if it was not the focus of their study, the breakup-coalescence ratio and the droplet shape deformation. The influence of the viscosity ratio, that they vary from 1 to 100, on the surrounding flow around a droplet is non-negligible. Their work showed that increasing the viscosity ratio creates discontinuities in the velocity field at the interface induced by the recirculation inside a droplet. This recirculation decreases when the viscosity ratio increases, but the velocity around the droplet, a contrario, increases, which leads to these instabilities.

The deformation rate is also correlated to the viscous ratio. Increasing the viscous ratio decreases the deformation of the droplet and for relatively high viscous ratio, the droplet behaves such as a particle [Grace, 1982]. They observed also that an increase of the volume ratio and the  $We_{RMS}$  leads to an increase of the collision rate. In their results they observed a correlation between the  $We_{RMS}$  and smallest droplets' diameter, the higher it is the smaller is the minimal droplets' diameter. Moreover, they showed that the  $We_{RMS}$  influences the direction of flattening of the droplets under pressure and normal viscous stresses. Finally, influence of the density ratio, from 1 to 1000, showed that the more inertial were the droplets, the more they deviate from the carrier fluid. Density ratio modifies the velocity profile inside the droplet and in its surrounding, it enhances dissipation and reduce collision/breakup events. From their results, it is possible to conclude that in a decaying HIT, key factor to study breakup are density ratio and Weber number. On the other hand, increasing viscosity changes the minimum droplet diameter.

In more recent work [Karimi and Andersson, 2020] focused on the validation of a theoretical breakup model with numerical investigation. They considered non-miscible droplet immersed in a forced HIT. Their results showed that the validation of a model was possible with numerical data. The first point of their work was to validate the numerical simulation through experimental data obtained in [Karimi and Andersson, 2018] in order to validate their study, that shows its closeness to experiment and recent models. Then, they showed that the increase in kinetic energy of the droplet was strongly related to the breakup as seen in the work of [Dodd and Ferrante, 2016] and proposed to include it in its future development.

It shows that numerical investigation is a powerful tool to validate analytical study and experimental observations. It permits going further in the understanding of the physic of the atomization. At Coria laboratory, we have the opportunity to observe experimental analysis of morphological droplets. In this manuscript, the objective is to provide statistics on the dispersed area to enhance the breakup modeling. A strong achievement would be to give numerical tools to experimentalists to enhance their understanding of the dispersed area.

## I.2 Numerical methods

Atomization is a complex phenomenon to study as it faces some limits in experiments and analytical analyses. In experiments, it is the complexity to provide an entire description of the spray, even if novel techniques are developed [Bothell et al., 2020]. In analytical analysis, it remains difficult to account for complex non-linear phenomenon involving the influence of every scale on the outcome of the simulation. Then, numerical simulation gives a priori more precise description of the spray. It permits to control the details of application with a high degree of freedom, as the density ratio, the geometry of the combustion chamber or the flow motion among others with 3D fields information. However, it requires robust numerical methods to be consistent with the physic of the spray.

Numerical simulation are derived from a mathematical set of equations. In our domain, it is called CFD for Computational Fluid Dynamic. In two-phase flow atomization, challenges are numerous. First, a suitable mathematical model that transports and represents accurately the interface between phases is required. Second, the action of the forces on its shape evolution needs to be properly represented. For example, the development of surface instabilities or breakup can be particularly challenging. Moreover, the transport of small droplets present in the secondary atomization needs to be consistent.

Several set of equations are used to model two-phase flows. Among them, two main approaches are referred in the literature: Navier-Stokes equations and Lattice-Boltzmann equations. The first

tracks the flow motion under the assumption of a continuum fluid, ensuring the conservation of the mass, momentum and energy. The second method solves the evolution of the flow at microscopic scale, with a statistical approach [Chen et al., 2019a]. Lattice-Boltzmann equations consist in the discretization of the fluid through the displacement of fictitious particles. They imply a totally different mathematical modeling based on statistical mechanics. One of the main advantages of Lattice-Boltzmann approach is its relatively low computational cost thanks to its massively parallel architectures. Both methods showed great capabilities to follow the fluid motion. The Navier-Stokes equations are more often used in CFD since it is straightforward to discretize them in Finite Volume framework and to ensure flux transfer. Other methods exist to represent the flow motion such as Smoothed Particle Hydrodynamics (SPH) which no longer requires discretization over grids. In experiments, the confidence in measurements can depend on the number of pixels and their resolution when optical methods are used. In numerical simulations, the reliability of the results depends on the number of cells. The present section provides a general description of the methods to solve the fluid motion. Then, a brief review of the two-phase flow treatment of the interface is done.

### I.2.1 Navier-Stokes framework

Navier-Stokes equations describe the motion of a fluid through the conservation of its global quantities. In the framework of this Ph.D., Navier-Stokes equations are used in their incompressible form:

$$\nabla \cdot \vec{u} = 0 \quad (\text{I.23})$$

$$\frac{\partial \vec{u}}{\partial t} + (\vec{u} \cdot \nabla) \vec{u} = -\frac{\nabla p}{\rho} + \frac{1}{\rho} \nabla \cdot (\mu(\nabla \vec{u} + \nabla^T \vec{u})) + \vec{g} \quad (\text{I.24})$$

The physical properties of the two phases are described locally in each cells. Density is constant in both phases and a discontinuity arises at the interface. This discontinuity is called a jump, for the density it is defined  $\rho_l = \rho_g + [\rho]$  when  $\rho_l > \rho_g$ . Here, the brackets represent the jump of density:  $[\rho]$ .

In the incompressible momentum equation I.24, all the terms can be treated individually and have an influence on the flow motion. Then,  $\frac{\partial \vec{u}}{\partial t}$ , is the acceleration of the fluid,  $\vec{u} \cdot \nabla \vec{u}$ , is the convective acceleration of the fluid,  $\frac{1}{\rho} \nabla p$ , represents the fluid pressure,  $\nabla \cdot (\mu(\nabla \vec{u} + \nabla^T \vec{u}))$ , is the viscous stress tensor and  $\vec{g}$  represents the volumic forces. However, this general form is not conservative due to the split of the density and the velocity in the flux terms. In *Archer* the convective term is solved in the full conservative form  $\nabla \cdot (\rho \vec{u} \otimes \vec{u})$  [Vaudor et al., 2017].

### I.2.2 Navier-Stokes numerical implementation

An accurate description of flow motion in two-phase flow atomization can require an important amount of cells. The number of cells is linked to the complexity of the phenomenon and length scales involved. The more cells are used to represent this phenomenon, the more expensive is the computational cost of the simulation. In this subsection, a description of the cell and the discretization of the variables on it, i.e. scalar and vector fields, is given. Then, a description of the influence of the turbulence on the mesh size is done. It permits to determine the most accurate mathematical model to describe the atomization.

In its simplest 2D Cartesian definition, a cell is a square. It contains the information that are needed to solve equations I.23 and I.24. They are the pressure, the velocity and the physical fluid properties and quantities of both phases. Two main grid discretizations are possible. Either all the variable are located on the center of the cell, it is called a collocated grid, either the scalar and vector field are split. The scalar field is located at the center of the cell while the vector fields are located onto the faces of the cell, called staggered grid. It has been used to overcome the numerical instabilities created by the central scheme calculation of the divergence operator of velocity and the gradient of pressure. For more information on the checkerboard pattern, the reader is referred to *Numerical heat transfer and fluid flow* from S. Patankar [Patanekar, 2018]. Nowadays, this issue has been overcome

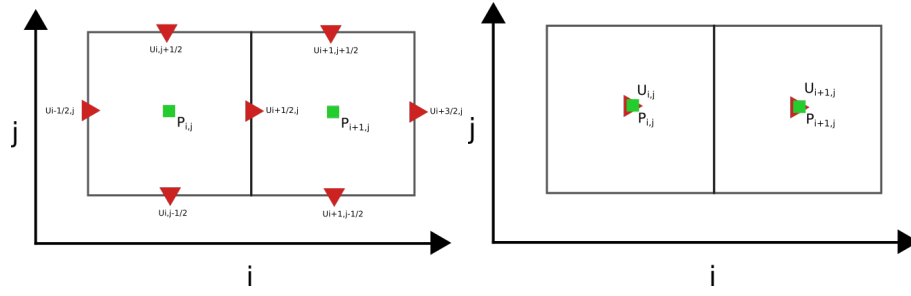


Figure I.14: On the left: staggered grid used in *Archer* and on the right: collocated grid. Pressures, in green squares, and velocities, in red triangles are computed on cells faces/centers along 2D axis  $i, j$ .

[Batteen and Han, 1981] and in Cartesian grid framework, there is no difference of accuracy between the collocated and staggered grid. An example of both grids is given on figure I.14, staggered grid on the left and collocated on the right.

In turbulent flow, incompressible Navier-Stokes equations intent to solve all ranges of energy of the process and the smallest cell size is related to the Kolmogorov length scale. An example of cell number estimation for HIT is given in Pope's book [Stephen B. Pope, 2000] using cubic Reynolds number:  $N_{cell} \sim Reynolds^3$ .

Direct Numerical Simulation solves Navier-Stokes equations without any modeling, no assumptions are made. In order to perform high Reynolds number simulation, which consists in the resolution of the largest scales, the smallest scales of the turbulence are modeled. For example of the order of the Kolmogorov length. This method requires less cells, it is called Large Eddy Simulation, LES [Smagorinsky, 1963]. It uses a scale decomposition of the turbulence, small scales are modeled. The goal is to define accurately the filter that will divide those scales and range of action. The action of the filter on the physic of the simulation is to reproduce the viscous sink of energy of the subscales. Then, it distributes it in the momentum equation through a subgrid scale stress tensor. The main advantage is to cut off the numerical cost of the simulation and go further in turbulent flows. A detailed review of the possible filters is done in Pope's book [Stephen B. Pope, 2000]. The accuracy of the simulations depends on the reliability of the model that is used. It is common to validate LES model with experimental results [Berlemont et al., 1990, Burluka et al., 2001]. Thanks to the increase of computational calculation capability, it is also done using DNS data results [Kedelyt et al., 2019, Beau et al., 2005, Duret et al., 2012, Duret et al., 2013, Shinjo, 2018].

### I.3 Interface Capturing Method (ICM)

In this section, we propose to introduce different models to treat the interface, at the cell size or with averaged quantities. Then, a description of DNS Interface Capturing Method (ICM) is done in order to understand the choices of implementation in *Archer*.

#### I.3.1 Introduction to interface numerical treatment

In the numerical analysis of atomization, several order of length scales are considered. The discontinuity between two phases is the interface, represented by the Greek letter  $\Gamma$  in this manuscript. It implies a strong variation of physical variables over a small thickness, which can lead to high discontinuities. These changes are challenging to represent in atomization since the scale of the interface is of the order of the molecular length. A solution is to treat the discontinuities at the interface through a *jump* condition, belonging to the sharp interface family. An example of infinitely small interface is presented on figure I.15, in opposition to diffuse family that spreads the interface of several cells [Gorokhovski and Herrmann, 2008].

It is convenient to consider the interface as infinitely small due to the multiscale issues, but, the jump conditions on each physical variables have to be accurately implemented. Considering that the evaporation speed is smaller than the atomization evolution, we can consider a non-reactive interface.

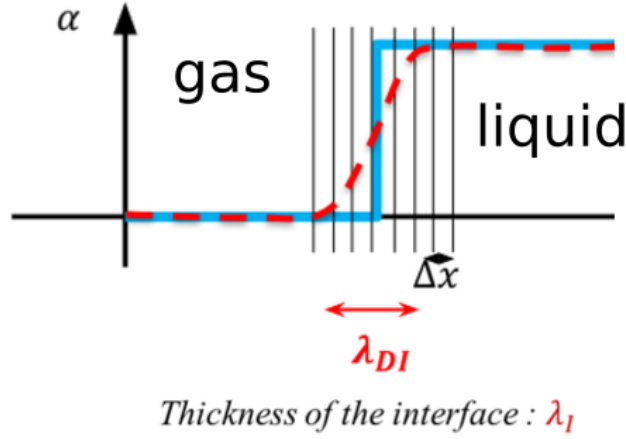


Figure I.15: Interface length scale illustration to compare sharp interface, in blue, and diffuse interface, in red, modelling.

Then, it is only influenced by its transport. One of the numerous advantages of this assumption is that the velocity vector in the normal direction at the interface is considered continuous, implying:

$$[\vec{V}]_{\Gamma} = 0, \quad (\text{I.25})$$

then, other fluid quantities are affected by the jump condition, giving for the density and viscosity:

$$[\mu]_{\Gamma} = \rho_l - \rho_g, \quad (\text{I.26})$$

$$[\mu]_{\Gamma} = \mu_l - \mu_g. \quad (\text{I.27})$$

Capillary forces affect the pressure jump at the interface. Considering two immiscible fluids, the pressure jump is expressed through:

$$[P]_{\Gamma} = \sigma \kappa, \quad (\text{I.28})$$

with  $\kappa$  the curvature at the interface.

### I.3.2 Interface Capturing Method in DNS

To track the interface in two-phase flow atomization, the requirements are to represent accurately the physic of the atomization with as many cells as possible with mass and momentum conservation. The description of the interface is a numerical challenge, it involves a lot of phenomena. The numerical methods must be capable to break the interface, to collide two interfaces and to follow complex shapes. Moreover, the numerical method must be robust and the physic independent of the numerical implementation. To reach the most accurate description, several methods have been developed [Shinjo, 2018]. They are using Lagrangian and Eulerian grids description. For example, the front tracking method [Tryggvason et al., 2001] consists in the transport of passive scalar markers at the interface, Lagrangian markers. The more markers, the more accurate is the capturing method. One of its strong disadvantage is its complexity to predict surface breakup which is not convenient in atomization study. This issue is treated in the work of [Glimm et al., 1998] but can computationally expensive in 3D.

We focus on the methods used in *Archer* in order to understand the numerical treatment of the interface. We first describe the color function to understand the concept behind the *Volume of Fluid* function. Then, we describe the *Level-set* that is implemented. The coupling between these methods, used in *Archer*, is described in section I.4.

### Color function

A method to describe the motion of the two non-miscible fluids is to tag each cell belonging to one of the phases, and to follow it with flux advection. The jump of variables between phases is characterized by a Heaviside function:

- in liquid fluid :  $H(\vec{x}) = 1$  if  $\vec{x} \in \Omega_l$ ,
- in gas fluid :  $H(\vec{x}) = 0$  if  $\vec{x} \in \Omega_g$ .

The physical properties of each phase depend on the local value of the Heaviside function. The transport of the Heaviside function is described in equation I.29:

$$\frac{DH(\vec{x})}{Dt} = \frac{\partial H(\vec{x})}{\partial t} + \vec{u} \cdot \nabla H(\vec{x}) = 0, \quad (\text{I.29})$$

where  $\vec{u} \cdot \nabla H$  is assimilated to the flux  $F_H$ :

$$F_H = \frac{1}{\Omega} \int H(\vec{x}) d\vec{x} \quad (\text{I.30})$$

To compute the exact flux that goes in and out of each cell, equation I.29 is discretized. An example of the discretization is given for 2D Cartesian grid over  $i, j$  in the direction  $j$ . The flux advection,  $F_H$ , is defined along  $j$ , the quantities are calculated at  $j - 1/2$  and  $j + 1/2$  and  $\alpha$  represents the occupied volume per cell:

$$\alpha^{t+\Delta t}(\vec{x}_{i,j}) - \alpha^t(\vec{x}_{i,j}) = \int_t^{t+\Delta t} F_{\alpha,i,j+1/2} \cdot dt - \int_t^{t+\Delta t} F_{\alpha,i,j-1/2} \cdot dt \quad (\text{I.31})$$

The main drawback of this method is the complexity to be consistent in the volume transport [Tryggvason et al., 2011], due to the rough averaging of the flux since an average operator is used to get the quantity of fluid in one cell. At each iteration, a new quantity of fluid is recalculated in each cell. The interface is not clearly defined and the method is diffusive. Then, a sharp description of the interface is used to improve it.

### Volume of Fluid method (Geometric)

The Volume of Fluid method, *VoF*, as described in [Noh and Woodward, 1976], uses the phase volume reconstruction in each cell. It is based on the liquid/gas ratio in a cell and the direction of transport, as detailed later.

Two families of transport schemes exist for *VoF* method, split and unsplit transport. The split method is based on the directional splitting of the mesh. The unsplit method works in multi-dimensional advection, it is helpful for unstructured mesh. The advantage of the split advection is its simplicity of implementation, the unsplit method is much more complex to implement. Mass conservation is a challenge for both methods [Bnà et al., 2013].

The *VoF* uses the flux calculation defined in the color function description. The difference is the reconstruction of the interface. Several methods exist [figure I.16], for example in [Hirt and Nichols, 1981], they used a perpendicular normal reconstruction and transport it among only one direction [bottom left figure I.16]. Drawback of this method is to favour one direction of transport. The Simple Line Interface Calculation, SLIC, reconstructs perpendicular interface for each direction of advection and transport it along x-y-z [top right figure I.16]. The three directions are inverted at each iteration to avoid preferential advection. The drawbacks of both methods are to enhance breakup leading to non-physical phenomena called floatsam.

Rudman [Rudman, 1997] proposed to reconstruct the exact plane equation in a cell based on normal vector at interface and the distance from the cell center to the interface in a cell,  $\zeta$ , with:

$$\vec{n} \cdot \vec{x} + \zeta = 0 \quad (\text{I.32})$$

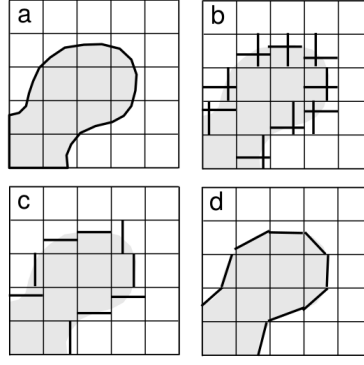


Figure I.16: Description of reconstruction and advection of interface from [Tryggvason et al., 2011]. Interface is represented in top left, SLIC top right, Hirt and Nichols down left and PLIC down right.

It is Piecewise Line Interface Calculation, PLIC, [bottom right figure I.16] and requires only one reconstruction.

In *VoF* approach, the normal can be obtained from the volume fraction gradient,  $\vec{n} = \frac{\nabla F}{|\nabla F|}$ . The volume fraction is obtained from a minimization algorithm between the volume under the normal  $V(\zeta)$  and the average volume on a cell. It is solved iteratively until  $g(\zeta)$  converges toward 0, see equation I.33 for a 2D Cartesian example. The volume  $V(\zeta)$  is obtained from equation I.34.

$$g(\zeta_{i,j}) = V(\zeta_{i,j}) - C_{i,j}\Delta x\Delta y \quad (\text{I.33})$$

$$V(\zeta_{i,j}) = \int_{y_{j-1/2}}^{y_{j+1/2}} \int_{x_{i-1/2}}^{x_{i+1/2}} \alpha(\vec{n} \cdot \vec{x} + \zeta_{i,j}) dx dy \quad (\text{I.34})$$

In 3D geometry, the challenge is to recover the exact plane equation and it is more complex than for 2D geometry. Note that external libraries are available: VOFTOOLS [López and Hernández, 2008] or Cube Chopping Algorithm. Then, a classical transport method is used [Weymouth and Yue, 2010].

### Level-set function

The methods that transport the interface with flux advection have the advantage to be theoretically mass conservative. However, they need to reconstruct the normal at every time step. In 3D, it can be challenging and non-accurate reconstruction can occur. In order to conserve the geometrical properties, an Interface Capturing Method, *Level-set*, is developed [Sussman et al., 1998]. A general description of the *Level-set* is given in the first part of this subsection. Implementation of surface tension force is then detailed as several models exist for sharp or thick interface.

The *Level-set* consists in the transport of geometrical information through the distance to the interface in each cell center of the Eulerian grid. It is a function that gives the closest interface to each Eulerian cell. Then, for the scalar field  $\phi$  that represents *Level-set*, the minimization equation is written I.35. The interface position is represented by  $\vec{x}_\Gamma$ , the closest distance to the interface is obtained from  $\vec{x}_\Gamma = \vec{x} - \phi(x)\vec{n}$ :

$$\phi(\vec{x}) = \text{sign}(\phi(\vec{x})) \min(|\vec{x} - \vec{x}_\Gamma|) \quad \forall \vec{x}_\Gamma. \quad (\text{I.35})$$

To represent the two phases, the distance is signed in each phase. For example, the distance is negative in the gas and positive in the liquid. On the interface, *Level-set* is equal to  $\phi_\Gamma = 0$ . The *Level-set* respects a slope that ensures the continuity of the distance in all the domain. This Euclidean distance is given by  $|\nabla \phi| = 1$ .

The transport of the *Level-set* is done in temporal and spatial space:

$$\frac{\partial \phi}{\partial t} + \nabla(\vec{u}\phi) = 0. \quad (\text{I.36})$$



The transport of the interface induces a loss of the *Level-set* distance property  $|\nabla\phi| = 1$ . This issue has been intensively studied [Tanguy and Berlemont, 2005]. Their solution is to use a redistanciation algorithm [Sussman et al., 1998].

This algorithm update the *Level-set* from the interface iteratively over a fictitious time,  $\tau$ , to conserve distance property:

$$\frac{\partial d}{\partial \tau} = \text{sign}(\phi)(1 - |\nabla d|). \quad (\text{I.37})$$

An example of 2D circle initialization with redistanciation algorithm is showed on figure I.17 with  $x - y$  axis for 2D Cartesian grid and  $z$  axis for distance function. Initially, the interface is described on the top left figure and the information of both phases are showed. In orange, the gas that represents the phase with a negative distance to the interface and in red the liquid, positive. After one iteration, the scalar field  $\phi(\vec{x})$  evolves. A peak is observed at droplet's center. It is the distance from the center of the droplet to the interface, it is equal to the radius of the droplet. In the gas, the redistanciation algorithm evolves and after some iteration, the distance to the interface is initialized in the entire domain (bottom right figure I.17). Since redistanciation algorithm has a computational cost, it can be limited to a given number of iterations.

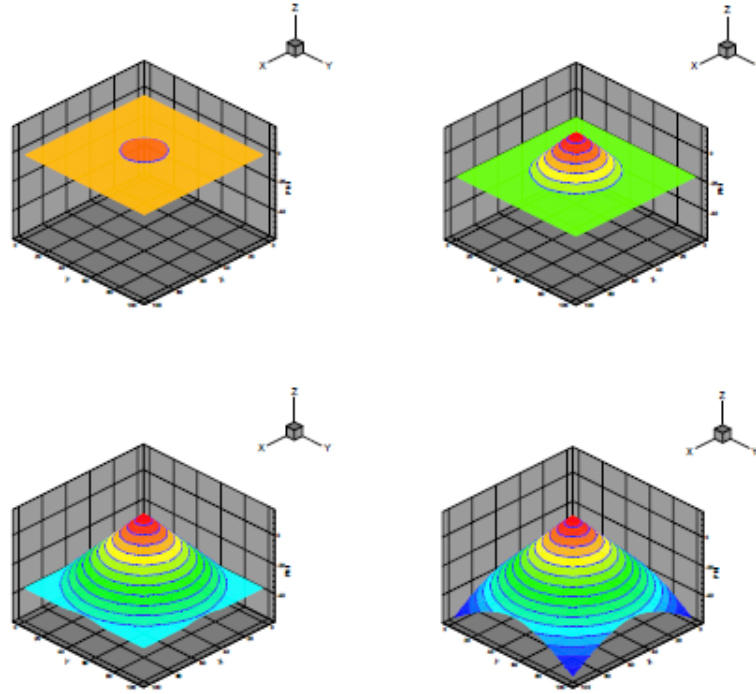


Figure I.17: Initialization of the *Level-set* field around a circular droplet, from [Tanguy, 2004].

As we conserve distance property, we can obtain normal and curvature,  $\kappa$ , from *Level-set* field at every iteration:

$$\vec{n} = \frac{\nabla\phi}{|\nabla\phi|}, \quad (\text{I.38})$$

$$\kappa = \nabla \cdot \vec{n} = \nabla^2\phi. \quad (\text{I.39})$$

## Summary

ICM methods must be mass and momentum conservative and transport accurately the interface. A solution is to consider sharp interface and to use normal and curvature at the interface to treat surface tension force. Some methods based on the *VoF* reconstruct the interface but face numerical limits due to mesh resolution. In these under resolved areas numerical instabilities appear and several solution have been developed considering momentum transport [Ahn and Shashkov, 2009, Lemoine et al., 2017].

Other approaches transport them: for example *Level-set* function. Geometrical information are conserved, normal and curvature computation are direct. The challenge of the methods is to ensure mass conservation, in accordance with this some developments improved it [Desjardins et al., 2008].

A coupling between those methods can be seen as natural [Sussman and Puckett, 2000], to improve the study of atomization. This strategy has been implemented in the numerical code *Archer* [Ménard et al., 2007], introduced in the next section.

## I.4 *Archer*

*Archer* is a Direct Numerical Simulation two-phase flow code that solves both incompressible and compressible Navier-Stokes equations. Its goals are to investigate on two-phase flow atomization, evaporation and all multiphase flow related topics. Development started during the PhD of Sebastien Tanguy [Tanguy and Berlemont, 2005] where the interface was transported with *Level-set* function. Drawbacks of *Level-set* function have been highlighted in prior section and further developments have been done in order to couple the advantages of the level set with the conservative properties of the Volume of Fluid method. This coupling has been implemented during the PhD of Thibaut Ménard [Ménard et al., 2007]. High Reynolds number were still complicated to perform and numerical breakup or local acceleration of the velocity induced by bad advection of fluxes appeared. A dual split of fluxes transport within cells has then been developed to avoid numerical breakdowns during the PhD of Geoffroy Vaudor [Vaudor et al., 2017]. More recent work proposed a more robust scheme to transport the thin structures with Moment of Fluid method [Mukundan et al., 2019b]. However, this method greatly increases the computational cost of the simulation.

Beside the fluid solver, it is important to quantify spray dispersion. An algorithm of droplets' detection has been implemented during the post-doctoral study of Vaudor. Its description is done in section III.2.

From his experience on the numerical analysis of finite size particle immersed in a turbulent flow [Brändle De Motta, 2013], Brändle de Motta implemented a Full Resolved Particle method in *Archer*. His conclusion is that the Immersed Boundary Method [Uhlmann, 2005] would be an interesting tool in *Archer* for further studies. All implemented Lagrangian techniques are detailed in section II.1. In this section we present the Eulerian solver in *Archer* and the parallel implementation.

### I.4.1 Treatment of the interface in *Archer*

The method in *Archer* consists in coupling the advantages of the *VoF* and *Level-set* method [Sussman and Puckett, 2000]. This method is called the coupled *Level-set* Volume of Fluid method: *CSLVof*. Improvements on the mass conservation were obtained with the flux advection of the *VoF* with the accurate definition of geometrical information thanks to the *Level-set* and the redistanciation algorithm. The coupling between these methods is described in this section.

The reconstruction of the volume fraction in one cell  $K = [x_0, x_1] \times [y_0, y_1] \times [z_0, z_1]$ , is defined in equation I.40 where  $\phi^R$  represents the reconstructed *VoF* based on the *Level-set* in a cell.

$$F_{i,j} = \frac{1}{K} \int_K H(\phi^R(\vec{x}, t)) d\vec{x} \quad (\text{I.40})$$

The *Level-set* function provides the normal and the advection of the fluxes is done through PLIC algorithm. The volume represented in a cell must be the same for the *Level-set* and the *VoF*, as seen in equation I.41 for a 2D Cartesian grid. The coefficients of the segment equation for the *VoF* method:  $a_{i,j}$ ,  $b_{i,j}$  and  $c_{i,j}$  are obtained from VOFTOOLS libraries. The coefficients  $a_{i,j}$ ,  $b_{i,j}$  give the direction of the normal vector and  $c_{i,j}$  is the perpendicular distance between the cell center and the interface position in a cell  $C_{i,j}$ .

$$\phi_{i,j}^R = (a_{ij}(x - x_i) + b_{ij}(y - y_j) + c_{ij}) \quad (\text{I.41})$$

An example is presented on figure I.18. In red the interface obtained from the *Level-set* function. In gray the volume fraction obtained for the *VoF* with equation I.40. The final interface location  $\phi_{i,j}^R$  is

showed in black for the *CLSVoF*. This reconstruction of the *Level-set* is as close as possible to the real *Level-set* to describe accurately the geometric properties of the interface with the conservation of the volume fraction.

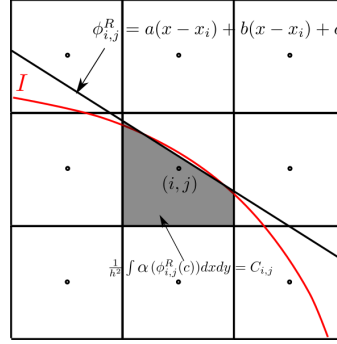


Figure I.18: Reconstruction of  $\phi_{i,j}^R$  on plane equation in solid black,  $\phi$  in red and the volume fraction within the central cell in grey from T. Ménard lecture.

A minimization algorithm is used to reduce the difference between the two interfaces description [equation I.41]. Equation I.42 is used with a nine points stencil discretization,  $3 \times 3$ , with the least square method to obtain new coefficients  $a, b, c$ .

$$E(a, b, c) = \sum_{i',j'} \omega_{i',j'} \left( \phi_{i',j'} - (a(x_{i'} - x_i) + b(y_{j'} - y_j) + c) \right)^2 \quad (\text{I.42})$$

Then, coefficient  $c$  is modified to get an equality between the surface under the interface and the liquid fraction of the cell,  $\phi_{i,j} \approx c$ . Finally, the distance function is reconstructed as described priorly and the *CLSVoF* method shows the benefits of mass and geometrical properties conservation. Moreover, breakup and coalescence events are directly obtained, with opposition to Front Tracking method, but still mesh size dependent.

Nevertheless, when the interface is not enough resolved, the problem is still the same and non-physical breakups occur due to bad reconstruction and the mass will be diffused within the domain.

### I.4.2 Navier-Stokes coupling

The description of the coupling between Navier-Stokes equations and the treatment of the interface is presented in the algorithm of figure I.19. We follow this figure to describe Eulerian temporal advection in *Archer* which are:

- flux transport: Rudman algorithm,
- other terms in Navier-Stokes equations: Sussman algorithm,
- Projection method,
- pressure terms: Poisson solver.

#### Convective term computation (Rudman algorithm)

The convective term  $\nabla \cdot (\rho \vec{u} \otimes \vec{u})$  is written in mass-conservative form to give consistency between mass and momentum transports in solving Navier-Stokes equations [Rudman, 1998]. Then, the mass flux  $\rho \vec{u}$  computation is done for the same control volume.

Since we use staggered grid, we have two control volumes: at the center of the cell for the density and on the face for the velocity. The challenge is to reconstruct flux balance for the control volume centered on the velocity and it has been developped in Vaudor 2017 [Vaudor et al., 2017]. From the

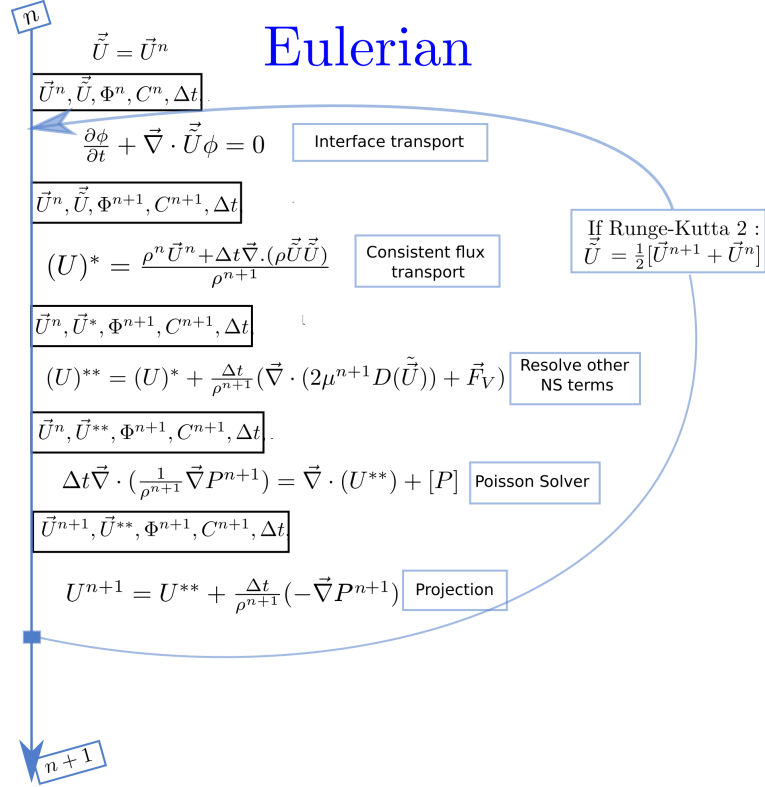


Figure I.19: Advection of the two-phase flow motion solving the transport of the interface and the Navier-Stokes equations for one time step in Euler Explicit and Runge-Kutta 2nd order.

interface transport, we know the fluxes that go in/out the cell, we have to determine the fluxes that go in the control volume. To get the balance we compute pseudo fluxes in each joined domain (in red on figure I.20). On this figure, we give a 2D Cartesian example of  $\rho u$  term for x and y component of the momentum flux. Mass flux is schemed along x-y direction by  $f^{m,x}$  and  $f^{m,y}$  on the joined control volume, it is expressed by:

$$[\nabla \cdot (\rho \vec{u} \otimes \vec{u})] \cdot \vec{e}_x = \frac{\partial(\rho u)u}{\partial x} + \frac{\partial(\rho v)u}{\partial y} \quad (\text{I.43})$$

The two derivatives, along x-y, are schemed on figure I.20 for the fluxes  $(\rho v)$  and  $(\rho u)$  on cell face  $(i + \frac{1}{2}, j)$ . We describe flux computation for derivative  $\frac{\partial(\rho v)u}{\partial y}$  at location  $(i + \frac{1}{2}, j + \frac{1}{2})$  for a positive velocity  $v > 0$ . The mass flux is obtained through the liquid volume fraction and is computed on each subvolume.

$$f^{m,y} = \rho v = \rho_l v \alpha_l + \rho_g v (1 - \alpha_l) \quad (\text{I.44})$$

Using half cells fluxes give the flux among each direction, the total flux among y at location  $(i + \frac{1}{2}, j)$  is:

$$f_{i+\frac{1}{2},j}^{m,y} = f_{i+\frac{3}{4},j-\frac{1}{2}}^{m,y} + f_{i+\frac{1}{4},j-\frac{1}{2}}^{m,y} - f_{i+\frac{3}{4},j+\frac{1}{2}}^{m,y} - f_{i+\frac{1}{4},j+\frac{1}{2}}^{m,y} \quad (\text{I.45})$$

The same procedure is used among x-component. Using local fluxes mass balance the flux at cell scale is obtained and used in the momentum flux computation  $\rho \vec{u} \otimes \vec{u}$  where velocity is obtained through 5<sup>th</sup> order WENO scheme.

### Viscous term computation (Sussman algorithm)

An important term to estimate is the viscous stress tensor. In Navier-Stokes equations, the viscous term is complex to implement because of sharp interface. The fluid physical properties are discontinuous and the velocity must be interpolated at the interface. Moreover, if the normal component of the velocity does not imply any jump, its derivatives do. It is complex to solve, and the

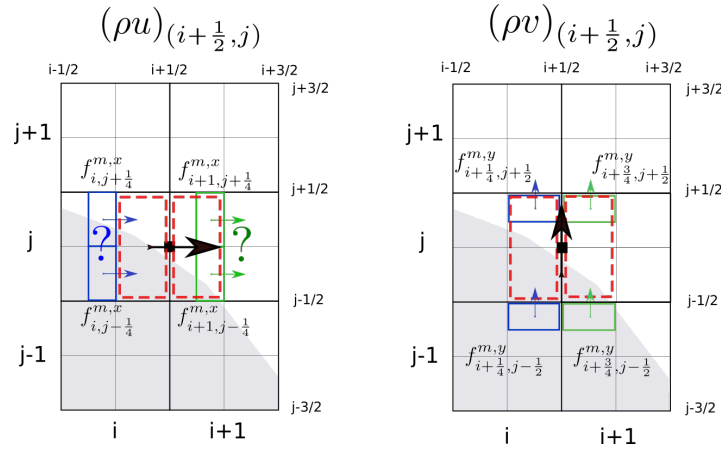


Figure I.20: Mass flux decomposition for consistent computation.

discretization is challenging in staggered grid. The solution implemented in the code is deduced from Sussman method [Sussman and Puckett, 2000].

$$(2\mu D) = \begin{bmatrix} 2\mu(\phi) \frac{\partial u}{\partial x} & \mu(\phi) \left( \frac{\partial v}{\partial x} + \frac{\partial u}{\partial y} \right) \\ \mu(\phi) \left( \frac{\partial v}{\partial x} + \frac{\partial u}{\partial y} \right) & 2\mu(\phi) \frac{\partial v}{\partial y} \end{bmatrix} \quad (\text{I.46})$$

The system of equation to solve is presented in 2D. The viscosity of the considered phase  $\mu(\phi)$  is interpolated with the *Level-set* function. Then, its discretization is expressed in *Archer* with a projection of the quantities using *Level-set* function [Vaudor et al., 2017]. A special care is done on the projection of the term along each direction because of the staggered grid. Since components of the velocity field are not located at the same position of the grid, the spatial derivative is complex. It must be calculated on the face's cell. In a cell centered in  $i, j$ , the spatial derivative along  $x$  is calculated for  $i + 1/2, j$ . It requires information of the velocity node located on  $i - 1/2, j$  and  $i + 3/2, j$ . An example of a 2D Cartesian discretization along the  $x$ -direction is given for the face  $C_{i+1/2,j}$  [equation I.47].

$$\frac{\partial \left( 2\mu(\phi) \frac{\partial u}{\partial x} \right)}{\partial x} \Big|_{i+1/2,j} = \frac{2\mu(\phi)_{i+1,j} \left( \frac{u_{i+3/2,j} - u_{i+1/2,j}}{\Delta x} \right) - 2\mu(\phi)_{i,j} \left( \frac{u_{i+1/2,j} - u_{i-1/2,j}}{\Delta x} \right)}{\Delta x} \quad (\text{I.47})$$

The physical properties are discretized through the projection of the *Level-set* function on the faces [Vaudor et al., 2017]. The discretization is done for all the faces of the cell. A detailed description of the discretization on the staggered grid is given in [Vaudor, 2015].

### Projection Method

The first step is to solve the momentum equation without pressure term [equation II.22], that provides the velocity field on the staggered grid, see figure I.19. The velocity field  $\vec{u}^*$  is obtained. It does not satisfy the mass conservation equation  $\nabla \cdot \vec{u} = 0$  that ensures divergence free. To ensure that  $\nabla \cdot \vec{u}^{n+1} = 0$ , we use:

$$\vec{u}^{n+1} = \vec{u}^* \frac{1}{\rho} (-\nabla P) \Delta t, \quad (\text{I.48})$$

on the which we apply divergence operator to obtain the Poisson equation to solve pressure term:

$$\nabla \cdot \left( \frac{1}{\rho} (\nabla P^{n+1}) \right) \Delta t = \nabla(\vec{u}^*). \quad (\text{I.49})$$

When the pressure at the next time step is computed in the domain, we implement it in in equation I.48 to get the velocity field at  $n + 1$  through a classical projection method, see figure I.19.

### Pressure term

The pressure term is obtained with linear iterative Poisson solver. To improve its efficiency, it is solved by a Conjugate Gradient preconditioned by a Multigrid Method [Jun, 1996] and Ghost Fluid Method, developed by Fedkiw and colleagues [Fedkiw et al., 1999, Liu et al., 2000, Kang et al., 2000]. It permits to have the pressure extrapolated at the interface. Then the jump on normal and tangential constraints is used to give directly  $\rho$  and  $\phi$  and pressure jump. A discontinuous variable is considered,  $P$ , with a known jump  $[P]_\Gamma$  obtained from Laplace equation.

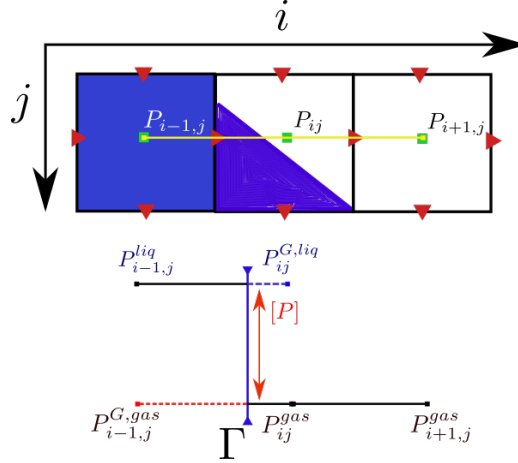


Figure I.21: Jump treatment in ghost fluid method for the pressure at the interface  $\Gamma$  in 2D. On top the volume fluid fraction. On bottom the linear interpolation into a fictitious domain, represented in dashed line, on the other side of the interface for the pressure term.

For example, the Ghost Fluid extension,  $G$ , through the liquid part of the gas pressure,  $P_{i-1,j}^{G,gas}$  [figure I.21], is calculated from the central discretization of  $P_{ij}^g$  and  $P_{i+1,j}^g$ , defined in equation I.50 for a 1D example. The characterization of the pressure jump at the interface is defined by  $[P]_\Gamma = a_\Gamma$  within the domain, where  $a_\Gamma$  is the function that express the jump across the interface depending on the curvature  $\kappa$  which is computed in each cell center. This jump is calculated with the information of neighboring cells and the *Level-set* distance information.

$$\left. \frac{\partial P_i}{\partial x_i} \right|_{i+1/2} = \frac{P_{i+1} - P_i}{\Delta} - \frac{a_\Gamma}{\Delta}, \quad a_\Gamma = \frac{a(x_i)|\phi_{i+1}| + a(x_{i+1})|\phi_i|}{|\phi_{i+1}| + |\phi_i|} \quad (\text{I.50})$$

The same methodology is used for all discontinuities at the interface.

Then  $\Delta p$  is discretized including the Poisson equation in each phase. An example of discretization along  $i$  is given in equation I.51 for an interface located between  $i$  and  $i - 1$ .

$$\left. \frac{\partial P}{\partial x} \right|_{i-1/2} = \frac{P_i^{gas} - P_i^{G,gas}}{\Delta x} = \frac{P_i^{gas} - P_i^{liq} + a_\Gamma}{\Delta x} \quad (\text{I.51})$$

### I.4.3 Block decomposition

In order to improve the accuracy of calculation, a fine mesh is required and time is increasing to obtain the results. Every time that the grid is split in two, in 3D, it takes more time to compute the simulation, for example when the CFL is parametrized by the viscous terms, this increase can reach 32 times the initial time. To reduce simulation time, it is possible to use more than one processor. The numerical simulation is done in parallel with several processors. It splits the computational time and results are obtained faster.

In *Archer*, the parallel implementation is done spatially. The initial domain is divided into various subdomains that belong to one processor. The subdomains are not independent, the solver needs the information on the neighboring ones. Thus information at the borders of each subdomain have to be

exchanged. The strategy is to allocate the Eulerian quantities array of two more cells, in its neighboring. Then, the information are exchanged using a Message Passing Interface, MPI, library.

#### I.4.4 Summary

*Archer* has been developed and improved during the last 15 years. Nowadays, its capacities permit the study of the primary atomization area of a jet at high Reynolds/Weber number. An example of the results obtained for a coaxial atomization simulation is now presented and we discuss its strength and weakness.

This coaxial atomization was performed during the PhD of Vaudor [Vaudor, 2015] with respect to experiments [Lasheras et al., 1998, Marmottant and Villermaux, 2004b] reproducing air/water conditions. In this specific configuration, the atomized liquid was injected at the center of the injector surrounded by a carrier phase at a higher velocity. The momentum ratio at the interface drives the evolution of shape deformation under aerodynamic force.

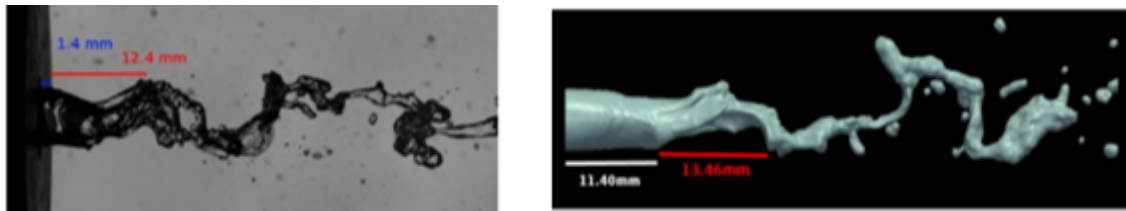


Figure I.22: Comparison of experimental atomization results [Marmottant and Villermaux, 2004b] against *Archer* results [Vaudor et al., 2017]

An overview of the interface is displayed [figure I.22]. *Archer* showed a great capability to reproduce the shape deformation and the length scales of the primary atomization, for example the breakup length. The weakness of this study is the impossibility to reproduce the small scales of the atomization. It is observed that only biggest droplets/ligaments are conserved. The solution to improve the accuracy of the method would be to refine the mesh. However, this simulation took large computational time and it is not possible to increase it indefinitely. It shows the necessity of the development of methods to improve the treatment of the dispersed area without a drastic increase of the computational cost.

### I.5 Limits of atomisation

To recall, the complexity of the simulation of atomization is to represent the entire spray. It must be able to accurately describe the primary atomization and the distribution of the small droplets. Moreover, breakup and coalescence events can occur. It depends on two main factors, a robust numerical method and enough cells to represent all the scales of the jet. In the first part of this section, we detail the consequences of an under resolved treatment of the interface and the strategy to remove under resolved structures. The volume restriction in *Archer* modifies the physic. It is illustrated on free-falling droplet on shallow water that creates small droplets. The volume restriction removes small droplets from the simulation. An introduction to the method that can solve this issue is proposed: the transformation of small droplets into particles under spherical and distance assumption, that are the objectives of this manuscript.

#### I.5.1 Under resolved treatment of interface

In under resolved simulation a non physical breakup modifies the physical behavior of the atomization and could result in non-physical ligaments or droplets. Moreover it can modify the motion of the flow. Two main problems can occur in such simulation.

First, interface stretching modifies locally the velocity field and can create an acceleration of the transported structures around this distortion. The increase of the velocity can overestimate the transport of flux and create numerical instabilities. In the worst scenario, the CFL account for velocity peak and can freeze the simulation.



The numerical breakup is observed in several simulations and pointed in [Shinjo and Umemura, 2010]. The result of their study showed that the smallest diameter was of the order of two mesh size and was 8 times smaller than the SMD diameter. It shows the impossibility to represent accurately the morphological evolution of a droplet in under resolved area. The solution proposed in their study is to remove the structures smaller than a threshold that depends on the method. The solution that is developed in our study is to transform them into particles and track them under Lagrangian approach.

Second, under resolved structures are frozen in interface transport. Since they are too small to be define with *Level-set* function and isolated from other structures, they are not transported and remain frozen during the simulation. It occurs when the liquid volume fraction is smaller than  $\alpha < 50\%$ , as seen for the scheme given on figure I.23 for 1D Cartesian grid. The advection of the liquid phase is represented along  $j$  for a control volume centered on  $C_{j-\frac{1}{2}}$ . Since no fluxes are exchanged in this cell, the liquid is frozen and it is removed from *Archer* through a volume restriction.

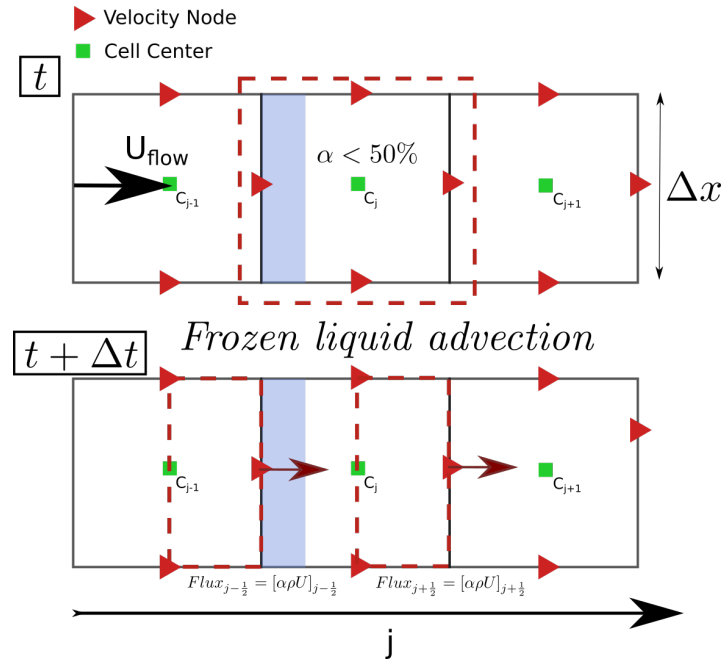


Figure I.23: Frozen liquid parcel in *Archer*.

## I.5.2 *Archer* volume restriction

In order to avoid non physical breakup and frozen structures, a volume restriction has been implemented in *Archer*. It is based on the volume fraction and the sign of the *Level-set* in and around a cell. In the example of positive sign function for liquid and negative for the gas, a cell can contain a small portion of liquid  $< 50\%$  and have  $\phi(\vec{x}) < 0$ . The interface is not represented in the cell by the *Level-set* function. In such configuration, if the neighboring cells do not have liquid, their sign will be negative too. The volume restriction is then used on the cell that contains the liquid fraction higher than zero with a negative sign function.

This method is schemed on figure I.24. The scheme represents the volume restriction in a splash configuration with ejected droplet, presented in the next subsection. The ideal structure is represented with fill area and its computed interface with plane equation calculated by the *VoF* in solid lines. The sign of the *Level-set* is positive in the liquid and negative in the gas. Since the droplet is under resolved, the *Level-set* is negative. Then, it is removed (second picture figure I.24). The phase transport is done and the redistanciation corrects the *Level-set* field at the next iteration. But, removing a structure implies a numerical inconsistency on the mass conservation.

Several solutions can be considered to avoid volume restriction. Some focus on the treatment of the interface, others focus on the normal reconstruction while other method add the transport of the momentum to be more conservative on Navier Stokes equation and fluxes advection. In *Archer* we can



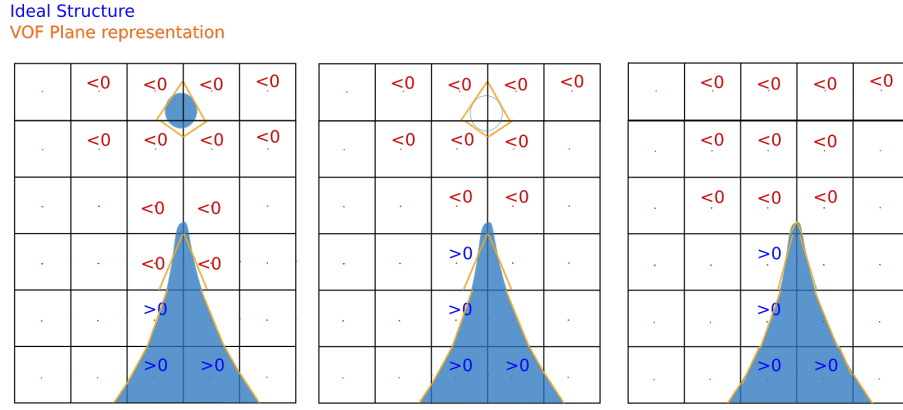


Figure I.24: Volume restriction in *Archer* for an under resolved droplet.

consider several solutions:

- to develop an algorithm to redistributed the mass removed by the volume restriction in smart areas,
- to use Adaptive Mesh Refinement (AMR) [Berger and Colella, 1989],
- to transport under resolved structures in Lagrangian framework.

In our study we develop the third solution following [Herrmann, 2010a]. The motion equation for spherical particles is used, under assumptions later discussed [section III.1], replacing the under resolved structure. Using this strategy avoid breaking mass conservation since droplets are considered as particles [figure I.25]. The main advantage is the light computational cost of Lagrangian advection and its accuracy for few cell across diameter, discussed in section II.1. The challenge of this method is to modify Eulerian and Lagrangian quantities at transformation to be mass and momentum conservative and avoid numerical instabilities and we thoroughly detail our choices of implementation in this manuscript.

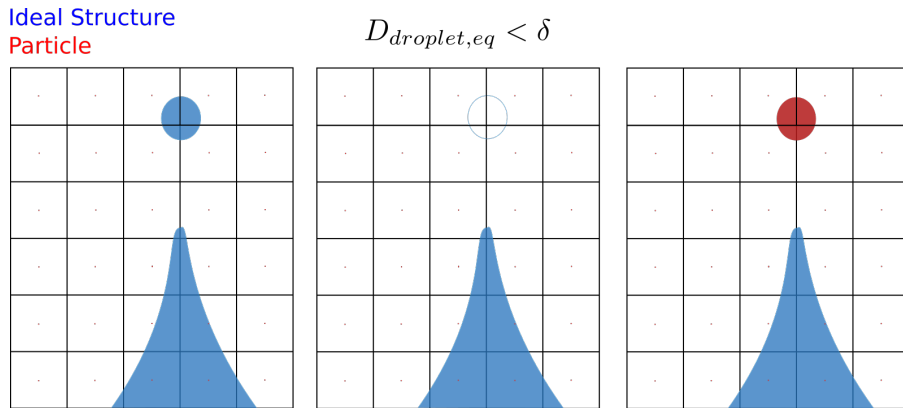


Figure I.25: Transformation of Eulerian droplet, in blue, into Lagrangian particle, in red.

---

# Implementation of Lagrangian Tracking Method

---

*In this chapter a brief introduction to the Lagrangian solver implemented in Archer is done implying several particle modeling. One of the major challenge of the code is to develop an efficient numerical solver that can adapt to a particle's number variation, it is presented in the second section of this chapter. The physical and temporal order of each Lagrangian method are then studied on a free-falling sedimented particle test case in our range of interest, few mesh cells across diameter. Finally, the results are compared to the ICM Archer solver in order to determine the range where particles' tracking algorithm improves small droplets transport. These results are used to parametrize the Hybrid approach.*

## Contents

---

II.1	Particles Lagrangian Modelling . . . . .	52
II.1.1	One-way coupling . . . . .	52
II.1.2	Two-way coupling . . . . .	54
II.1.3	Full Resolved Particles (FRP) approach . . . . .	57
II.1.4	Collision modelling . . . . .	61
II.1.5	Summary . . . . .	62
II.2	Implementation of the Lagrangian solver . . . . .	62
II.2.1	Storage per processor . . . . .	62
II.2.2	Multi processors strategy . . . . .	67
II.2.3	Temporal scheme description . . . . .	68
II.3	Validation of the Lagrangian tracking . . . . .	68
II.3.1	Description of the test cases . . . . .	70
II.3.2	One-way Lagrangian model in Archer . . . . .	72
II.3.3	Two way method validation . . . . .	73
II.3.4	Temporal scheme analysis . . . . .	79
II.3.5	Full Resolved Particles results . . . . .	85
II.3.6	Summary . . . . .	91
II.4	Comparison of methods . . . . .	92
II.4.1	Physical results . . . . .	92
II.4.2	Summary . . . . .	94

---

## II.1 Particles Lagrangian Modelling

To improve the treatment of under resolved ICM structures, we implement an Eulerian-Lagrangian Hybrid coupling. The first step is to determine the particle tracking method that we use when droplets are transformed. We decide to implement three methods and analyze them, the goal is to use the most accurate Lagrangian tracking method, based on the following approaches:

- One-way coupling,
- Two-way coupling,
- Full Resolved Particle (FRP) approach.

We first detail the physical assumption behind each implemented method, and then briefly introduce the strategy to treat particles. Next we describe their numerical implementation in *Archer* through a general Lagrangian framework, entirely created during this Ph.D. We also present our temporal coupling choices with the Eulerian solver. Then, we validate the implementation of these Lagrangian approaches with a well known academic test case that permits us to evaluate their range of applicability for a given number of cells across the droplet diameter. Finally, a comparison of implemented methods is done to define the range of application of each Lagrangian approaches transporting under resolved droplets.

### II.1.1 One-way coupling

One-way coupling is a Lagrangian particle tracking method that uses numerical technique to simulate tracking of particle trajectory within an Eulerian phase. The transport of particles is done through an advection scheme for a particle  $p$  of position  $\vec{X}_p$ , velocity  $\vec{U}_p$ , and subject to fluid forces  $\vec{F}_p$  [Maxey and Riley, 1983]:

$$\dot{\vec{X}}_p = \vec{U}_p, \quad (\text{II.1})$$

$$m_p \dot{\vec{U}}_p = \vec{F}_p + m_p \vec{g}. \quad (\text{II.2})$$

The force applied on the particle is computed using the undisturbed Eulerian velocity interpolated at particles position:  $\vec{u}_{f@p}$ . This can be assumed because the size of the particle for One-way coupling is considered small with respect to the physical phenomena. It means that the particle does not influence the flow motion.

$\vec{F}_p$  represents the forces exerted by the flow motion onto the surface of the particle:

$$\vec{F}_p = \rho_f \oint_{\partial S_p} (-Ip\nu(\nabla\vec{u} + \nabla\vec{u}^T) -) \cdot \vec{n} dS_p \quad (\text{II.3})$$

with  $\vec{n}$  the normal at the interface toward the flow and  $S_p$  the surface of the particle. Next we describe the forces implemented in  $\vec{F}_p$  *Archer* modelling, others than gravity  $m_p \vec{g}$ .

#### Drag Force:

The drag force represents the resistance that is created when an object moves through a fluid. The general expression of the drag force applied to particle is:

$$\vec{F}_D = \frac{3}{4d_p} C_D(Re_p) \rho_p V_p [\vec{u}_{f@p} - \vec{U}_p] ||[\vec{u}_{f@p} - \vec{U}_p]||. \quad (\text{II.4})$$

The velocity difference:  $[\vec{u}_{f@p} - \vec{U}_p]$  represents the slipping motion between the particle and carrier phase called  $\vec{U}_{slip}$ , it can be reduced to  $\vec{U}_{slip} = -\vec{U}_p$  for steady state flow. The mass of the particle is

given by  $\rho_p V_p$ . The particle Reynolds number is:  $Re_p = \frac{\rho_p U_{slip} d_p}{\mu_f}$ , and the dimensionless drag coefficient  $C_D$  given by empirical relations [Clift, 1978].

$$C_D(Re_p) = \frac{24}{Re_p} (1 + 0.15 Re_p^{0.687}) \quad (II.5)$$

This coefficient is obtained for several flow regimes. Analytical solution provides the upper limits of the regimes while experimental results give the entire scope of this coefficient. To the author knowledge, there are no analytical solution that cover the entire range of Reynolds number.

Nevertheless, a wide range of Reynolds number,  $Re_p < 3 \cdot 10^5$  are covered by empirical relation [Clift, 1978], thus we implemented it. When particle Reynolds number is small  $Re < 10$ , we consider Stokes assumption to transport particles. The equation is then simplified as follows:

$$\begin{aligned} \vec{F}_D &= \frac{3}{4} \frac{1}{d_p} \frac{24}{Re_p} \rho_p V_p |\vec{U}_{slip}| \vec{U}_{slip} \\ &= 3\pi \rho_g \nu_g d_p \vec{U}_{slip} = m_p \frac{\vec{U}_{slip}}{\tau_p}. \end{aligned} \quad (II.6)$$

This relation can also be expressed with  $m_p \frac{\vec{U}_{slip}}{\tau_p}$ , where  $\tau_p$  represents the relaxation time of the particle:

$$\tau_p = \frac{\rho_p}{\rho_g} \frac{18\nu_g}{d_p^2}. \quad (II.7)$$

Some models consider the presence of particles in the close vicinity of the tracked particle using corrective coefficient to consider particles volume fraction as it influences drag force calculation [Simonin et al., 2016]. Since we assume that under resolved droplets are isolated from other structures before to be transformed, these corrections are not implemented.

### Archimede:

The gravity term has an influence on the carrier phase that has been displaced by the presence of the particle. It is called a buoyant force and it relies on *Archimede's principle*. This force is derived from  $\int_{S_p} (\vec{n}\sigma - p)\vec{n}dS_p$  and is expressed through:

$$\vec{F}_b = m_p \frac{\rho_g}{\rho_p} \vec{g}. \quad (II.8)$$

It represents the action of the displaced fluid around the particle. The smaller is the density ratio, the more important is the influence of this force on the particle's motion. When particles' force is redistributed toward Navier-Stokes equations, this force is subtracted.

### Added Mass Forces:

The added mass force,  $\vec{F}_{AM}$ , represents the inertia of the fluid displaced by the immersed particle. It is modeled by the acceleration of the fluid and shape dimensionless coefficient  $C_m$ . For spherical object, it is fixed to 0.5 [Auton et al., 1988]. Then we have:

$$\vec{F}_{AM} = C_m \frac{\rho_g}{\rho_p} (\vec{u}_{f@p} - \vec{U}_p). \quad (II.9)$$

It is computed with the derivative of the particle/carrier slipping motion:  $(\vec{u}_{f@p} - \vec{U}_p)$ . Since this force depends on the derivative of the slipping velocity, the density ratio does not modify the terminal velocity but influences velocity evolution. In this configuration, an inaccuracy due to the derivative of the slipping velocity computation. It can be solved through the consideration of the history force that requires a time integral [Basset, 1888].

### General relation:

Finally, drag, gravity, buoyancy, and added mass forces are used in *Archer* particles' motion equation:

$$\begin{aligned}
 \vec{U}_p &= (\vec{F}_D + \vec{F}_b + \vec{F}_{AM} + \vec{F}_g) m_p^{-1} \\
 &= -3\pi\rho_g\nu_g d_p \vec{U}_{slip} C_D(Re_p) \\
 &\quad + \frac{\rho_g}{\rho_p} \vec{g} \\
 &\quad + C_m \frac{\rho_g}{\rho_p} (\vec{u}_{f@p} - \vec{U}_p) \\
 &\quad + \vec{g}.
 \end{aligned} \tag{II.10}$$

Other forces can be used in particles motion, for example the viscous unsteady forces, the lift force responsible for the Magnus effect or the history forces. The selected forces are consistent for our application [*Multiphase flows with droplets and particles* of Crowe [Crowe et al., 2011]]. Moreover, for  $\rho_p \gg \rho_g$  we can desactivate the modelling of added mass and buoyancy, reducing the model to drag and gravity forces:

$$\vec{U}_p = -3\pi\rho_g\nu_g d_p \vec{U}_{slip} C_D(Re_p) + \vec{g}. \tag{II.11}$$

### II.1.2 Two-way coupling

Particles' momentum redistribution toward Eulerian field is implemented in *Archer* and is called Two-way coupling. It uses the force computed in equation II.10 and redistributes it through filter function into Navier-Stokes equations to have a volume force:  $|F_p| \rightarrow |f_p|$ . Considering particles' influence modifies the flow motion that adapts to the presence of the particle. We scheme the difference between One-way, Two-way and real particle on figure II.1, respectively from left to right. The One-way coupling does not modify the flow motion while Two-way coupling influences the flow motion since it redistributes its momentum. The difference with the real case is that the flow does not adapt at the interface of the particle.

In the present section the implemented filter function to redistribute particles' momentum toward Navier-Stokes equations is described. Since the momentum coupling perturbs the flow at particles location, it yields to an inaccurate interpolation of  $\vec{u}_{f@p}$ . We present the strategy implemented in *Archer* that consists in an averaging strategy to interpolate  $\vec{u}_{f@p}$  and a flow filter disturbance.

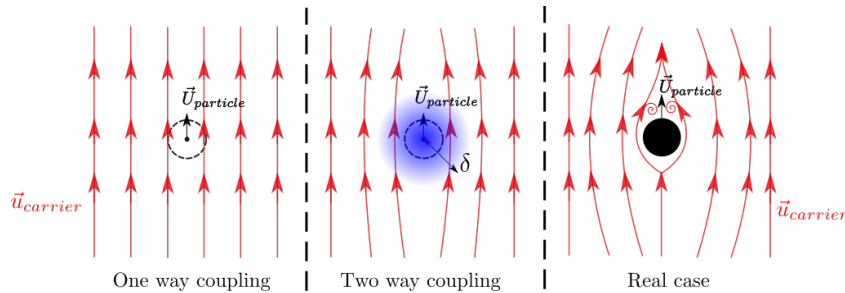


Figure II.1: Scheme representing One-way coupling and Two-way coupling with transfer of particle's momentum through kernel function over a distance  $\delta$  from the particle's radius center.

### Redistribution of the momentum

The momentum redistribution can be directly transferred to the particle where they are interpolated, it is used in Lagrangian Parcel Tracking method [Dukowicz, 1980] that permits to consider small particles influence in dense flows [Climent and Magnaudet, 2006]. This method is suitable for particles when  $d_p \ll \Delta x$ . For particle of cell size, it reduces the accuracy of particle transport and

a volumic redistribution over few cells is preferred. The area of redistribution is of a length  $\delta$  [m], often wider than particles' diameter [Maxey et al., 1997]. The filter function ensures that particle's force is entirely redistributed over a volume  $\frac{4}{3}\pi\delta^3$ , with a maximum reached at particle's center, its mathematical description is given in [Anderson and Jackson, 1967] and several implementations are found in literature [Kitagawa et al., 2001, Squires and Eaton, 1990, Elghobashi and Truesdell, 1992, Simonin and Squires, 2003, Ireland and Desjardins, 2017, Capecelatro and Desjardins, 2013, Evrard et al., 2020, Zhang and Prosperetti, 1997, Horwitz and Mani, 2016].

The filter function implemented in our study is a Gaussian filter function [Maxey et al., 1997], defined by:

$$G_\delta(\vec{x}) = (2\pi\sigma^2)^{-3/2} e^{-\frac{|\vec{x}|^2}{2\sigma^2}}, \quad (\text{II.12})$$

this function is not compact and the standard deviation  $\sigma$  must be chosen consequently to ensure that the force is redistributed under a threshold  $\epsilon$ . The latter is computed with the difference between the ideal domain of redistribution  $\Omega$ , and the volume of redistribution,  $K_\delta$ . The support depends on the filter length and the particle size, computed from:

$$\left| \int_{\Omega} F_p d\Omega - \int_{K_\delta} f_p dK_\delta \right| < \epsilon \quad \text{with} \quad K_\delta = \left[ |\vec{x} - \vec{X}_p| < \delta \right] \quad (\text{II.13})$$

Other filter functions have the advantage to be compact on  $[-\delta : \delta]$  [Elghobashi and Truesdell, 1992, Kitagawa et al., 2001, Wendland, 1995] but the advantage of the Gaussian function is to have an analytical discretization for uniform Cartesian grid. It can be obtained from Gauss integral or from error function. In *Archer* we implement the error function discretization defined for a cell  $K = [x_0, x_1] \times [y_0, y_1] \times [z_0, z_1]$  with a particle:

$$G_{\delta,K}(\vec{X}_p) = \frac{1}{\Delta x^3} \int_K G_\delta(|\vec{x} - \vec{X}_p|) d\vec{x} = \frac{[\text{erf}(\frac{x-X_p}{\sigma\sqrt{2}})]_{x_0}^{x_1} [\text{erf}(\frac{y-Y_p}{\sigma\sqrt{2}})]_{y_0}^{y_1} [\text{erf}(\frac{z-Z_p}{\sigma\sqrt{2}})]_{z_0}^{z_1}}{8(x_1 - x_0)(y_1 - y_0)(z_1 - z_0)}. \quad (\text{II.14})$$

In future developments, we can consider to couple Two-way coupling with AMR and a filter function independent to the grid could be integrated such as Wendland filter function [Wendland, 1995].

### Interpolation of $\vec{u}_{f@p}$

A developed analysis [Maxey et al., 1997] showed that the direct interpolation of the velocity of the particle from its Cartesian location is less accurate. They propose to interpolate the velocity over the entire area of feedback forces redistribution. They use the filter function and average the velocity field to recover  $\vec{u}_{f@p}$ , we call it  $\mathcal{A}(\vec{u}_{f@p})$  and it is done over  $\lambda$  that is defined by:

$$\lambda = \max(\delta, 2\Delta x). \quad (\text{II.15})$$

We define a volume of interpolation  $K_\lambda$  where the interpolation is done:

$$\mathcal{A}(\vec{u}_{f@p}) = \int_{K_\lambda} \vec{u}_f(\vec{x}) G_\lambda(|\vec{x} - \vec{X}_p|) d\vec{x} \quad \text{with} \quad K_\lambda = \left[ |\vec{x} - \vec{X}_p| < \lambda \right]. \quad (\text{II.16})$$

This strategy is used in *Archer* to interpolate the velocity at particles positions when the Two-way method is used.

### Particles momentum filter at $\vec{u}_{f@p}$

The velocity at the position of the particle,  $\vec{u}_{f@p}$ , is modified by the presence feedback force presented above. Since Two-way coupling is advected with undisturbed flow, it is important to account for this disturbance. In this section we present the filter that is implemented in *Archer* to remove the flow disturbance and improve Two-way model. We can decompose the flow disturbance by:

$$\vec{u}_{f@p} = \vec{u}_{f@p} + \vec{u}_{f@p}.$$

Where  $\vec{u}_{f@p}$  is the filtered interpolated velocity from the flow disturbance  $\vec{\hat{u}}_{f@p}$  that we want to use in our Lagrangian motion equation. It has been evaluated from particles feedback in [Gualtieri et al., 2015] and a filter is proposed for low Reynolds number:

$$\vec{u}_{f@p} = \frac{\vec{f}_p}{2\pi\mu_f\delta}. \quad (\text{II.17})$$

Following their work, a filter suitable for finite Reynolds number based on Gaussian filter function momentum transfer has been proposed [Balachandar et al., 2019]. They derived from Oseen approximation a correction that is used multiplying the particle's disturbance [equation II.17], defined by:

$$\Phi_{Os}(Re_\delta) = \frac{3}{\sqrt{2\pi}} \frac{\left[ \pi - \sqrt{2\pi}Re_\delta + (\pi/2)Re_\delta^2 - \pi \exp Re_\delta^2/2 \operatorname{erfc}(Re_\delta/\sqrt{2}) \right]}{Re_\delta^3}, \quad (\text{II.18})$$

where the Reynolds number is no longer computed on particle's size but on filter's size.

We implemented this correction in *Archer* following their work using a linear interpolation. It is still under developments since we observed a relative sensibility to the number of cells across particles' diameter. At  $d_p/\Delta x > 4$  we do not reach results observed in [Balachandar et al., 2019]. It is supposed that the challenging implementation of those corrections for Gaussian filter function is a issue in the code.

Another strategy to correct particle's disturbance is derived from Wendland filter function [Evrard et al., 2020]. It uses the averaged velocity,  $\mathcal{A}(\vec{u}_{f@p})$ , and has the advantage to be expressed through polynomial form:

$$\Phi_{Stk}(x) = \frac{1}{2145} \begin{cases} 2145 - 1001x^2 + 910x^4 - 735x^5 + 250x^6 - 33x^7 & \text{if } x \in [0 : 1] \\ 2145/x - 1001/x^3 + 910/x^5 - 735/x^6 + 250/x^7 - 33/x^8 & \text{if } x > 1 \end{cases} \quad (\text{II.19})$$

$$\Phi_{Os}(Re_\delta) = \frac{9\pi}{4Re_\delta^3} \left( 9\pi(1 - \operatorname{erfc}(Re_\delta^3/3\sqrt{\pi}) \cdot \exp(Re_\delta^2/9\pi)) - 6Re_\delta + Re_\delta^2 \right). \quad (\text{II.20})$$

In *Archer* those corrections have been implemented for the Gaussian filter function. They commented in their work that the type of kernel that is used (i.e. Gaussian or Wendland) has no impact on the velocity disturbance at the centre of the particle [Evrard et al., 2020]. Then, they found that at:

$$G_\delta = W_\delta \sqrt{2/9\pi},$$

the Gaussian and Wendland kernels have the same normalised integral over the real half-line. In *Archer* we use these corrections with the multiplicative factor. Since we want to ensure that both filters size have exactly the same normalized integral, the velocity interpolation is defined  $\sqrt{2/9\pi}$  times wider than the area of momentum redistribution. This assumption has an influence on simulation's results, showed later in this manuscript [section II.3].

The implementation of the Two-way coupling is resumed on figure II.2, below we define the main stages.

1. We interpolate  $\mathcal{A}(u_{f@p})$  using the Gaussian filter function over the volume centered on the particle  $K_\lambda$ .
2. We correct the flow disturbance induced by particles feedback.
3. We transport the particle with equations II.1-II.2 using corrected averaged slip velocity with  $\mathcal{A}(\vec{u}_{f@p})$
4. Finally we redistribute the particles momentum with  $G_\delta \vec{f}_p$  on the updated area  $K_\delta$ .

The implementation of this method is validated in subsection II.3.3. It is done against a method without correction. The expectations are to reduce the grid dependency improving accuracy and stability of the method. Note that following [Evrard et al., 2019], another solution can be considered.

- 1 Get  $A(\vec{u}_{f@p})$  through  $G_\lambda$
- 2 Apply correction on  $A(\vec{u}_{f@p})$
- 3 Transport particle
- 4 Redistribute  $\vec{F}_p$  through  $G_\delta$

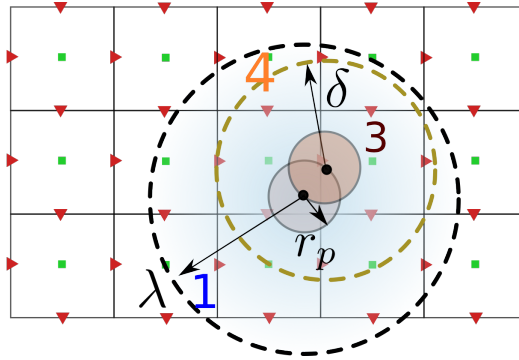


Figure II.2: Steps to advect particle with Two-way coupling in *Archer* for one time step. The interpolation is done over the volume  $K_\lambda$  and redistribution on  $K_\delta$  onto the uniform Cartesian staggered grid (red triangles: velocity, green square: pressure).

### II.1.3 Full Resolved Particles (FRP) approach

This approach directly considers the interface of the particle within Navier-Stokes equations and momentum transfer is done at its interface. To represent the interface, the no-slip/no-penetration is forced like a boundary condition. This approach usually requires a numerous cells across the diameter. A brief literature review of some applications involving different FRP approaches showed that 16 cells across the diameter was an acceptable balance between accuracy and computational time [Wang et al., 2014, Uhlmann and Chouippe, 2017, Brändle de Motta et al., 2019]. Although, recent works showed that the number of Eulerian cells across particles' diameter is not of first importance when ensuring no-slip/no-penetration boundary condition at particles' interface but the number of mesh cells belonging to the boundary layer surrounding the particle, whatever the particle diameter [Chadil et al., 2019]. Then, the redistribution of the particles' momentum at the resolved particle interface must be considered in this study since it influences particles/fluid interactions. Our purpose is to evaluate the capabilities of FRP approach in the under resolved area to transport under resolved droplets. Several FRP approaches exist in the literature, they are developed in Navier-Stokes or Lattice Boltzmann framework and some of them are briefly described.

An example of Lattice Boltzmann FRP is the bounce back method. This method resolves interaction at mesoscopic scale considering a Lattice Boltzmann framework to solve motion of fictitious particles [Chen et al., 1992a]. The concept of a Lattice Boltzmann method is to consider a fluid composed of multiple fictitious particles that are propagating on a given distance. Advection of those fictitious particles is calculated through Bhatnagar-Gross-Krook equation [Bhatnagar et al., 1954]. In this framework no-slip/no-penetration boundaries is implemented canceling transport of fictitious particles toward resolved particles' interface.

In Navier-Stokes framework, some FRP approaches are developed using ICM to force the boundary conditions of the particle. For example the penalty method uses a volume force at the interface [Ritz and Caltagirone, 1999]. It is directly implemented in Navier-Stokes equations which makes this method implicit. The strategy is to consider high viscosity inside the particle to represent the behavior of a pseudo-rigid non-elastic interface, but it can increase the computational time. It yields to reduce the rate of strain tensor to 0 inside of the fluid particle. In the carrier phase, the divergence free equation is respected.

Other FRP approaches are developed using a description of the interface to force the boundary conditions [Uhlmann, 2005, Marella et al., 2005, Mark and van Wachem, 2008]. This is the strategy that we implemented in *Archer*: an Immersed Boundary Method (IBM), following the work of Uhlmann [Uhlmann, 2005]. The reason is that it showed great scalability, numerical robustness and physical accuracy [Brändle de Motta et al., 2019]. Its description is given below, with the strategy of implementation in *Archer*.



### Immersed Boundary Method (IBM)

Immersed Boundary method combines a second order finite volume pressure correction scheme with a direct forcing IBM through a regularized delta function inspired from the first immersed interface method [Peskin, 1972]. This method is composed of two grids, a fixed Eulerian grid that discretizes the carrier phase through the flow solver and a Lagrangian grid to discretize the surface of the particle. Figure II.3 extracted from [Breugem, 2012] schemes the particle in yellow, with Lagrangian markers at its interface onto the Eulerian grid in black. The main advantage of this method is to force interactions between an Eulerian and Lagrangian grid without modification of the Eulerian flow solver. It has been applied on several applications such as the influence study of finite size particle immersed in a forced homogeneous isotropic turbulence [Uhlmann and Chouippe, 2017], sediment transport in open channel flow [Vowinckel et al., 2012] and in fluidized bed analysis [Guo et al., 2015] to give some applications.

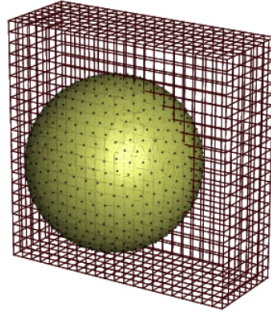


Figure II.3: Eulerian and Lagrangian grid representing the surface of the yellow particle [Breugem, 2012].

#### Numerical modelling:

Particles momentum is transferred from its surface toward Eulerian grid through a discrete Dirac function,  $\delta_h$ , that gives  $\vec{f}_\delta$ . It is coupled with Navier-Stokes equations:

$$\frac{\partial \vec{u}}{\partial t} + \vec{u} \cdot \nabla \vec{u} = -\frac{1}{\rho} \nabla p + \frac{1}{\rho} \nabla \cdot (\mu(\nabla \vec{u} + \nabla^T \vec{u})) + \vec{g} + \frac{\vec{f}_\delta}{\rho} \quad (\text{II.21})$$

To ensure that all the momentum of the particle is transferred toward the Eulerian grid, the Dirac function must be implemented following [Roma et al., 1999]. It is used to interpolate the velocity at particles interface and to redistribute the momentum of the particle toward Eulerian grid. The surface of the particle is discretized using a Lagrangian grid composed of  $N_L$  markers where exchanges between Lagrangian and Eulerian grid are done. We describe it following figure II.4.

To compute particle force, the first step is to interpolate the velocity of the Eulerian grid at particles interface using the dirac function  $\delta_h$ . We recover it after solving viscous and pressure terms [see section I.4.2].

$$\vec{u}^* = \vec{u}^n + \Delta t \left( -\vec{u}^n \nabla(\vec{u}^n) + \frac{1}{\rho} \nabla \cdot (\mu(\nabla \vec{u} + \nabla^T \vec{u})) + \frac{\vec{f}}{\rho} \right) \quad (\text{II.22})$$

In here, we consider  $\vec{u}^*$  the intermediate velocity of particles' interpolation  $\vec{u}^{**}$ , and at the Lagrangian markers' positions  $\vec{U}^{**}(\vec{X}_L)$ . The force of the fluid onto the surface is at every Lagrangian marker on particles' interface, calculated with:

$$\vec{F}(\vec{X}_L) = [\vec{U}^d(\vec{X}_L) - \vec{U}^{**}(\vec{X}_L)] \Delta t \quad (\text{II.23})$$

The velocity  $\vec{U}^d$  is obtained using rigid no-slip/no-penetration assumption. It is computed from:

$$\vec{U}^d(\vec{X}_L) = \vec{U}_p + \vec{\omega}_p(\vec{X}_L - \vec{X}_p) \quad (\text{II.24})$$

where  $\vec{\omega}_p$  is the particles' rotation. Through the difference between these velocities at the marker's position  $[\vec{U}^d(\vec{X}_L) - \vec{U}^{**}(\vec{X}_L)]$ , the third step of figure II.4 is obtained. Next we gather fluid force at every marker to obtain the total force exerted on particle's surface. Particles motion equations from [Uhlmann, 2005] are used to compute the velocity and rotation of the particle:

$$V_p[\rho_p - \rho_g]\vec{U}_p = -\rho_g \sum_L \vec{F}(\vec{X}_L)\Delta V_L + [\rho_p - \rho_g]V_p\vec{g} \quad (\text{II.25})$$

$$I_p\vec{\omega}_p = -\rho_g \sum_L (\vec{X}_L - \vec{X}_p) \times \vec{F}(\vec{X}_L)\Delta V_L + \rho_g \frac{d}{dt} \int_S [(\vec{x} - \vec{X}_p) \times \vec{u}] \quad (\text{II.26})$$

Then, we redistribute particles force at every Lagrangian marker on its surface and we transfer it through the dirac function [equation II.21]. Finally, we update  $\vec{u}^{**}$  to  $\vec{u}^{n+1}$  with projection method.

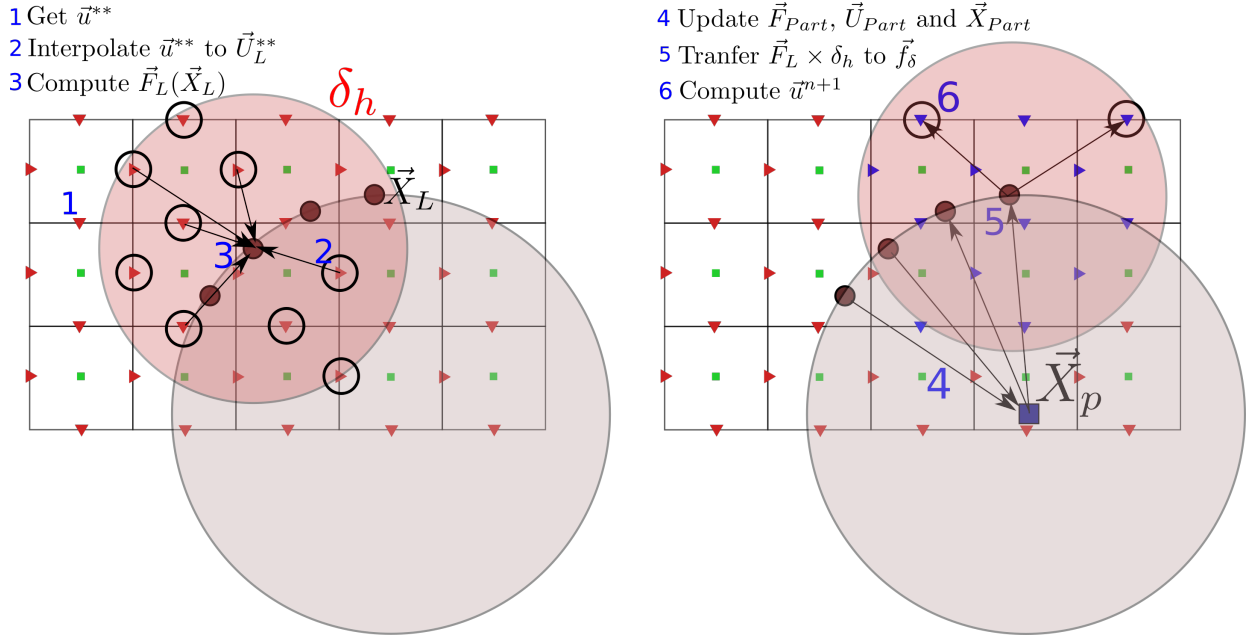


Figure II.4: Steps to advect IBM particle in *Archer* for one time step on a uniform Cartesian staggered grid. Interpolation of  $U_L^{**}$  over  $\delta_h$  (in red), at each Lagrangian marker (brown circle) over the surface of the grey particle. Particle's force is computed and redistributed over  $\delta_h$  (in red) on the velocity nodes of interpolation (in blue on second figure) for each Lagrangian marker. It ensures no-slip/no-penetration condition at particle's interface.

### Improvements:

In the classic implementation a drawback was pointed out: the limit of phase density ratio  $\frac{\rho_p}{\rho_g} = 1.2$ . This is because rigid body assumption is made in the general equation of motion of the particle [equation II.25]. We detail it in this section.

For the motion of the particle, the general equation is showed below.

$$\rho_p V_p \vec{U}_p = -\rho_g \oint_{\partial S} \vec{\tau} \cdot \vec{n} d\vec{\sigma} + [\rho_p - \rho_g]V_p\vec{g} \quad (\text{II.27})$$

In this expression, the hydrodynamic tensor represents the forces acting on its surface. It can be expressed such as:

$$\oint_{\partial S} \vec{\tau} \cdot \vec{n} d\vec{\sigma} = - \int_S \vec{f} d\vec{x} + \frac{d}{dt} \int_S \vec{u} d\vec{x}, \quad (\text{II.28})$$

in this equation,  $-\int_S \vec{f} d\vec{x}$ , represents the sum of the fluid-solid coupling force which is obtained from the sum of the Lagrangian force points:  $\sum \vec{F}(\vec{X}_L)$ . This expression can be simplified under

rigid body assumption. Then, the volume integral that estimates the rate of change of the particle;  $\frac{d}{dt} \int_S \vec{u} d\vec{x} \approx V_p \vec{u}_p$  is approximately solved. The reason is to gain computational time avoiding an integral but it leads to singularities when the density ratio is close to 1.

In [Breugem, 2012] they compute this integral and avoid the assumption  $\frac{d}{dt} \int_S \vec{u} d\vec{x} = V_p \vec{u}_p$  that limits the density ratio. They use a second-order accurate midpoint rule [Kempe et al., 2009] to compute the particles volume fraction on Eulerian grid. The particles' volume fraction is used to compute integral forces:

$$\frac{d}{dt} \int_S \vec{u} d\vec{x} = \sum_{\vec{x}} \vec{u} \alpha \Delta^n \quad (\text{II.29})$$

where the coefficient  $\alpha$  represents the particle's volume fraction on a cell and  $n$  the dimension of the problem. That improvement unbounded equation II.25 from the term  $\frac{\rho_g}{\rho_p - \rho_g}$ , moreover it improves the robustness of the method.

The second modification is on the redistribution of the particles' force [Breugem, 2012]. His analysis showed that the interpolation between the Eulerian and Lagrangian grid points, in order to recover the exact forcing of the particle onto the Eulerian grid through the calculation of its velocity and torque, was inaccurate. It is because of the interdependency of both grids in this forcing and the use of same information for several Lagrangian markers, i.e. the volume of control is of the order of the mesh. Then, a correction on this step has been implemented through a multi direct forcing scheme [Luo et al., 2007]. It consists in an iterative redistribution of forces from the Eulerian to Lagrangian grid from the obtained preliminary velocity  $\vec{u}^{**}$ . It is an iterative solver, then, the number of iterations is selected and it must be relatively low in order to restrain the computational time of the simulation. In *Archer* the number of iterations is set to 6 [Breugem, 2012]. The iterative loop is recalled in the algorithm II.1 where we iterate over a temporary velocity,  $\vec{u}^{**,q}$  to force boundary conditions at particles interface through Lagrangian markers.

```

1 Get  $\vec{u}^{**}$ 
2  $\vec{u}^{**} = \vec{u}^{**}$ 
3 do q=1, 6
4    $\vec{u}^{**,q-1} \rightarrow \vec{u}_L^{**,q-1}$ 
5   Update  $\vec{F}_p^q, \vec{U}_p^q$  and  $\vec{X}_p^q$ 
6   Redistribute  $\vec{F}_p^q, \vec{U}_p^q$  to  $\vec{X}_L$ 
7    $\vec{F}_L^q \rightarrow \vec{f}^q$ 
8    $\vec{f}^q \rightarrow \vec{u}^{**,q}$ 
9 end do
    
```

Algorithm II.1: Iteration loop over the particle's momentum redistribution at its Lagrangians markers position.

Finally, he observed that drag force was not accurately computed for particles because of the numerical treatment of the interface. Since Lagrangian markers are located at  $|\vec{X}_p - \vec{X}_L| = R_p$ , the redistribution area expand to  $|\vec{X}_p - \vec{X}_L| = R_p + 3\Delta x/2$ . He proposed a *ad-hoc* solution to converge faster toward the desired drag force that consists in retracting them inside particle's interface. From a serie of numerical validations, they observed that the optimal retraction was of the order of 30% of the mesh size. Then the points representing the numerical interface of the particle are located at  $|\vec{X}_p - \vec{X}_L| = (R_p - 0.3\Delta x)$ . All those improvements yield IBM to second order of accuracy [Breugem, 2012].

Recently, the second order of accuracy has been discussed in [Peng et al., 2019]. They showed that it was not obtained near particles' interface due to velocity gradient discontinuity at the interface. It leads to an underestimation of energy transfer at the interface, more especially for the dissipation. A restriction on the redistribution of the particle toward the fluid is considered in [Peng and Wang, 2020] where the boundary force is restricted in the solid region. Then, the forces are distributed only in the carrier phase, which corrects velocity gradient issues. Moreover, they propose to amplify the force redistributed to the Eulerian grid from the particle in order to avoid the iterative scheme proposed in

[Breugem, 2012]. These results are promising and their extension toward Navier-Stokes framework are considered as perspectives.

### Lagrangian grid generation

The generation of the exact control volume is complex to achieve for spheres. The first step is to determine the optimal number of Lagrangian markers to exchange quantities from Lagrangian toward Eulerian fields and vice versa. Then, their location on particle's interface to interpolate/redistribute on the same volume for each marker.

An optimal number of elements is provided for circular and spherical objects considering the particle's radius and the number of cells across its diameter [Uhlmann, 2005]. It permits to generate the same control volume per marker and ensures a stable particles' force redistribution, defined by:

$$N_L \approx 2\pi \frac{R_p}{\Delta x} \quad \text{in } 2D \quad (\text{II.30})$$

$$N_L \approx \frac{\pi}{3} \left( 12 \frac{R_p^2}{\Delta x^2} + 1 \right) \quad \text{in } 3D \quad (\text{II.31})$$

Knowing  $N_L$  we have to determine a position for each markers that ensures them a constant control volume. An inaccurate discretization of control volume can lead to numerical instabilities of particles motion. He proposed to initialize the markers through a minimization algorithm that permits to determine the equivalent volume of redistribution per point. Since mesh generation is expensive, we generate an array that store their location in the sphere reference framework.

In our Hybrid approach we generate particles of a wide range of sizes at irregular instants. We use an analytical solution to generate the position of the markers developed in [Saff and Kuijlaars, 1997]. In their work they compared mathematical solutions to provide a constant control volume per marker at sphere's interface. The accuracy of the method depends on the number of Lagrangian points. The solution retains from their analysis is a distribution of markers through the use of latitude and meridians onto a sphere using spherical coordinates  $\theta \in [0 : \pi]$  and  $\phi \in [0 : 2\pi]$  [equations II.32 and II.33].  $N$  represents the total number of points on particles surface [equation II.31]. The constant  $C$  is set to 3.6 which represents distance shrink when hexagonal lattices are orthogonally projected from a tangent plane to a sphere.

$$\theta_k = \arccos(h_k), \quad h_k = -1 + \frac{2(k-1)}{(N_L-1)}, \quad 1 \leq k \leq N_L \quad (\text{II.32})$$

$$\phi_k = (\phi_{k-1} + \frac{C}{\sqrt{N_L}} \frac{1}{\sqrt{1-h_k^2}}), \quad 2 \leq k \leq N_L - 1, \quad \phi_1 = \phi_{N_L} = 0 \quad \text{and} \quad 0 < \phi_k < 2\pi \quad (\text{II.33})$$

They comment that this relation is accurate until 12 000 points, in our case it represents a sphere with 62 cells across its diameter. For low mesh number, it is an elegant solution to get rid of the initialization of the position of the markers onto the grid. This solution is used in this manuscript where under resolved droplets are transported with particle tracking method. We evaluate the results of this mesh generation in section II.3.

#### II.1.4 Collision modelling

A collision algorithm is implemented to model all particle interactions through collision force,  $\vec{F}_c$ , computation. Two models are dominant in the literature. The first model is a solid sphere collision, it is used to treat binary collision. The second is a soft sphere collision model that considers particles' overlap to treat several collisions during one iteration. Other forces can be added to the particle interaction model for more complex flows such as cohesive force or van der Waals forces [Curtis and Hocking, 1970]. They are often considered when the wetting of the particle has an influence. In viscous flows, lubrication forces can also be considered [Brändle de Motta et al., 2013]. We chose to incorporate the soft sphere model in *Archer* [ $\vec{F}_c$  in equation II.34].

$$\vec{F}_c = \frac{m_i (\pi^2 + [\log e_d]^2)}{(Nc\Delta t)^2} \delta_{a,b} \vec{n}_{a,b} + \frac{2m_i [\log e_d] (\vec{U}_{n,a} - \vec{U}_{n,b})}{Nc\Delta t} \delta_{a,b} \vec{n}_{a,b} \quad (\text{II.34})$$

The overlap of particles at the collision is assimilated to a spring. In equation II.34, it is the factor  $\delta_{a,b} [m]$  for the two particles  $a$  and  $b$ .  $m_i$  is the mass of the  $i$ th particle. In the example of a collision between two particles, it is calculated using the relative mass of particles  $a, b$ :  $m_i = (m_a^{-1} + m_b^{-1})^{-1}$ . Time step is included in this force calculation,  $\Delta t$ . The time step calculated on the flow solver is often too high with respect to the collision time, a solution would be to decouple the collision from the main time solver. A parameter that represents the characteristic time of the collision is used:  $Nc$ . It is not implemented in *Archer* because it is not the purpose of our study. To recover accurately the physic of the damping system,  $Nc$  is set to 8 [Brändle De Motta, 2013]. The diffusion of the energy at the collision is considered with the coefficient  $e_d$ , which depends on the material properties. If this coefficient is set to 1, there is no diffusion of energy.

### II.1.5 Summary

In this section, we presented the methods that we chose to implement in *Archer* based on One-way coupling, Two-way coupling and IBM. We detailed our choices of implementations. The motivation of these implementations is to compare these Lagrangian approaches in order to consider the most accurate in the under resolved area over the range  $d_p/\Delta x \ll \Delta x$  to  $d_p/\Delta x \approx 6$ . The upper limits of their use are discussed in this chapter.

Using several Lagrangian approaches implies a general Lagrangian solver implementation that permits to go from unresolved droplet toward the most accurate particle tracking method. Its numerical implementation and coupling with the Eulerian solver is described in the next section.

## II.2 Implementation of the Lagrangian solver

We present the general Lagrangian solver implemented to treat the Lagrangian approaches detailed in the prior section. The purpose of this solver is to have a general numerical treatment of particles meanwhile using several transport models with respect to the particle type. The solver uses an Eulerian grid decomposition with the following goals:

- to enhance the Message Passing Interface (MPI) Lagrangian strategy reducing non-necessary exchanges between processors,
- to compute faster collisions between particles thanks to the Eulerian grid splitting allowing to look only around the particle,
- to facilitate allocation/deallocation of arrays storing particle since we expect several transformations,
- a general treatment of boundary conditions.

We first detail these points and we then present the second order temporal coupling with Navier-Stokes equations.

### II.2.1 Storage per processor

The treatment of Lagrangian particles in atomized spray involves a wide number of particles that is not constant. Thus, arrays storing particles information such as position, velocity and force are evolving along the simulation. Moreover, particles can switch of processor for MPI simulations since we use a spatial splitting, and we have to transfer the particle and all its information toward its new *owner*. The processor called *owner* represents the processor that owns the particle storing all particle's information. Another specificity of MPI is the coupling with the Eulerian grid, for example in the redistribution of the Gaussian filter that can extend toward several processors. We present here the

numerical algorithm that works for every kind of particles based on the Eulerian domain splitting. We first detail the Eulerian splitting and the strategy to store particles' information. Then we give an example of algorithm to show the Eulerian splitting advantages in *Archer*. We conclude with the strategy to exchange MPI Lagrangian information.

## Eulerian splitting

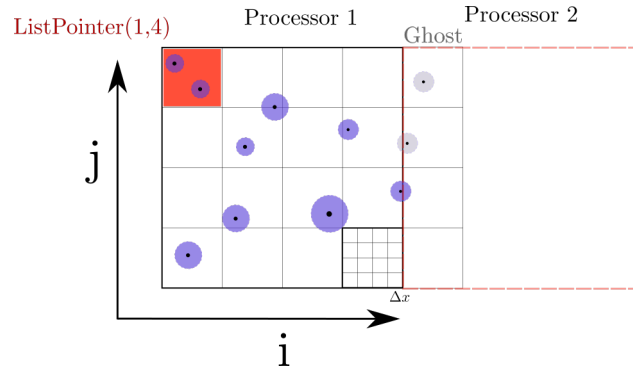


Figure II.5: Representation of the hierarchy of information for one processor with a uniform Cartesian grid, where every processor is split into an amount of subprocessor containing information on particles (in red). Ghost lists are used to exchange information with neighbouring processors, see ghost particles (in grey).

The Eulerian splitting strategy that is implemented is based on a spatial uniform Cartesian division [Capecelatro and Desjardins, 2013]. The number of subdomains,  $Nd$ , depends on its Cartesian division, in 2D or 3D:  $Nd = Nx \times Ny \times Nz$  and they have an equal size among each x-y-z component. This splitting is optimal for a square/cubic spatial domain that has the same load for each processor. It is ideal for our numerical solver because its use is optimal when cubic spatial division is set.

The Eulerian splitting is represented on figure II.5 for a 2D example. It is divided by 4 in each x-y direction, meaning that we have 16 subdomains for this processor, we call them list of pointers. At the position  $i = 4, j = 1$  we can see that particles are within a list of pointers represented in red, they belong to this subdomain. All of their relative information are stored in this list. A procedure is used to exchange MPI information from neighbors processors using *Ghost list*, detailed in the treatment of boundaries.

## Particles information storage

In Hybrid approach the position of particles is not constant since we expect to observe transformations. We select to fix the size of the array allocation to store their information and to propose an elegant strategy to increase particles' number per subdomain. It permits avoiding non-necessary allocation and reallocation. An optimal array size must be found to avoid an overwhelming allocation of the lists. If there are more particles than expected, we use a *linked list* that we call *Next list*. It has the same fixed size and properties that the prior list, and if there are more particles than available memory, the *Next list* is allocated.

We extract *Archer* source code to present the numerical implementation of the Eulerian splitting and the lists of particles:

```

1  TYPE :: TabRef
2      character(3) :: Name
3      integer :: id
4      integer :: Nd
5  END TYPE TabRef
6  TYPE :: ParticlePacketPTR
7      CLASS(ParticlePacket), POINTER :: P => Null()
8  END TYPE ParticlePacketPTR
    
```

```

9
10 TYPE :: ParticlePacket
11     real(rp), dimension(:,,:), pointer :: rData
12     integer, dimension(:,,:), pointer :: iData
13     type(TabRef), dimension(:,), pointer :: rVar => null(), iVar => null()
14     integer :: Np=0, NpAlloc=0
15     integer :: Nb_iVar=0, Nb_rVar=0
16     integer :: Size_iData=0, Size_rData=0
17     logical :: alloc = .False.
18     character(3) :: ParticleType
19     type(ParticlePacket), POINTER :: Next => null()
20     contains
21     procedure :: iLook => iLook
22     procedure :: iLookVec => iLookVec
23     procedure :: rLook => rLook
24     procedure :: rLookVec => rLookVec
25 END TYPE ParticlePacket
    
```

Algorithm II.2: Dynamic allocation of list of particles for various subdomain within one processor.

In this algorithm, several structures are observed, we detail their role in our solver. A general type is created to store the list of pointers, it is *TabRef*. The lists of pointers are called *ParticlePacket* and they store all particles' information that belong to their subdomain. For *ParticlePacket* we see the pointer *Next* that is our *linked list* which permits to allocate another array whenever the current one is filled. Relative information to the particle tracking algorithm are stored such as the total number of particles, *NpAlloc*, or the type of particles stored in the *ParticlePacket*: *ParticleType*. Then we detail the procedure to access particles' information stored in the *ParticlePacket* called *iLook*, *iLookVec*,...

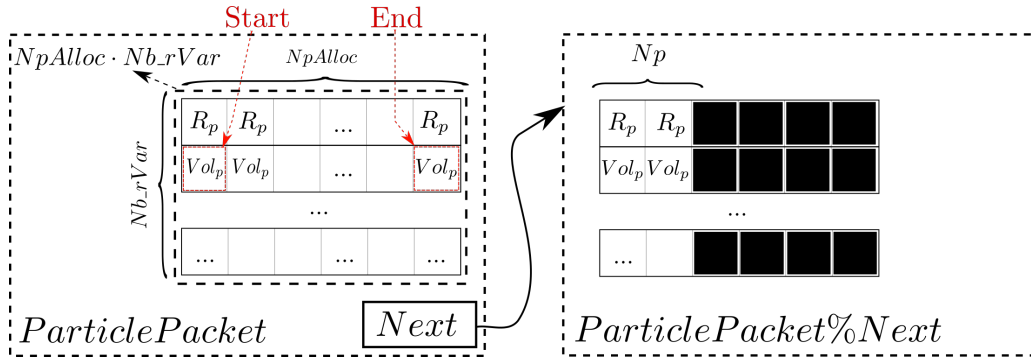


Figure II.6: Sketch of *TabRef* arrays storage for one *ParticlePacket*. Example given for two dimensions *rVec* array (storing real one dimension). The total memory size is  $NpAlloc \times Nb\_rVar$ , when  $Np$  exceed  $NpAlloc$  we point use *linked list* to allocate more memory. The access to data is done through arguments given in procedure, it permits to access the exact memory position of the information, from **start** to **end**.

We divide information belonging to particle into four kinds: integer, vector integer, real, vector real that belong to four kinds of procedure *iLook*, *rLookVec*, *rLook*, *rLookVec*. Then data are split among these four kinds with respect to their types, for example particles radius are real and Cartesian particles position are vector integer. When the number of particles are updated inside a *ParticlePacket*, these arrays are updated. We scheme their constructions for one dimension real variable [figure II.6]. The total allocated size depends on  $NpAlloc$  and  $Nb\_rVar$ . When  $Np = NpAlloc$ , we use the *linked list* to store more particles in a new *ParticlePacket*. We store the variables successively, it allows us to know exactly their location in the array using an argument given to the procedure. We can determine where does the list of information starts and finishes in memory.

We illustrate the strategy used to recover particles' information through an algorithm description (algorithm II.3). The first step is to iterate over each dimension of the 2D Cartesian Eulerian splitting among x-y. We do it through the allocation of a pointer, *List*, toward the subdomain, *ParticlePacket*, and we check if there are particles using the associated function. If there are particles, we create pointer associated to the *List* to recover stored particles information. The pointer Radius is created

and oriented toward the procedure *rLook* that points to the real type array. The methodology used to identify the location of the variables that we want to recover in the array is:

- use the name of the variable that we want to recover to get the position in the array, in our example *Rad* belongs to the first real variable stored in the array.
- From *NpAlloc* we know when this information starts and ends in the stored array.
- We recover only the necessary number of variables using the size *Np*.
- We store these information in the created pointer *Radius*.

Then we can iterate over the entire number of particles in a subdomain through *Np*. The main advantage of this strategy is that it avoids displacing arrays from subroutine to subroutine and it simplifies the MPI interactions, detailed later, and that we iterate in one processor only on subdomain that have particles which reduces requirements in memory storage.

```

1  do j = 1,ParticlePacket%Ny
2      do i = 1,ParticlePacket%Nx
3          List => ParticlePacket%ListCart(i,j)%P
4          do while (associated(List))
5              print *, 'i=',i,'j=',j
6              Radius => List%rlook("Rad")
7              do n = 1,List%Np
8                  print *, "Particle' radius : ", Radius(n), " for particle ", n," over",
ParticlePacket%Np
9              end do
10         end do
11     end do
12 end do
    
```

Algorithm II.3: Example of loop on dynamic allocated list of particles.

### Example of Eulerian splitting

We present one of the advantage of the Eulerian splitting with the example of collisions treatments. To determine if a particle collide with others, we have to compute its distance from the surroundings particles and if two overlaps, we compute collision force. The strategy is to reduce the area of research of collision using the Eulerian splitting inspired of [Capecelatro and Desjardins, 2013]. We reduce the research of collision to the neighboring lists because a particle can overlap two subdomains. It permits to reduce the use of the root-mean-square which is non-negligible on the computational cost. This implementation is similar to a Verlet list.

We give a 2D Cartesian example where particles are randomly initialized in a single processor split among  $6 \times 6$  dimensions. We chose one particle and start computing distance calculation with others, we reduce the computation to neighboring subdomains, filled area. Then we compute the distance between particles in this filled area iterating over the subdomains. Then, we see that the particle overlap with another one and we compute the collision force. Collision force is a repulsive force in our model and we add it to the general motion of particles. Details of the algorithm [algorithm II.4] is given below:

```

1  do j1 = 1,ParticlePacket1%Ny
2      do i1 = 1,ParticlePacket1%Nx
3          List1 => ParticlePacket1%ListCart(i1,j1)%P
4          do while (associated(List1))
5              do j2 = 1,ParticlePacket2%Ny
6                  do i2 = 1,ParticlePacket2%Nx
7                      if ((i1==i2) .and. (j1==j2).and.&
8                          (List2%ParticleType == List1%ParticleType)) then
9                          List2 => List1
10                     else
11                         List2 => ParticlePacket2%ListCart(i2,j2)%P
12                     end if
                    
```



```

13      do while(associated(List2))
14          if (associated(List1,List2)) then
15              same = .TRUE.
16          else
17              same = .FALSE.
18          end if
19          PositionL1 => List1%rlookVec("Pos")
20          PositionL2 => List2%rlookVec("Pos")
21          do id = List1%Np, 1, -1
22              if (same) then
23                  id2min = id+1
24              else
25                  id2min = 1
26              end if
27              do id2 = id2max, id2min, -1
28                  call checkdistance(PositionL1(id1),PositionL2(id2))
29                  if distance<Threshold:
30                      call CalculCollision
31                  end if
32              end do
33          end do
34          List2 => List2%Next
35      end do
36  end do
37  end do
38  List1 => List1%Next
39  end do
40  end do
41  end do
    
```

Algorithm II.4: Research of collision with two list, differentiation when the pointer point toward the same ParticlePacket, i.e.  $i=i2$  and  $j=j2$  for the 2D example.

In this algorithm we iterate on the entire Eulerian subdomains checking if they contain particles. When collisions are computed for the same subdomain, we first check if we look at the same type of particle. If we do, we check if we are not looking at the same particle for the two lists updating the logical *same*. Then we iterate over all particles computing the distance between two particles, see function *checkdistance*. If the distance is below a given threshold, we compute the collision force through the function *CalculCollision* and integrate it in particles motion. Since the particles in a subdomain can exceed the *ParticlePacket* memory, we call the *Next* list at the end of each loop using the *linked list* strategy.

Collisions can occur with particles from other processors and this is detailed in the MPI boundary conditions presentation with the use of the *Ghost* lists seen on figure II.5.

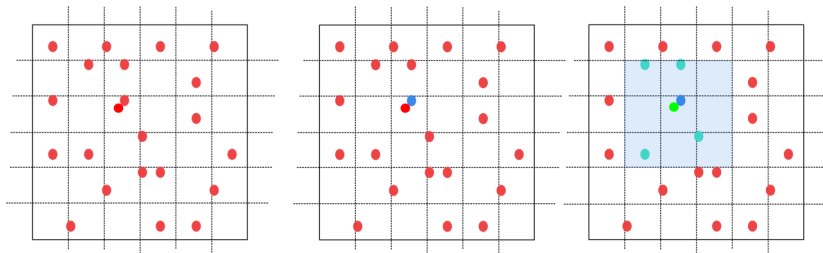


Figure II.7: Research of collision for one particle (blue) in single processor's implementation reduced to neighboring lists of particles (green) in the filled area (light blue).

## II.2.2 Multi processors strategy

### *Ghost lists presentation*

The treatment of the boundary conditions for Lagrangian solver is presented in this section. It consists in the allocation of *Ghost* lists that extend the Eulerian subdomain splitting of one dimension for each component x-y-z. Particles of neighboring processors are stored in these subdomains. It permits to consider the boundary conditions and to treat particles interactions between processors. The algorithm below present the modification to iterate over *Ghost* lists:

```

1  do j = 0,ParticlePacket%Ny+1
2      do i = 0,ParticlePacket%Nx+1
3          List => ParticlePacket%ListCart(i,j)%P
4          do while (associated(List))
5              print *, 'i=',i,'j=',j
6              Radius => List%rlook("Rad")
7              do n = 1,List%Np
8                  print *, "Particle' radius : ", Radius(n), " for particle ", n," over", List%Np
9              end do
10             end do
11         end do
12     end do

```

Algorithm II.5: Example of loop on dynamic allocated list of particles and ghosts.

The difference with algorithm II.3 is only on the dimensions of iteration, going from 0 toward  $Ny + 1$ . This strategy is used for MPI research of collisions. Similarly to the lists inside the domain, these *Ghost* lists are updated at every iteration through MPI exchanges. To update them, MPI exchanges are needed and the transfer of information from processor to processor is done at every iteration. The main advantage is that an entire list is sent into an already allocated array of the good size. The issue is the computational cost because we have to ensure that lists coincide, so we send list per list to neighbor processor and we use a *ISEND/RECV* strategy that include a wall time.

Improvements are required for the MPI strategy and ongoing tests are done to improve it with MPI function *PACK/UNPACK* that can send all the subdomains in one MPI exchange to the neighbors processors. Then, the neighbors processors unpack the lists and order them. The main advantage is to be independent of the number of lists to send.

### Boundary conditions

We consider three kinds of borders for particles: crossing processor border with and without periodic condition, going out of the domain or wall collision. We detail their treatment in *Archer* using the *Ghost* lists.

At every iteration we check and update the number of particles inside a subdomain through its Cartesian location. The same strategy is used for MPI exchanges including *Ghost* lists. If the particle is out of subprocessor subdomain, it is sent to neighbors through these lists and removed from the master. Then, its new master includes it in its computation. To ensure that MPI exchanges are not modifying the total number of particles, we use a check function that gather the quantities of particles per processor after exchanges. For periodic exchanges, we simply add the domain's length to the particle's position.

For wall collisions we do not initialize *Ghost* lists in this dimension and simply compute wall bouncing collision. Since we have Eulerian splitting we compute the distance only for subdomains next to the walls.

Then we describe outflow conditions which is the only border that depends on the Lagrangian tracking method. The reason is that forces are redistributed meanwhile the particle is going outside the domain and it can lead to numerical instabilities because of the non homogeneity of the redistribution. For example when half particle is out of the domain and the other half inside. To avoid these issues, we assume that the particles are no longer impacting the two phase flow atomization when they are about to exit the domain. Then, we transform IBM and Two-way into One-way particles which has the advantage to freeze the velocity of the particle, their influence is no longer considered.

### II.2.3 Temporal scheme description

The temporal splitting of the projection method enhances the accuracy of the simulation. In the in house code *Archer* various temporal scheme are implemented such as Adam Bashforth, Euler Explicit or Runge-Kutta at 2<sup>nd</sup> and 3<sup>rd</sup> order. They have the advantage to be accurate and stable in terms of Total Variation Diminishing. The Lagrangian implementation within *Archer* is done with an Euler Explicit temporal scheme, EE, and explicit Runge-Kutta 2, RK2.

The choice of temporal coupling between Lagrangian and Eulerian solver is to split both solvers. This choice is not optimal in terms of accuracy but allows more flexibility: the temporal scheme of each solver can be chosen independently. In the future, it will be also possible to use different time step for Lagrangian and Eulerian solvers.

The temporal description of the Eulerian/Lagrangian advection over one entire  $\Delta t$  is described in Euler Explicit and Runge-Kutta 2 on figure II.8. We first detail the EE scheme. On this figure, the update of the quantities is showed all along the Eulerian quantities evolution, represented with the blue arrow, with the upper script  $n$  and  $n + 1$ , see subsection I.4.2 for Eulerian solver description. The same strategy is used for the Lagrangian side, following the red arrow. In here, we consider directly that the intermediate velocity field has been obtained,  $\vec{U}^{**}$  and that it is used as velocity field in the Lagrangian solver.

The first step is to recover  $\vec{U}_{f@p}$  from the velocity field at  $\vec{U}^{**}$ . According to the Lagrangian tracking method that is used, various strategy have been presented, from the linear interpolation toward a more sophisticated interpolation for FRP, for example. The forces exerted from the fluid onto the particle,  $\vec{f}^{n+1}$ , is computed and the redistribution of particles' momentum is extrapolated onto the Eulerian grid, which is called  $\vec{F}_{Lag}^{n+1}$ . Then, the classical equation of motion of the particle are solved to obtain the velocity and position of the particle at  $n + 1$ . Finally, the particle influence,  $\vec{F}_{Lag}^{n+1}$ , is redistributed toward the Eulerian solver. The pressure is solved through the Poisson equation and the projection of the velocity at  $n + 1$  is obtained with the intermediate velocity considering Lagrangian source terms and the updated pressure. It ensures that the velocity field is divergence free.

With RK2 scheme, we halve the time step to transport particles. We compute forces at half time step from the particle's information at  $\vec{x}^n, \vec{u}^n, \vec{f}^n$  and use those information to transport more accurately particles over an entire time step. Then we can redistribute particles influence,  $\vec{F}_{Lag}^{n+1}$ , toward Eulerian grid with the Eulerian solver.

When RK2 scheme is used for Eulerian solver, we do not compute again  $\vec{F}_{Lag}$  in the second loop, we consider it *frozen*. Then Eulerian-Lagrangian schemes are not fully coupled which can reduce the temporal order of the method. However, it permits to increase Lagrangian Runge-Kutta scheme orders without modification of the Eulerian solver.

The purpose of the Hybrid method is to be able to go from droplet toward particle without any numerical perturbation on the accuracy and stability of the code. The strategy and results of this coupling are discussed later. However, it is important to point out that the strategy to go from Eulerian toward Lagrangian solver and vice versa has been done after obtaining the divergence free in the velocity field. This choice influence the strategy that has been used in the rewriting of the velocity field, as seen in [Ling et al., 2015]. This implementation is commented.

## II.3 Validation of the Lagrangian tracking

To validate the implementation of the particle tracking algorithm and to study its capability to be incorporated into the Eulerian-Lagrangian two phase flow simulation, a test case is studied: the sedimented free-falling particle. First, the methods are studied to understand their sensibilities to the mesh resolution. On this test case, the temporal schemes, Euler explicit and Runge-Kutta 2, are presented for the One-way and Two-way method. Then, the results for all the particle tracking methods are compared. It permits to determine their capability in the purpose of Eulerian-Lagrangian simulation.

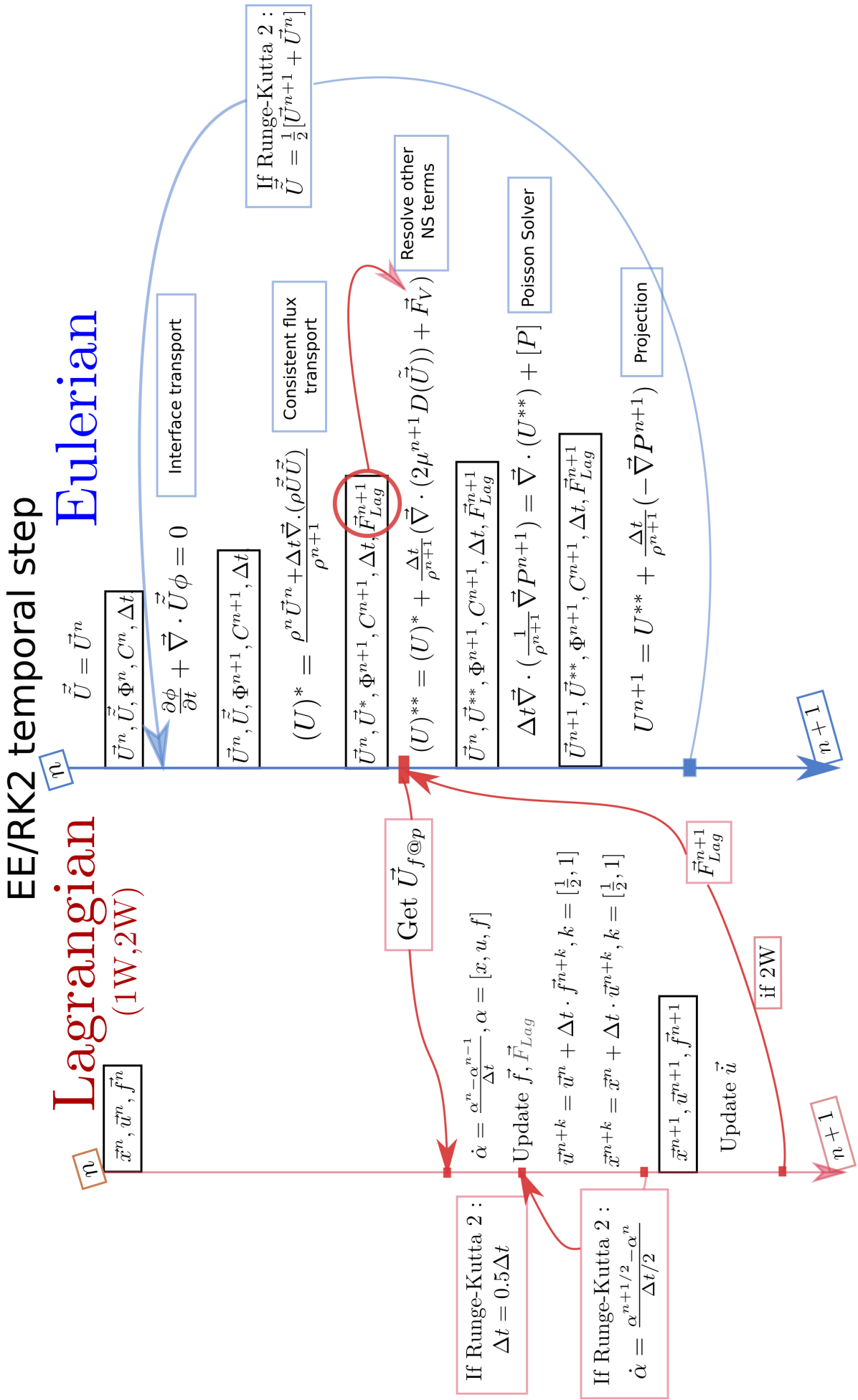


Figure II.8: Archer Eulerian / Lagrangian temporal scheme for Euler Explicit and Runge-Kutta 2 method.

In this section, we also study the IBM (FRP) order of convergence on a specific test case: an array of particles.

### II.3.1 Description of the test cases

#### Sedimented free-falling particle

From the numerical study of Ling et al. [Ling et al., 2015], a falling droplet in a confined environment has been studied, physical properties of the case are referred in table II.1. The characteristic numbers

$\rho_l$ [kg.m <sup>-3</sup> ]	$\rho_g$ [kg.m <sup>-3</sup> ]	$\mu_l$ [Pa.s]	$\mu_g$ [Pa.s]	$\sigma$ [N.m <sup>-1</sup> ]	$g$ [m.s <sup>-2</sup> ]	$d_p$ [m]	$L_x = L_z$ [m]	$L_y$ [m]	$X_{p,t=0}$ [m]
1000	10	10 <sup>-3</sup>	10 <sup>-4</sup>	0	9.81	10 <sup>-4</sup>	10 <sup>-3</sup>	2 · 10 <sup>-3</sup>	[1., 1.5, 1.] · 10 <sup>-3</sup>

Table II.1: Physical parameter of the falling droplet simulation from [Ling et al., 2015]

of the study are Reynolds particle number,  $Re = 0.43$ , and characteristic particle time  $\tau_p = 5.55 \cdot 10^{-3}$ . We give the length ratio between box width and particle's diameter;  $d_p/L_x = 0.1$ , it shows that the test case is confined. The terminal free-falling particle velocity can be estimated using semi-empirical analysis [Beard, 1976]. In our configuration we use a correction on the drag force computation to consider wall effects since they influence particle's motion. This correction is not analytic and it creates uncertainties on the terminal velocity accuracy.

A first relation to consider the influence of the wall on a single free-falling particle is derived in [Richardson and Zaki, 1954] for cylinders, the *Francis* equation. Later this equation has been generalized to avoid box's shape dependencies [Di Felice and Parodi, 1996, Di Felice, 1996] and we use it for our square domain:

$$\eta = \frac{v_{t,bounded}}{v_{t,unbounded}} = \left[ \frac{1 - \frac{d_p}{L_x}}{1 - 0.33 \frac{d_p}{L_x}} \right]^{2.7}. \quad (\text{II.35})$$

It uses the domain's length in the perpendicular direction to the gravity  $L_x$  and gives a corrective factor,  $\eta$ , implemented in particles' motion equation [equation II.10].

The influence of this parameter is non-negligible. The example of the terminal velocity difference with and without correction is given for two models of transport. First, in the simplest model of particle, that only considers  $\tau_p \vec{g}$  to model particle's motion, we have:  $V_{Sto.}(t = \infty) = 0.0539$  [m.s<sup>-1</sup>]. Then we include bounding correction,  $\eta$ , to the Stokes particle motion:  $V_{Sto.,\eta}(t = \infty) = 0.0440$  [m.s<sup>-1</sup>]. The influence of the borders reduces the velocity of 20%. Using the bounding correction and Schiller and Naumann drag correction we have a terminal value of  $V_{S.\&N,\eta}(t = \infty) = 0.04192$  [m.s<sup>-1</sup>].

Figure II.9 shows analytical results for One-way method. We present the three free-falling velocity evolution with the correction presented before:  $V_{Sto.}$ ,  $V_{Sto.,\eta}$  and  $V_{S.\&N,\eta}$  respectively in bold dashed, dashed and solid line. The velocities obtained here can be considered as exact reference for the Two-way model, without considering the physic. The reason is because in this test case, the undisturbed velocity is  $\vec{u}_{f@p} = 0$  since One-way method does not redistribute momentum toward the fluid and the carrier phase is initialized at rest, we have  $\vec{u}_{f@p} = \vec{u}_{f@p} = 0$ . The test case is then ideal to observe the influence of the filter on the undisturbed velocity interpolation. The reference is considered to be between the Stokes/Schiller and Naumann corrections for the particles/droplet terminal velocity.

#### Array of fixed particle

The fixed particle array's simulation is a well known test case in the literature [Lévy, 1983]. A gradient of pressure is initialized in one direction in the cubic box, in our case among x, and, interaction between the flow motion and the fixed particle is studied. This simulation is done to study the accuracy and order of the IBM method that is implemented in *Archer*.

The gradient of pressure is initialized numerically using the volume force inside the Navier-Stokes equation. For a single particle at stationary state, these equations reduce to the balance between the

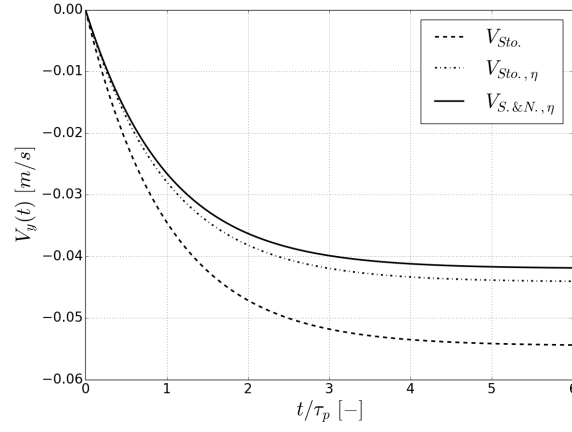


Figure II.9: One-way coupling for unbounded Stokes, bounded Stokes and Schiller and Naumann bounded free-falling velocity evolution against characteristic time.

drag force exerted on the fixed particle and the pressure gradient among the direction of the flow times particle's volume [equation II.36]. Numerically, the pressure gradient can be assimilated to the gravity force acting on the entire domain, we use it to scale the velocity evolution against time. In *Archer* it is what we considered to perform this simulation.

$$\begin{aligned}
 V_p \frac{\partial P_g}{\partial x} &= F_D \quad F_D = -3\pi\mu_g d_p \vec{u}_{slip} \\
 \frac{\partial P_g}{\partial x} &= -3\pi\mu_g d_p \vec{u}_{slip} \cdot \left[ \frac{4}{3}\pi \frac{(d_p)^3}{8} \right]^{-1} \\
 \frac{\partial P_g}{\partial x} &= -\frac{18\mu_g \vec{u}_{slip}}{d_p^2}
 \end{aligned} \tag{II.36}$$

The domain is fully periodic which creates a network of particles. The physical properties for this test case are:

$\rho_g$ [kg.m <sup>-3</sup> ]	$\mu_g$ [Pa.s]	$g$ [m.s <sup>-2</sup> ]	$d_p$ [m]	$Lx = Lx = Lz$ [m]	$\langle u_f \rangle$ [m.s <sup>-1</sup> ]
1.	10	0.184	1	8	1

Table II.2: Physical parameter of the single fixed particle

To respect Stokes flow assumption, the Reynolds number of the simulation has been conserved relatively small  $Re = 0.1$ , for domain centered on the particle's diameter,  $d_p = 1$  [m]. The magnitude of the mean flow velocity averaged in space has been set to  $\langle u_f \rangle = 1$  [m.s<sup>-1</sup>] which provides a kinematic viscosity of the flow of  $\nu_f = \frac{\langle u_f \rangle d_p}{Re} = 10$  [m<sup>2</sup>.s<sup>-1</sup>]. Density of the flow is set to  $\rho_g = 1$  [kg.m<sup>-3</sup>] for simplicity, that leads to a dynamic viscosity of  $\mu_f = 10$  [kg.s<sup>-1</sup>.m<sup>-1</sup>].

The reference solution has been obtained with icoFoam solver in openFoam code. We consider it as such because we can use a more refine unstructured grid with the same boundary conditions than what is possible in *Archer*. Moreover, the freedom of the unstructured mesh permits to represent the solid particle with no cells inside, and, imposing the velocity at the interface of the particle at 0 through embedded boundary method. Therefore gradient of pressure in the normal direction to the particle surface is set to 0. Additional cells are added at the interface of the solid particle to increase accuracy of the calculation and a rendering of the mesh is showed on figure II.10a where the refinement is clearly observed at the particle's interface.

The studied post treatment for this test case are global and local parameters. First, we study the averaged flow velocity motion evolution in space:  $\langle u_f \rangle$  [m.s<sup>-1</sup>], and its converging value at stationary state. Then, local information are collected: three probes are set in the low pressure area behind the particle, at the respective position of  $\vec{x}_1, \vec{x}_2, \vec{x}_3 = [X_p + d_p; Y_p + \frac{d_p}{2}; Z_p], [X_p + d_p; Y_p -$

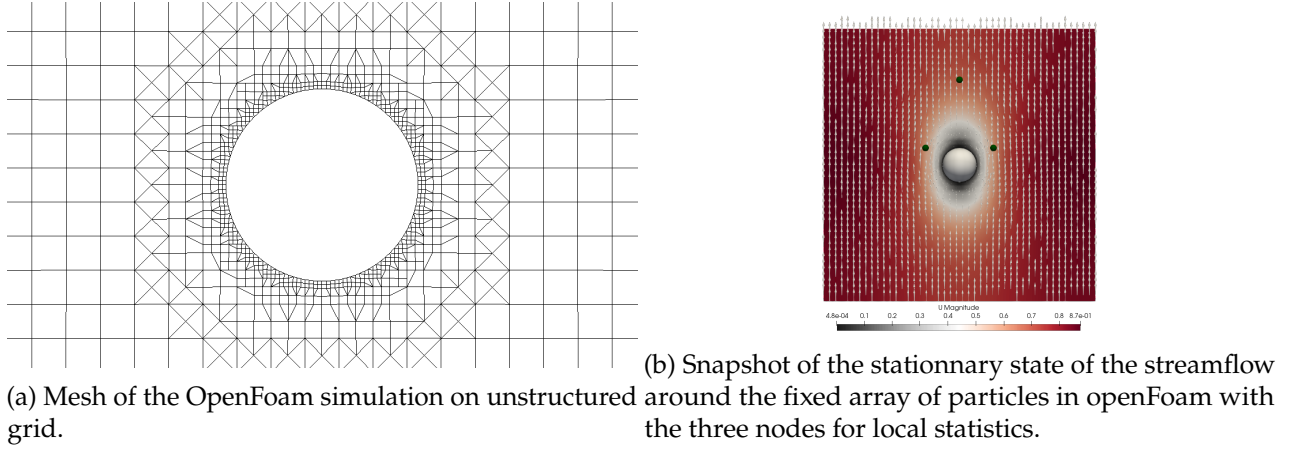


Figure II.10

$\frac{d_p}{2}; Z_p], [X_p + \frac{5}{2}d_p; Y_p; Z_p]$ , where the evolution of the velocity magnitude is studied. These probes are here to assess the results showing that IBM is second order of accuracy for global properties and to determine its order of accuracy near particle interface [Peskin and McQueen, 1989]. They are represented by small spheres behind the particle on figure II.10b. As commented, some are in the vicinity of the particle and are following the velocity evolution. The probe far from the particle is in the downstream area and it is less influenced by the presence of the particle. Results from icoFoam are showed on figure II.11 and are the references for this test case, for all implementation of Lagrangian tracking method.

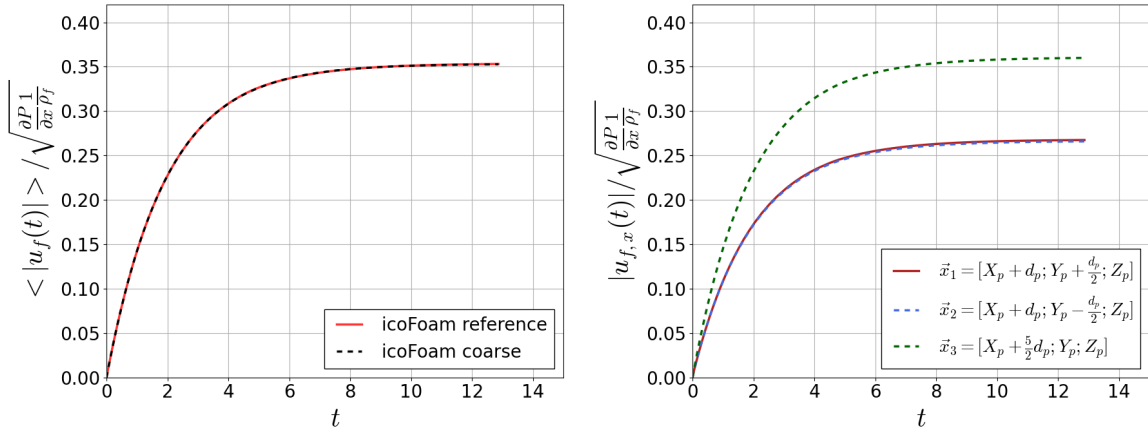


Figure II.11: Temporal mean velocity evolution within the domain (left), temporal velocity magnitude evolution for three nodes behind the particle (right) against characteristic time.

### II.3.2 One-way Lagrangian model in Archer

We presented *Archer* particles motion implementation [section II.1], we validate it through the free-falling sedimented particle test case. The results are compared to analytical solution for the granular motion, Stokes motion and bounded Stokes motion [figure II.12]. The models that are implemented in the code are represented by dashed lines while their analytical solutions are plotted in same colors solid lines.

The analytical granular solution is well recovered in *Archer* Lagrangian solver, it ensures that the action of the gravity is well implemented in the code and that granular motion can be simulated.

Next, we compare the implemented particle motion with added mass, drag and buoyancy forces against analytical solution:  $V_{Sto}$ . The consideration of the fluid through the drag correlation implies

that the particle might reach an equilibrium velocity state [section II.1]. It is different from the previous model that increases infinitely. *Archer* and analytical results are similar, the difference observed on the zoomed area is of the order of  $10^{-4}$  [m/s].

Then we study the bounded correction implementation in our solver from [Di Felice and Parodi, 1996],  $V_{Sto.,\eta}$ . Again, the evolution are overlapping that conclude on the accurate implementation of the Lagrangian model in *Archer*.

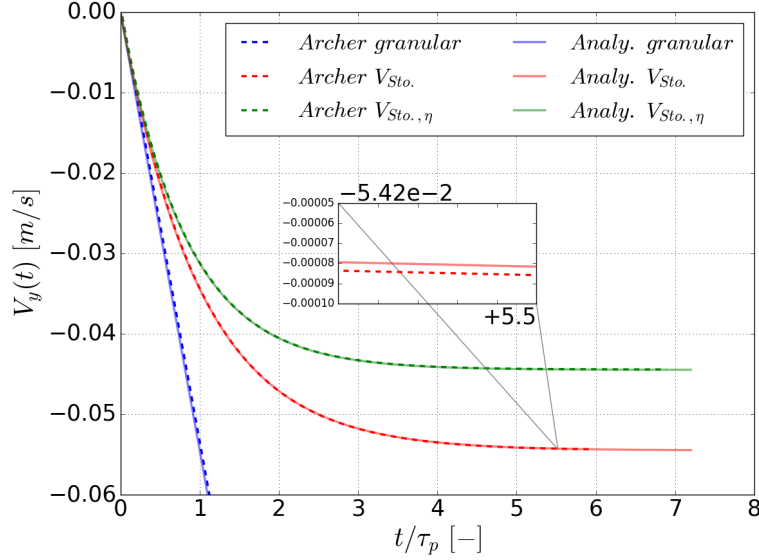


Figure II.12: Comparison *Archer* / Analytical solution of free-falling particle's velocity against characteristic time for granular,  $V_{Sto.}$  and  $V_{Sto.,\eta}$ .

### II.3.3 Two way method validation

In this section, we analyze the influence of the redistribution of the momentum toward the fluid on the free-falling particle using the Two-way method. Two methods are compared in this section, the first one uses the Gaussian filter function, [equation II.12], to redistribute its momentum toward Eulerian grid. Second, we implement the correction on the computation of the undisturbed fluid velocity,  $u_{f@p}$ . The analysis is carried for several mesh across particles' diameter and for several filter size. The results that we analyze are the evolution of the particle's velocity against characteristic time and its terminal velocity. The reference is the One-way method solution since it permits to have an interpolated velocity without perturbation.

The Gaussian filtered function smoothly redistributes the force of the particles onto the fluid. Various filters exist, and they are described [subsection II.1.2]. Since this function is not compact on the range  $[-\delta; \delta]$ , it is important to select a standard deviation that permits to redistribute entirely the particles' momentum. A relationship between the standard deviation,  $\delta$  and  $R_p$  is used to always ensure that more than 99% of particles' momentum is redistributed. The choice of  $\delta$  is important because it gives the redistribution area, when it is of the order of one radius, the momentum is mostly redistributed toward the cells where the particle is located. When the area of redistribution increases, the area where the particles' momentum is redistributed is wider.

An example of redistribution of the energy with a variation of the filter size is given on figure II.13. It shows the area of influence of the particle to the carrier phase for three filter size:  $\delta = [3., 5., 7.] \cdot R_p$  for  $d_p/\Delta x = 3.2$ . The results are weighed by the maximal value of the momentum redistribution, and we verify that the force volume source term integral gives the particle's force. One of the purpose of this section is to determine the influence of the filter size on the accuracy of the method. In the literature [Ling et al., 2013], it is commented that the smaller is the redistribution area, the higher is the underestimation of the drag force, we comment these observations later. Since we want to observe



the evolution of the accuracy of the method in the unresolved area, a variation of the number of cells across the diameter is done for all filter sizes.

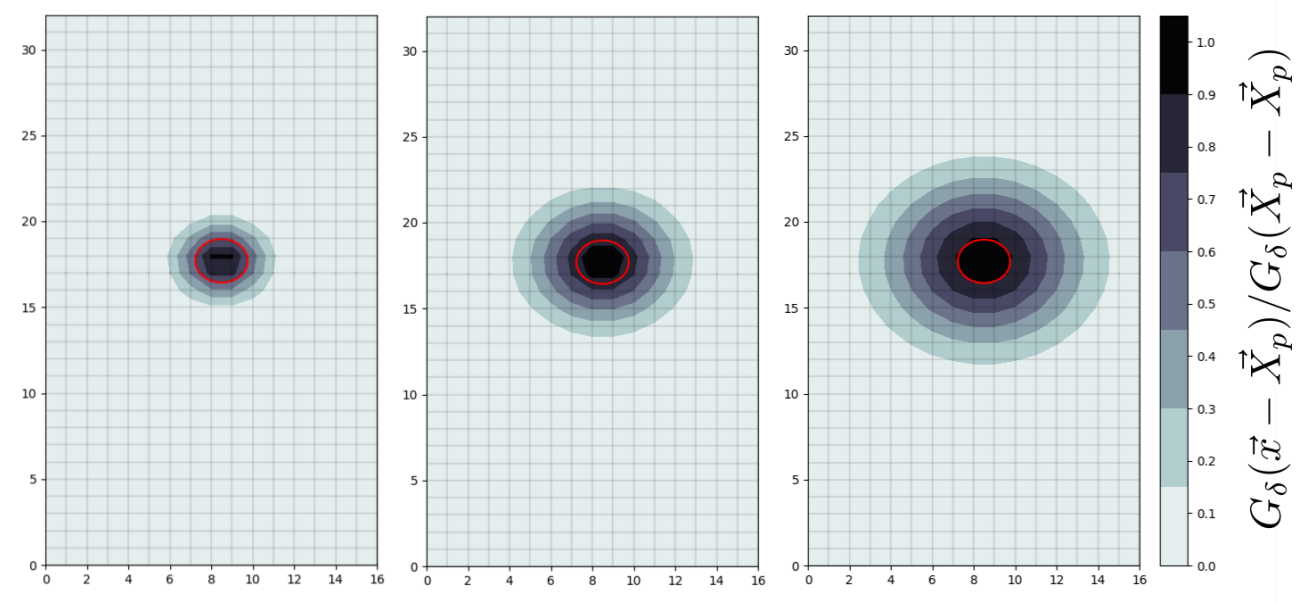


Figure II.13: Redistribution of the momentum of the particle for various filter's size  $\delta = [3., 5., 7.] \cdot R_p$  using the Gaussian filter function.

Free-falling sedimented particle simulations are performed for filter size:  $\delta = [3., 5., 7., 10.] \cdot R_p$  and several meshes resolution  $\frac{d_p}{\Delta x} = [0.4, 0.8, 1.6, 3.2, 4.8]$  covering our guess of the ICM droplets' unresolved area. Since several parameters are involved we express mesh resolution in particles' diameter and filter length in particles' radius. We compare three configurations of Two-way method, the first one considers  $\lambda = \delta$  without correction. Second, we consider the implementation of undisturbed interpolated velocity correction following [Evrard et al., 2020], it implies that  $\lambda = \delta \sqrt{2/9\pi}$  [subsection II.1.2]. Then the simulations with this configuration are done with parameters set to  $\lambda = [3., 5., 7., 10.] \cdot R_p$  and  $\delta = [0.78, 1.3, 1.82, 2.6] \cdot R_p$ . We perform the same simulations without interpolated undisturbed velocity correction. Then we can compare the influence of the correction in terms of:

- Area of redistribution/interpolation since the first and second configuration have the same  $\lambda$ .
- Influence of the correction since the second and third configuration have the same parameters length  $\delta$  and  $\lambda$ .

We plot the simulations' results at constant filters' size and variation of the mesh resolution [figure II.14]. The One-way solution evolution is given as a reference in solid line. On the left, the results for the Gaussian redistribution without correction are presented. On the right, the results with correction on  $\mathcal{A}(\vec{u}_{f@p})$  are presented.

### Free-falling particle's velocity evolution

We first comment the results observed for the method without correction [left figure II.14]. In most of the configuration, it occurs that the results for  $d_p/\Delta x = [3.2, 4.8]$  overlap and the terminal velocity study provides more information for those configurations. When  $\delta = \lambda = 3R_p$ , it appears that the mesh ratio influences the results, the higher it is the faster evolves the particle. It shows that the drag force is underestimated in these results. This confirms the well-known analysis on this method, it does not converge when  $R_p/\Delta x \rightarrow 0$ . It appears that increasing the filter size decreases the error of

velocity evolution. The higher is  $\delta$ , the better are the results. At  $\delta = 7 \cdot R_p$ , all resolutions lies between 1 and 1.2 times the reference velocity. When the filter is set to the maximum size given by the domain's length, results converge fast toward the reference. However, the references' velocity is not reached, it is expected that the correction of the interpolated velocity can improve them.

These results are showed on center figure II.14, and similar evolutions are observed. The higher is the resolution of the simulation, the higher is the terminal velocity while increasing the filter size decreases the underestimation of the drag force. Again, the convergence is faster when the filter is wider and for  $\delta = 2.6 \cdot R_p$ , all the results lie in between 1 and 1.1 times the reference velocity. Since the filter size is much smaller in this configuration, we observe that the implementation of a correction improves the accuracy of the method. We compare these results to the same configuration without correction [right figure II.14]. It appears that for all configurations only smallest mesh resolution gives an acceptable accuracy for particle velocity evolution, 1.08 times the reference's solution. It shows that the correction drastically improves the results and that we must consider a relatively wide filter redistribution to avoid underestimation of drag force. The next step is to evaluate the terminal velocity of those simulations to determine the factor influencing the convergence order.

### Terminal velocity analysis

The terminal velocity is studied computing the absolute difference between the Two-way simulation and the One-way simulation. Since the major improvement is obtained modifying the filter size, the results are plotted at constant filter size against numerical resolution. We express the convergence against  $\frac{\Delta x}{R_p}$ , with  $\frac{\Delta x}{R_p} = [0.42, 0.625, 1.25, 2.5, 5.0]$  ( $\frac{d_p}{\Delta x} = [4.8, 3.2, 1.6, 0.8, 0.4]$ ). A general observation is that the coarser is the simulation the closer to the reference are the results.

We first comment the results that do not include correction [figure II.15a]. On these results we confirm that the wider is the filter, the more accurate are the terminal velocities. For example, at  $\delta = 10R_p$ , we observe a range of error of less than  $\approx 5\%$ . The other observation from those results is that the smaller is the filter, the higher is the importance of the numerical resolution. For example, when the filter size is set to  $\delta = 3R_p$ , we observe an evolution of the accuracy going to the coarse mesh. On the other hand, the wider is the filter, the smaller are the improvement decreasing the numerical resolution. It confirms that for this method, the filter size is the first criteria to select to ensure the accuracy of particles' transport.

The general evolution of the results obtained for the interpolated velocity correction is similar, [figure II.15b]. We observe that increasing the filter size and decreasing the numerical resolution improve the accuracy of the method. On these results, a clear gap is observed between the coarsest simulation and others,  $d_p/\Delta x > 0.4$  ( $\Delta x/R_p < 5$ ). It can be explained by the smaller number of cells that are used to compute the averaged velocity at particle's position. The observed results are of the same order of accuracy while the corrected results have a filter size 3.75 times smaller, moreover, we observed that the filter size has a strong influence on the accuracy of the method regardless the numerical resolution.

We compare these results to the same configuration without correction [figure II.15c]. In the best scenario we increase the order of accuracy of at least one order, ( $\lambda = 10R_p$ ,  $\delta = 2.6R_p$ ), again we observe the great improvements thanks to this correction. We can go further to quantify the influence of the correction comparing the maximal interpolated velocity for these series of simulation.

### Influence of the interpolated velocity

To understand the improvements obtained with the correction, the maximal interpolated velocity is analyzed. It is scaled by the reference's terminal velocity to have the amplitude of the error. To recall, in this configuration the interpolated velocity must be 0, thus the closer the ratio  $\mathcal{A}(\tilde{u}_{f@p})/V_{S\&N,\eta}(t = \infty)$  is to 0, the better it is.

It was commented before that the inaccurate redistribution of the particles' momentum locally accelerates the flow. Then, this accelerated flow induces an error that is transferred to the particle motion equation through the velocity interpolation. Thus we expect to observe a pattern similar to terminal velocity results [figure II.15]. We observe that the coarser is the simulation the smaller is the

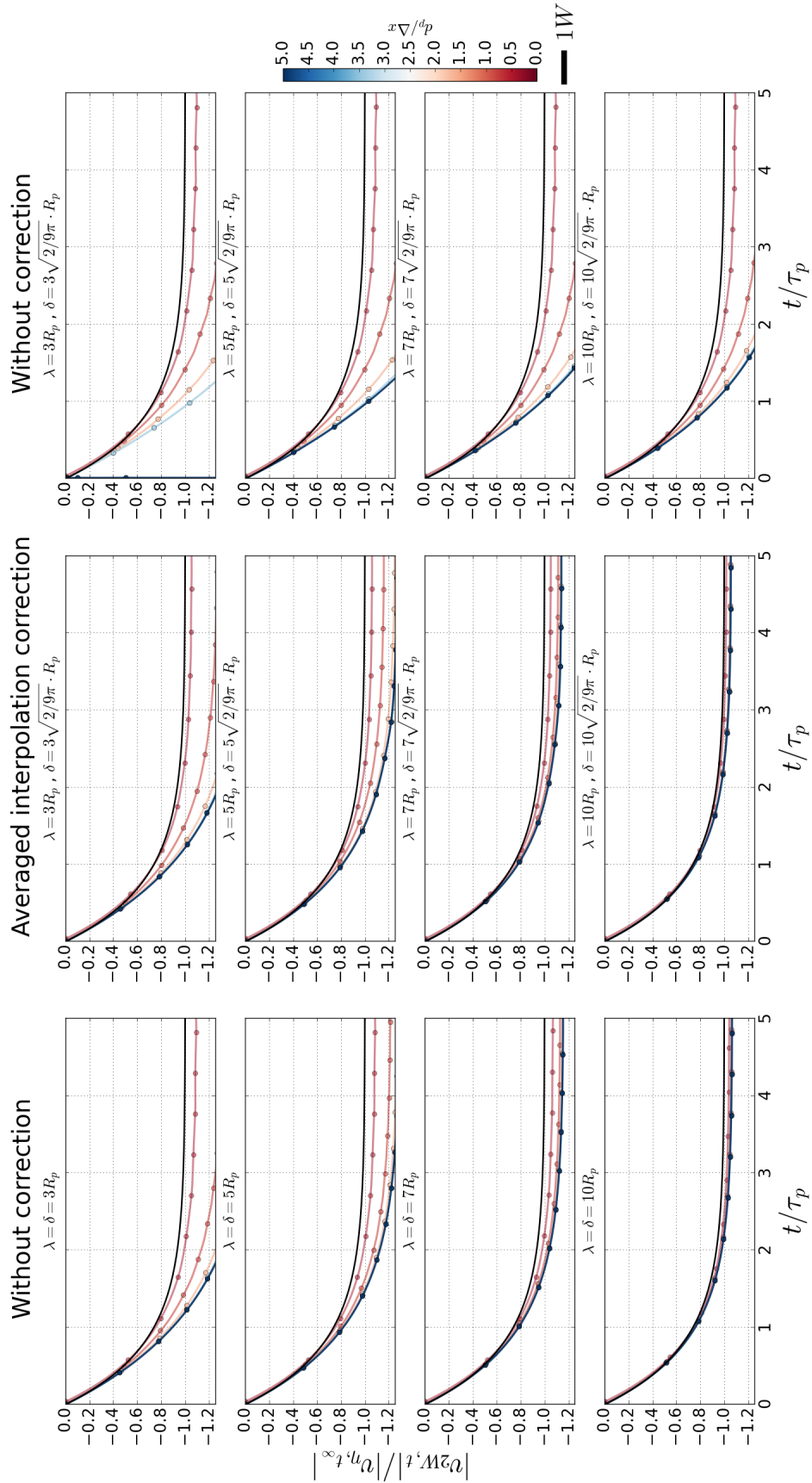


Figure II.14: Free-falling particle's velocity dimensionless by One-way results against characteristic time for three Two-way approaches using Gaussian filter function:  $\lambda = \delta = [3., 5., 7., 10.] \cdot R_p$  without correction,  $\lambda = [3., 5., 7., 10.] \cdot R_p$  and  $\delta = \sqrt{2/9\pi} \cdot [3., 5., 7., 10.] \cdot R_p$  with  $\mathcal{A}(u_{f@p})$  correction,  $\lambda = [3., 5., 7., 10.] \cdot R_p$  and  $\delta = \sqrt{2/9\pi} \cdot [3., 5., 7., 10.] \cdot R_p$  without correction. Mesh resolution evolves from  $\frac{d_p}{\Delta x} = [0.4, 0.8, 1.6, 3.2, 4.8]$ .

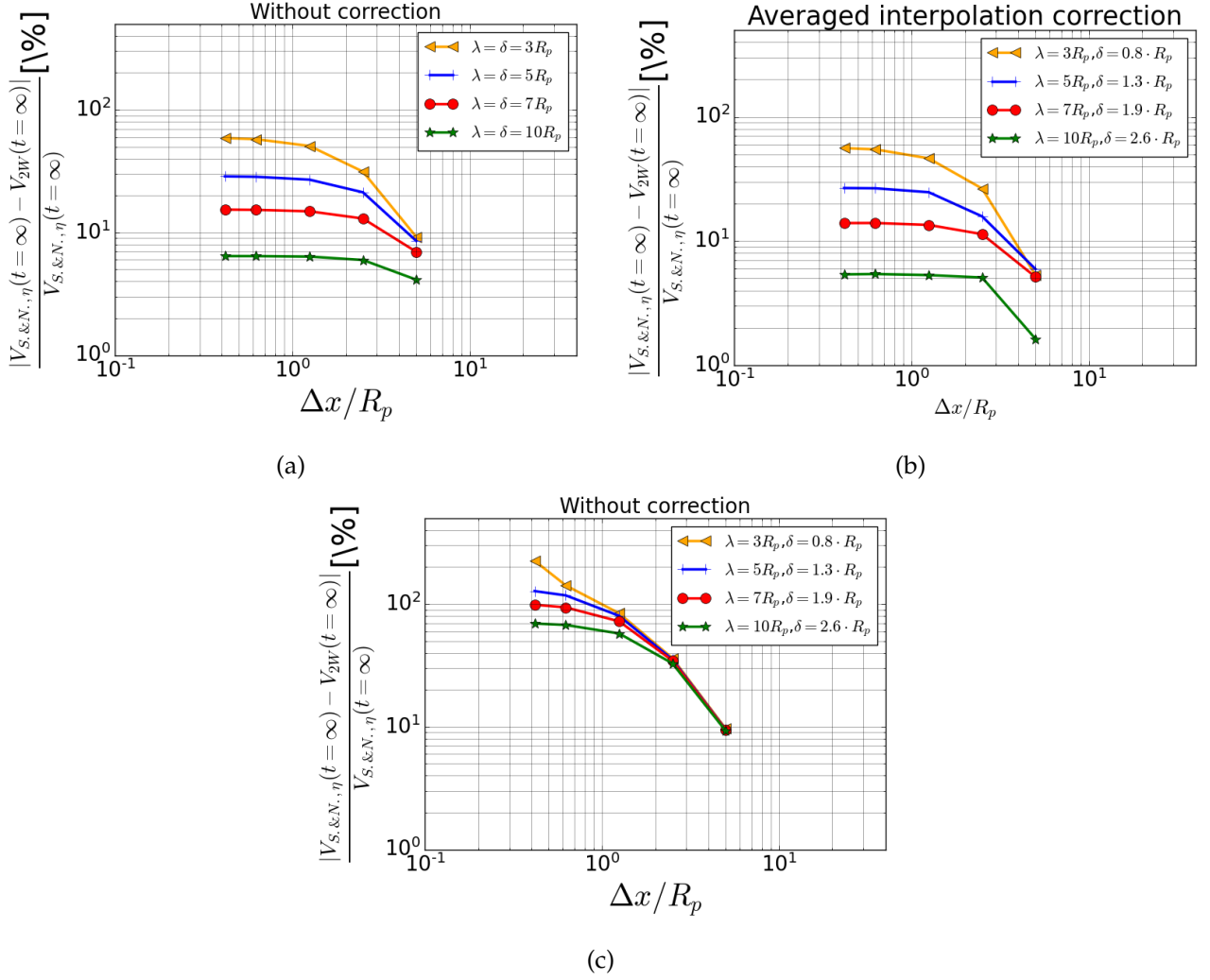


Figure II.15: Terminal velocity error compared to One-way results against mesh resolution  $\frac{\Delta x}{R_p} = [0.42, 0.625, 1.25, 2.5, 5.0]$  for three Two-way approaches:  $\lambda = \delta = [3., 5., 7., 10.] \cdot R_p$  without correction,  $\lambda = [3., 5., 7., 10.] \cdot R_p$  and  $\delta = [0.78, 1.3, 1.82, 2.6] \cdot R_p$  with  $\mathcal{A}(u_{f@p})$  correction,  $\lambda = [3., 5., 7., 10.] \cdot R_p$  and  $\delta = [0.78, 1.3, 1.82, 2.6] \cdot R_p$  without correction.

ratio  $\mathcal{A}(\tilde{u}_{f@p})/V_{S.\&N.,\eta}(t = \infty)$  [figure II.16]. It is coherent with prior results. We observe the influence of the area of interpolation/redistribution, then smaller are those length scales the higher is the ratio  $\mathcal{A}(\tilde{u}_{f@p})/V_{S.\&N.,\eta}(t = \infty)$ . It explains the strong deviation in the results.

As expected, the correction of the interpolated velocity permits decreasing particle's disturbance influence and improve the results. In the best scenario where  $\delta = 2.6 \cdot R_p$  and  $\lambda = 10 \cdot R_p$ , we have a ratio  $\tilde{u}_{f@p}/V_{\eta,t_\infty} < 0.07$ . It is a strong improvement with respect to the results without correction at  $\lambda = \delta = 3 \cdot R_p$  where  $\tilde{u}_{f@p}/V_{\eta,t_\infty} \approx 0.6$ , almost ten times higher. Moreover, comparing to the results with same length scales  $\lambda$  and  $\delta$ , [figure II.16c], we observe that the correction permits to reduce the momentum's disturbance of one order of magnitude in the best scenario.

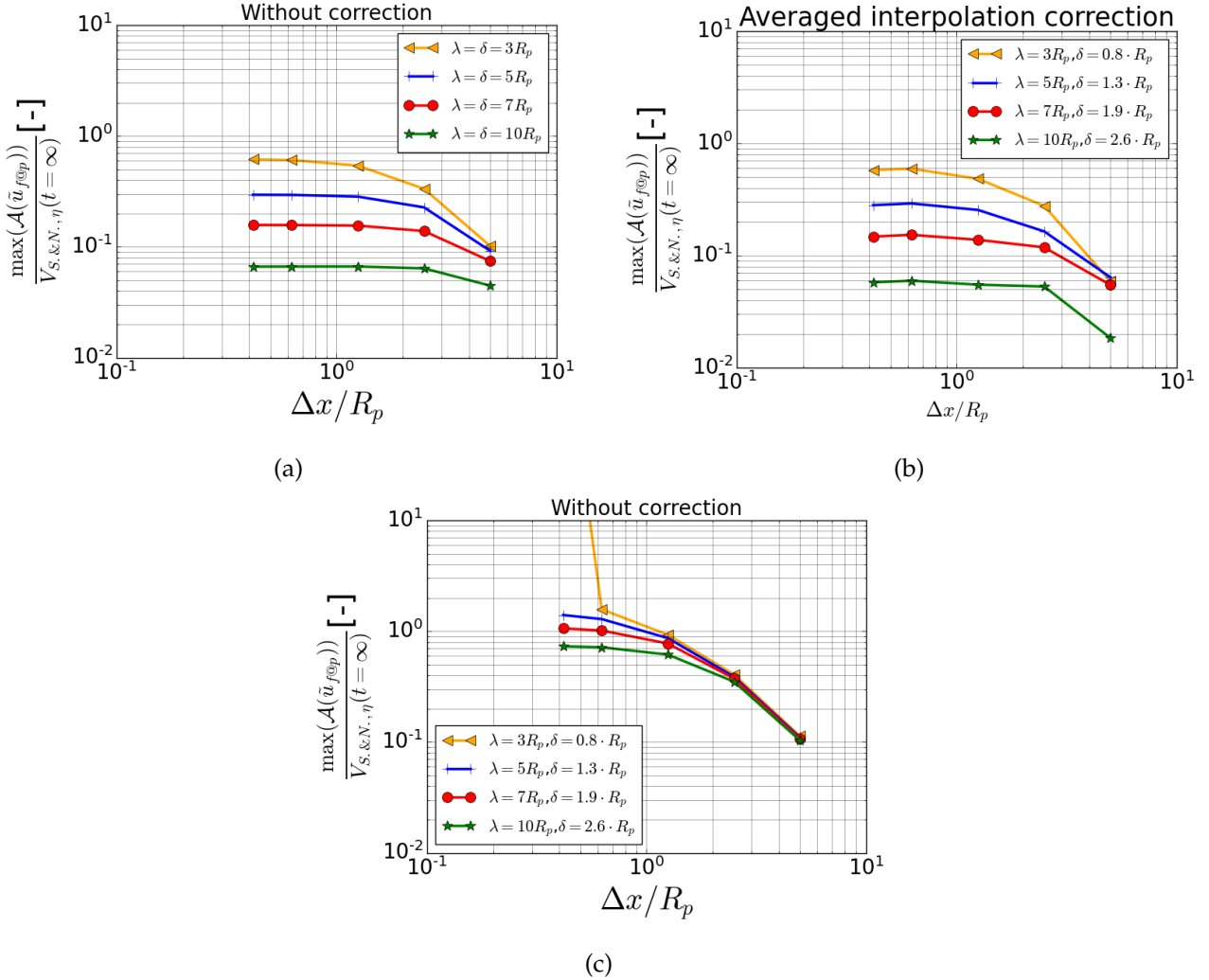


Figure II.16: Maximal carrier velocity scaled by One-way terminal velocity against mesh resolution  $\frac{\Delta x}{R_p} = [0.42, 0.625, 1.25, 2.5, 5.0]$  for three Two-way approaches:  $\lambda = \delta = [3., 5., 7., 10.] \cdot R_p$  without correction,  $\lambda = [3., 5., 7., 10.] \cdot R_p$  and  $\delta = [0.78, 1.3, 1.82, 2.6] \cdot R_p$  with  $\mathcal{A}(u_{f@p})$  correction,  $\lambda = [3., 5., 7., 10.] \cdot R_p$  and  $\delta = [0.78, 1.3, 1.82, 2.6] \cdot R_p$  without correction.

## Summary

In order to improve the accuracy of Two-way approach, we implemented a correction on the particle momentum's disturbance and we compared it to the method without correction. The results in this manuscript show the importance of this correction onto the particles' motion evolution.

However, this correction needs a wide area of interpolation since we have the factor  $\sqrt{2/\pi 9}$  between interpolation and redistribution. In dense simulation, it is possible that liquid cell are considered into the interpolated velocity which can modify our results. Then we have to study

the influence of momentum's redistribution toward an interface, we study these questions on two references test case; a free-falling droplet over free surface at high Reynolds number and a Plateau-Rayleigh excited atomization. To the author knowledge, it has not been addressed in the literature where the transformation was always done far from any interface to avoid those interrogations [Ling et al., 2015, Evrard et al., 2019].

In order to reduce the wideness of velocity interpolation, we are currently implementing two solutions. First, the Wendland filter function [Wendland, 1995]. The results obtained are currently not satisfactory and we observed a lack of stability of the method, more developments are required in order to go further in this analysis.

Second, the correction based on [Balachandar et al., 2019] which decreases the computational time since it does not require averaging on the domain but we are still facing a lack of stability for particles with a mesh ratio higher than 4;  $d_p/\Delta x > 4$ . We still have to keep working on its implementation to improve its stability. Nevertheless, we performed some simulation with Hybrid approach in this manuscript and results are showed later [section IV.1].

### II.3.4 Temporal scheme analysis

In section II.2.3 we described the strategy to implement the temporal scheme for the Lagrangian solver and its coupling with the Projection method to transport the interface and solve Navier-Stokes equations. Two schemes have been implemented, the Euler Explicit, EE, and Runge-Kutta 2<sup>nd</sup> order, RK2. The order of the temporal integration is now evaluated on the free-falling sedimented particle. The study is carried on all implemented forces for the One-way and Two-way approaches.

#### One-way method analysis

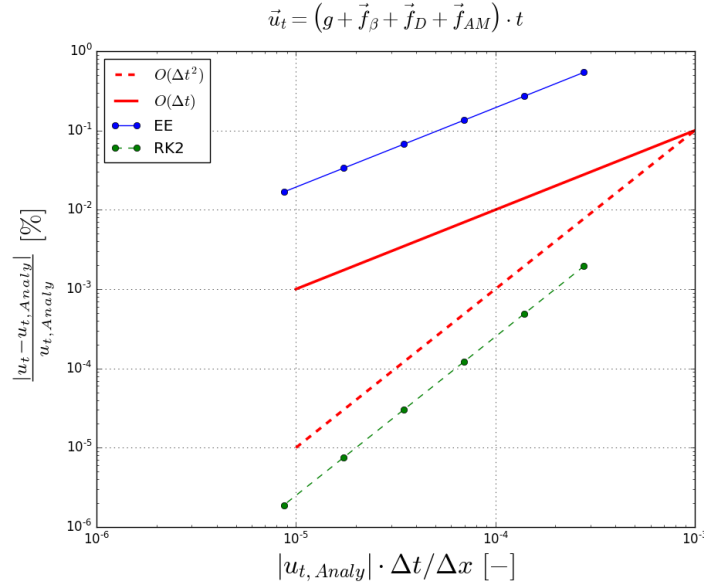
The One-way method analysis is done on the free-falling particle test with the same physical properties [subsection II.3.1]. The goal is to validate the implementation of a second order of convergence scheme in time, thus a convergence study is done for several fixed temporal time step at constant numerical resolution. We recall that by default in *Archer* the time step is computed every time step considering CFL stability criteria, fixed for this study.

The simulation resolution is  $\frac{\Delta x}{d_p} = 1.25$  and temporal time step varies from  $\Delta t = [6.0 \cdot 10^{-5}; 3.0 \cdot 10^{-5}; 1.5 \cdot 10^{-5}; 7.5 \cdot 10^{-6}; 3.75 \cdot 10^{-6}, 1.875 \cdot 10^{-6}]$  [s]. We chose a reference time,  $t_{ref} = 1.8 \cdot 10^{-5}$  [s], to compare our results on the velocity at this time. We compare those extracted velocities to the analytical solution,  $u_{t_{ref}, Analy}$  to get the order of convergence of each temporal scheme. Then we modify the Lagrangian model to study the temporal implementation of each force, buoyancy, added mass and drag forces.

First we study the convergence order of the Eulerian Explicit (EE), and Runge-Kutta 2<sup>nd</sup> order, (RK2) schemes in *Archer*. The results are displayed on figure II.17 where the convergence order, first and second, are respectively plotted in dashed and solid lines. The obtained results are plotted in solid and dashed for the EE and RK2. It is clear that the Euler Explicit scheme reaches the first order of convergence while the Runge-Kutta 2 scheme reaches the second order of convergence. Plus, the error of accuracy for both methods at the same time step varies from 2 order of magnitude to almost 4 order of magnitude from the less to the more restrictive time steps. This analysis shows the importance of an accurate temporal scheme to enhance the Hybrid method.

Next, we focus on the forces implemented in *Archer*. We commented that the Lagrangian solver temporal implementation is independent to the Eulerian solver [subsection II.2.3]. This choice influences the temporal convergence order that one can achieve in these forces' computation. We recall that the model used in *Archer* considers gravity, drag, buoyancy and added mass forces [equation II.10]. It is sensitive to the density ratio and an analytical parametric study is done varying this parameter in order to understand the importance of an error computing these forces for several density ratio.

The density ratio,  $\rho^*$ , has been varied from 1 to 100 and it is plotted for two Lagrangian models. The first model uses drag with added mass forces and the second model uses drag with buoyancy forces. The analytical particle's velocity evolution is scaled by the Stokes terminal velocity. It permits observing what is the dominant force in the particle's motion and to quantify the importance of an


 Figure II.17: Convergence study of *Archer* Lagrangian model using EE and RK2 against CFL.

error on their temporal scheme implementation. The results are displayed on figure II.18, on the left considering the added mass force and on the right the buoyancy force.

For drag with added mass model, the density ratio only modifies the transitory regime since it is computed from the acceleration of the slipping motion:  $\vec{u} - \vec{u}_{f@p}$ . To be second order on this model computation, we would need to modify our strategy of temporal solvers coupling, we detail it later. Density ratio has an influence on drag with buoyancy model [right figure II.18], we observe that it modifies particle's terminal velocity. An accurate computation is required.

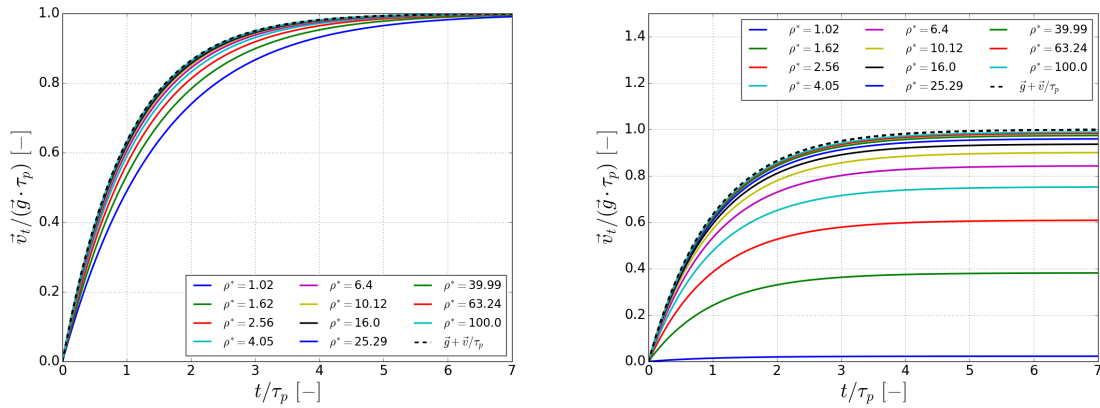


Figure II.18: Density ratio influence on particle's velocity evolution for added mass force model (left), and buoyancy force model (right).

The detailed analysis of the computation of these forces is done for three density ratio  $\rho^* = [2.; 10.; 100.]$ . Again, these simulations are performed for the EE scheme, solid line, and the RK2 scheme, dashed line. The results are compared to their analytical solution and the same strategy is used to select the time step on the which the velocity is analyzed. We first analyze the results obtained for the model including only the drag force computation [figure II.19a].

It appears that the temporal convergence scheme is conserved, first order for the EE scheme and second order for the RK2 scheme. This result was expected for this force from the general particle force modelling [figure II.17]. We saw that for the free-falling particle, the drag force is dominant in our One-way model. Since we reached the second order of accuracy for this model, we expected to

reach it also for the model that only has the drag force. Again, a high order temporal scheme improves the accuracy of the solution of various orders of magnitude. Moreover, it is observed that the higher is the density ratio, the smaller is the error with reference to the analytical solution. We observed on left figure II.18 that the motion acceleration was not the same for each density ratio. It is conceivable that this modification varies the temporal evolution of the particle. The time step that has been calculated on the terminal velocity is probably not suitable for each density ratio but it is necessary to keep it fixed.

Then, we analyze the results obtained for the buoyancy force implemented in the Lagrangian model. The velocity evolution is linear, since we use first and second order temporal scheme to compute the velocity, we reach machine error when studying this quantity. Since particle's position evolution is polynomial, we expect to recover the error machine for the RK2 scheme, we evaluate it [figure II.19b]. The strategy remains the same and it is compared to the analytical result for the position at the same time step. Again, the EE scheme is first order of convergence and whatever the density ratio, the accuracy is exactly the same. For RK2 scheme, second order of accuracy is recovered since the accuracy reaches error machine. These results were expected because this force depends only of the density ratio.

The added mass force is then studied [figure II.19c]. The results for both temporal schemes show first order convergence. We do not recover second order of accuracy for the added mass computation because it involves information from the Eulerian field. Since we do not update the Eulerian field in the second loop of the RK2 scheme, we cannot converge to an higher order. As long as we study atomization application, this force is not of first importance and we do not modify our temporal implementation. Moreover, we observe that RK2 scheme reduces the error of 2 order of magnitude which is a positive result.

## Two-way method analysis

The redistribution of the momentum of the particle toward the Eulerian grid modifies the simplicity of the temporal convergence priorly seen. We have seen that several parameters are involved such as the ratio  $d_p/\Delta x$ ,  $\delta/\Delta x$ ,  $d_p/\delta$ ,  $\lambda/\delta$ , and  $\Delta t$ . Their influence has been addressed in section II.3.3. We do not consider any correction on interpolated velocity in this study. To reduce the dependency to this parameters, we chose to set the Two-way method with Gaussian size filter:  $\delta = 3.5R_p$ , and velocity interpolation area:  $\lambda = \delta$ . The parameters that are modified for this study are the mesh size  $\Delta x$  and the CFL. A modification of the CFL constraint leads to a smaller time step  $\Delta t$  calculated with  $\Delta t = \frac{CFL \cdot \Delta x}{|u_{1W,t=\infty}|}$ . Here,  $|u_{1W,t=\infty}|$  represents the terminal velocity of the free-falling particle for the One-way model. The CFL evolves from  $CFL = [0.8, 0.4, 0.2, 0.1, 0.05]$  and the mesh size  $\Delta x = [Lx/4, Lx/8, Lx/16, Lx/32]$ , the simulations are resumed in table II.3. We use the same temporal scheme for both Lagrangian/Eulerian solvers.

The analysis of these simulations is done in two parts. First, the velocity of the free-falling particle at a reference time step is compared for all simulations with EE and RK2 schemes. We chose a reference time,  $t_{ref} = 3 \cdot 10^{-5}$  [s], to compare our result on the velocity at this time. Due to the variation of the CFL and the mesh size, more iterations are required for the more restrictive time step: when the coarse simulation does 1 iteration, the finest does 130 iterations. The error done on the estimation of the velocity is compared to the Richardson extrapolated value, we do not use analytical solution since the results do not converge toward analytical solution [subsection II.3.3]. The details of the Richardson extrapolation are given in Appendix V.3.

The first analysis is done on the raw velocity at the same time step for simulations listed in table II.3 is displayed on figure II.20. On the left the results for the EE scheme are showed and on the right for RK2 scheme. The velocity is plotted against the fixed simulation's time step. To recall, it is calculated depending on the mesh size and CFL. The marker shape/color represent the following information: the same color represents the same mesh size, the same shape represents the same CFL restriction.

The results are displayed following a linear trend converging toward the more restrictive time step [left figure II.20]. We observe a convergence toward  $4.24 \cdot 10^{-3}$  [ $m.s^{-1}$ ] and that the higher is the time step the more deviated from this velocity are the results. For example we observe for the configuration  $Nx = 4$  and  $CFL = 0.8$  a velocity of  $4.424 \cdot 10^{-3}$  [ $m.s^{-1}$ ]. From these values we expect a



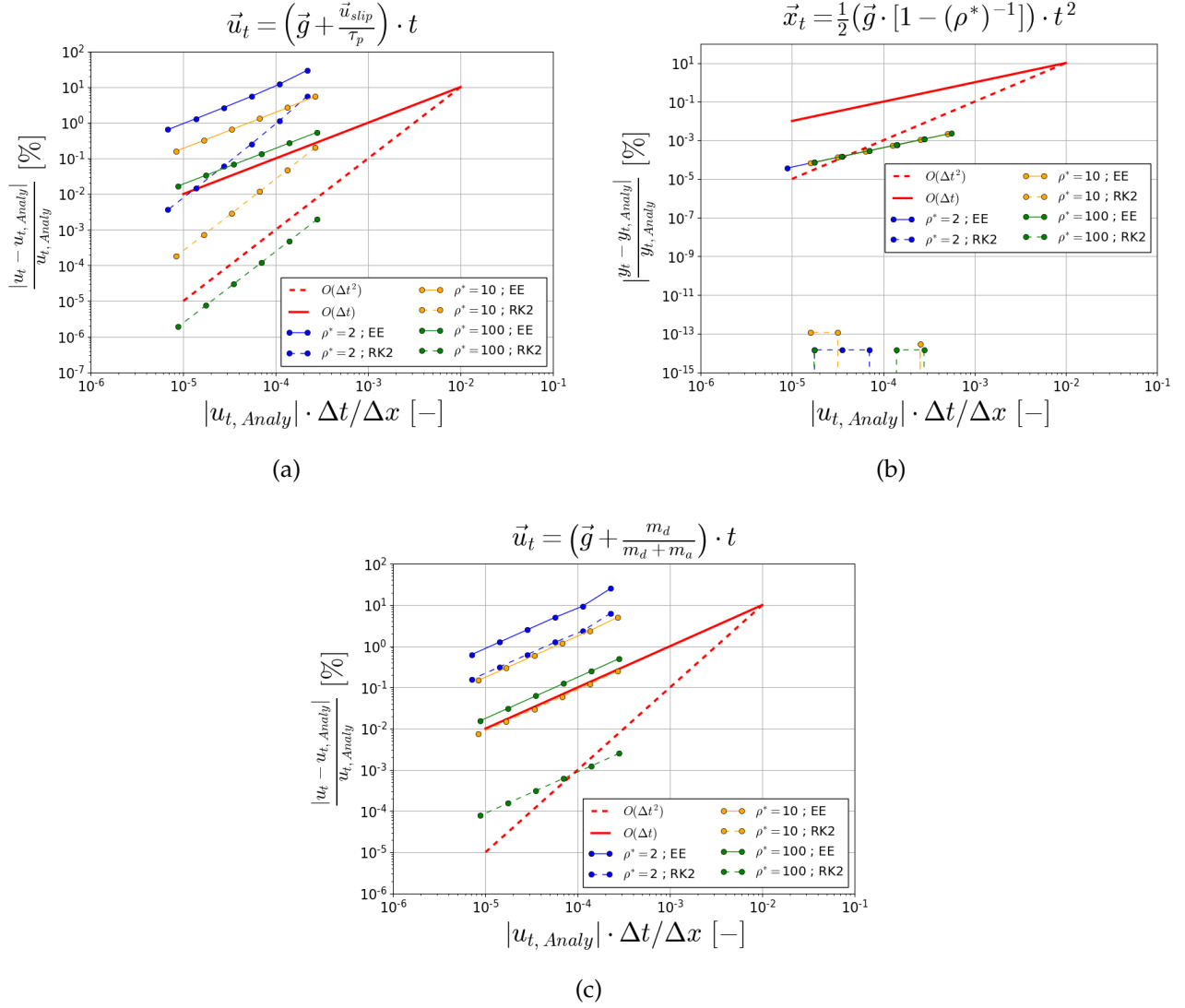


Figure II.19: Error of accuracy for velocity or position against analytical value for three density ratio,  $\rho^* = [2, 10, 100]$  [-], and CFL. From left to right: Drag force model, Added mass model, Buoyancy model.

<b>Nx</b>	<b><math>\Delta x</math> [m]</b>	<b>CFL</b>	<b><math>\Delta t</math> [s]</b>	<b>Name config</b>
4	$2.500 \cdot 10^{-4}$	0.8	$4.545 \cdot 10^{-4}$	<i>Nx4_CFL8</i>
4	$2.500 \cdot 10^{-4}$	0.4	$2.273 \cdot 10^{-4}$	<i>Nx4_CFL4</i>
4	$2.500 \cdot 10^{-4}$	0.2	$1.136 \cdot 10^{-4}$	<i>Nx4_CFL2</i>
4	$2.500 \cdot 10^{-4}$	0.1	$5.682 \cdot 10^{-5}$	<i>Nx4_CFL1</i>
4	$2.500 \cdot 10^{-4}$	0.05	$2.841 \cdot 10^{-5}$	<i>Nx4_CFL0.5</i>
8	$1.250 \cdot 10^{-4}$	0.8	$2.273 \cdot 10^{-4}$	<i>Nx8_CFL8</i>
8	$1.250 \cdot 10^{-4}$	0.4	$1.136 \cdot 10^{-4}$	<i>Nx8_CFL4</i>
8	$1.250 \cdot 10^{-4}$	0.2	$5.682 \cdot 10^{-5}$	<i>Nx8_CFL2</i>
8	$1.250 \cdot 10^{-4}$	0.1	$2.841 \cdot 10^{-5}$	<i>Nx8_CFL1</i>
8	$1.250 \cdot 10^{-4}$	0.05	$1.420 \cdot 10^{-5}$	<i>Nx8_CFL0.5</i>
16	$6.250 \cdot 10^{-5}$	0.8	$1.136 \cdot 10^{-4}$	<i>Nx16_CFL8</i>
16	$6.250 \cdot 10^{-5}$	0.4	$5.682 \cdot 10^{-5}$	<i>Nx16_CFL4</i>
16	$6.250 \cdot 10^{-5}$	0.2	$2.841 \cdot 10^{-5}$	<i>Nx16_CFL2</i>
16	$6.250 \cdot 10^{-5}$	0.1	$1.420 \cdot 10^{-5}$	<i>Nx16_CFL1</i>
16	$6.250 \cdot 10^{-5}$	0.05	$7.102 \cdot 10^{-6}$	<i>Nx16_CFL0.5</i>
32	$3.125 \cdot 10^{-5}$	0.8	$5.682 \cdot 10^{-5}$	<i>Nx32_CFL8</i>
32	$3.125 \cdot 10^{-5}$	0.4	$2.841 \cdot 10^{-5}$	<i>Nx32_CFL4</i>
32	$3.125 \cdot 10^{-5}$	0.2	$1.420 \cdot 10^{-5}$	<i>Nx32_CFL2</i>
32	$3.125 \cdot 10^{-5}$	0.1	$7.102 \cdot 10^{-6}$	<i>Nx32_CFL1</i>
32	$3.125 \cdot 10^{-5}$	0.05	$3.551 \cdot 10^{-6}$	<i>Nx32_CFL0.5</i>

Table II.3: Parameter variation for the Two-way temporal scheme analysis

first order of accuracy for this method.

The results for the RK2 scheme [left figure II.20], show a higher sensibility to the time step since we do not observe a clear convergence for higher  $\Delta t$ . For time step below  $\Delta t < 2 \cdot 10^{-4}$ , we observe that using higher temporal scheme reduces the gap between the results. For configuration with  $Nx = [16, 32]$ , we observe a linear tendency. We will use those converged results to determine the convergence order of the method for the EE/RK2 comparison.

To quantify the deviation between the two schemes, we compute the highest deviation between all velocity at reference time step and the averaged velocity for all configuration:

$$\sum_{j=1}^{N_{config}} \max\left(\frac{1}{N_{config}} \sum_{i=1}^{N_{config}} |V_i(t = t_{ref})| - |V_j(t = t_{ref})|\right)$$

We get a maximal deviation of 4.1% and 0.083% respectively for EE and RK2 schemes. We see that using a higher temporal scheme reduces the dependency to the mesh ratio. Indeed, the smaller the time step the more accurate for both schemes. But, fast, we observe that RK2 schemes results converged, and we can save computational time avoiding using restrictive CFL.

To obtain the order of convergence of the method, the Richardson extrapolation has been used [Appendix V.3]. To compute it we use the series of results using a constant CFL and mesh size variation, and we study it for three CFL values:  $CFL = [0.2; 0.1; 0.05]$ . We obtain the same value for the RK2 results [table II.4], it was expected since the maximum deviation was lower than  $1 \cdot 10^{-1}\%$ . We show the results for EE/RK2 schemes, respectively in solid and dashed lines, against the time step [figure II.21].

For the EE temporal scheme we recover the first order of convergence,  $O(\Delta t) = 1$ . From the convergence analysis, the smallest set of CFL provides a convergence order of  $O(\Delta t) = 1.05$ . It is observed that the grid refinement improves the results as for reducing the CFL. Since the gain of accuracy are of the same order, it is important to determine which of refining the grid or reducing the CFL yields to a smaller computational cost in *Archer*.

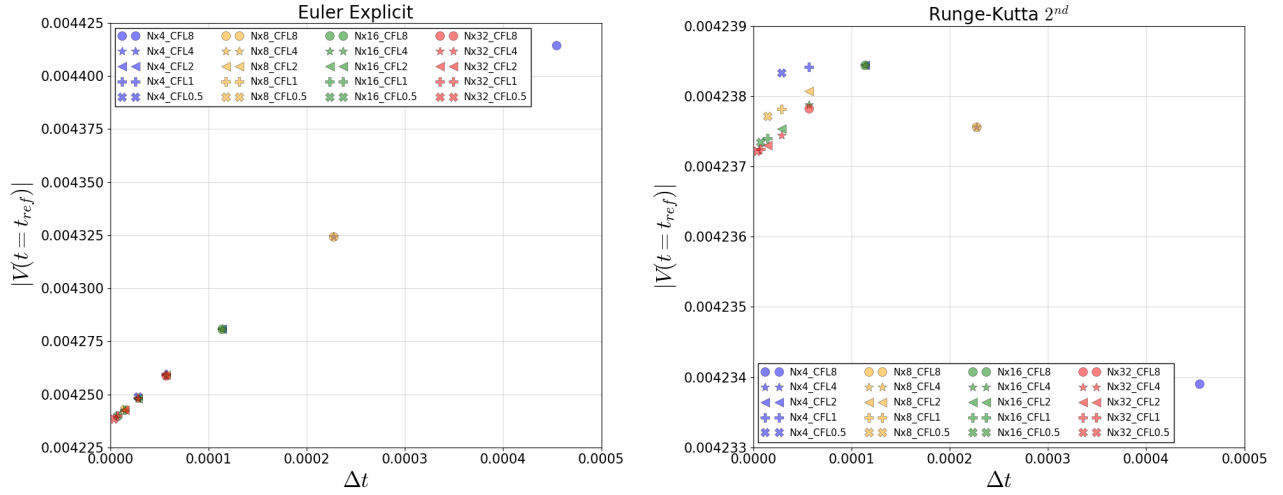


Figure II.20: EE scheme (left), and RK2 scheme (right), results for velocity at  $t = t_{ref}$  against time step. Configurations:  $CFL = [0.8, 0.4, 0.2, 0.1, 0.05]$  and  $\Delta x = [Lx/4, Lx/8, Lx/16, Lx/32]$ .

For the RK2 temporal scheme, it appears that reducing the CFL improves the order of accuracy of the method [table II.4]. For the most restrictive CFL, we obtain a relatively good improvement:  $CFL = 0.05 \rightarrow Order = 1.56$ . We observe that second order of convergence is not recovered because the particles' momentum redistribution onto the fluid is not updated during the second iteration of the RK2 scheme of the projection solver [figure II.8]. This choice has been made because the action of the particle is not predominant within two phase flow atomization study. However, it is noted that error magnitude is reduced of one order with respect to EE results.

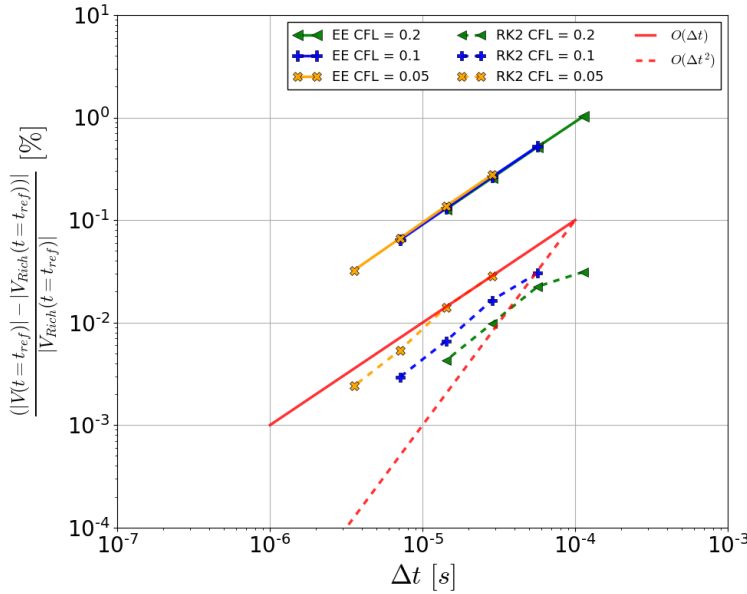


Figure II.21: Temporal convergence for Euler Explicit (solid lines), and Runge-Kutta 2 (dashed lines), temporal scheme for three CFL;  $CFL = [0.2; 0.1; 0.05]$ , respectively in green, blue and yellow.

	EE	RK2
CFL	$O(\Delta t^n)$	$O(\Delta t^n)$
0.2	1.009	1.20
0.1	1.023	1.442
0.05	1.05	1.563
	$V_{Rich}(t = t_{ref})$	$V_{Rich}(t = t_{ref})$
0.2	-4.23720	$-4.23712 \cdot 10^{-3}$
0.1	-4.23719	$-4.23712 \cdot 10^{-3}$
0.05	-4.23716	$-4.23712 \cdot 10^{-3}$

Table II.4: Order of convergence and Richardson velocity extracted of figure II.21.

To conclude, in terms of accuracy, the Two-way method is improved using a higher temporal scheme. The higher is the time step restriction, the better are the results in terms of accuracy for both methods. The CFL has a strong influence in the accuracy improvement for the EE scheme and that might be considered before selecting the temporal scheme of the simulation. The reason is that the RK2 scheme improves the results, but it is more costly on the temporal integration scheme. Moreover,

a restrictive CFL is required in order to have a strong improvement on the convergence of the method. Finally, we showed the limits of the coupling between the Lagrangian and Eulerian solver since we do not update Eulerian quantities. In a dilute application, such as atomization, this strategy is precise enough.

### II.3.5 Full Resolved Particles results

Next, we analyze the accuracy of the IBM method that is implemented in the code. This study is done on two test cases. The first one is the study of the free-falling particle test case. The goals are:

- Determine the range of applicability of the method in unresolved area.
- Study the influence of the Lagrangian mesh generation.
- Study the influence of the numerical radius retraction.

The Lagrangian mesh generation was explained in subsection II.1.3. Here, we compare the method used in [Uhlmann, 2005] and the analytical mesh generation of [Saff and Kuijlaars, 1997]. The results using these methods are respectively called *Forced* and *Analytical*. Following [Breugem, 2012], we implemented the retraction of the radius, we evaluate its influence on the accuracy of the method. When retraction is used,  $\mathbf{R}$  is added.

The second goal of this section is to study the order of convergence of the method for global and local statistics. From the results obtained on the first test case we can determine the most suitable mesh generation to simulate the fixed particles' array.

#### Analysis of the Lagrangian mesh on the free-falling droplet

From IBM literature, most of the studies focused on the convergence study refining mesh resolution. In this manuscript, we study the viability of the IBM method to transport under resolved ICM droplets. We are interested in a coarsening convergence study of the IBM to determine if it is robust and accurate enough to transport those under resolved droplets. The range of mesh ratio used for the free-falling particle simulation is  $\frac{d_p}{\Delta x} = [1.6; 3.2; 4.8; 6.4; 8.; 16.]$ . We consider  $\frac{d_p}{\Delta x} = 16$  as our reference [Breugem, 2012, Wang et al., 2014, Uhlmann and Chouippe, 2017, Brändle de Motta et al., 2019].

#### Presentation of the configuration:

The simulations are performed for four Lagrangian mesh generation. The first two series of simulation compare the *Analytical* mesh generation around a sphere [Saff and Kuijlaars, 1997] to the *Forced* method [Uhlmann, 2005]. To recall, the difference in the mesh generation is that the *Analytical* method uses analytical equation [equations II.32-II.33]. The *Forced* method uses a minimization algorithm between Lagrangian markers to generate their positions. The issues of this method were detailed in subsection II.1.3. The next two series of simulation use the retraction of the radius to generate the Lagrangian mesh [Breugem, 2012]. The numerical radius of the particle is then:  $R = R_p - 0.3\Delta x$ .

In the coarsening study, the importance of a good mesh generation lies in the stability of the method. The smaller is the mesh ratio, the more important is the position of the Lagrangian marker. A non-equilibrium between their control volume might unequally redistributes the force and strongly modify the velocity field at particle position. It yields a physical inaccurate result, and, worst, it can lead to numerical instabilities.

For this test case, we propose to study the particle velocity evolution against the characteristic time of the simulation for the 6 mesh ratio. Then, we compare the order of convergence of the two methods, calculating the error done on the terminal velocity. The velocity of reference that is used to compute the error on the terminal velocity is obtained through the Richardson extrapolation [Appendix V.3]. It would lead to a simulation of  $65 \cdot 10^9$  cells which is not the purpose of this study, moreover we already used approximately 20,000 CPU hours for the more resolved case. Then, we compare the CPU time averaged over one iteration for this two simulations in order to determine which mesh generation is the more efficient.

### Velocity evolution without retraction:

The results for the evolution of the free-falling particle normalized by the Richardson terminal velocity are displayed on figure II.22. The first point is that the method used to generate the Lagrangian mesh does not influence the physic of the results. The velocity evolution is of the same order for both methods and the conclusions are the same for the two IBM mesh generations. At the lowest mesh resolution, the velocity evolution is underestimated of 50% of the reference. It shows that the drag force is overestimated on the particle's motion and this error is reduced increasing the mesh resolution. In the unresolved area that is of our interest,  $d_p < 8\Delta x$ , we observe that the best results have an error of at least 10%. The terminal velocity results for both methods, [right figure II.22], reach almost first order of convergence, [table II.5]. We observe that the results obtained for both mesh generation are again similar. Next, we study the influence of the retraction of the radius on the terminal velocity.

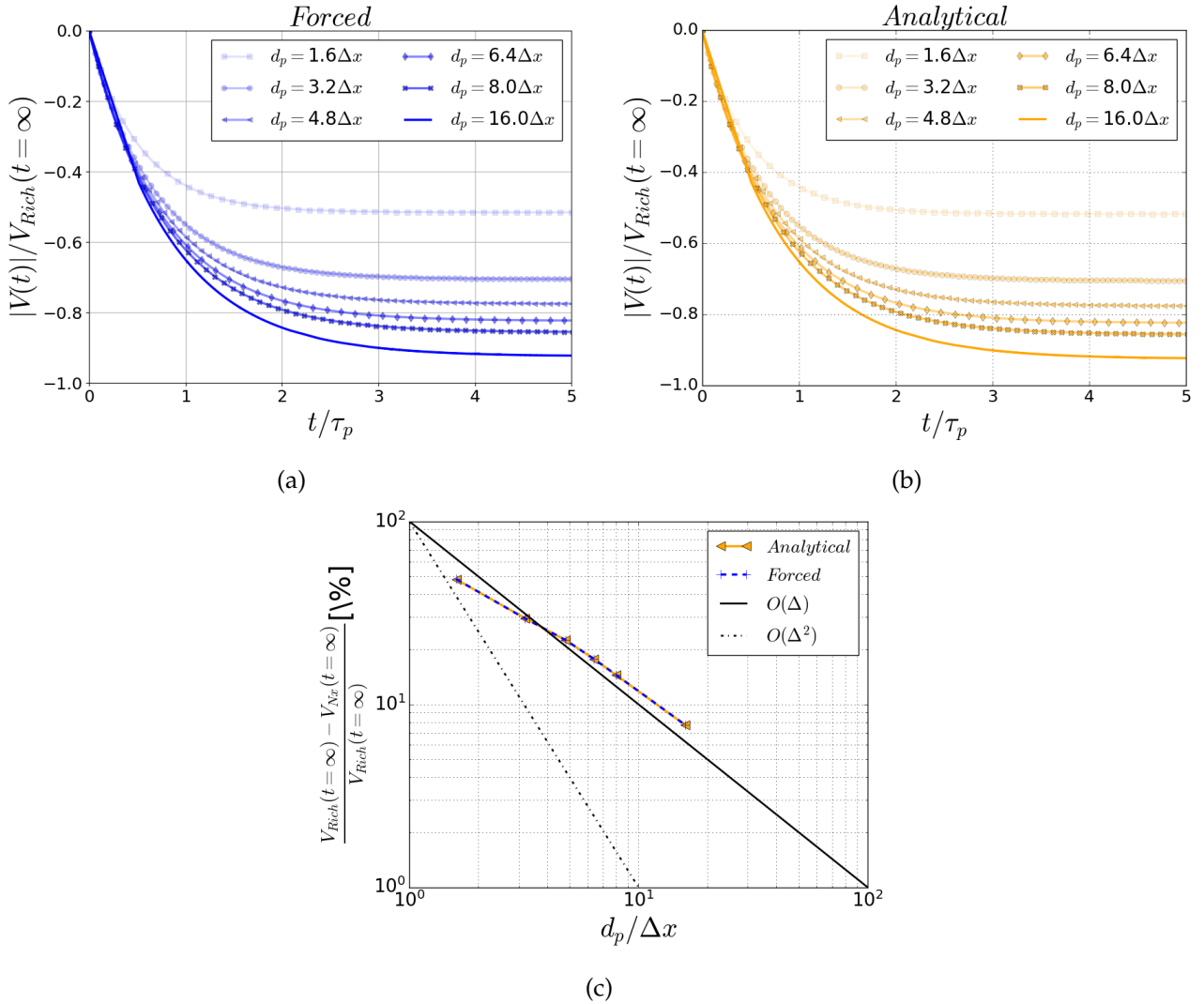


Figure II.22: Comparison of the accuracy for *Analytical* [figure II.22a], and *Forced* [figure II.22b], against characteristic time. Evolution of the error on the terminal velocity estimation with respect to the number of cell across the diameter [figure II.22c].

### Influence of radius retraction:

The purpose of the retraction of the radius is to be more representative of the physic placing the numerical shell of the particle inside its body. As suggested, the retraction is set to  $0.3\Delta x$

	IBM Forced	IBM Analytical	IBM Forced R	IBM Analytical R
$V_{Richardson} [m.s^{-1}]$	0.04424	0.04425	0.04373	0.04373
$O(\Delta^n)$	0.90	0.90	1.28	1.28

Table II.5: Richardson terminal velocities and convergence order for each IBM free-falling particle simulations.

[Breugem, 2012]. Its implementation within *Archer* has been done and results are showed on figure II.23, similarly to what is done on figure II.22.

Again, the more refined the more accurate are the results. For the coarsest mesh,  $\frac{\Delta}{d_p} = 1.6$ , the drag forces exerted onto the particles are not correctly calculated. Then, the terminal velocity value is again strongly underestimated even if the implementation of retraction decreases the magnitude of the error.

Generally, the retraction of the radius improves the accuracy of the free-falling simulation [right figure II.23]. For example, the method that does not use the mesh retraction has an error 1.08 times higher than the retracted one for the coarsest mesh. At  $\frac{\Delta}{d_p} = 3.2$ , this difference increases, we note that the terminal velocity is 1.15 times higher with retraction. It shows that the retraction of the radius is relevant in our research of accuracy at low mesh resolution. Moreover, the convergence rate is faster with those improvements and lies in between first and second order of convergence.

More details are given on the results of those simulations in table II.5. We observe that the Richardson's velocity are different for the two mesh generations strategies without retraction. This difference is relatively small, of the order of  $1 \cdot 10^{-4}$ , and does not influence our conclusions. Moreover, this difference vanishes using retraction (**R**). The terminal velocity reached with retraction is smaller than without and it is complex to determine this surprising result since drag was overestimated without retraction.

### Numerical cost of Lagrangian mesh generation:

We evaluate in this section the numerical cost of the Lagrangian marker generation comparing the two implemented methods. We recall that the number of markers is determined by equations II.30 and II.31 and that the methods used respectively a minimization algorithm (Forced), and an analytical solution (Analytical) to generate the Lagrangian grid.

The purpose of the generation of this analytical meshing are various. First, it avoids the minimization algorithm that is costly to generate, the more markers at the surface, the higher is the computational cost. Moreover, we perform simulation with polydisperse particles, it means that several Lagrangian grid are created in order to get the optimal Lagrangian markers on its interface. Since analytical mesh generation is straightforward, it is not influenced by the number of points on particles' surface and can easily generate mesh for a wide range of sizes.

Another point is that mesh generation has numerical cost, thus, we store the position of the markers in a mesh array. For highly resolved particles ( $R_p/\Delta x = 32 \rightarrow N_L \approx 12.800$ ), its storage is a charge. Then, we have to recover it every times we use information from Lagrangian markers through the generation of a pointer object. The second improvement using the analytical solution is to avoid its storage since we can compute markers position at any time.

We study the time spent in the subroutine that treats IBM,  $t_{CPU,IBM}$ , using both mesh generation for the free-falling sedimented particle and the total time spent in one iteration,  $t_{CPU,it}$ . We average those information over 50 iterations and we do not consider the first iteration since it involves the initialization of the code. It implies that we do not consider the generation of the mesh in this analysis but only its use which is a relative advantage in this comparison for the *Forced* method. The reason is because it is complex to filter all sections of the code initialization that does not belong to the IBM. We vary the numerical resolution and the number of processors  $N_x = [16; 32; 64; 128] \rightarrow N_{procs} = [1; 2; 16; 128]$ . It gives the following number of Lagrangian markers;  $N_L = [10, 34, 128, 516]$ , we plot the time spent against this number since it determines the number of interaction between Lagrangian grid and Eulerian fields [figure II.24a].

So far, we observe that the more Lagrangian markers are used, the more time is spent in the IBM

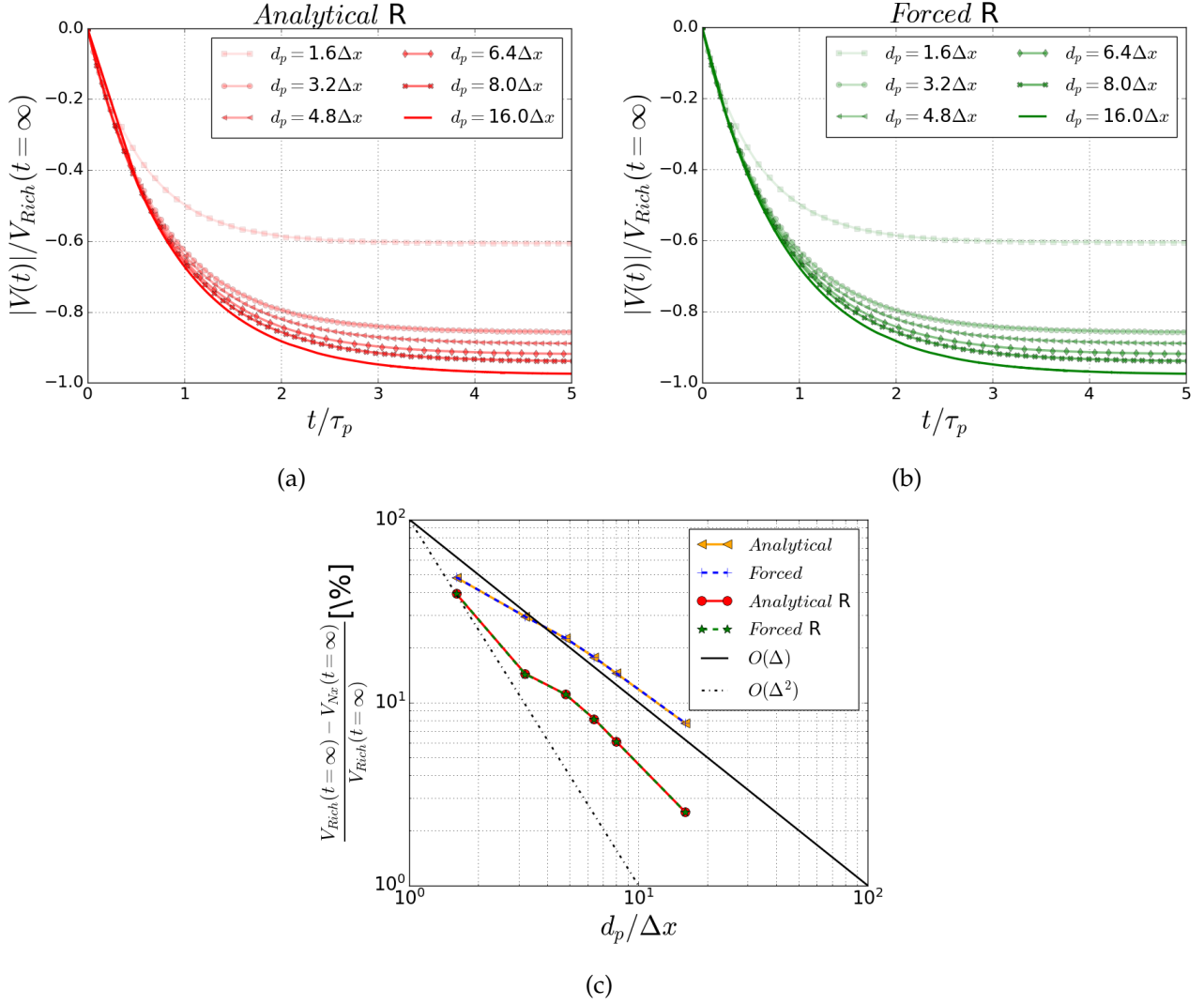
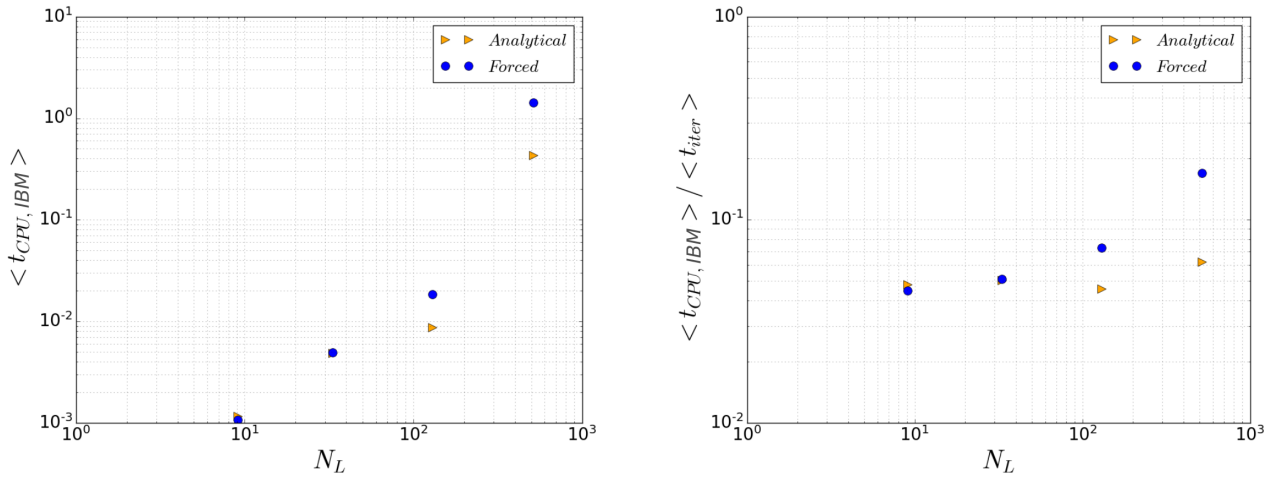


Figure II.23: Comparison of the accuracy for *Analytical R* [figure II.23a], and *Forced R* [figure II.23b], where *R* stands for the retraction set to  $R = R_p - 0.3\Delta x$  against characteristic time. Evolution of the error on the terminal velocity estimation with respect to the number of cell across the diameter is plotted for all mesh generations [figure II.23c].

subroutine. For  $N_L = 10$  we observe that the *Analytical* grid generation is slightly above in terms of computational cost. Increasing the number of Lagrangian markers,  $N_L > 100$ , shows that the *Analytical* grid generation has a smaller computational cost, it shows the interest in using this method. We observe that the scaling of the method is lost when several processors are used,  $N_L = 516 \rightarrow N_{procs} = 128$ . We need to improve exchanges of information between processors. We study the influence of this inefficient MPI implementation comparing the time spent in this subroutine against the total time spent in one iteration [figure II.24b].

Two clear tendencies appear, first, the IBM subroutine using *Analytical* grid generation has a total time spent representing 6% of the iteration time at maximum. For the other method, it represents almost 20% in the worst scenario. This quick analysis on the mesh generation confirms that the *Analytical* mesh generation is a good tool to save numerical resources without any loss of accuracy.

A remaining question would be to study the influence on the computational time of the number of points on the Lagrangian mesh, but, it is reminded to the reader that the optimal number of points is obtained through equation II.31 and going outside this optimal range would be numerically interesting but can degenerate the solution. For a similar accuracy, this *analytical* mesh generation is faster and those improvements are increasing with a mesh refinement.



(a) Averaged  $t_{CPU, IBM}$  against the Lagrangian markers per simulation for *analytical* and *forced* mesh, respectively in orange and blue.

(b) Averaged  $t_{CPU, IBM}$  scaled by averaged time spent in one iteration against the Lagrangian markers per simulation for *analytical* and *forced* mesh, respectively in orange and blue.

Figure II.24

### Array of fixed particles

This configuration uses *Analytical retracted* Lagrangian mesh generation with a retraction set to  $R = R_p - 0.3\Delta x$ . The resolution varies from  $\frac{d_p}{\Delta x} = [1.6; 3.2; 4.8; 6.4; 8.]$  and are compared to the icoFoam solver reference. We do not extract the order of convergence of our method in this section because we did not perform enough simulation with icoFoam reference in order to extract its Richardson's reference value. Same for our method, we did not reach the convergence regime that permits to extract the Richardson's reference value. However, the icoFoam solver permits to refine the grid around the particle, to ensure the no-slip/no-penetration boundary, thus it gives the reference for this study.

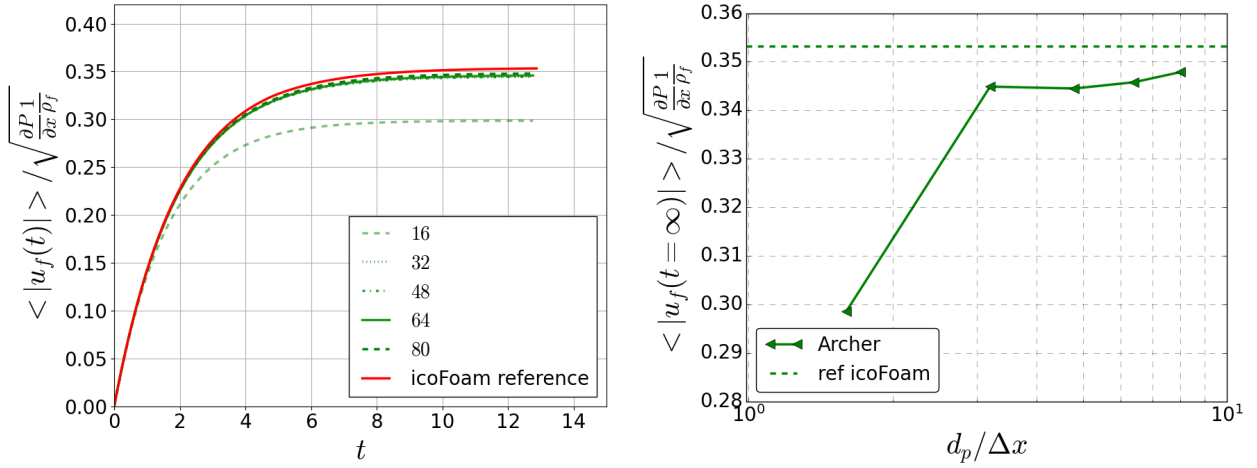
First, the analysis of the scaled mean flow evolution averaged in space is performed during sufficient time to converge to stationnary state (Mean velocity variation below 1% after  $1t$  [s]). The average is done using the velocity field inside the particle and we expect to converge toward dimensionless velocity icoFoam reference: 0.3532 [–].

The results for the evolution of the dimensionless mean flow velocity against dimensionless time are showed [figure II.25a]. It appears that the coarsest simulation converges toward  $\langle u_f \rangle \approx 0.3$  [–]



and is far from being accurate. It shows that to be representative of the physics, IBM method requires at least 3.2 cells across its diameter for this specific configuration.

The stationary state velocity against mesh resolution shows that for  $d_p/\Delta x > 3.2$  we reach the range of icoFoam's reference value [figure II.25b]. As said previously, here, we do not reach the convergence regime of the IBM method. Higher numerical resolutions would be required to obtain a converged solution and verify if the discrepancies decrease. The IBM method forces the boundary through the same assumptions (n-s/n-p), but ensures it through a diffusive method and has a non-physical flow inside its interface. Then, we suppose that this difference in the method must lead to a slightly different convergence value. A finer grid is needed to go further on this assumption. Now, we compare the convergence of nodes near and far from particle's interface,  $\vec{x}_1, \vec{x}_2, \vec{x}_3 = [X_p + d_p; Y_p + \frac{d_p}{2}; Z_p], [X_p + d_p; Y_p - \frac{d_p}{2}; Z_p], [X_p + \frac{5}{2}d_p; Y_p; Z_p]$ .



(a) Evolution of the mean flow velocity,  $\langle u_f \rangle$  within the domain against the characteristic time for  $\frac{d_p}{\Delta x} = [1.6; 3.2; 4.8; 6.4; 8.]$  (b) Stationary mean flow velocity,  $\langle u_f(t = \infty) \rangle$ , against the mesh resolution  $\frac{d_p}{\Delta x} = [1.6; 3.2; 4.8; 6.4; 8.]$

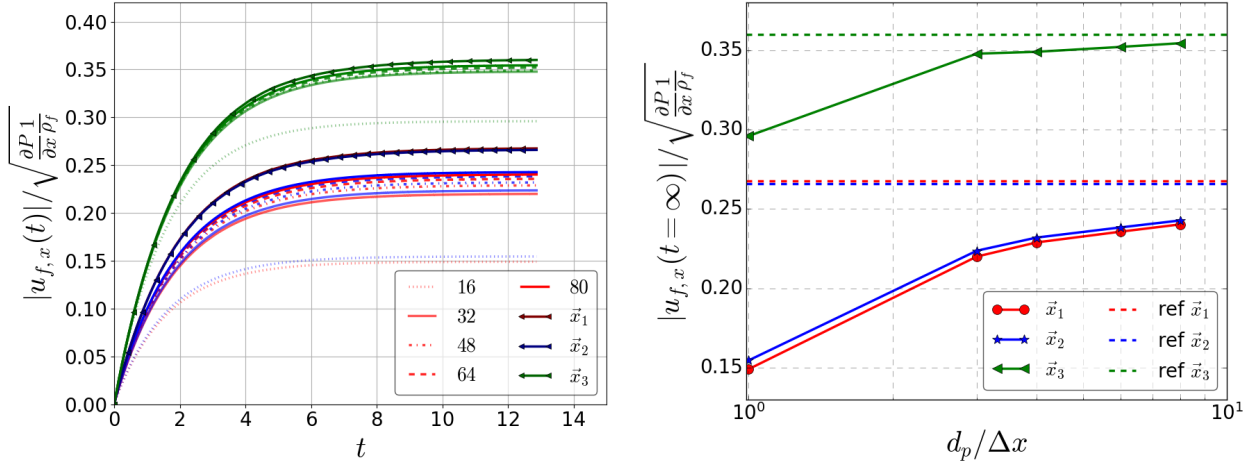
Figure II.25

The three nodes flow velocity evolution against characteristic time [figure II.26a] are studied adding the three velocities of reference (represented with markers). Again, for the coarse simulation we have a stationary flow velocity far from the reference, the drag force is over estimated of approximately 1.33 times the reference for each nodes. Increasing the numerical resolution shows a different convergence toward stationary velocity with respect to the nodes' position. Two clear regimes are observed, far from interface,  $\vec{x}_3$ , we converge toward the icoFoam's stationary velocity, 0.3599. The reference's convergence velocity is close to the one observed for the mean flow velocity [figure II.25b].

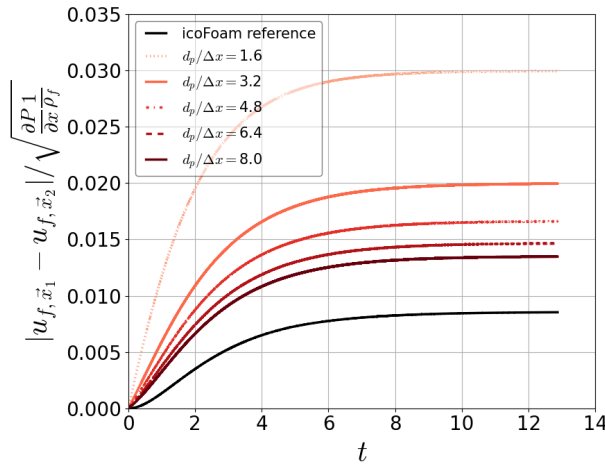
For probes near interface  $\vec{x}_1$  and  $\vec{x}_2$ , the results are far from the reference's solution, respectively 0.2659 and 0.2675, thus we do not expect to recover them since boundary treatments are different. An asymmetry is observed between velocity at probes  $\vec{x}_1$  and  $\vec{x}_2$ . This result is not expected since the simulation is performed at low particle's Reynolds number ( $Re_p < 1$ ), its evolution against time is studied [figure II.26c]. It shows that the position of the Lagrangian markers has an influence on the flow generation, for few cells across the diameter we observe the higher difference. Then, increasing the numerical resolution leads to a convergence toward icoFoam's reference. It shows that numerical instabilities can appear in particle transport because of an inhomogeneity in the Lagrangian grid and that increasing the resolution might decrease this inhomogeneity. Improvements must be done in computation of equivalent control volume from Lagrangian grid toward Eulerian grid.

Finally, we note that the convergence toward the icoFoam reference is different with respect to the node that we study [figure II.26b]. For near interface nodes, the flow velocity is underestimated of almost 10% in the best scenario. This is because the no-slip/no-penetration is not explicitly imposed at particle's interface. Then, we do not expect to recover second order of accuracy near the interface refining the simulation as suggested by [Peng et al., 2019]. For the node far from interface, we observe

that the order of convergence is similar to the mean flow velocity. In the best scenario the difference with the reference is lower than 1% and we expect converging with a second order of accuracy refining the simulation [Peskin and McQueen, 1989, Breugem, 2012].



(a) Evolution of the velocity for two nodes near interface, (b) Stationary velocity for two nodes near interface, blue and red, and far from interface in green, for  $\frac{d_p}{\Delta x} = [1.6; 3.2; 4.8; 6.4; 8.]$ , against the characteristic time. [1.6; 3.2; 4.8; 6.4; 8.], against the characteristic time.



(c) Evolution of  $|u_{f,\vec{x}_1} - u_{f,\vec{x}_2}|$  for  $\frac{d_p}{\Delta x} = [1.6; 3.2; 4.8; 6.4; 8.]$ , against the characteristic time.

Figure II.26

### II.3.6 Summary

The purpose of this section is to study the accuracy of three Lagrangian tracking method in the under resolved range of the ICM. The three Lagrangian techniques are the One-way method, the Two-way method and the IBM. It is found that the various forces implemented in the Lagrangian model influence the result.

The selected model needs to be accurate in Lagrangian transport. To be more consistant in the treatment of small droplets, the Two-way method is considered. It permits to consider the influence of the particle onto the Eulerian grid improving the consistency of the momentum conservation. This method shows relatively accurate results with a good convergence in the coarse area. Finally, the IBM method has been studied. A new Lagrangian mesh generation is tested and the results showed that there are no clear modification on the Lagrangian transport. Also, the computational cost is decreased. The retraction of the radius improves fluid/particle coupling at particles' interface. This ad

hoc solution permits to reduce its influence with a redistribution of the particles' force mainly inside the physical immersed boundary. The next step is to compare those results against the results of the ICM method in order to have a map of use of each method. The goal is to determine a range of use of each method to improve the treatment of small droplets in secondary atomization area.

## II.4 Comparison of methods

To assess the capability of each method to be as close to the desired physic with respect to the number of cells in the diameter, a comparison is done. The methods compared are the IBM [Breugem, 2012], ICM in *Archer* [Ménard et al., 2007], Two-way and One-way method using averaged corrected interpolated velocity. This analysis is carried on the free-falling sedimented droplet [subsection II.3.1], from [Ling et al., 2015]. The physical analysis is done over each method for a given range of  $\frac{d_p}{\Delta x}$  for the velocity evolution and the terminal velocity obtained. The goal is to get the best coupling in our hybrid method.

### II.4.1 Physical results

In order to represent the velocity evolution of the free-falling particle with the ICM method, the fluid properties are chosen following a detailed numerical implementation [Zuzio et al., 2018]. The numerical configuration of this simulation is  $d_d/\Delta x = [3.2, 4.8, 6.4, 8., 16.]$ . It has been impossible to perform this study for a smaller number of cells per diameter because of the ICM requirements: for coarser mesh,  $d_d/\Delta x = 1.6$ , the initial droplet is not created. The analysis of the results of this simulation is done as follows: first we evaluate the morphological shape of the droplet to ensure that the droplet remains approximately spherical. Next, we study its velocity evolution. The velocity evolution is weighed against a terminal velocity obtained through a Richardson interpolation [Appendix V.3]. We conclude our analysis comparing the terminal velocity results against the results obtained for the Lagrangian simulations.

#### ICM results

The morphological analysis is done for  $d_p/\Delta x = 6.4$ . It is represented with its interface at  $\phi = 0$  in red, for the initial and near end time steps:  $t/\tau_p = [0, 4.5]$  [figure II.27b]. The top droplet is initialized spherical and fall in the box. Its shape evolves when it reaches the vicinity of the bottom border. We observed that the droplet is slightly flattened on its bottom at  $t/\tau_p = 4.5$ . Since at this time we already reached terminal regime's velocity, we can assume that the droplet remains spherical during this simulation and conclusions can be drawn out of this velocity evolution.

To go further on the droplet's quantitative analysis, we compare the flow around the droplet/-particles using stream flow vectors. The flow is represented by the magnitude of the velocity on the extracted planes (2D vectors) and the thickness of the arrow represents its magnitude. For visualization purpose, the droplet/particle has been represented from its position with a solid black line [figure II.27a]. The boundary conditions and the droplet/particle momentum create two areas of recirculation. Those areas are represented by the two vortices that are observed for every simulation. It shows that the physic of the droplet/particle's influence is similar for every simulation. A difference is observed at the interface of the falling object, it is due to its treatment. Since the general behavior of the droplet is similar in the flow creation, and that in most of the free-fall the spherical assumption is hold, we can pursue the analysis of the simulations.

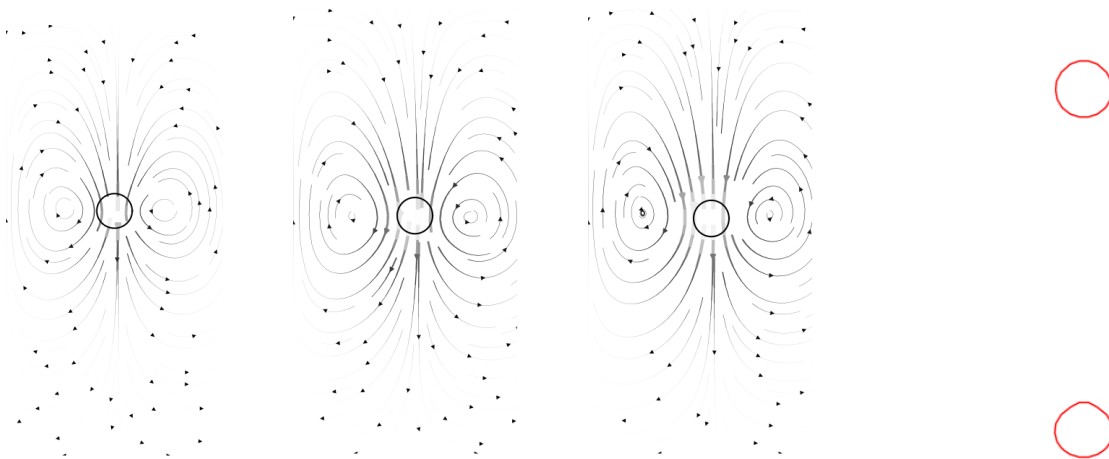
We evaluate the free-falling droplet velocity evolution for the 5 mesh resolutions [figure II.28a]. First, for the smallest number of cell per diameter some oscillations are observed. Different reasons can explain these oscillations. Our guess is that these oscillations are mainly due to the post treatment approach. This post treatment is based on the assumption of velocity continuity across the interface (no phase change). Since a staggered grid is used, the velocity is interpolated into the cell centers. Then, all cells with a volume fraction higher than  $\alpha > 1 \cdot 10^{-10}$  are used to post treat the velocity:  $\int_{\Omega} H(\alpha > 1 \cdot 10^{-10}) \vec{u} \cdot d\Omega$ . Since this average considers different velocities values that those computed by

*Archer* with the dual grid algorithm, some uncertainties are introduced. This uncertainty is considered later when the droplet to Lagrangian particle transformation is detailed [section III.6]. Then, refining the simulation leads to converging toward the reference solution, a first order of convergence has been observed for this method.

### All methods' comparison

Since the purpose of this comparison is to determine the robustness and accuracy of these methods, we focus on this analysis comparing the results for all methods. Then, droplet free-falling terminal velocity is evaluated. The results of the Two-way method are used for two filter size:  $\delta = [1.3; 2.6] \cdot R_p$  with corrected averaged interpolated velocity. The IBM results are used with radius retraction and analytical mesh generation. The results obtained for three One-way models are displayed, respectively the terminal velocity for unbounded/bounded velocity with drag consideration and bounded stokes terminal velocity:  $|V_{Sto.}(t = \infty)|$ ,  $|V_{S.\&N.,\eta}(t = \infty)|$ ,  $|V_{Sto.,\eta}(t = \infty)|$ , over the entire range of meshes since its not mesh dependent. All results are displayed on figure II.28b.

We first focus on the ICM's terminal velocity. For the intermediate mesh resolutions, ICM terminal velocity is in between the correlations given by  $\tau_p \vec{g}$  and the one considering the drag correction. Different phenomena can explain why the velocity does not reach the One-way results: the correlation to account the bounded domain, the internal recirculation within the droplet, or the non-spherical shape of the droplet analyzed just before. In *Archer* we observe a clear tendency to converge toward the terminal velocity:  $|V_{ICM}(t = \infty)| = 0.044 [m/s]$ . The results observed in the literature displayed a different behavior [Zuzio et al., 2018]. Their free-falling droplet's simulation converged toward  $d_p/\Delta x = [2.4, 4.8, 9.6] \rightarrow |V_{ICM}(t = \infty)| = [0.04185, 0.04047, 0.04143] [m/s]$ . The drag force is overestimated when the number of cells is not sufficient. It is complex to compare our results to their work even if both solver use *CLSVoF* method to treat the interface, more simulations are required to have a better comprehension of the physic of this specific test case. From this test case we note that ICM converges toward One-way reference's solution between  $4.8 < d_p/\Delta x < 6.4$ . We estimate the limits of the ICM to transport under resolved droplets in the range  $d_p/\Delta x \approx 5$ . The conclusion is that we must treat droplets below this numerical resolution with particle tracking method. The remaining question is to determine which solver we might use, and we answer it comparing with particles' results.



(a) From left to right, streamflow around the free-falling sedimented droplet/-particle for the *CLSVoF* (droplet), IBM (particle) and Two-way (particle). The arrow size represents the magnitude of the velocity field.

(b) Droplet interface in red at  $\phi = 0$ , for  $t/\tau_p = [0, 4.5]$

Figure II.27

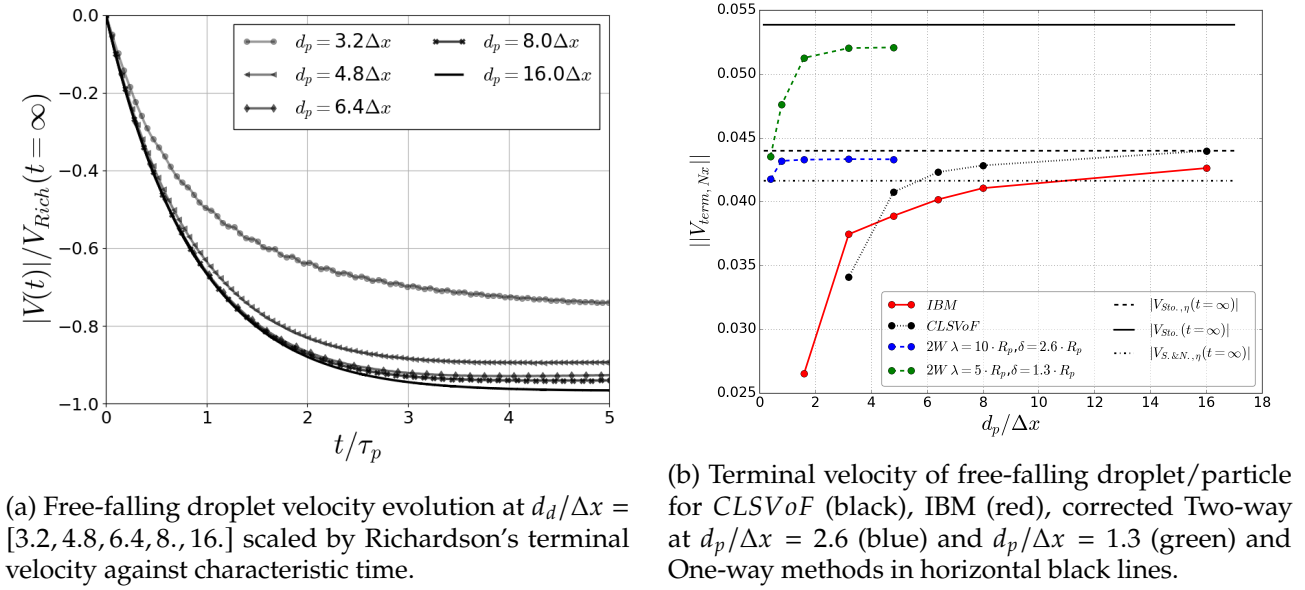


Figure II.28

ICM and IBM results have a similar evolution, increasing the numerical resolution leads to a convergence between  $|V_{S.\&N.,\eta}(t = \infty)|$  and  $|V_{Sto.,\eta}(t = \infty)|$ . We consider that both methods are far from being converged and for the ICM simulation, since its shape can evolves, we do not ensure that a convergence is conceivable.

It appears that the IBM method is not improving the treatment of under resolved droplets in the coarse area and we are not going to use this method. Since AMR can be implemented in *Archer* future developments, the IBM method can be used as a milestone following [Zuzio et al., 2018] strategy. For those future developments the treatment of the transformation from ICM toward IBM is presented in chapter III.

In the range  $d_p/\Delta x < 5$ , we observe that the ideal method to use is whether a Two-way or One-way method. It confirms that the wider is the area of redistribution, the more accurate are the results. The next steps are the evaluation of the influence of a wide momentum's redistribution in the domain and its use in realistic application. A One-way method can be considered for the relatively small droplets, it permits to reduce the computational cost of the Two-way method, those assumptions would be tested further.

## II.4.2 Summary

The conclusions from our study of particles' tracking implementation permits to determine which method is conserved in our Hybrid approach.

For the Hybrid approach, we consider the coupling between ICM [Ménard et al., 2007] and Two-way method with correction on the interpolated velocity [Evrard et al., 2020]. In the next section of this manuscript, we are going to compare Hybrid approach with One-way and Two-way methods in order to study the influence of momentum's redistribution in the physic of the simulation. This study is done on three test cases; free-falling droplet over a free liquid surface, an excited Plateau-Rayleigh atomization and immiscible immersed droplets in a decaying HIT.

Since FRP approach (IBM) does not solve the issue of accuracy for under resolved particles, we do not consider it in our Hybrid approach. Nevertheless, transformations are validated from droplets toward all Lagrangian approaches since the IBM method can be useful for specific configurations. This is the purpose of the next chapter, the description of the Hybrid approach detailing the procedure to remove a droplet from the Eulerian domain ensuring mass and momentum conservation.

---

# Implementation of Hybrid Method

---

*The goals of this chapter are to detail step by step the procedure to implement the Hybrid approach. Several hypothesis are implied when going from the resolved interface framework toward particle tracking algorithm, we detail there meaning and our choices of implementation. At transformation Eulerian fields are updated and global quantities, mass and momentum, have to be conserved, implementation and validation are presented in this chapter. Finally, an illustrative simulation of head-on collision is performed to compare the capability of the Hybrid approach to recover ICM refined simulation results.*

## Contents

---

III.1	State of the Art . . . . .	96
III.2	Detection of structure . . . . .	97
III.2.1	Algorithm . . . . .	97
III.2.2	Parallel efficiency . . . . .	101
III.2.3	Summary . . . . .	102
III.3	Distance to interface criteria . . . . .	103
III.3.1	Resolved droplet to Lagrangian particle . . . . .	104
III.3.2	Particle to resolved droplet . . . . .	104
III.4	Sphericity criteria . . . . .	105
III.4.1	Introduction . . . . .	106
III.4.2	Numerical Methods . . . . .	106
III.4.3	Droplet to particle transformation criteria . . . . .	109
III.4.4	Lamb oscillation . . . . .	110
III.4.5	Immersed Droplet in a HIT . . . . .	111
III.4.6	Airblast atomizer . . . . .	113
III.5	Reconstruction of the interface . . . . .	115
III.5.1	ICM to Particle . . . . .	115
III.5.2	Particle to ICM . . . . .	116
III.6	Reconstruction of the velocity field . . . . .	118
III.6.1	Velocity field reconstruction . . . . .	120
III.6.2	Configuration . . . . .	122
III.6.3	Results . . . . .	122
III.7	Treatment of collisions in Hybrid coupling . . . . .	124
III.7.1	Strategy for particles interactions . . . . .	125
III.7.2	Head-on collision . . . . .	126

---

### III.1 State of the Art

In two phase flow atomization, various solutions exist to treat the under resolved droplets [chapter I]. In this manuscript, the strategy is to apply the Eulerian Lagrangian Hybrid approach. It consists in transporting under resolved droplets with a Lagrangian tracking method.

A detailed review of the Hybrid approaches is given here to present the different strategies. Since it depends on the ICM implemented in the Eulerian solver, the strategies are different in the literature. We present key papers highlighting the milestones of Hybrid implementation and conclude on the open questions that we aim to answer in this manuscript.

In 2010 [Herrmann, 2010a] and [Tomar et al., 2010] developed simultaneously an hybrid method.

The first step to be able to transform an under resolved droplet into a particle is to identify the isolate liquid structures. An algorithm to identify these structures is developed in parallel based on the *Level-set* field [Herrmann, 2010a]. Similarly, [Tomar et al., 2010] uses the Volume of Fluid to detect these structures. This kind of labeling algorithm is well known in the literature and links neighboring cells belonging to the same structure and attributing them an unique tag. In *Archer* a tagging algorithm has been developed in MPI using the Volume of Fluid field [Vaudor, 2015]. A coupling of *Level-set* and Volume of Fluid is used in this manuscript to improve the detection algorithm present in *Archer* [section III.2].

Once the structures are identified, it is necessary to provide a criterion to choose the droplets that are transformed. Since the Lagrangian solver is motivated to avoid transport of under resolved structures or jetsam, the first criterion is based on the droplet size with respect to the mesh size, [Tomar et al., 2010, Herrmann, 2010a]. However, the size criterion is not sufficient.

- First, in order to ensure that the transformation does not modify the other neighboring structures, a criterion based on the distance to the other structures has been proposed by [Ling et al., 2015]. The numerical implementation of such criteria is detailed later [section III.3].
- Second, since the transport is based on spherical assumption of the droplet, different sphericity criteria have been introduced [Herrmann, 2010a, Zuzio et al., 2018, Ling et al., 2015]. A conference paper on this topic has been published during this Ph.D [section III.4]. Novel morphological criteria are implemented based on experimental literature [Malot and Blaisot, 2000] to be more consistent in droplet morphological analysis.

In this Ph.D. we address the self-sufficiency of these morphological criteria. We consider that the physical state of a droplet has to be considered. This question is opened in the next chapter [chapter IV]. This analysis is a first step toward secondary breakup model (SBM) that must be implemented in Hybrid method in order to avoid the mesh dependency of the droplets' distribution. Moreover, we want to study the influence of the criteria on the final droplets distribution, for example restrictive criteria might decrease the number of transformations. This behavior has not been addressed in the literature, and we propose to study it to show the importance of the criteria definition on simulation outcomes.

When the droplets that will be transformed are chosen, the Eulerian and Lagrangian fields have to be updated. Our strategy is to remove entirely the Eulerian information: the *Level-set* and the *VoF*. In the literature the strategy to remove the *Level-set* is to inverse its sign, in *Archer* we did not successfully removed the Eulerian field with this strategy and the solution that we implemented are later detailed [section III.5].

These first communications [Tomar et al., 2010, Herrmann, 2010a] opened two main interrogations.

- First, the velocity field was not updated and this problem is addressed in [Ling et al., 2015] that showed the inconsistency in velocity evolution at the transformation for the Two-way approach. They proposed to reconstruct a velocity field to ensure smooth transition and we implemented it in *Archer*[section III.6].
- Second, the volume of the particle is not considered in the coupling with Navier Stokes. The mass conservation is broken by this assumption and in dense simulation it is observed that the particles' transport is less accurate. In [Evrard et al., 2019] they coupled the particle volume

fraction with Navier Stokes equations to improve Hybrid approach. Since this approach modifies Navier-Stokes implementation, we do not consider it in our study.

After transformation, particles are transported with a Lagrangian solver that are different among the literature. We explained that ICM modifies the strategy of transformation, grid refinement such as AMR also modifies the transformation strategy. The current state of *Archer* does not permit to use AMR but future developments aim to implement it, and we briefly review the AMR Hybrid method strategy.

The first purpose of the Hybrid approach is to relax the grid, after transformation from droplet toward particle, the grid was coarsened [Herrmann, 2010a, Tomar et al., 2010]. Then One-way or Two-way approaches were used to transport particles. It was commented that the transformation and coarsening of the grid was inaccurate and an additional step has been implemented in the Hybrid approach [Zuzio et al., 2018]. They transformed the resolved droplet into FRP on the same grid, then the FRP moves toward coarse grid and it is transformed into point particle. At this instant, the grid is updated. This additional step improves the transport of the interface without causing any numerical instabilities or modification of the local flow topology.

Without AMR there are two main communications [Ling et al., 2015, Evrard et al., 2019] where the particles are transported with Two-way approach, and Two-way approach coupled with voidage function to improve mass conservation. In *Archer* we consider One-way or Two-way methods to transport particles [chapter II].

In Hybrid method the reverse transformation, from particle toward droplet, is also considered. It happens when the Lagrangian particle is in the vicinity of any Eulerian interface [Tomar et al., 2010]. The first step is to update Eulerian fields and remove the particle. The purpose of the Hybrid method is to transport under resolved droplets with particle tracking, it means that the reconstruction of the resolved droplet can be complex. This has not been addressed in the literature later analyzed [section III.5]. To be conservative in momentum for the reverse transformation, the velocity field is updated following the work of [Ling et al., 2015]. We study it in section III.7 where we detail our choice when we study Lagrangian particle collisions.

## III.2 Detection of structure

During the Post-Doc of Geoffroy Vaudor, a detection algorithm has been implemented in *Archer* based on the Volume of Fluid information. This will be the base of the transition between the Interface Capturing Method and the Lagrangian Tracking Method. This algorithm has been implemented in MPI formulation and can identify all the structures of a simulation. The first part of this section focuses on the description of the methodology and the second part will focus on the efficiency of implementation of this algorithm.

### III.2.1 Algorithm

The idea behind this algorithm is to be able to detect all structures in the domain and to identify them. It provides information on the droplet distribution, and it identifies the structures from different area of the spray with the analysis of the radius/velocity/morphological distribution. First, it will be explained on a single processor example, before describing a multi processor identification of structures.

#### Single processor presentation

As represented on left figure III.1, two information are available, the volume of fluid represented in orange and the *Level-set* at its iso 0 value represented in blue. To identify a structure, this detection algorithm is using the volume of fluid of the two-phase flow solver information. Each cell containing a value of fluid higher than a threshold will receive a tag value according to its position in the Cartesian space loop [center figure III.1]. Next, the minimal value of the adjacent cell will be conserved and



will be given to the structure to identify it. This tag is unic for one structure, all the cells containing a volume of fluid information in the neighboring receive it [right figure III.1].

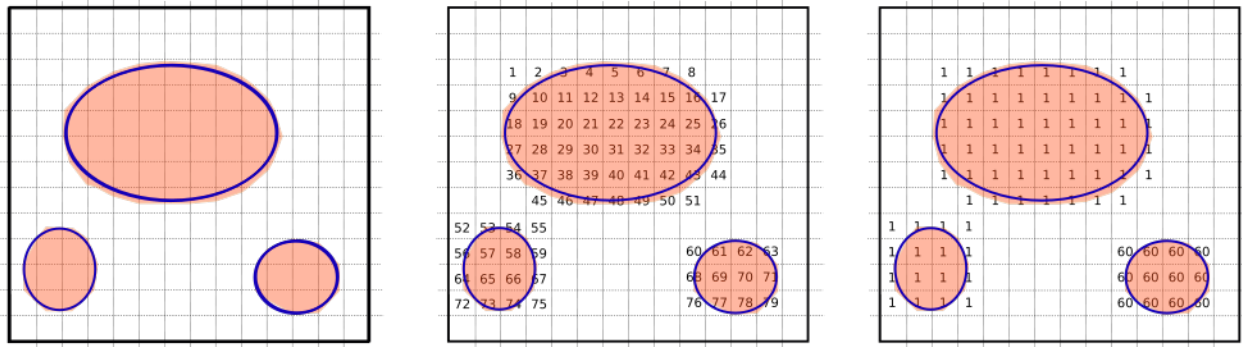


Figure III.1: Left figure: Structures identified with *VoF* in orange and their interface in blue. Center figure: adding tag information to each cells. Right figure: uniformization for the tag to get an identity per structure.

From right figure III.1, it can be observed on this really simple scheme that the junction between the two structures identified with the number one is well separated by the *Level-set* function, however, they share the same tag. It can occur because a relatively small volume fraction is trapped in a cell which extends the tag. We take advantage of the *Level-set* properties to improve the detection algorithm. The strategy is to use also the distance to the interface of a cell to refine the detection. In 2D Cartesian framework, we select a distance value above the one the particle's tag is removed. for example if the volume fraction of the cell is below  $10^{-10}\%$  and the cell center is at a distance higher than  $\Delta x \frac{\sqrt{2}}{2}$ , in 2D, and  $\Delta x \frac{\sqrt{3}}{2}$ , in 3D, from the interface. This distance is equal to the half diagonal width of the cell, it permits to be as much restrictive as possible on this tag refinement. The first goal of this modification is to isolate droplets in dense area.

Those improvements on the structure detection are showed on a simple test case. Two droplets are initialized in a box for two numerical resolutions:  $d_d/\Delta x = [10, 20]$ . The distance from both center of mass,  $\sqrt{(\vec{x}_{d,1} - \vec{x}_{d,2})^2} = \frac{d_d}{5}$ . It gives a distance from both interface of  $\approx 2\Delta x$  for the coarse grid and  $\approx 4\Delta x$  for the refined grid. The coarse simulation is executed twice, one with corrections and one without. The corrections are set to volume fraction  $\alpha < 1 \cdot 10^{-10}$  and *Level-set* distance  $\Delta x \frac{\sqrt{3}}{2}$ . We show the real interface at  $(\phi = 0)$  for the three simulations and the resulting tag [figure III.2].

The first line shows the coarse results without corrections. We observe that the interface represents accurately two droplets, however the same tag is shared for the two droplets (in blue). On the second line for  $d_d/\Delta x = 20$ , we observe that more cells are tagged which is due to the higher resolution. It leads to a clear identification of the two droplets, respectively in blue and green. On the last line we observe that the two droplets are identified separately. Using the *Level-set* information for the tag algorithm permits us to detect the two isolated droplets. Since we implemented a threshold on the volume fraction, we ensure that the volume conservation is done with a variation of  $10^{-10}$  per cell which does not influence our droplets statistics.

### Track droplets Lagrangian information

The main drawback of this algorithm is the update of the tag process at each iteration without conserving recovered structures information. Since the structure evolves along the simulation, a droplet might not be at the same position or on the same processor further iterations later. Those statistics are important to improve the treatment of small droplets and an algorithm to follow them during the simulation is implemented.

This algorithm is based on a research of the droplets' center. Since we want to conserve the information on the droplets, their information are stored in a list of pointers similarly to the particles,

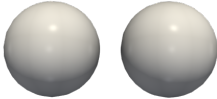
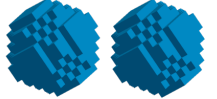
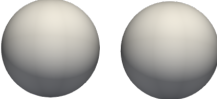
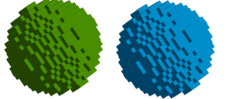
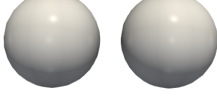

	$\phi = 0$	$Tag$
$d_d/\Delta x = 10$		
$d_d/\Delta x = 20$		
$d_d/\Delta x = 10$ + correction		

Figure III.2: Results showing tagging correction based on *Level-set* information.

see the description of the Lagrangian solver in section II.2. In this list we can store the structures mass center every time that we use the algorithm.

The strategy implies a research of collision algorithm between droplets identified at successive iterations:  $n$  and  $n - 1$ . The center of gravity at the prior iteration is updated using a simple first order linear advection [equation III.1]. Then, the distance between the two center of gravity at the same time step is calculated. Since we use the same strategy to store information on droplets than particles, the same algorithm is used to do the distance calculation [algorithm II.4]. Then, its implementation in MPI is straightforward using the ghost lists. Results of this identification are showed on figure III.3 where all the steps going from the newly identified droplet toward the recovering of the prior id is done. Finally, the tag is updated at every iteration, giving a value of identification of the droplet,  $id$ , that is constant if the droplet does not evolve during the simulation because of breakup or coalescence events. The goal is to conserve the  $id$  to follow the droplets.

$$\vec{x}_{recons} = \vec{x}_{n-1} + \vec{v}_n \Delta t \quad (\text{III.1})$$

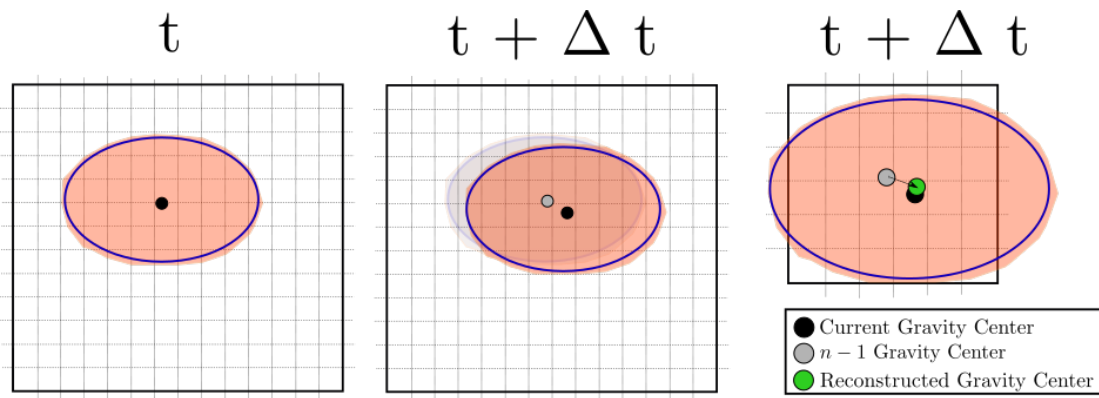


Figure III.3: Reconstruction of the center of gravity of a structure to conserve identity during time evolution.

The drawback of the algorithm is the frequency of use. If we use this algorithm at every time step, the distance between the current center of mass and the prior one is relatively small and recovering the droplets' history is straightforward. On the other hand, a small frequency implies larger distance to

recover and we can loose the history of the droplet. In order to improve the algorithm, we implement a volume conservation detection. It consists in checking if the old droplet has the volume of the current droplet. Since we assume that fluctuations can occur, we set a threshold of 5% variation. History droplet identification is described [algorithm III.1]. We first evaluate the distance between the two droplets using the reconstructed position of the droplet. Next, we evaluate the volume of the two structures and if all criteria are validated, we can transfer the information.

In some natural events of atomization, it is impossible to follow the droplets' information with such simple algorithm, for example for breakup or coalescence events. Then the history droplets is not recovered and we have to set a new identification to the droplet. To improve our statistics, we implement two algorithms to detect breakup/coalescence events.

```

1 if ((x_recons - x_n)**2 + (y_recons - y_n)**2) <= (Dx/2)**2) .and.&
2   (Vol_drop_n = +/- 5\% Vol_drop_nm1) then
3   NewId = OldId
4 else
5   NewId = max(OldId(:)) + value*my_rank
6   call MotherDroplet() !check breakup history
7   call CollidingDroplets() !check coalescence history
8   end if
9 end if

```

Algorithm III.1: Algorithm used to update droplets' information and redirect to breakup/coalescence functions if required.

We first detail the strategy to evaluate breakup events. The idea is to use the Eulerian tagging field of the prior iteration and to compare it to the updated one. The first step is to define an area around the droplet that received a new identification. Since we expect to have more than one droplet in this area (breakup event), the first step is to count the number of structures at each iteration,  $n$  and  $n - 1$ . Next, we sum the volume of each structure inside the area for the two iterations, we expect to have the same quantity even if the number of droplets are different at  $n$  and  $n - 1$ . It permits to define a volume conservation in the area which is the first step to determine the mother droplet because the volume of this new droplet is coming from an identified droplet at prior iteration. Then, we can determine which structure at iteration  $n - 1$  breaks to create this droplet. We can finally add the identification of the mother droplet to our newly identified droplet improving our Lagrangian statistics.

An example of this process is represented on the two successive snapshots of the Plateau-Rayleigh atomization. In this simulation, we observe that a small droplet is ejected from the main liquid core. At this instant a new tag appears on the tagged Eulerian field leading to a new identification [figure III.4a].

The evolution of the two structures  $id$  that are respectively called 10,000 and 11,000 is observed [figure III.4b]. The liquid core conserves the same  $id$  along the simulation thanks to the research of center algorithm. At an instant, a droplet is ejected and a new identification is given. Then, we use the reseach of breakup algorithm and determine the mother droplet [figure III.4b]. The algorithm can identify from which structure droplets are ejected and can be used for primary atomization area analysis, however, we only conserve one mother droplet in history.

The coalescence events algorithm is in somehow the inverse phenomenon. We use the tag of the prior iteration and we compare it to the current one. It identifies the droplets that were in the area before, and we compute the total volume. If it coincides, we conclude that the new droplet is created from the droplets identified in the area. We store the identification of the prior droplet into the new droplet's information. We illustrate the coalescence for a simple configuration: two droplets coalescence. The two droplets are initially identified separately and when they get close to each other, they unify into one unic droplet [figure III.5a]. Because the center of gravity moved, in 1D  $x_{new} = \frac{x_1+x_2}{2}$ , and the volume is doubled, the identification of the droplet is lost. A new  $id$  is given to the droplet, and, information on the droplets that coalesced to create this new droplet are stored to recover its evolution. On figure III.5b, it is observed that those two droplets were identified as 10,000 and 20,000, and, at the coalescence event, they became 30,000. At this instant, the id of former droplets are stored, and, they are observed to be equal to the one of the droplets that disappeared.

For the Hybrid method, all pieces of information are not of first importance, and, strongly slow

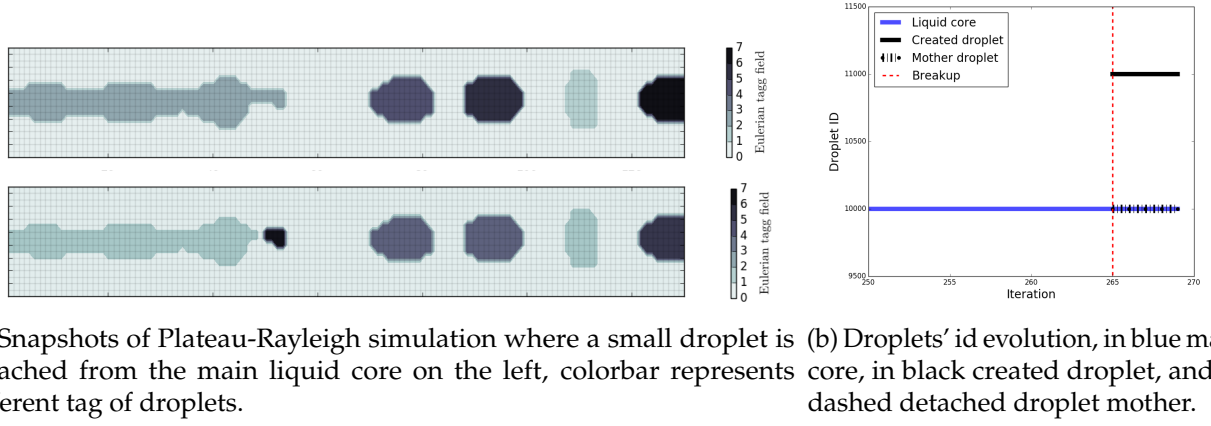


Figure III.4

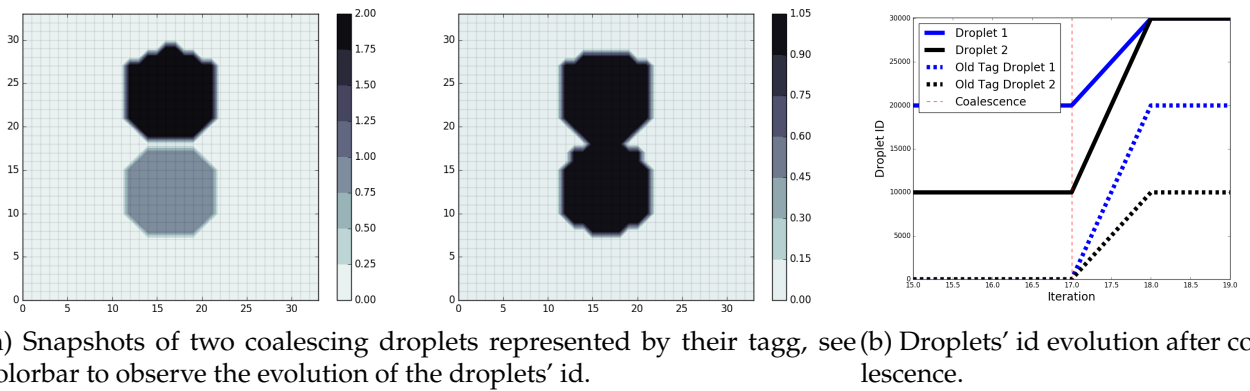


Figure III.5

down the calculation. But, the possibility to recover those information on droplets and to observe their evolution within a two phase flow simulation is relevant for two reasons. First, it permits taking droplets from the dispersed area of the jet and to trace their path within the simulation until the initial liquid jet. This provides information of primary breakup, and consecutive structures' breakup before to become droplets of the dispersed area. Second, it permits to evaluate the life time of a droplet or a particle since identification is conserved at the transformation. We can follow the entire evolution of one droplet which could enhance breakup modeling. To determine the cost of this algorithm, it is important to study its numerical implementation. A scaling efficiency of the detection algorithm is done in the next subsection to quantify its cost.

### III.2.2 Parallel efficiency

#### Presentation of the case

To study the computational cost of the detection algorithm in the code, a scaling study similar to [Herrmann, 2010a] has been realized. The simulation consists on the following steps:

1. Initialize 1000 particles randomly in the domain with a fixed radius.
2. Transform all particles into droplets.
3. Transform them back into particles.

The domain's length of this 3D cubic simulation are set to  $Lx = Ly = Lz = 1 [m]$ , the radius of particles is fixed,  $R_p = Lx/128 [m]$ . The distance between particles is not specified implying possible overlap. The particles are initialized far from borders to avoid volume loss: particles' center are between  $0.1Lx$  to  $0.9Lx$ . In this specific case Navier Stokes equations are not solved.

The transformation towards particles (step 3) uses the transformation criteria detailed later in this Ph.D. [section III.3, section III.4]. At the end of the simulations, more than 90% of the initial particles for all simulations are recovered.

The strong and the weak speed-up are analyzed in this test case. The strong speed up consists in executing the same mesh varying the number of processors. Thus the charge per processor is reduced. The weak speed up consists on increasing the total number of nodes proportionally to the number of processors. Thus, the charge per processor is constant.

We analyze here the three subroutines of the code that are relevant for the transformation: the transformation from particle to droplet, the detection algorithm and the transformation from droplet to particle. The list of tests is given in the following table:

Case	$N_p = N_{\text{processors}}$	$N_{\text{cells}}$	Load = $N_{\text{cells}}/N_p$	Symbol	Color
Run 1	1	$256^3$	$256^3$	Circle	Blue
Run 2	8	$256^3$	$128^3$	Circle	Green
Run 3	64	$256^3$	$64^3$	Circle	Red
Run 4	512	$256^3$	$32^3$	Circle	Black
Run 5	8	$512^3$	$256^3$	Triangle	Blue
Run 6	64	$512^3$	$128^3$	Triangle	Green
Run 7	512	$512^3$	$64^3$	Triangle	Red
Run 8	64	$1024^3$	$256^3$	Star	Blue
Run 9	512	$1024^3$	$128^3$	Star	Green

Table III.1: List of simulations performed for the weak/strong speed up analysis in *Archer*. The same symbol represents the strong scaling: the load is modified at constant cells. The same color represents the weak scaling: the load is conserved and the resolution is modified. Those colors/symbols are listed in this table to simplify the analysis of figure III.6.

## Results

The time spent in each subroutine is presented [figure III.6]. For each figure the ideal strong scaling is given by a dashed line and can be compared using the same symbols. Similarly, the ideal weak scaling is given by a continuous line and can be compared using the colors.

The comparison of the time spent in each figure shows that the transformation algorithm from particle toward droplet is two orders of magnitude more expensive than the other two subroutines.

The transformation algorithm from particle toward droplet consists on a loop over all the particles and updating *Level-set* and Volume of Fluid fields. The number of particles is initially the same for all the simulations. The strong scaling shows a surprising results after the load of  $128^3$  per processors. This is still under study. Our first guess is that this is due to the a bad optimization of the size of the subdomain size that increases the number of particles treated by each processor. Future work will be done in this direction analyzing the impact of the number of particles treated, their sizes and the number of the subdomains per processor. The weak scaling shows good behavior since the subdomain length is the same when the number of processors increases. Similar conclusions can be done for the behavior of the Eulerian to Lagrangian transformation. For this case, the weak scaling shows that it can be improved while being sufficiently efficient.

Note that the tagging algorithm shows a good weak and strong scaling. This algorithm has been deeply analyzed during this thesis, not presented here, showing an efficient implementation.

### III.2.3 Summary

An algorithm to detect the droplets is used as corner stone to transform droplets toward particles efficiently. We implemented an optimization on the classical algorithm through the use of the *CLSVoF* method. It permits to first detect the structures with an efficient detection of the cells with *VoF* information and to correct the discrepancies with the *Level-set* function that gives us exactly the distance

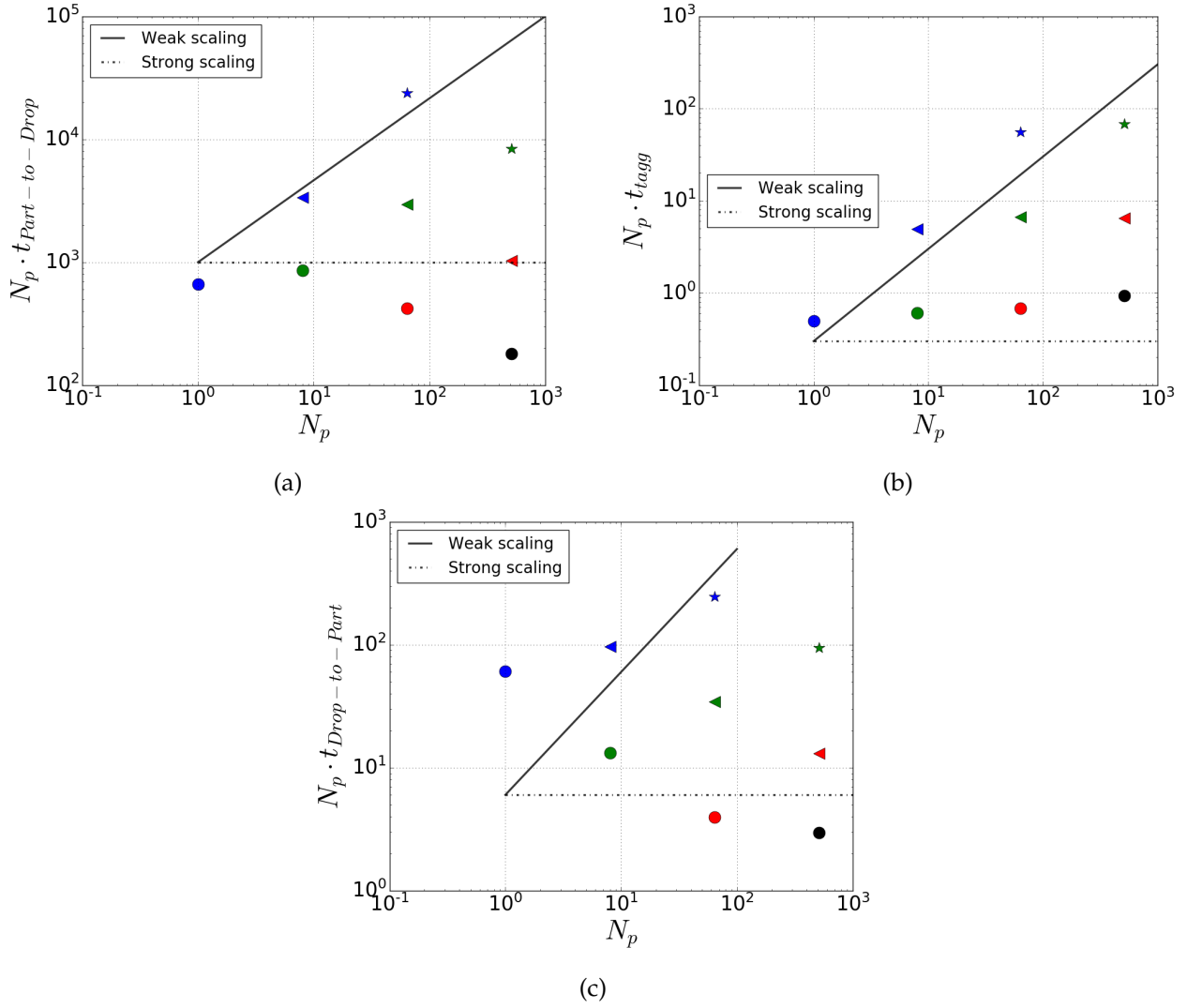


Figure III.6: Results of the time spent in those three algorithms, transformation of particle toward droplet [figure III.6a], time to detect droplets [figure III.6b], transformation of droplet toward particle [figure III.6c]. The same color represents the weak scaling, the same symbol represents the strong scaling [table IV.7].

to the closest interface in each cell. From this algorithm, statistics on the structures are possible such as morphological evolution or breakup/coalescence events.

Then, the numerical implementation of the algorithm and the transformation steps have been studied. It is observed that the MPI implementation of the algorithm is satisfactory, improvements could be done in the strong scaling, but, regarding the time spent in this algorithm, they are not relevant. It is seen that the transformation from particle to droplets and vice versa has a relative influence on the simulation. It is supposed that the reason is because of the modification of the Eulerian fields. This assumption is detailed later. Nevertheless, the advantage of the transformation algorithm is that it is not required at each iteration. For example, the frequency of use can be kept low in order to avoid modifying the computational cost. Finally, the transition from both models is numerically transparent and it is encouraging for the next steps of the Hybrid method's implementation.

### III.3 Distance to interface criteria

The purpose of this Ph.D. is to couple interface capturing method and Lagrangian tracking algorithm in order to lighten the CPU consumption of a DNS simulation and to improve its physical accuracy. The capability of the ICM to accurately transport the small droplets of the atomization can



be defined in a criterion based on the number of cell in the equivalent radius of the structure, obtained from the detection algorithm through  $R_d = (3 \times Vol_{VoF}/4\pi)^{1/3}$ . This criterion depends on the accuracy of the Lagrangian/ICM techniques and it is studied on a free-falling sedimented particle/droplet [section II.3]. The next step is to determine if the droplet that must be transformed is far from other structures. This criterion is simply called distance to interface and permits to ensure the transformation. This criterion is also used to treat the particles toward droplets transformation when they are close to each other. Its implementation is detailed in this section.

### III.3.1 Resolved droplet to Lagrangian particle

The criterion of distance from other structures is important to ensure that the reconstruction of the Eulerian field does not modify other properties. The importance of the parametrization of this distance is discussed later [section IV.1]. In complex atomization, it is expected to see transformation in the secondary atomization because a lot of structures are present in the primary breakup area. In [Herrmann, 2010a], the transformation is executed whenever its detection algorithm identifies a new structure. In [Ling et al., 2015], the distance criterion is set to the droplet's diameter and evolves with the droplet that is studied. In [Evrard et al., 2019], the filter function  $\delta$ , set to several radii, defining distance criterion and it evolves with its value:  $||\vec{x}_d - \vec{x}_T|| > \delta + 3\sqrt{3}\Delta x/2$ .

In *Archer* the criterion of distance from other structures is based on the diameter of the droplets similarly to [Ling et al., 2015], that we define  $\mathcal{L}_{\mathcal{D} \rightarrow \mathcal{P}}$ . It is later determined how many diameters we set for this criterion. First, we describe its simple implementation.

Since the detection algorithm provides a tag to all cells that have a liquid structure, we use that information to determine the distance from other interface. We recall that an empty cell has a value set to 0. The first step is to determine a box centered on the droplet with a size based on droplets' information. Then, we check if a tag is different from the droplet's tag in the box, if there are no other tag the criterion of distance,  $\mathcal{L}_{\mathcal{D} \rightarrow \mathcal{P}}$ , from other interface is validated.

This criterion is represented on figure III.7 where it is possible to observe that the interface of two droplets is represented with their *Level-set* in blue at  $\phi(\vec{x}) = 0$ . One of these droplets is in the vicinity of a main liquid structure, the other one is more isolated. Then, we design a box centered on those droplets, since we use Cartesian grid it is centered on the grid cell where the droplets' center is located. We evaluate if other structures are identified in the box, for the left droplet, there is the main structure and it is not transformed. The other droplet is isolated enough and no other structures are found in the box, the criterion of distance is validated.

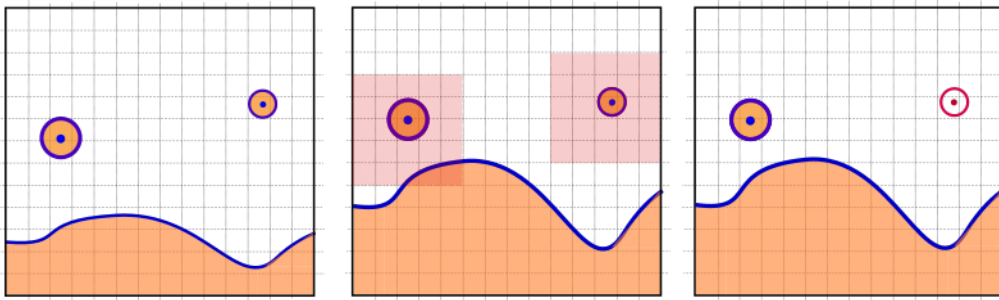


Figure III.7: Distance criterion based on control volume, in blue: interface represented by the *Level-set* at  $\phi(\vec{x}) = 0$ , in orange: *VoF* when  $\alpha > 0$ ., in pink: particle's interface.

### III.3.2 Particle to resolved droplet

In some applications, the reversed transformation is necessary because the droplets transformed into particles are getting in the vicinity of other structures that are transported with ICM. Then, it is necessary to determine the distance of the particle to the closest interface. The advantage of the particle is that it does not modify the *Level-set* at its position. Then, we can interpolate the distance to the

closest interface using the distance properties of the *Level-set* on the Eulerian cell where the particle is located. If the distance is higher than a threshold,  $\mathcal{L}_{p \rightarrow \mathcal{D}} > \epsilon$ , the particle is transformed into droplet. The threshold is selected based on the other transformation. Since the purpose is to transform as much unresolved droplets into particles as possible, we set the threshold for the reverse transformation two times smaller than for the droplet toward particle transformation,  $\mathcal{L}_{\mathcal{D} \rightarrow p} = 2 \times \mathcal{L}_{p \rightarrow \mathcal{D}}$ . It permits to favor the direction of transformation that we prioritize.

An example is given for the distance calculation on figure III.8 In this example we present two particles and their distance to the closest interface is evaluated thanks to the *Level-set* function. Since the particle on the left is close to the interface, it is transformed back into a droplet. At the next iteration the *Level-set* field is updated [figure III.8], and the other particle updates its distance to the closer interface [section III.5].

Another situation where the necessity to use ICM method can occur is particles interactions. Particles can collide and it has been seen in the work of [Rabe et al., 2010] that the outcome can be far from the model implemented for collision in particle tracking. In order to respect the physic of the collision, the particles are transformed back into droplets [section III.7].

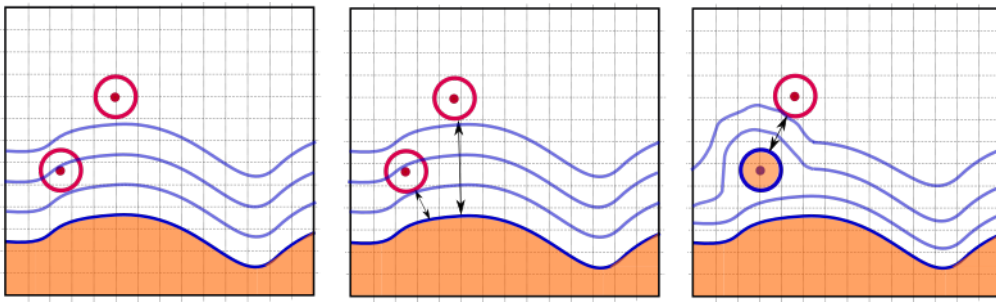


Figure III.8: Distance criterion based on *Level-set* information, in blue: interface represented by the *Level-set* at  $\phi(\vec{x}) = 0$ , in orange: *VoF* when  $\alpha > 0$ , in red: particle's interface.

### III.4 Sphericity criteria

As introduced in the first section of this chapter, morphological criteria to ensure the sphericity of the structure are required and the strategy to implement them is explained in the work that we communicated for the 29th European ILASS conference in 2019 September. This communication is following the next step. A first section focuses on the information available with the interface tracking method in *Archer* with a short definition of *Archer*. A simple test case is simulated to determine which information are consistent with the second order accuracy of the code. Then, the morphological criteria will be constructed, and, in opposition to the literature that focuses on information relative to the center of gravity of the structure to the interface, here, implementation of surface criteria will be done. Two academical test cases are executed to validate our assumptions. The first one is based on the shift theory of Lamb and has been widely tested on oscillating droplets, first experimentally [?] and numerically [Aniszewski et al., 2014]. The linear solution of this test case will simplify the study of the time evolution of the morphological criteria. The second test case is a pseudo HIT flow, this is performed in order to create a strong shear at the interface to observe the role of the morphological criteria defined with surface of droplet information. Finally, the purpose of this Ph.D. is to determine on one iteration if a structure can be qualified such as a droplet. A combination between the most accurate criteria based on distance to interface information with the newly implemented surface criteria will be used on an iteration of an already developed air blast atomizer.



### III.4.1 Introduction

Atomization is a phenomenon encountered in many applications such as sprays in cosmetic engineering or aerospace engineering for jet propulsion [Lefebvre and McDonell, 2017]. In the combustion chamber, the total surface of the interface separating the two phases is a key parameter. Primary and secondary breakup have been extensively investigated in the literature. However, in order to fully describe the complete process, one has to capture droplets in dispersed zone 100 times smaller than jet diameter. Atomization is then a multiphase and a multiscale flow phenomenon which is still far from being understood.

Due to this wide range of scale, the Direct Numerical Simulation (DNS) of such process requires robust and efficient codes. DNS is an important tool to analyse the experimental results and go further into the atomization understanding. In the past few years, numerical schemes of Interface Capturing Method (ICM) have been improved but faced numerical limitation. For instance, the treatment of the small droplets is the most challenging part when the entire process is treated in DNS. When dealing with unresolved structures we face different problems such as the dilution or the creation of numerical instabilities. To avoid them, a strategy is to remove small structures during the simulation [Shinjo and Umemura, 2010]. But, those methods do not collect information on smallest droplets in atomization application. Introduction of Adaptive Mesh Refinement (AMR) in DNS is a first answer to this issue, it consists in refining unresolved area under numerical concept and focus on the interface between two phases instead of refining the entire domain. In dense spray, AMR tends to refine the entire zone and becomes as expensive as a full domain refinement. A solution is to transform the smallest droplets into point particles and remove AMR in this area. This strategy is called Eulerian-Lagrangian coupling [Herrmann, 2010a], it assumes that small droplets will no longer break during the simulation and that the Lagrangian models reproduce correctly the droplet transport. These physical assumptions are implemented to answer numerical issue and improve the computational cost. This Eulerian-Lagrangian coupling is based on transformation criteria that defines when an ICM structure has to be transformed into Lagrangian particle and when a Lagrangian particle has to be transformed back into ICM. The main purpose of the present communication is to provide a detailed analysis of the ICM to Lagrangian transformation criteria. The geometric criteria in [Herrmann, 2010a] is based on the droplet's volume,  $VOF$ :  $Re_q = Re_{q,VOF} = \left(\frac{3V_{VOF}}{4\pi}\right)^{1/3}$ . If  $Re_Q$  is equal or smaller than the mesh size,  $\Delta x$ , transformation is applied. Based on the conclusion of Shinjo et al. 2010 [Shinjo and Umemura, 2010] and previous work [Zuzio et al., 2018], implemented a second Lagrangian tracking method to transform intermediate size droplets with  $Re_Q \leq 4\Delta x$ . Those coupling methods focus on unresolved droplets (i.e. small droplets compared to the mesh size) under the assumption that they are spherical. Because two different Lagrangian methods are used, new transformation criteria is used to quantify the sphericity. This criteria is adapted to intermediate size of unresolved structures and it can be enhanced by adding breakup criteria. For this kind of relations some models can be used [Lasheras et al., 2002]. To ensure that the Lagrangian transport is physical, it is also necessary to take into account the droplet stability.

In this communication, authors resume existing geometric criteria, compare them and propose new ones. After the introduction of our numerical approach, the methodology to determine geometrical information globally and locally on our structures is described. Then, the accuracy of computation of the geometrical properties is analyzed on a spherical droplet. Next, their implementation on an oscillatory droplet case, following the Lamb theory, is studied to determine their capability to reproduce shape deformation. Then, we treat the case of a droplet in a pseudo-turbulent flow to produce surface variation and study the evolution of geometrical transformation criteria at low Weber number. Finally, a 3D airblast atomization has been performed to analyze the implemented criteria in a realistic case.

### III.4.2 Numerical Methods

Our in-house multiphase code *Archer*, is a DNS code which has strong experience in interface treatment and atomization process [Osmar et al., 2014]. It solves incompressible Navier Stokes equation on a cubic staggered grid where the pressure and the velocity are decoupled. Interface is tracked with

*CLSVoF, Coupled Level-set Volume of Fluid method* [Ménard et al., 2007], coupling a *Level-set* distance function [Tanguy and Berlemont, 2005] and a *Volume of Fluid* (VOF) method. The *Level-set* function  $\phi$  describes the interface at its zero level curve of a continuous function defined by the signed distance to the interface. To ensure that the function remains the signed distance to the interface, a redistancing algorithm is applied.

$$\frac{\partial d}{\partial t} = \text{sign}(\phi)(1 - |\nabla d|) \quad \text{where} \quad d(x, t, \tau)_{\tau=0} = \phi(x, t) \quad (\text{III.2})$$

The redistancing of the *Level-set* coupled with a sign function helps to determine the distance between various structures as it is shown on the top right part of the figure III.9a. The *CLSVoF* method uses a ghost fluid method in order to capture sharp discontinuities at the interface, it is second order on the curvature. Distance information are illustrated on the top left part of the figure III.9a. The *CLSVoF* is a second order method conservative in mass where the *VoF* represents the amount of each phase in a cell. A coupling ensures conservation of the mass, thanks to a robust advective scheme of the fluxes [Vaudor et al., 2017], its representation is illustrated on the down right part of the figure III.9a, all cells have a percentage of volume represented in orange, their amount of *VoF*. The surface of a structure  $S_{VoF}$  is computed by adding the surface contained in each cell  $S_{i,Vof}$ . This local surface is approximated by the surface of the plane obtained from the volume of fluid and the normal. The normal to the surface,  $\mathbf{n}$ , and the curvature,  $\kappa$ , are related to *Level-set* function, see equation III.3.

$$\mathbf{n} = \frac{\nabla \phi}{|\nabla \phi|}, \quad \text{and} \quad \kappa = -\nabla \cdot \mathbf{n}. \quad (\text{III.3})$$

The two main curvatures,  $\kappa_1$  and  $\kappa_2$ , at a given point of the surface are obtained from the work of Kindlmann et al. 2003 [Kindlmann et al., 2003]. Here we average the main curvatures over the surface of the structure. This computation is done by using the curvature of each cell pondered by the interface surface, see equation III.4.

$$\kappa_{1,S}(\phi) = \frac{\sum_i^{N_{cell,tag}} S_{i,Vof} \kappa_{1,i}(\phi)}{S_{VoF}} \quad \text{and} \quad \kappa_{2,S}(\phi) = \frac{\sum_i^{N_{cell,tag}} S_{i,Vof} \kappa_{2,i}(\phi)}{S_{VoF}}. \quad (\text{III.4})$$

Tag represents the cells of a given structure from a tagging algorithm. Information that are obtained at the interface of the structure are resumed on the down right part of the figure III.9a.

Viscous terms are discretized with Sussman algorithm. Projection method estimates spatial derivatives at a second order central scheme and convective terms are approximated by a fifth order WENO scheme. Pressure is obtained with a Poisson equation discretization and second order scheme is used. Sharp interface is described with a jump function for the pressure, density and viscosity in order to carefully describe all discontinuities. Eulerian-Lagrangian coupling is implemented in the in-house code with two Lagrangian tracking methods, as in Zuzio et al. 2017[Zuzio et al., 2018].

### Geometrical computation

To transform droplets into particles, geometrical properties are needed to characterize the structure. The *CLSVoF* method gives various information such as the total volume of a structure, the position of its interface, the distance to other interfaces, principal curvature or the total surface. Numerical algorithm have been implemented in the in-house code to recover geometric information, see figure III.9a for a graphical overview. To determine all the cells belonging to the same structure  $\mathbf{X}_{cell}$ , the tag algorithm of Herrmann 2010 [Herrmann, 2010a] is used. The center of mass of a structure  $\mathbf{X}_{struct}$  is obtained from the amount of *VoF*,  $\alpha_i$ , in a tagged cell centered in  $\mathbf{x}_i$ :  $\mathbf{X}_{struct} = \sum_i^{N_{cell,tagg}} \alpha_i \mathbf{x}_i$ . The strategy is to compute the equivalent radius that a structure would have if it was spherical. The *CLSVoF* method offer various possibilities and some are listed below. A first is to use the properties of the *VoF* to respect the mass conservation, and determine a  $R_{EQ,Vof}$ , similar to [Herrmann, 2010a]. The obtained equivalent spherical droplet is drawn in dashed green [figure III.9a]. An equivalent radius can also be calculated with the total surface of the structure  $R_{S_{VoF}} = \sqrt{\frac{S_{VoF}}{4\pi}}$ . One can also use *Level-set* properties to determine an equivalent radius based on minimal curvatures [equation III.5].

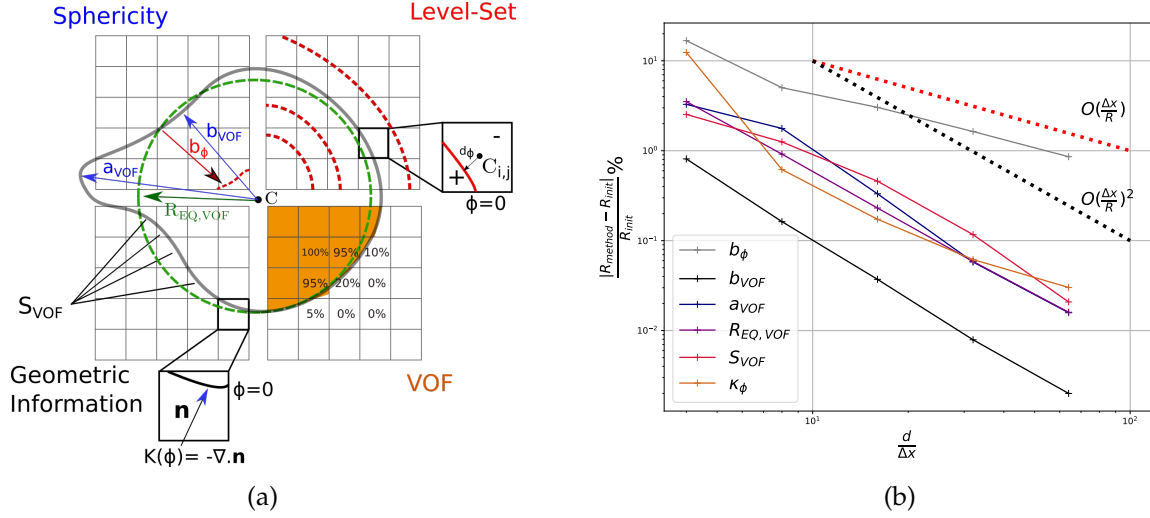


Figure III.9: (a) Information from CLSVoF Method, top-left: sphericity, top-right: distance, down-left: geometric information, down-right: VoF. (b) evolution of the accuracy for each geometrical parameter increasing number of mesh in the droplet.

$$R_\kappa = \frac{2}{|\kappa_{1,S}(\phi)| + |\kappa_{2,S}(\phi)|} \quad (\text{III.5})$$

The information of the CLSVoF method can also help to determine the deformation of a structure. In particular, we can compute the maximum and minimum distance to the center, noted here  $a$  and  $b$  respectively. They are illustrated on the top left part of the figure III.9a. A first method to obtain these distances is based on the volume of fluid ( $a_{VoF}$  and  $b_{VoF}$ ). Based on the tag algorithm, the maximal and minimal distance from the center of the structure,  $\mathbf{X}_{struct}$ , to the furthest and closest cell belonging to the same structure can be obtained with a simple distance calculation. This calculation does not give the exact distance to the interface but to the cell center containing the interface. Thanks to another property of the *Level-set*, the exact distance from the cell center,  $\mathbf{X}_i$ , to the interface in the cell can be calculated and it is represented on figure III.9a with the parameter  $d_\phi$ . This distance calculation is shown on equation III.6 for the maximal deformation,  $a_{VoF}$ .

$$a_{VoF} = \max_i (|\mathbf{X}_{struct} - \mathbf{X}_i| + d_{\phi,i}). \quad (\text{III.6})$$

To obtain  $b_{VoF}$ , the same algorithm is used. Deformation  $b$  can also be obtained as the maximum value of the *Level-set* inside a given simple structure. It is important to notice that  $R_{eq}$ ,  $a_{VoF}$  and  $b_{VoF}$  give accurate information when the center of mass is inside of the structure.

### Computation accuracy of geometrical properties

In order to better understand the reliability of each distance calculation, a simple test case is run before implementation of those calculation in sphericity calculation criteria. A single 3D static droplet is initialized at rest. The diameter of the droplet is 50% the domain length. The density ratio and viscosity ratio are set to 1. The droplet is initialized in the domain with the *Level-set* function. Then, the VoF is computed based on the *Level-set* as described in [Ménard et al., 2007]. The number of cells is increased,  $\frac{d}{\Delta x} = [3; 6; 12; 24; 48]$ , in order to determine the order of accuracy of each geometrical property. They must provide the radius of the initial droplet and errors are computed [equation III.7].

$$\frac{b_{VoF} - R_{init}}{R_{init}}, \quad \frac{a_{VoF} - R_{init}}{R_{init}}, \quad \frac{a_\phi - R_{init}}{R_{init}}, \quad \frac{R_{EQ,VoF} - R_{init}}{R_{init}}, \quad \frac{R_{S_{VoF}} - R_{init}}{R_{init}} \quad \text{and} \quad \frac{R_\kappa - R_{init}}{R_{init}} \quad (\text{III.7})$$

In order to analyze the influence of the initial position of a droplet with respect to the grid, 9 cases are studied by varying droplet's center on the 3D grid. The dispersion of the errors depending on the

initial position has only been observed for unresolved solutions  $d = 3\Delta x$ . As expected, refining the mesh reduces the influence of the initial position of the droplet. Here, for comparison, we average the errors over the 9 treated cases. The evolution of the error with respect to the mesh is given in figure III.9b.

From figure III.9b, one can conclude that the results of the in-house code,  $R_{eq}$ ,  $a_{VoF}$ ,  $b_{VoF}$ ,  $S_{VoF}$  and  $\kappa_\phi$  are all second order of accuracy while  $b_\phi$  is first order. In addition to the order of accuracy, one can see that for unresolved droplet,  $d \sim 3\Delta x$ ,  $b_{VoF}$  is 40 times more accurate than  $b_\phi$ . Thus, to study the minimal distance from the center of the droplet to the interface,  $b_{VoF}$  is used in the code. A non negligible error of over 1% is observed for  $a_{VoF}$ ,  $R_{eq,Vof}$ ,  $S_{eVoF}$  and  $\kappa_\phi$  for unresolved droplet. This error will be considered in the deformation analysis.

Implementation of a more accurate method [Müller et al., 2017], to determine the surface of a structure in a cell has been implemented in 2D, based on geometrical properties. This method proposed different order of accuracy but the computational cost of the second order accuracy is 10 times more expensive than current method. In addition, according to the knowledge of the author, 3D extension have not been developed yet and its implementation would be challenging. Since the computation based on the  $VoF$  is accurate even for unresolved droplet this extension has not been developed. The curvature has an initial non negligible error and this is due to the averaging process which is based on the local surface area [equation III.5]. It is important to recall that this global error is not related to local curvature errors, indeed, as seen on figure III.9b, the method implemented is second order of accuracy. This has been shown on previous work where the Laplace-Young law was verified for a single spherical droplet at rest [Aniszewski et al., 2014]. Geometrical parameters of the droplet are implemented in the determination of deformation criteria. These criteria are introduced in the following section.

### III.4.3 Droplet to particle transformation criteria

The hypothesis of transformation of unresolved droplets is based on various assumption. First, droplet has to be enough isolated from other structures. Then, if the droplet is small enough, it is transformed into particle. In another hand, if the droplet has an intermediate size,  $\sim 4\Delta x$ , sphericity criteria are studied to ensure that the droplet is spherical enough and that it will no longer break, in order to validate particle tracking assumption.

#### Calculation of the deformation

In [Herrmann, 2010a], a calculation of the deformation is based on the ratio of the maximal distance from the center of the droplet to the interface,  $a$ , divided by the equivalent radius of the droplet,  $R_{eq}$ , equivalent to  $\tilde{a} - 1$  in this communication. In [Zuzio et al., 2018], they define the deformation criteria as the ratio between the minimal distance from the center of the droplet to the interface,  $b$ , divided by the equivalent radius of the droplet,  $R_{eq}$ , equivalent to  $1 - \tilde{b}$  in this communication. In their work,  $b$  is calculated with the *Level-set*,  $b_\phi$ , but in our in-house code, the most accurate is  $b_{VoF}$ , then, we can not claim that our implementation is exactly the same that [Zuzio et al., 2018], but it has a similar purpose. Here, we refer to the equivalent radius as  $R_{EQ,Vof}$  introduced before. Both of those parameters are a global calculation and do not consider the fluctuation on the interface in their calculation. Here, two others parameters are defined based on the same geometrical parameters: the *Flattening* and the *eccentricity* [equation III.8].

$$\tilde{b} = 1 - \frac{b}{R_{EQ}}, \quad \tilde{a} = \frac{a}{R_{EQ}} - 1, \quad Flattening = \frac{b}{a}, \quad \text{and} \quad Eccentricity = \sqrt{\frac{b^2}{a^2}} \quad (\text{III.8})$$

All the deformation criteria defined in equation III.8 are set in order to remain always positive and converging towards 0 when the structure is spherical. With these deformation criteria, the surface ratio and curvature ratio are implemented to obtain more information on the local surface behavior that simple deformation criteria could not provide, see equation III.9.

$$\Delta\tilde{S}(\phi) = \frac{R_{EQ,Vof}}{R_{S_{VoF}}} \quad \text{and} \quad \Delta\tilde{\kappa}(\phi) = \frac{R_{EQ,Vof}}{R_\kappa}. \quad (\text{III.9})$$

Here both criteria are also set in order to converge to 0 when the structure is a sphere. For some geometrical examples of the curvature criteria we refer to [Canu et al., 2018]. The mathematical definition of the sphericity of a structure of volume  $V$  and surface  $S$  is given by  $\pi^{\frac{1}{3}}(6V)^{\frac{2}{3}}/S$ . In the surface criteria,  $\Delta\tilde{S}(\phi)$ , the surface of the droplet is already compared to the volume (recall that  $R_{EQ,VoF}$  is computed from the total volume of the structure). Then,  $\Delta\tilde{S}(\phi)$  criteria is redundant to the sphericity. Here we study the surface criteria given in equation III.9.

#### III.4.4 Lamb oscillation

Deformation of a droplet is studied on an academic test case [Aniszewski et al., 2014]. This validation case is well-known in the literature to find the linear decrease evolution of an oscillating droplet based on the Lamb's theory.

A 3D spheroid at rest is initialized in a  $64^3$  domain with 32 cells in its equivalent diameter. Physical parameters of the droplet are the surface tension,  $\sigma = 0.074 [kg.s^{-2}]$ , the viscosity ratio,  $\mu^* = 1.05$  with  $\mu_{liq} = 1.79.10^{-3} [m^2.s^{-1}]$  and the density ratio,  $\rho^* = 10$  with  $\rho_{liq} = 1000 [kg.m^3]$ . The initial deformation rate of the ellipsoid is initialized with the *Level-set* function. Here, we select  $z$  as the symmetry axis, then and the initial prolate spheroid is initialized such as the major axis is 1.15 times the minor axis. Due to the capillary force, the spheroid will oscillate, going from prolate to oblate with an oscillatory period of 0.05 s seconds, and, due to dissipation, tends to a spherical droplet where all deformation criteria should converge to 0.

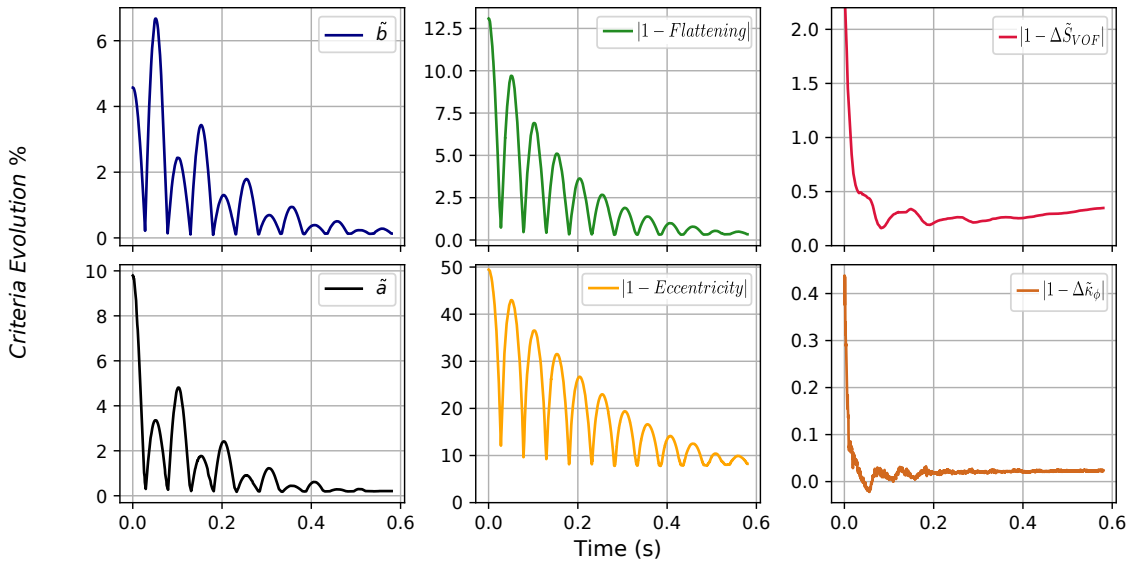


Figure III.10: Evolution of deformation criteria for Lamb oscillation.

In figure III.10 the time evolution of computed criteria are given. As expected, all parameters tend to the value obtained for a sphere. The prior convergence of the error study allows us to determine the error of calculation that is made for each parameter. It is the reason why the eccentricity criteria can not reach the expected value of 0, the error made on the maximal and minimal distance is drastically amplified, an error of 1% on  $a$  and  $b$  creates an error of  $\sim 10\%$  on the eccentricity. To our purpose that is to transform unresolved droplet into particle, this criteria is too sensitive to the errors on the distance and it can not be conserved, even if the trend gives interesting information on the deformation of the ellipsoid-spheroid evolution.

The morphological criteria introduced in [Herrmann, 2010a, Zuzio et al., 2018] only characterize variation of maximal or minimal deformation. To illustrate this point for  $\tilde{a}$ , we focus on the second and third oscillations on figure III.10 (i.e.  $t \sim 0.01$  s and  $t \sim 0.015$  s). According to the physical dissipation, the magnitude of the oscillation is expected to decrease. That can be observed on the *Flattening*

that decreases from 10% to 7%. Nevertheless, here we observe an increase of  $\tilde{a}$ . Same comment for  $\tilde{b}$  at third and fourth oscillation (i.e.  $t \sim 0.015$  s and  $t \sim 0.02$  s). Both parameters are not able to correctly estimate the decrease of the droplet's deformation and this is because they only focus on extreme values compared the equivalent radius, that is constant in this case. Then, each parameter can give different information on a structure, for example,  $\tilde{a}$  can evaluate the elongation of a droplet. However, from figure III.10, we can notice that for a given value of  $\tilde{a}$ ,  $\tilde{b}$ , eccentricity or *Flattening*, it is impossible to determine if the structure corresponds to an oblate or a prolate spheroid. To extract such information a combination of these parameters is necessary. Again at  $t = 0.01$  s or other oscillations, all shape deformations are well described, as seen with the eccentricity. Our goal is to provide the criteria that describes the best the deformation, the *Flattening* seems to be the better candidate.

Surface criteria converges to a threshold value before increasing next when the droplet is at rest. This increase remains below the error of 1% obtained in the accuracy computation, which can explain this deviation below 0.5%. It is interesting to note that from  $t = 0.3$  s, this criteria of deformation is not able to reproduce the oscillations. The evolution is more related to the local surface evolution due to local instabilities.

Curvature analysis show oscillations over and under the spherical final value. This criteria is the only one that can discriminate the prolate to oblate droplets. It can be seen that at rest, the value is still evolving. This can be due to the increase of the surface which is used to average the value of the curvature. With respect to the eccentricity which is the most sensitive method for the shape variation. The curvature shows small variations during the oscillations.

It has been seen that the magnitude of the local maxima at each period is not well described by deformation criteria introduced in [Herrmann, 2010a, Zuzio et al., 2018] which can misevaluate the droplet's shape. In order to diminish the influence of the error and to better characterize the shape of the droplet, the *Flattening* is conserved. This deformation criteria does not consider the equivalent radius of the spheroid reducing the sources of errors.

Nevertheless, the study of a spheroidal droplet is not enough to determine the stability of realistic droplets. In this study, we need to consider most complex droplets where the criteria based on the surface local properties, i.e.  $\Delta\tilde{S}_{Vof}$  and  $\Delta\tilde{\kappa}_\phi$ , could be more relevant. The following section is devoted to the case of a droplet in a turbulent-like carrier flow.

### III.4.5 Immersed Droplet in a HIT

The purpose of this study is to release a droplet inside of a decaying homogeneous isotropic turbulence (HIT) to observe fluctuations of velocity at the interface of the droplet and thus, local deformation. The simulation domain has  $64^3$  nodes, droplet diameter  $\frac{\Delta x}{d} = 32$ , with enough cells to reduce the error of calculation on each deformation parameter. In order to conserve one single droplet without breakage, the Weber number based on the initial velocity fluctuations is set to 1, density ratio and viscosity ratio are set to 1. Here the carrier flow is similar to the case from [Chen et al., 2019a], with the same flow field initialization. To obtain the surrounding flow, a single phase simulation is first performed to obtain a pseudo-turbulent flow. Next, a particle is added with no slip/no penetration condition, to avoid non-physical shear at the interface when we add the droplet inside of the single phase forced flow. When the flow is established around the particle, the particle is transformed into droplet and deformation can occur in the decaying HIT. One can find more information on this process in [Chen et al., 2019a]. Even if the turbulent flow is not fully developed, authors argue that this is not a relevant parameter for the study of geometrical parameters because we focus on the influence of the shear at the interface is our unique consideration. As it has been done before, the parameters of deformation will be compared to the equivalent radius. Their evolution must give us information on the current shape of the droplet, and its stability.

The evolution of all parameters can be split in three distinct steps, according to the results of the simulation. Those steps are illustrated with results of the droplet shape [figure III.11]. Intermediate value for each step have been selected and initial droplet released have been added. First step, under the influence of the surrounding flow, the droplet deformation strongly increases till a local maxima at  $t^* = 0.0012$ . After reaching its maximal deformation, it oscillates and reaches a pseudo-equilibrium, from  $t^* = 0.0012$  to  $t^* = 0.003$  which is considered as the second step of the droplet's shape evolution.



Figure III.11: From left to right, initialization ( $t^* = 0$ ), step 1 ( $t^* = 0.0005$ ), step 2 ( $t^* = 0.0015$ ), and step 3 ( $t^* = 0.0035$ ).

Step 1 and 2 on figure III.11 show clearly a non spherical shape due to carrier flow influence. In third step, the droplet moves toward its spherical initial shape and the surrounding fluid will no longer deform the droplet. During this step the droplet follows simple transport within the domain with small oscillations.

On figure III.12, the evolutions of all criteria with respect to the spherical shape initialization are displayed as a function of the dimensionless time  $t^* = t/t_c$ , where  $t_c$  is the capillary time  $t_c = \frac{\mu_{carrier} V_{RMS}}{\sigma}$ , and  $V_{RMS}$  the initial root-mean-square velocity of the single phase flow. All criteria are analyzed based on these three steps.

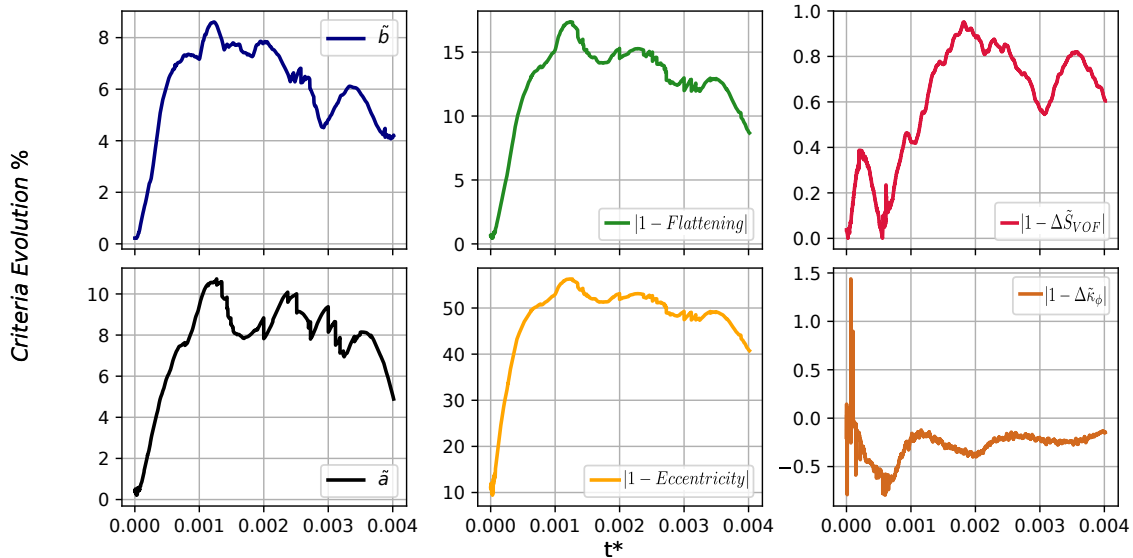


Figure III.12: Evolution of deformation criteria with respect to the dimensionless time for a droplet immersed in a HIT

One can observe on figure III.12 that  $\tilde{a}$ ,  $\tilde{b}$ , *Flattening* and eccentricity exhibit a similar behavior for each steps.

These parameters increase under the motion of the surrounding flow till a maximum value at  $t^* = 0.0012$ , as expected, they characterize accurately the deformation of the droplet. Then, a plateau is reached and one can see small variations on the curve, representing the surface oscillations of the droplet shape, from  $t^* = 0.0012$  to  $t^* = 0.003$ . Only noticeable difference is the order of magnitude of the variations of deformation criteria. From the simulation, we observed that the influence of the flow on the droplet only transports it during step 2 and this is mainly the reason of those variations. After  $t^* = 0.003$  no breakage can then occur since the droplet is only transported.

For  $\tilde{a}$  and  $\tilde{b}$ , maximum and minimum of variation are not synchronous, this phase difference is due to the alteration of maximum and minimum as explained for the prolate-oblate variation on the ellipsoid case. Discontinuities are observed in the time evolution of  $\tilde{a}$  and not on  $\tilde{b}$  which is relevant with the accuracy of each parameter [figure III.9b]. Their impact is observable on the results of the *Flattening* and the eccentricity. Even if these discontinuities do not affect the general

conclusions, improvement on this distance calculation has to be done and this could lead to have a value of eccentricity able to converge towards 0 for spherical structure.

As mentioned before, the surface and the curvature are introduced in order to highlight local surface oscillations. It can be observed that these criteria exhibit a different behavior during step 1, i.e. till  $t^* = 0.0008$ . This can be understood by the presence of a strong shear at the interface. During first step of  $\Delta S_{VoF}$ , its evolution reaches a local maximum at  $t^* = 0.0004$  and then decreases to reach minimal value. This shows that this criteria can provide other information. Our guess is that the surface criteria can provide information on the stability of the droplet determining impact of the strong shear at the interface. Nevertheless, the second step shows that similar variations are obtained compared to global deformation parameters. This criteria must be studied on a wide range of structures to determine if it is relevant. Similarly to the surface,  $\Delta \tilde{\kappa}_\phi$  presents strong variations due to the initial shear at the interface during step 1. A minimum is obtained before the second step, at  $t^* = 0.0005$ . Even if deformation keeps increasing,  $\Delta \tilde{\kappa}_\phi$  decreases. This can be understood if we assume that the shear decreases at the interface as expected in decaying HIT. Thus, this parameter can give information on a decrease of local instabilities on the surface. It is also observed for  $\Delta S_{VoF}$  and characterizes the end of the strong increase of the deformation for other parameters. It is interesting to notice that the curvature gives negative values. This is explained because the local surface can be locally convex and is not anymore purely concave as for the previous case where the structure were assimilated to a spheroid. Shape evolutions of the droplet are well characterized by all the distance parameters and exhibit a similar behavior. For the surface and the curvature, it is complicated to extract information on the stability of the droplet. A test on a real application has to be carried out to study those criteria on a wider range of droplets and then, they could be considered as stability criteria.

In the next section the criteria are applied to an airblast atomizer and the focus will be on the surface and curvature criteria for a wide range of droplets of undetermined shapes at a selected time of the simulation. Both criteria are coupled with the *Flattening* which is selected as a reliable criteria for the deformation.

### III.4.6 Airblast atomizer

To apply our local and global deformation criteria on a real application, we used the results of a planar sheet airblast atomizer [Mukundan et al., 2019a]. Details on the configuration can be found in its communication. Here we analyze with our criteria a time step of this atomization process [figure III.13a].

On top figure III.13b, a scatter of the criteria selected in our previous discussion, i.e. *Flattening*, surface and curvature, is given for all the liquid structures that are observed. The marker size represents their radius expressed in  $R_{EQ,Vof}$ . Red color represents the droplets below the threshold value  $R_{EQ,Vof} < 2\Delta x$ , according to the size criteria of Ling et al. 2015 [Ling et al., 2015] In the Eulerian-Lagrangian method these droplets are transformed due to the size criteria. In this paper, we focus on intermediate sizes.

On figure III.13b top, we observe a relative clear correlation between surface and *Flattening* going from low  $\Delta S_{VoF}$  and *Flattening* to high  $\Delta S_{VoF}$  and *Flattening* in a parabolic evolution. Large structures, defined for high  $R_{EQ,Vof}$ , are located next to highest *Flattening* value. In general, these structures are large ligaments as we can observe on the snapshot of the simulation, due to their elongation, we expect such a value of *Flattening*. It is important to recall that by definition the maximal value of the *Flattening* is 1. These structures appear in dense regions close to the primary atomization area. According to their size, their shape and their position in the simulation, they are not considered for the transformation. We can observe that most of the small droplets that have to be transformed based on the size criteria, i.e. red marker on figure III.13b, are located next to 60% of *Flattening*. Due to their size, these droplets are not well treated by the ICM method. Nevertheless, the *Flattening* value is too large, meaning that these droplets are not completely spherical. The Lagrangian tracking could not be as accurate as expected to transport them. Intermediate size structures are displayed all along the *Flattening* criteria and it shows that this deformation criteria is able to select the spherical droplets in real application.



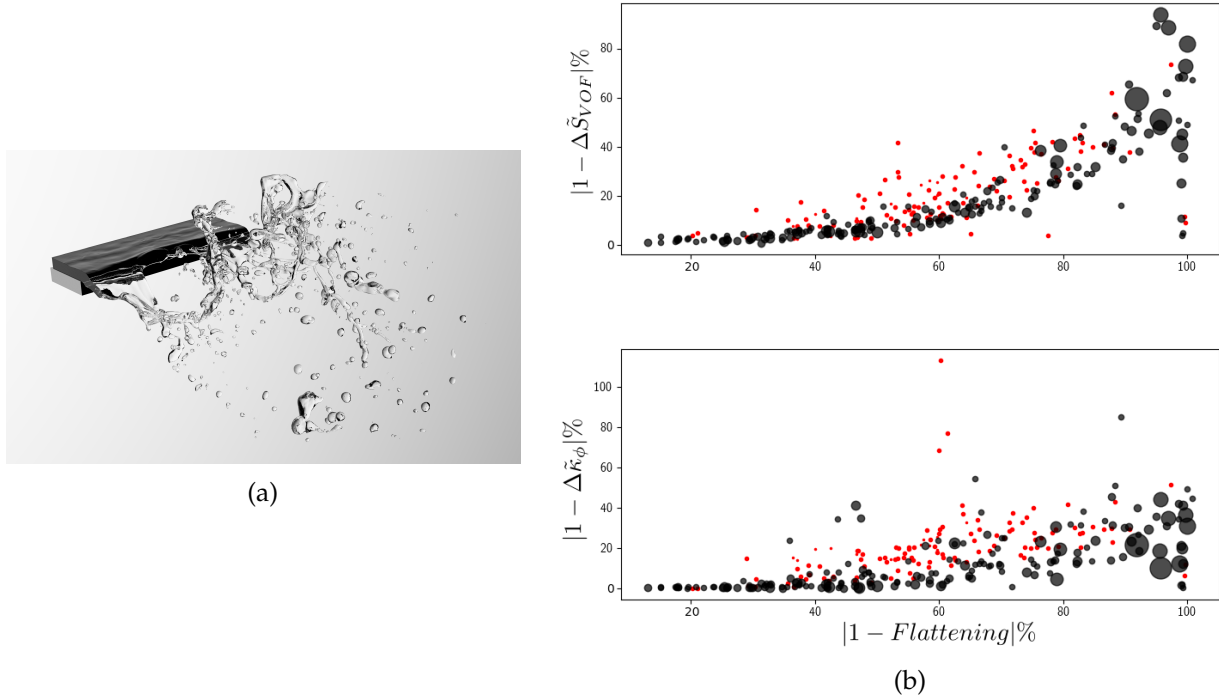


Figure III.13: (a) Airblast atomizer snapshot. (b) Scatter of structures in terms of *Flattening*,  $\Delta S_{VoF}$  and  $\Delta \tilde{\kappa}_\phi$

At this point of the analysis, it is complicated to conclude on the stability of a droplet from the *Flattening*– $\Delta S_{VoF}$  coupling. Authors plan to go further on the analysis.

On bottom figure III.13b,  $\Delta \tilde{\kappa}_\phi$  scatter is showed. We can observe small droplets with unrealistic  $\Delta \tilde{\kappa}_\phi$  over 60%. These values are given by the error on computation of the geometrical proprieties. While figure on the top shows a strong correlation between  $\Delta S_{VoF}$  and the *Flattening*, the correlation between  $\Delta \tilde{\kappa}_\phi$  and the *Flattening* is less pronounced. However, below 30% of *Flattening*,  $\Delta \tilde{\kappa}_\phi$  is close to 0 and this is expected for quasi spherical droplets which are expected stable. In the future work an analysis of the droplets one by one will be done in order to better understand the role that plays the curvature in this study.

## Conclusions

Geometric information on structure have been implemented in the code and their accuracy has been validated on a simple test. Then, from those geometric information, deformation criteria have been built and tested on simple case to study their evolution with respect to deformation of the shape of a spheroid and oscillations on the surface of the droplet. All of the criteria based on the distance showed a similar behavior in the representation of the deformation of the droplet. Nevertheless, the *Flattening* has been selected because it represents most accurately the deformation of the droplet and its computation is very accurate. Different behavior have been observed for the surface and curvature criteria.

In order to go further, the three later criteria have been applied to a wide range of droplets, generated by an airblast atomizer simulation. The surface showed a similar evolution with the *Flattening* while the curvature behavior provides less clear tendency.

Due to the definition of the surface that has been implemented in *Archer*, it is the most reliable criteria to determine the deformation of a droplet and to study complex geometries, nevertheless, at the current level of developments, the *Flattening* remains the best criteria to determine if unresolved structures of intermediate size,  $\sim 8\Delta x$ , are spherical or not. In order to provide a better description of the deformation and the stability, the coupling between the surface and the curvature criteria is actually under study.

Indeed, this criteria will have a strong influence on the area of transformation of a droplet into a particle inside of the computational domain. A strong requirement will be to study this dependence on a convergence study of a real atomization case on the simulation results. Its influence on the drop size distribution, the vorticity in the secondary atomization area and the enstrophy are to study. Eventually, such as our purpose is to qualify a structure with as less information as possible, a physical criteria must be later coupled with those numerical and geometrical criterion.

## Acknowledgments

This work was granted access to the HPC resources of IDRIS, TGCC and CINES under the allocation A0012B1010 made by GENCI (Grand Equipement National de Calcul Intensif). The authors would thank Anirudh Asuri Mukundan for sharing its airblast numerical results and Alexandre Poux for the fruitful exchanges. We also thank the Normandy region for their funding of this research.

## III.5 Reconstruction of the interface

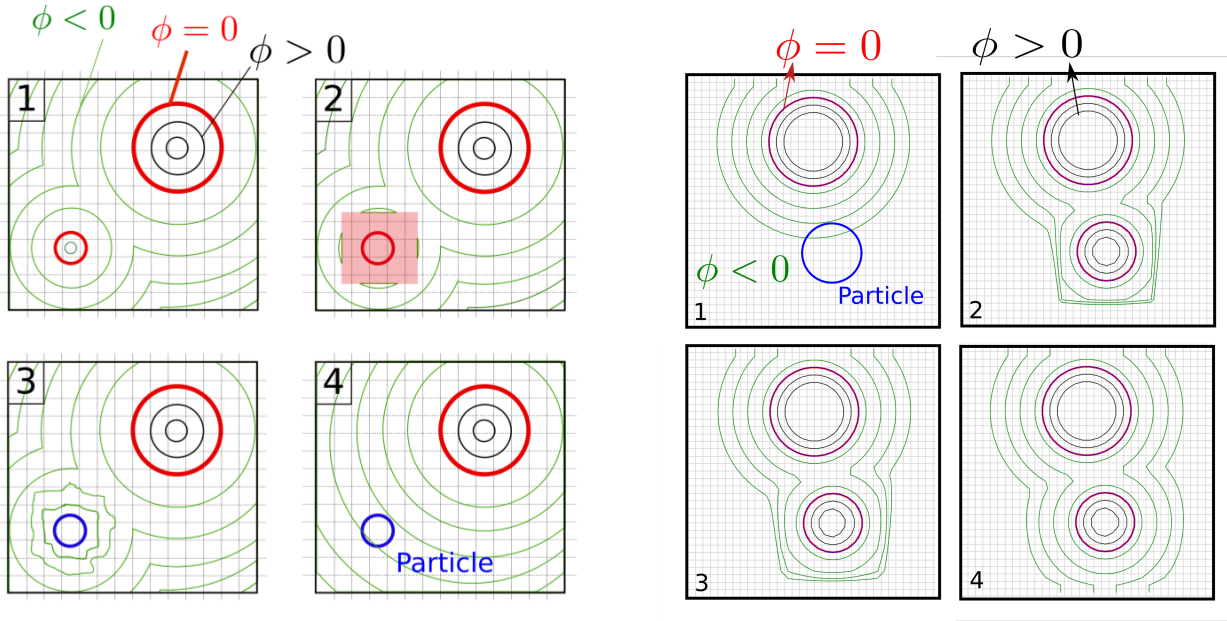
A droplet candidate to transformation or a particle that get in the vicinity of an interface implies a modification of the velocity/*Level-set*/*VoF* Eulerian fields. The modification of those fields is required in order to go from resolved Eulerian interface toward particle and vice versa. To consider the exact influence of the particles volume fraction, a voidage coefficient can be introduced in Navier Stokes equation [Evrard et al., 2019]. In our situation, the voidage coefficient is not introduced in the Hybrid strategy and the focus is hold on the reconstruction of the interface. This section describes the strategy to rewrite the Eulerian fields when a droplet is transformed into particle. Then, we describe the reverse transformation, particle toward droplet.

### III.5.1 ICM to Particle

In transformation, the main challenge is to conserve general atomization physic even though we modify Eulerian fields locally. In the literature, there are as much method of reconstruction as developed ICM method. For example in [Herrmann, 2010a] they have to remove the refined *Level-set* on the AMR grid. In [Tomar et al., 2010] they remove a *VoF* function from a refined grid. Numerical code using *VoF* method have a lighter treatment than methods using the distance function when reconstruction of an area is needed. A configuration closer to our ICM method is in [Zuzio et al., 2018] where they use a CLSVoF method with AMR. In our configuration, we do not use yet AMR and we focus on removing the CLSVoF information at particles' location. *Archer* initializes the volume of fluid onto the *Level-set*, and, the distance function is a sensitive function to treat with which explains the redistanciation at every transformation that increases the cost of the hybrid coupling. To ensure mass conservation we use the volume of the droplet to compute an equivalent radius;  $R_d = [\frac{3Vol}{4\pi}]^{1/3}$ , identified from tagging algorithm. Then we set the particles' radius to  $R_p = R_d$ . In this subsection we detail the procedure to remove the droplets that validate transformations' criteria in order to be transported with Lagrangian techniques ensuring the mass conservation.

The procedure to remove the droplet follows 4 steps [figure V.2a]. On the first image, two droplets are represented with the *Level-set* field, the interface is represented in red and the positive/negative distance to the interface are represented respectively in black/green. We recall that inside the droplet the *Level-set* is positive to represent the liquid phase. Since both droplets are spherical, the only criterion that validates the transformation is the number of cell across the diameter and only the small droplet is transformed. In order to improve the transformation efficiency, we select an area around the droplet to reconstruct the Eulerian fields, this area is centered on the droplet and has a length of two droplets' diameter. During this iteration, the *VoF* field is updated: the cells that belongs to the droplet, identified with the detection algorithm, are switched to 0. Finally, we have to modify the *Level-set* field, which is a challenging step because we have to ensure conserving its distance property. We detail the methodology to update it.

To ensure that the droplet totally vanished from the *Level-set* point of view, we have to determine the right equation to implement in our code. This equation depends on the number of structures in



(a) Scheme representing the transformation of a droplet into a particle with reconstruction of the distance function. (b) Scheme representing the transformation of a particle into a droplet with redistancing.

Figure III.14: Illustration of the reconstruction of the Eulerian field after transformation from droplet toward particle and vice versa.

the surrounding, the area of rewriting and the number of iterations used in the redistance algorithm. We tried various equations for two main methods. The first method consists in the modification of the *Level-set* only where the box is designed, the second is to update the *Level-set* in the entire domain.

Using the first technique, we recover *Level-set* box sides values and set this value to the entire area to create a plateau area. The main issue of this method is that when it is surrounded by a lot of structures, it can recreate a positive *Level-set* and small structures can appear which is not desired. However, when the droplet is far from other interface, this method works fine. In order to improve the efficiency of the method when there are a lot of surrounding structures, we used an inverted sphere equation (bubble) and rewrite the *Level-set* in the box. The radius of the sphere is set to 3 particles' radius and it permits to avoid mass reconstruction in most of the simulations but we experienced some issues in massively MPI calculation. Due to the complexity to correct these issues in such configuration, we decided to rewrite the entire *Level-set* domain when we face a complex simulation such as highly atomized jet. After some tests, the function that is used to rewrite the domain is a sphere equation based on the droplets' position/radius, we use it as follows:

$$\phi(\vec{x})^{rec} = \min(\phi(\vec{x}), \sqrt{(\vec{x}_d - \vec{x})^2} - 6 \cdot R_d). \quad (\text{III.10})$$

It ensures that we do not modify the liquid *Level-set* in the domain. Then, the redistancing algorithm is used over various iterations until the property  $||\nabla\phi|| = 1$  is recovered in the domain. Both strategies have their advantages, the second strategy can be expensive when the load of the processor is relatively high, see the conclusions obtained on the speed up analysis of the reconstruction subroutine [section III.2], but it ensures that no mass is recreated in complex simulation. At the end of step 2, the droplet has been entirely removed from the Eulerian field, a special care is hold for the velocity field and section III.6 is dedicated to its presentation. Finally we see that the *Level-set* distance function evolves and that the particle is not seen by the distance function, see image 4 of figure V.2a.

### III.5.2 Particle to ICM

The transformation from particle to droplet is more complex because the challenge is to reconstruct an unresolved droplet using the *Level-set* field ensuring the mass conservation. The first part

of this subsection details the transformation from particle to droplet pointing the issue with the classic reconstruction method. The second part of this subsection details the method that has been implemented to improve the mass conservation for those unresolved droplets.

### Description of the procedure

The distance criterion determines if a particle is transformed in droplet, we use the *Level-set* information to compute the distance from the interface [section III.3]. When the particle validates this criterion, it is transformed into a droplet, it is schemed on the two first snapshots of figure III.14b. An area centered on the new droplet is determined to reconstruct the Eulerian fields. The first step is to reconstruct the *Level-set* field, is it straightforward since we compute it from a sphere equation using particles' position/radius. Then, the *VoF* is computed from *Level-set* where  $\phi > 0$ , we determine the cells that are cut by the *Level-set* 0, where we have to calculate the volume of liquid to define *VoF* value. In other cells, the volume fraction is directly set to 0 or 1. We ensure  $||\nabla\phi|| = 1$  with the redistanciation algorithm outside the square domain. The redistanciation algorithm evolution is showed on images 3 and 4 figure III.14b. The momentum conservation from particle toward droplet is ensured and detailed in section III.6. We observe that using the radius of the particle to reconstruct the droplet leads to a strong mass fluctuation in the domain and that mass conservation is broken. We detail it in the next part of this section.

### Mass conservation improvements

The mass conservation when a droplet is reconstructed with few cells across its diameter can be challenging and it can lead to a variation of the mass in the domain. For the droplets below  $d_p/\Delta x < 3$ , we observe wide variation of more than 1.2 times the initial droplet volume. To study this mass variation, we analyze the transformation of a particle toward a droplet for a range of grid resolution. The purpose is to quantify the accuracy of the volume conservation against the number of cells across the diameter. The accuracy is calculated using the volume of the particle and the volume of the reconstructed droplet:  $\frac{|V_d - V_p|}{V_p}$ . A first study has been done to determine the general behavior of the method, that is not represented here. Thanks to this analysis, we observed that the volume was always overestimated in the reconstruction which allows us to use absolute error without modifying the analysis of the results.

The particle's position on a grid determines the quantity of volume occupied per cell. For example a particle centered onto one cell with a diameter  $d_p = \Delta x$  is defined only in one cell while a particle centered on the face's cell is defined on two cells. Particle position modifies the mass conservation at transformation and we modify the position of the transformed particle to study it. The resolution of the simulations is evolving from  $\frac{d_p}{\Delta x} = [1 : 12]$  varying  $Nx$ , and the position of the particle is initialized from  $\vec{X}_p = [0, 0, 0], [0, 0, \Delta x/2], [0, 0, \Delta x] \dots [\Delta x, \Delta x, \Delta x]$  centered in a cubic box of  $Lx = 4 \cdot d_p$  [m], we have a total of 27 initial positions.

The simulation is performed for two iterations, first to generate the particle and then to transform it. From the 27 positions, we study the averaged, minimal and maximal reconstruction error. We expect to observe a reduction of the gap between the extrema values at higher mesh resolution. We first comment the results obtained when the radius of the droplet used in the sphere equation to reconstruct the *Level-set* is the one of the particle. Then, we describe the two methods that are implemented to reduce the error on the mass conservation.

As we can observe on top figure III.15, the classical reconstruction, (triangles), shows that the second order accuracy is well recovered and that the more refine the simulation is, the lower is the error [Vaudor et al., 2017, Mukundan et al., 2019b]. The influence of the initial particle position does not modify the volume variation. For under resolved droplets,  $d_d/\Delta x < 4$ , we observe an overestimation of droplets' volume of approximately 1.2 times the initial volume. Then, increasing the numerical resolution decreases the gap between minimal/maximal value, and reduces the overestimation of the volume. The finest resolution provides an error smaller than 1%. It shows that we need to improve droplets reconstruction in order to reduce the inconsistencies that are observed in the mass

conservation. We propose two methods, an *ad hoc* method that diminishes the droplet's reconstruction radius and a method using a minimization algorithm.

The first method that is presented is the method using a retraction factor on the radius of the particle to reduce the mass creation. This new radius is simply called  $R_p^*$  [m], in this subsection. The new radius is obtained with  $R_p^* = R_p - \frac{1}{4}(\Delta x)^3$ . The coefficient  $\frac{1}{4}$  is based on the results obtained from a parametric study, weighed by the volume of the cell. The results obtained for this new method are displayed on bottom figure III.15. For the coarsest simulation, the mass variation is reduced of an order of magnitude and the averaged value is  $\approx 4\%$  of error. Then, the influence of this retraction decreases, but, always reduces the error with respect to the classic method. The influence of the retraction is less visible when the mesh increases and the second order of accuracy is recovered. The drawback of this method is that it is more sensitive to the position of the particle when transformed, as seen by the wideness of the results at low resolution. But generally, we observe that the volume's overestimation is reduced and higher accuracy is obtained, moreover, it does not require any additional computational cost.

The second implemented method uses an iterative Newton's method. The purpose of this method is to determine a numerical radius for the *Level-set* sphere equation in order to be conservative on the volume. An iterative method is used to converge toward the most accurate reconstruction's radius. First we describe its implementation in *Archer* and we observe its accuracy in a second time.

To iterate on the exact reconstruction radius that permits to have the exact volume, we have to reconstruct the *Level-set* on the domain and compute the droplets' volume. In *Archer* we implemented the Lagrangian and Eulerian loops separately, and we send a group of particles to the reconstruction subroutine to avoid multiple iterations between Eulerian and Lagrangian solvers. Moreover, the MPI strategy is totally different in the Lagrangian and Eulerian solver and it is simpler to send a packet of particle using the ghost domain [section II.2]. Then, the iteration from particles information toward Eulerian field is complex to handle because it breaks the methodology, forcing the exchange for each particle between Lagrangian and Eulerian loops. To avoid breaking Lagrangian loops and to conserve the strategy to send a group of particles, we create a fictitious Eulerian grid. This fictitious domain permits to generate a *Level-set* and to recover the exact reconstruction's radius without going out of the Lagrangian loop. Finally, we update the particle's radius and send the group of particles toward Eulerian subroutine that update the *Level-set* and the *VoF* fields.

Since those algorithms can be time-consuming, the number of iterations and the accuracy are fixed. We evaluate accuracy evolution with iterations' number at fixed mesh size;  $\frac{d_p}{\Delta x} = 4$ , for the 27 positions with fixed accuracy criterion at  $10^{-5}$ . We observe that the area of accuracy is reached after 9 iterations [figure III.16]. Below this number of iterations, we observe that the algorithm iterates until reaching desired accuracy, we observe the iterating process at  $N_{iter} = 3$  and  $N_{iter} = 2$ . Since the desired accuracy is fast to obtain, we set the number of iterations of this algorithm to 10.

Then, we study the convergence of this algorithm conserving the same accuracy criterion/number of iterations [*Newton* on bottom figure III.15]. We see that the accuracy for volume reconstruction is drastically improved. For the coarsest simulation, the best scenario is reaching an accuracy of  $10^{-4}\%$  of mass variation. The average value is of the order of  $\approx 2 \cdot 10^{-2}\%$  which is satisfactory for this resolution, with respect to the  $\approx 20\%$  of the classical reconstruction. Then, the average error is decreasing and improve the results of various order of magnitude with respect to the two other methods. At  $d_p/\Delta x = 9$  a jump of accuracy is observed, more iterations are required.

The Newton iterative method drastically improves mass conservation and must be used to accurately treat particle toward droplet transformation. It is implemented in the code and we fixed the number of iterations to 20 in order to avoid the jump observed on bottom figure III.15 and an accuracy of  $10^{-5}$ . We know that this algorithm has a relative cost of computation, thus we also conserved the numerical reconstruction  $R_p^*$  to give the opportunity to switch between them.

### III.6 Reconstruction of the velocity field

To ensure momentum conservation at transformation from droplets to Two-way and One-way methods and vice versa, the velocity field must be updated [Ling et al., 2015]. In the context of FRP

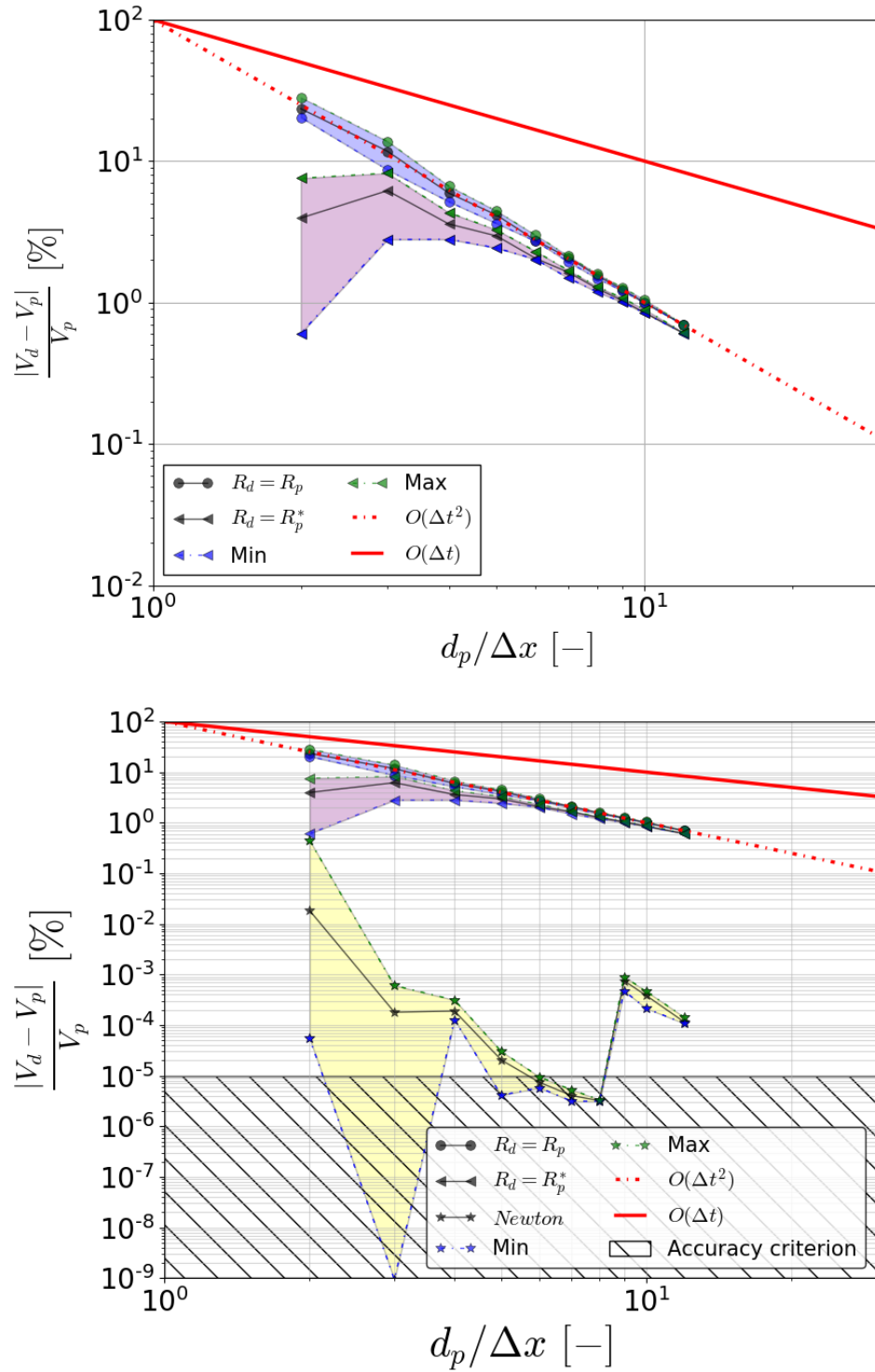


Figure III.15: Top figure: evolution of the mass variation when particle is transformed into resolved droplet for the classic *Archer* reconstruction: triangles markers, and a reconstruction with retraction on the radius: circles markers. Bottom figure we add the Newton minimization algorithm with stars markers.

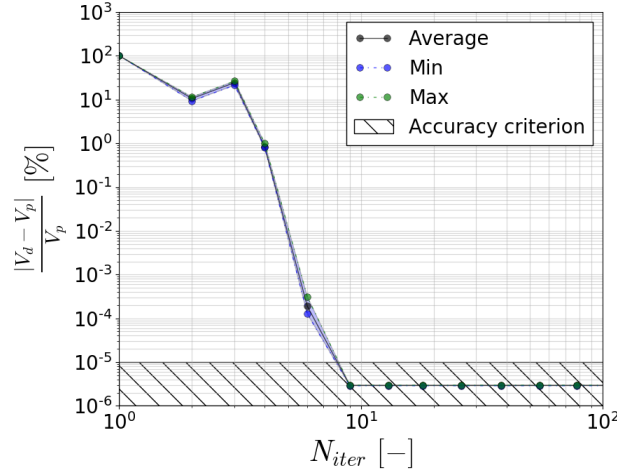


Figure III.16: Evolution of the mass variation when particle is transformed into resolved droplet with several iterations in Newton algorithm at fixed accuracy criterion:  $10^{-5}$  at fixed resolution  $d_p/\Delta x = 4$ . Average, minimal and maximal errors are represented in black, blue and green circles markers.

(IBM), particle's interface is represented by smooth Eulerian-Lagrangian interactions at particles' interface. From the literature, when droplet transforms toward FRP, no special care is hold on the reconstruction of the velocity field [Zuzio et al., 2018]. Moreover, the velocity field is numerically smoothed within the reconstruction of the divergence free forcing,  $\vec{\nabla} \cdot \vec{u} = 0$ .

Then in *Archer* the velocity field is rewritten when the transformation is as follows:

- all particles tracking toward ICM,
- ICM toward Two-way and One-way method,

and it is conserved when going from ICM toward FRP. In this section, we focus on the transformation from ICM toward particle, in the next section, we focus on the transformation from IBM (FRP family) toward ICM on a head on collision application. We describe the strategy developed in [Ling et al., 2015] to reconstruct the velocity field for all transformations. Then, we detail the application that we used to validate momentum's conservation.

### III.6.1 Velocity field reconstruction

The transfer of droplet to particle's momentum and reverse transformation can induce error of calculation, as the velocity fields that the particle/droplets see are not the same. For example, the velocity of the carrier phase that transport the particle is not similar to the one inside a droplet. It can modify the motion of the droplet and then, the momentum's conservation is not respected. It is the same for the particle, the flow that is seen inside the droplet is not similar to the flow created by a particle.

Following [Ling et al., 2015], we first describe the reconstruction from droplet toward particle. The first step is to determine an area of reconstruction, they consider a square/cube (2D/3D) centered on the droplet with a length of two droplet's diameters. They use velocity nodes at square/cube sides and update the area with first order linear interpolation, and divergence free is recovered:

- The velocity at the boundaries of the cube used to interpolate the reconstructed velocity respect the divergence free assumption,
- the divergence components  $\partial u_{g,x}/\partial x$ ;  $\partial u_{g,y}/\partial y$  and  $\partial u_{g,z}/\partial z$  are constant within the reconstructed area since we use a linear reconstruction for each velocity component.

Since this reconstruction is done in order to conserve the momentum, it should not be considered in the overall mass conservation calculation. The reason is that the reconstruction of the velocity field



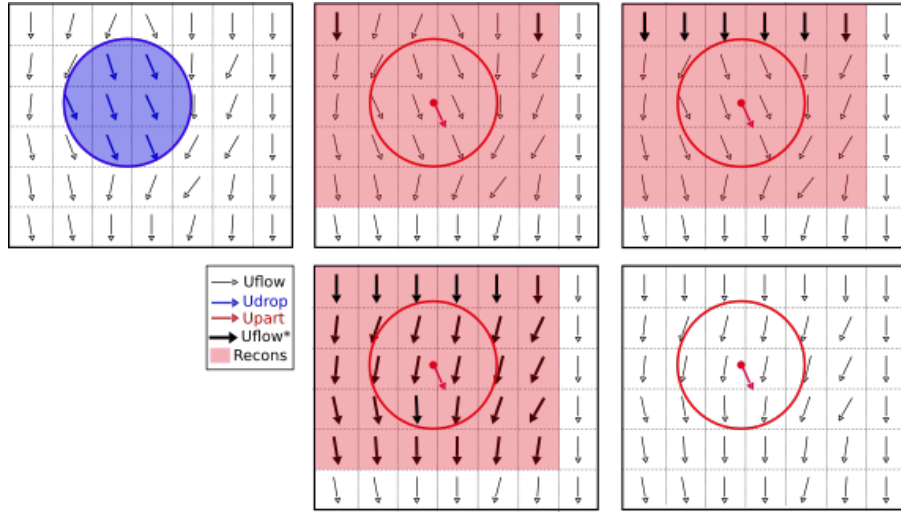


Figure III.17: Scheme of reconstruction of the unperturbed velocity when resolved droplet is transformed toward Two-way particle on collocated grid, inspired from [Ling et al., 2015].

around the droplet is considered to be a mixed state between gas and liquid that has only one purpose: to enhance the calculation of the transport of Lagrangian particle. We describe the methodology to linearize the velocity field [figure III.17].

At droplet transformation, we define a square area around the droplet where we use its sides to reconstruct the velocity field. In this example we only show the reconstruction for one component of the velocity field. Then we linearize the velocity field from both sides of the area until it has been entirely updated. It permits to avoid inconsistencies for Two-way and One-way methods.

For reverse transformation, we reconstruct the velocity field only inside the droplet. The area of reconstruction is determined after *Level-set* reconstruction and we can simply determine it using its distance properties. There are two strategies of reconstruction with respect to the approach that we use, we detail them.

For One-way and IBM approaches, we fix the velocity of the particle to be the one of the velocity field inside the droplet ( $\phi(\vec{x}) > 0$  with  $K = [x_0, x_1] \times [y_0, y_1] \times [z_0, z_1]$ ):

$$U_p \rightarrow u_{p,K}.$$

For the Two-way approach, it is noted that using this velocity breaks momentum conservation through energy overestimation [Ling et al., 2015] since we include the self induced particle's perturbation  $\vec{u}$  through:

$$\vec{u}_{f@p} = \vec{u}_{f@p} + \vec{u}_{f@p}.$$

They propose to compute an intermediate velocity that filters the particle's disturbance,  $\vec{u}'_p$ , from  $\vec{u}_p$ :

$$\rho_p Vol_p [\vec{u}'_p - \vec{u}_{f@p}] = \rho_p Vol_p [\vec{U}_p - \vec{u}_{f@p}] + \int_{\Omega} \rho_g [\vec{u}_{f@p} - \vec{u}_{f@p}] d\Omega. \quad (\text{III.11})$$

The second term of right hand side equation III.11 represents the momentum of the perturbed flow field by particles over the particle occupied volume,  $\Omega$ . An approximation of this quantity is proposed in [Ling et al., 2015] considering the fluid volume displaced by the particle equal to particle's size:

$$\int_{\Omega} \rho_g [\vec{u}_{f@p} - \vec{u}_{f@p}] d\Omega \sim \alpha \rho_g Vol_p [\vec{U}_p - \vec{u}_{f@p}]. \quad (\text{III.12})$$

The dimensionless parameter  $\alpha$  is the ratio between the volumes of the virtual fluid and the droplet representing the added mass and history forces. In our configuration, it only represents added mass force and following [Ling et al., 2013] we can approximate its value to  $\alpha = 4$ . Then we have:

$$[\vec{u}'_p - \vec{u}_{f@p}] = [\vec{U}_p - \vec{u}_{f@p}] + \alpha \rho_g \frac{\rho_g}{\rho_p} [\vec{U}_p - \vec{u}_{f@p}]. \quad (\text{III.13})$$



In their work, they assume that  $\vec{u}_{f@p} \approx \vec{\tilde{u}}_{f@p}$  which simplifies the treatment of the perturbed velocity:

$$[\vec{u}'_p - \vec{u}_{f@p}] = [\vec{U}_p - \vec{u}_{f@p}] + \alpha \rho_g \frac{\rho_g}{\rho_p} [\vec{U}_p - \vec{u}_{f@p}]. \quad (\text{III.14})$$

From the importance of the correction on the self-induced particle velocity [section II.3], we can think that their implementation improve the momentum's jump at tranformation toward ICM droplet but does not ensure a perfect momentum's conservation. Thus, we suppose that the corrections implemented in our particles' interpolation velocity improve the treatment of the velocity field's reconstruction. Nevertheless, we expect that increasing the particles' momentum redistribution area leads to a convergence toward an accurate momentum's conservation.

### III.6.2 Configuration

We studied the transformation from droplet to particle in the free-falling sedimented particle [subsection II.3.1]. This test case is ideal because we can compare our results against the results obtained for droplets/particles [section II.4]. The main advantage of this simulation is that particle tracking method has been studied on it, weakness of the ICM has been highlighted, a reference solution is known and the deviation to this reference is also known. Then, we can evaluate the particle tracking method's influence on the terminal free-falling velocity of the transformed droplet. Moreover, it permits going further on the conclusions obtained in section II.4 that showed the difficulty to determine the ideal method in the range  $d_p/\Delta x \approx 4$ .

To evaluate the influence of the transformation, three characteristics times,  $t_{trans}$ , are chosen:  $1.25 \cdot t/\tau_p$ ,  $3.125 \cdot t/\tau_p$  and  $5 \cdot t/\tau_p$ . These times are chosen as they are three different instants of the simulation. First and second represent an acceleration of the particle with different magnitude while the last time represents the instant where the droplet reaches its terminal velocity. It is expected to observe a higher sensibility to the transformation when the droplet is transformed during acceleration.

The physical properties are listed in subsection II.3.1, the numerical resolution is set to  $d_p/\Delta x = 4.8$ . The IBM method is used with the retraction of the numerical radius set to  $R_p^* = R_p - 0.3\Delta x$  and the analytical mesh generation. The Two-way method is used with the correction on the averaged interpolated velocity with the filter set at its maximum size with respect to the cube's dimensions. The model used is the same for Two-way and One-way method, drag correction obtained from Schiller and Naumann and wall's influence is considered [Di Felice and Parodi, 1996]. To evaluate the influence of the transformation, we evaluate the evolution of the velocity against the characteristic time. The behavior of the method at the transformation during this temporal evolution is analyzed with the evolution of the position, velocity and acceleration at the three transformations' time. It is expected to enhance the understanding of the terminal velocity for all methods.

### III.6.3 Results

The free-falling particle's velocity evolution is showed for the three characteristic times of transformation. At each transformation's time, a zoomed on the position/velocity/acceleration is done to evaluate discontinuity in the velocity motion of the droplet/particle. The acceleration is computed from the velocity of the particle, we use the velocity at the prior and current iteration,  $n$  and  $n - 1$ , and scale the difference by the current time step:  $\frac{\vec{u}_{p,n} - \vec{u}_{p,n-1}}{\Delta t_n}$ . We recall that the goals of this analysis are: to validate the momentum conservation at transformation from droplet toward particle and to determine which method is the most suitable to transport the under resolved droplets in the range  $d_p/\Delta x \approx 4$  cells across the diameter.

#### Velocity evolution

We evaluate the influence of the transformation from droplet to particle when the droplet is accelerating, at  $t_{trans} = 1.25 \cdot t/\tau_p$ . The results are displayed on figure III.18a. We observe that the zoom area on the velocity/position/acceleration evolution are different for each method. Since the

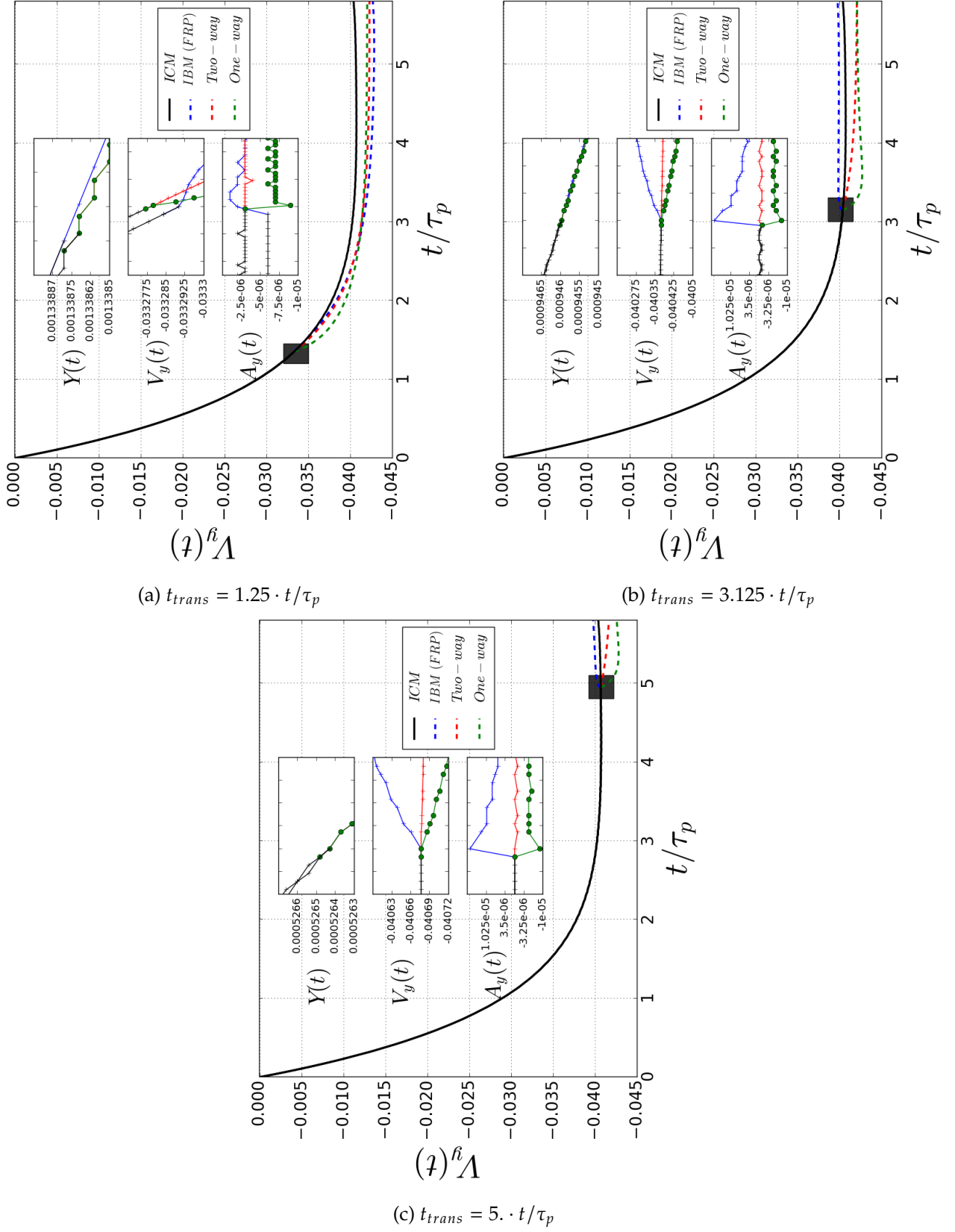


Figure III.18: Free-falling droplet/particle velocity against characteristic time at transformation time  $t_{trans} = [1.25, 3., 5.] \cdot t/\tau_p$ , respectively figure III.18a-III.18b-III.18c, with zoom on acceleration/velocity/position at transformation time.

results are different, we first study the transformation time's influence per method, then we conclude comparing the results.

For the IBM method, the velocity field is not reconstructed because it is naturally done in the projection scheme. We observe that the evolution of the velocity slightly decelerates at transformation and it is observed in the acceleration field, it is the only method that decreases its acceleration. These small discontinuities do not modify the position evolution which is linear, see the zoomed area. The drag force is overestimated by the IBM method at the transformation but after some iterations a constant acceleration is reached and the velocity evolution converges toward a terminal velocity in the range of other methods. At transformation time  $t_{trans} = [3.125, 5] \cdot t/\tau_p$  [figures III.18b and III.18c], a similar trend is observed. The IBM have a velocity deceleration of approximately 0.08% and it a discontinuity is observed on the acceleration evolution, it reaches a positive value. For this resolution, the IBM already reached its terminal velocity, different from the droplets' simulation which explains its velocity evolution. After transformation, the results are stable and the particle is accurately transported. We guess that the difference in terminal velocity with respect to the transformation time lies in the velocity field in the domain.

We focus on One-way method at  $t_{trans} = 1.25 \cdot t/\tau_p$  [figure III.18a], we observe that particle accelerates after transformation. It yields to a particle's velocity increase which reduces after some iteration. At  $t/\tau_p = 3$  we observe that the velocity of the One-way method is slower than other methods which is coherent with the results observed for the methods' comparison (Two-way faster than One-way). At the end, it reaches the smallest terminal velocity. The evolution is similar at  $t_{trans} = [3.125, 5] \cdot t/\tau_p$ , the velocity of the particle evolves over some iterations before reaching its terminal velocity. At later transformation, we observe that even though the particle increases its velocity, it always decelerates to converge toward its terminal reference velocity.

For the Two-way method, we observe the same evolution for all transformation times. The acceleration evolves linearly which results in a linear evolution of the velocity and the position. It shows that the velocity field reconstruction is well implemented for Two-way method since the velocity field around the droplet before transformation is not highly perturbed. More tests must be done to study the influence of velocity's reconstruction in more complex cases [chapter IV].

Comparing the result for the One-way and Two-way methods, we can propose an assumption to explain the One-way acceleration after transformation. In this simulation the velocity field is linearly reconstructed at the transformation. Since the droplet's motion perturbs the velocity field, the new velocity field is no longer at rest. Then, the interpolated velocity at particle's position,  $\vec{u}_{f@p}$ , is not equal to 0 which explains the acceleration at the transformation. In an infinite domain, we could use a bigger area of reconstruction where the droplet's influence would be smaller, then we could reach  $\vec{u}_{f@p} \rightarrow 0$ . It is supposed that the observed acceleration would decrease. We think that it is the reason why the One-way velocity converges toward its reference after some iterations, because there are no more feedback of momentum in the domain. Since the Two-way method uses a filter to correct the interpolated velocity, we do not observe such discontinuity. For the IBM method, it is coherent with the conclusions obtained from the particles tracking comparison.

In this section we observe that the instant of transformation has an influence on the velocity evolution. The One-way method is the less sensitive, the velocity evolution after transformation has the same pattern whatever  $t_{trans}$ . The Two-way method has a smooth evolution toward its terminal velocity, it seems that the sooner it is transformed the higher is the terminal velocity and this is understandable by the difference of terminal velocity between ICM and Two-way method. The IBM method tends to overestimate the drag force on the particle's evolution for coarse simulation, we find the same conclusions for this analysis. We are globally satisfied from these results because we observe that the velocity motion is conserved for every method after transformation. Moreover, we observe that the terminal velocity depends only on the Lagrangian method that is used.

### III.7 Treatment of collisions in Hybrid coupling

In atomization, primary atomization is a complex area that involve lot of liquid structures interactions. A transformed droplet into particle can collide with other liquid structures or particles.

An algorithm is implemented to treat particle-particle collisions and particle-structure collisions. In the first situation, we use a soft sphere algorithm, in the second we use a transformation from particle toward droplet through the distance criterion. In some situation, the particle-particle collisions assumption is inaccurate. We discuss the assumption validity in the first part of this section studying droplets collision regime.

In order to improve particle collisions treatment, a reverse transformation is implemented to treat accurately some particle-particle collisions. A numerical threshold is set to avoid the transformation of numerically small particles that can worsen the simulation, it is set to  $\frac{d}{\Delta x} \approx 5$ . It involves a transformation from particle toward droplet where the velocity field is reconstructed inside the droplet [Ling et al., 2015]. It permits to treat those collisions with ICM method that allows shape deformation. The method is applied on an illustrative simulation already performed with *Archer* [Tanguy and Berlemont, 2005] based on experiments [Ashgriz and Poo, 1990]. Indeed, this is not representative of under resolved collisions that occur in the secondary atomization area, but it permits to validate the methodology on an experimentally and numerically documented physical application.

### III.7.1 Strategy for particles interactions

In section II.1 we introduced the strategy to treat collisions between particles. When a droplet is transformed into a particle, we assume that its shape no longer evolves even for collisions. In some situation, this assumption is inaccurate and we detail it here. To determine it, a Weber number of collision is computed to estimate collision regime. In the example of binary collision, this Weber number considers the relative velocity between two droplets of same fluid properties, 1 and 2, with velocity and diameters respectively  $\vec{u}_{d,1}, \vec{u}_{d,2}$  and  $d_{d,1}, d_{d,2}$ . The characteristic length is the smallest droplet diameter:  $d_{min} = \min(d_{d,1}, d_{d,2})$ . It is expressed in equation III.15 from [Rabe et al., 2010].

$$We_{coll} = \frac{\rho_l d_{min} |\vec{u}_{d,1} - \vec{u}_{d,2}|^2}{\sigma} \quad (III.15)$$

The Weber number of collision is coupled with the impact parameter,  $b_\delta$ . It is the distance between the droplets when one of them is projected onto the second droplet through their relative velocity, obtained with  $\delta_{coll}$ . The impact parameter goes from 0, representing a head on collision to 1, representing a raking collision, see:

$$b_\delta = \frac{2\delta_{coll}}{d_{d,1} + d_{d,2}}. \quad (III.16)$$

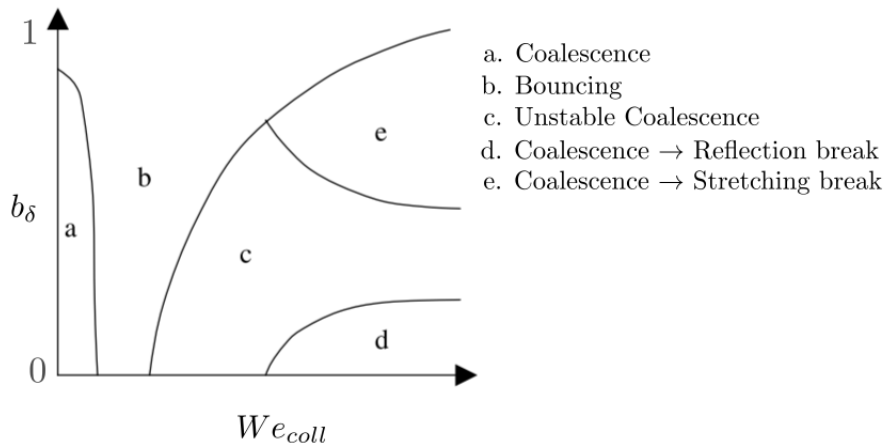


Figure III.19: Collision Weber number against impact parameter to define the outcome of binary collisions[Tanguy and Berlemont, 2005].

From the impact parameter and the collision Weber number, the outcome of a collision can be estimated [figure III.19]. Weber axis depends on fluid properties and is not given on this illustrative

graph. The results obtained in [Rabe et al., 2010] can give a good approximation of these ranges thanks to multiple series of experiments with several fluid properties compared to models from [Ashgriz and Poo, 1990]. We observe that the only regime that can be represented accurately with the particle assumption is the bouncing regime [figure III.19]. It is complex to determine because it lies in between coalescence regime and unstable coalescence regime. Nevertheless, we can suppose that in head-on small collision Weber number, the soft sphere model is accurate<sup>1</sup> It opens the question for other regimes and the assumption to treat collisions with particles in the Hybrid method. Two solutions can be used, either to use a breakup model that create small particles, either to transform into ICM method. The solution that is selected in this manuscript is to transform the particles into droplets because the ICM method is the most accurate to treat such events [Tanguy and Berlemont, 2005] when the resolution is sufficient enough to do so. We compare our Hybrid implementation of collisions against ICM method in the next subsection.

### III.7.2 Head-on collision

To illustrate the transformation of particle into droplet and validate the conservation of the momentum of Ling et al. 2015 [Ling et al., 2015], a head-on binary droplet collision is compared with respect to the experiment for both ICM and Hybrid methods. The simulation is directly inspired from Section 4.1 [Tanguy and Berlemont, 2005] that consists in the collision of two droplets with the same physical properties [table III.2]. The distance between the droplets has been set to 1.71 diameter. The Weber of collision is set to  $We_{coll} = 23$  which implies a relative velocity of  $|\vec{u}_{d,rel}| = 1.44 [m.s^{-1}]$  and the impact parameter is set to  $b_\delta = 0$ . Collision regime is a reflection (regime  $d$  of figure III.19). A characteristic time is defined for this simulation, it is the physical time against the required time to observe the collision  $t/t_{ref}$  with  $t_{ref} = \frac{|Y_{d,1} - Y_{d,2}| - 2 \cdot R_d}{|\vec{u}_{d,rel}|}$ . A coalescence followed by a *clean* separation by reflection is expected as outcome of this simulation.

$R_d [\mu m]$	$\rho_l [kg.m^{-3}]$	$\mu_l [kg.m^{-1}.s^{-1}]$	$\rho_g [kg.m^{-3}]$	$\mu_g [kg.m^{-1}.s^{-1}]$	$g [m.s^{-1}]$	$\sigma [kg.s^{-2}]$
400.0	1000	$1.137 \cdot 10^{-3}$	1.226	$1.78 \cdot 10^{-5}$	0,0,0	0.072

Table III.2: Physical properties of head on binary collision from [Tanguy and Berlemont, 2005] to recover experiments [Ashgriz and Poo, 1990]

In [Tanguy and Berlemont, 2005], the simulation was executed in axi-symmetric framework and the 2D simulation was done for  $[Nx, Ny] = [60, 120]$  which set approximately 20 cells across the diameter of the droplet. The simulation in axi-symmetric framework is not done for particle method because it is developed in full 3D. The parameters of simulation are listed in table III.3 where the numerical resolution of the droplet has been divided by two. The numerical resolution allows us to recover the results in [Tanguy and Berlemont, 2005]. The Hybrid method is initialized using IBM particles with the retraction of the radius and the analytical mesh generation.

$[Lx, Ly, Lz]$	$[Nx, Ny, Nz]$	$\frac{d_d}{\Delta}$	$\Delta [m]$
$[3d_d, 6d_d, 3d_d]$	$[64, 128, 64]$	21.33	$3.75 \cdot 10^{-5}$

Table III.3: Numerical configuration of head on binary collision from [Tanguy and Berlemont, 2005] to recover experiments [Ashgriz and Poo, 1990]

Results of the simulation are showed [figure III.20] and are qualitatively compared to the reference results. The general behavior of the coalescence reflection is well recovered in this collision regime for both simulations. Even though mesh resolution is decreased, we recover the hole inside the torus shape [third image figure III.20], which is encouraging for the method. We recover the two droplets at the end of the collision with a similar shape. They are not exactly at the same position and this is because the events occur sooner in the ICM simulation. The reason is because of the flow initialization.

<sup>1</sup>Droplets collisions regimes have been studied during an internship that I conducted at CORIA Laboratory. Obtained results have been used for scientific vulgarization purpose at *La Fête de la Science*. Jet breakup length was also analyzed with laser light.

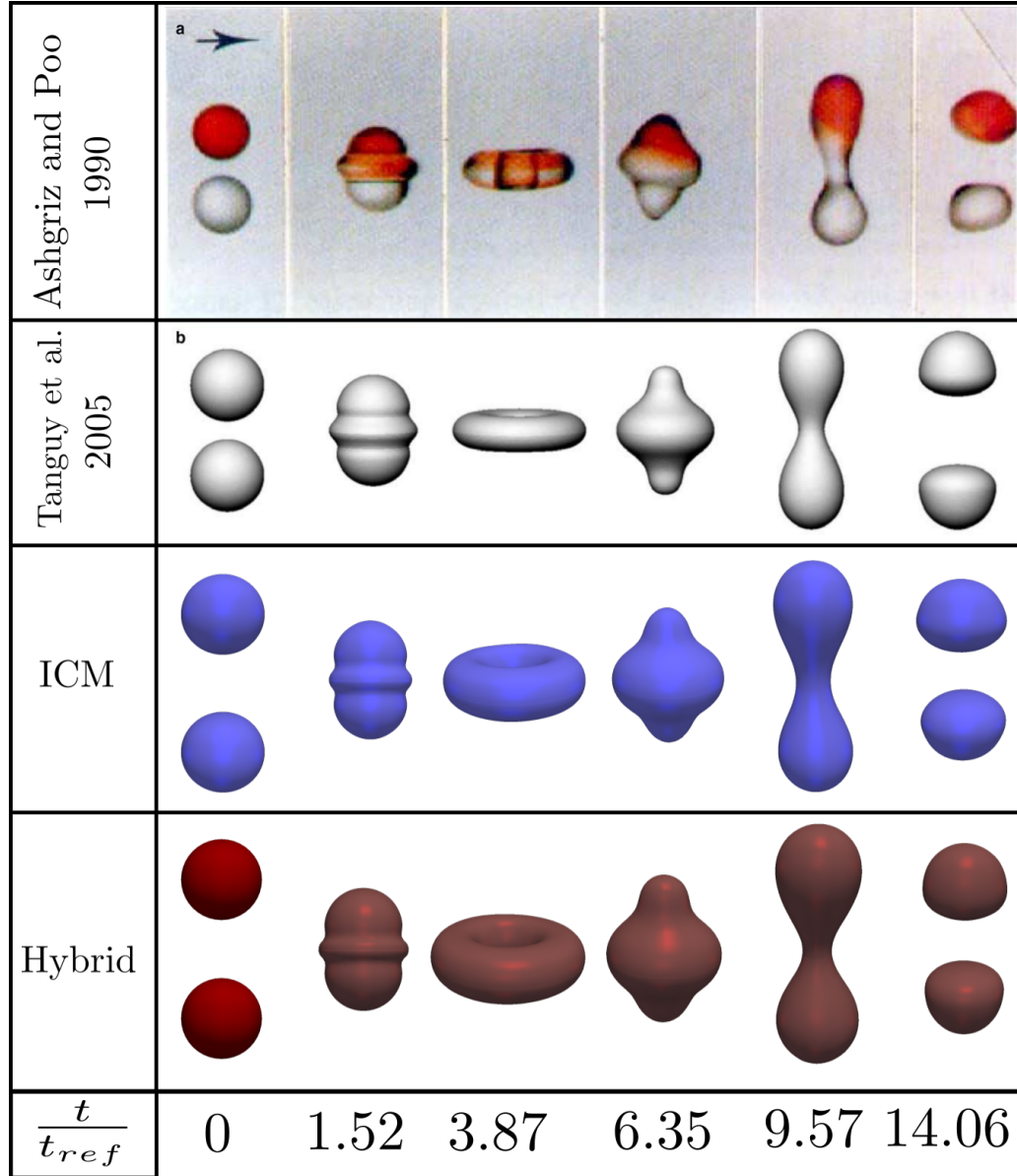


Figure III.20: Comparison of results for head-on binary collision at  $b_\delta = 0$  and  $We_{coll} = 23$  for, from top to bottom, experimental results [Ashgriz and Poo, 1990], numerical reference results [Tanguy and Berlemont, 2005], *Archer* ICM [Ménard et al., 2007] and Hybrid coupling.

In Hybrid simulation the IBM initial velocity is given to the particle as a Lagrangian quantity, the momentum is redistributed toward the Eulerian grid around its shell and initializes the Eulerian velocity field. At the instant of transformation, the velocity from the particle is transferred toward the Eulerian grid and the same strategy is used to update the Eulerian grid. For the ICM simulation, the droplets' velocity is initialized through an identification of the cells that belong to the droplet. Using the *Level-set* field we set  $\vec{u}_{\vec{x}} = [0., \pm 0.77, 0.]$  when  $\phi(\vec{x}) > 0..$  Then, the droplets are transported and collision happens.

We see that this initialization does not modify the physic of the collision, it is limited to the beginning of the simulation. To evaluate the influence on the initialization of the simulation, we compute the maximal centered velocity magnitude and observe its evolution against the characteristic time. Moreover, we can study the update of the velocity inside the reconstructed droplet at transformation.

The results are plotted on figure III.21, a marker and a dashed line are used to represent the time of transformation and collision. As expected, the ICM method has a maximal velocity field of  $\approx 0.77$  [m/s] which is its initialized velocity. At  $t/t_{ref} = 0.4$ , the ICM magnitude starts increasing which is the moment where the droplets are in close vicinity, it represents the moment where the thin trapped air layer is pushed out by the motion of the droplets. Then, the coalescence starts and the velocity decreases in the domain until reaching a plateau  $t/t_{ref} \approx 1.1$ . We observe fluctuations at  $t/t_{ref} \approx 2.$  that represents the surface oscillations leading to the torus shape observed [figure III.20].

Since the velocity field is not directly initialized, we observe a lower maximal velocity magnitude for the Hybrid simulation. After few iterations, it reaches the order of the ICM simulation. At transformation, the velocity field is updated and the particles' velocity is set inside the droplets, it increases the Eulerian grid's maximum velocity. After this transformation, we observe that the phenomenon of pushing out trapped air is recovered with a higher maxima due to the transformation. Then, the maximum velocity decreases until coalescence and the collision freely evolves. The physic of the simulation observed on figure III.20 is then totally recovered by the Hybrid method.

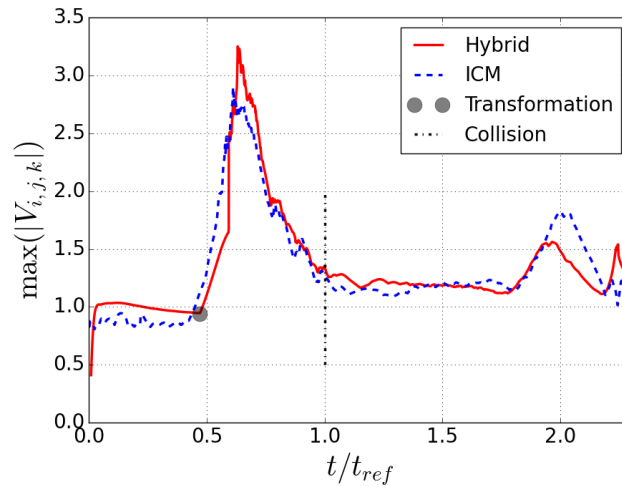


Figure III.21: Evolution of the maximal velocity in the domain against reference time for the Hybrid (red) and ICM (blue) methods. Black marker: particles' transformation, black dashed line: collision.

Finally, the global results are conserved. We can ensure that when there are enough cells across the diameter the reversed transformation permits to conserve the momentum. For the smallest droplet, it is more complex to evaluate it on such test case and the conservation of the momentum is going to be analyzed in the next Chapter. We expect to be conservative on the momentum since we drastically improved the conservation of the mass for the under resolved structures at the transformation.

---

## Enhancement of transformation criteria

---

*The purpose of this chapter is to study the influence of the transformation parameters on the outcome of the simulation on well documented applications. Parameters of transformation such as distance between structures, numerical resolution or sphericity influence the physic since they can lead to early transformation. We study their influence on simulation's outcome varying those criteria. Since Hybrid approach is used only in under resolved areas, these simulations are performed at low mesh resolution. The results of the Hybrid approach are compared to ICM method at same mesh resolution and a finer ICM. The tests that we perform are the following.*

1. *Free-falling droplet over liquid surface in a box.*
2. *Plateau-Rayleigh instability of a round liquid jet.*
3. *Immersed droplets in Decaying Homogeneous Isotropic Turbulence (D-HIT).*

*The first simulation is carried out in 2D and 3D, its low computational cost permits to perform a series of simulation with several transformation criteria parametrization. We have three goals in this study, to define the particle transport method after droplets transformation, to evaluate the influence of transformation's criteria and to study the transformation from particle toward droplet. We note that this event is not favoured in our Hybrid approach, nevertheless we have to study its implementation. From this comparison of transformation's criteria, we expect to increase our understanding on their influence, and it will permit to select them more accurately for the Plateau-Rayleigh and D-HIT studies.*

*The Plateau-Rayleigh instability is set to observe a main isolated droplet, ideal case to represent transformation in the primary atomization area. Due to breakup, surface oscillations are observed until the droplet converges toward its spherical shape. This test case is ideal because we can show the advantages and drawbacks of defined morphological criteria since droplets regime evolves [section III.4]. This analysis is coupled with the introduction of a physical criterion based on the inside droplet velocity field. Then, we compare ICM and Hybrid approaches influence on the outcome of the simulation.*

*Finally, droplets are immersed into a Decaying HIT that can represent the physic of the secondary atomization area in diesel spray. This study is exploratory since we do not have any reference solution and the comparison of the Hybrid approach is done against an under resolved ICM solution. Morphological criteria are analyzed, and the introduction of a physical criterion based on velocity fluctuations at droplets' interface is presented.*



## Contents

---

IV.1	2D and 3D droplet's splash . . . . .	<b>131</b>
IV.1.1	Splash configuration . . . . .	131
IV.1.2	Numerical configuration . . . . .	133
IV.1.3	2D Results . . . . .	136
IV.1.4	3D Results . . . . .	144
IV.1.5	Summary . . . . .	148
IV.2	Plateau-Rayleigh instability of a round liquid jet . . . . .	<b>150</b>
IV.2.1	Plateau-Rayleigh configuration . . . . .	150
IV.2.2	Numerical configuration . . . . .	151
IV.2.3	Results . . . . .	152
IV.2.4	Summary . . . . .	166
IV.3	Decaying Homogeneous Isotropic Turbulence . . . . .	<b>167</b>
IV.3.1	Decaying Homogeneous Isotropic Turbulence configuration . . . . .	167
IV.3.2	Results . . . . .	168
IV.3.3	Summary . . . . .	173

---

## IV.1 2D and 3D droplet's splash

The first application of the hybrid method is the free-falling droplet on a free surface in a box. This study is done in 2D and 3D in order to parametrize the hybrid method implementation. Two transformations are observed, then, the momentum's conservation for droplet to particle transformation and vice versa are studied. We shortly describe the physic of the splash with Hybrid approach.

At start, the droplet is initialized at rest and falls under gravitational acceleration. Since its numerical resolution is coarse, a first transformation from droplet toward particle is observed. Then, it gets in the vicinity of the liquid surface and a reverse transformation, from particle toward droplet, is noticed. Finally, the coalescence occurs, small droplets are ejected and surface deformation appears. Since the simulation's domain is a cube, the interface rises at every oscillation [figure IV.1]. In refine simulations, droplets are ejected from those oscillations. Thus, the more refined is the simulation, the more and the smaller are the ejected droplets. The mass conservgence cannot be studied on this test case for two reasons: the volume restriction [section I.5] and the strong change due to the numerical resolution. For example the coarser simulation does not eject droplet from the rising structure [figure IV.1]. Even though the simulation is consider fine enough to be used as a reference, it appears that due to high Reynolds number, surface instabilities appear that lead to an asymmetry in the liquid rising structure. The result of these instabilities is clearly observed when droplets are ejected from the interaction with wall boundaries [bottom left figure IV.1].

The ICM reference is 8 times (in 2D -  $256^2$ ) and 2 times (in 3D -  $64^3$ ) more refined than the most resolved Hybrid simulation. For the Hybrid method, the three Lagrangian tracking methods: One-way, Two-way and IBM, are used. In this study the focus is on the transformation's distance criterion for particle to droplet transformation. The motivation is to have more insight on the influence of updating Eulerian fields near other interfaces. The morphological criteria are fixed since the initial droplet is spherical.

The Two-way method showed great capabilities to transport under resolved droplets but is limited by its filter length. In atomization, particle can be close to other structures and it is possible that interpolation/redistribution is done in a liquid cell. Filter length is varied in the splash study to evaluate the consequences of momentum redistribution toward liquid cells since to the author knowledge it has not been commented in major Hybrid literature where Two-way method was principally used [Tomar et al., 2010, Ling et al., 2015, Evrard et al., 2019].

The other advantage of the Two-way method is its capability to transport lagrangian particle accurately on the ICM under resolved range, solving the multiscale issue [section I.5]. On the other hand, the One-way method and IBM method are usually not used to treat the same scales. The One-way method is often found when there are few cells across the diameter. On the other hand, the IBM method is usually used when the resolution is sufficient to treat accurately all interactions [section II.1]. Since these methods are implemented, it is of interest to go further on the obseervations made on the free falling sedimented particle/droplet analysis [section II.4], in order to conclude on their reliability to reproduce the physic of this specific test case.

Finally, one of the aspect of this parametric study is to evaluate the method's influence on the outcome of the simulation: is the implementation of the Hybrid method independent of the particle tracking method ?

### IV.1.1 Splash configuration

#### Physical configuration

This study is directly inspired from [Zuzio et al., 2018]. The computational domain is a cubic box with  $Lx = Ly = Lz = 2$  centered in  $[1, 1, 1]$ , using no-slip boundaries (normal velocity set to 0 and tangential velocity set to wall's velocity) except on  $y+$  that is an outflow boundary. Initialization of the free surface and the free-falling droplet is given in table IV.1, and then physical properties in table IV.2.

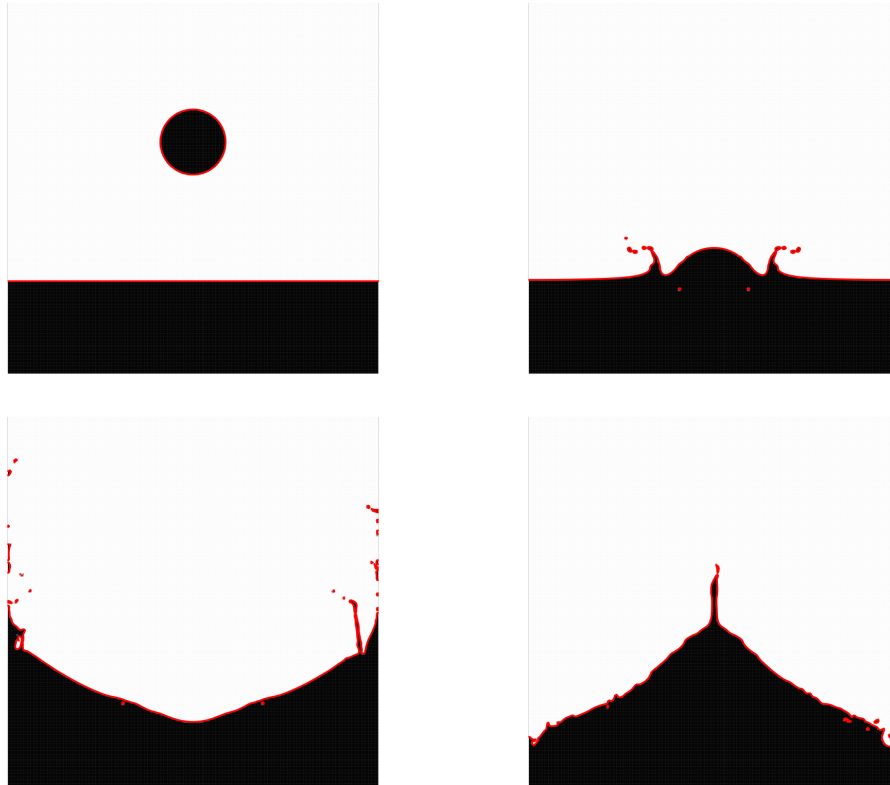
Dimensionless time is defined using the time where the top interface is at its minimum, it occurs slightly after the coalescence. Since the numerical resolution modifies this time [Zuzio et al., 2018], we consdier using the finest grid for each reference time, it gives  $T_{ref} = 0.395$  [s] in 2D and  $T_{ref} = 0.428$

Box Size [m]	$\vec{x}_{d,t_0}$ [m]	$\vec{x}_{Surface-top,t_0}$ [m]
$[0 : 2.], [0. : 2.], [0. : 2.]$	$Lx/2., Ly/1.6, Lx/2.$	$-, Ly/4., -$

Table IV.1: Simulation domain 3D splash, remove Z direction for 2D configuration.

Diameter [m]	$\rho_l$ [kg.m <sup>-3</sup> ]	$\mu_l$ [kg.m <sup>-1</sup> .s <sup>-1</sup> ]	$\rho_g$ [kg.m <sup>-3</sup> ]	$\mu_g$ [kg.m <sup>-1</sup> .s <sup>-1</sup> ]	$g$ [m.s <sup>-2</sup> ]	$\sigma$ [kg.s <sup>-2</sup> ]
$Lx/11.36$	1000	$10^{-3}$	1.225	$10^{-5}$	$0, -9.81, 0$	0.072

Table IV.2: Parametrization of the 3D splash, remove Z direction for 2D configuration.


 Figure IV.1: Snapshots from 2D ICM reference splash simulation at  $t/T_{ref} = [0., 1., 2.3, 3.6]$  [-] at four stages: Initialization-Coalescence-Ejected droplets-Rising tip. In red: interface at iso 0 *Level-set* , in black: *VoF*.

[s] in 3D. The physical time simulation is 1.6 seconds giving  $t/T_{ref} \approx 4$ , in order to observe the development of the liquid column ejected from the splash [figure IV.1].

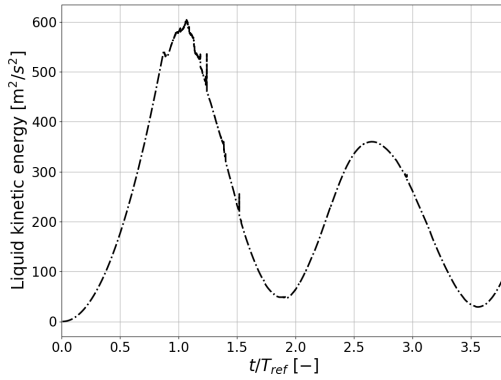
To quantify the influence of criteria parametrization and the particle tracking method on the momentum's conservation, qualitative and quantitative results are used. The qualitative analysis permits to remove the simulations that do not reproduce the physic of the splash with respect to the ICM simulation. In the quantitative analysis, to understand the variations in the results, the liquid kinetic energy evolution is compared [figure IV.2a]. Since small details can lead to modification in momentum conservation. We also study:

- the particles/droplets' velocity evolution at transformation,
- the top/bottom interface evolution with a focus on the crater depth [figure IV.2b].

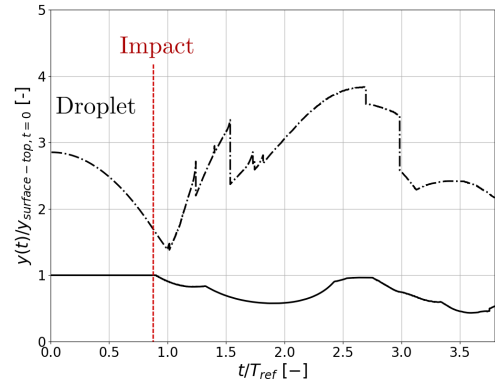
The reference liquid kinetic energy against characteristic time evolves through droplet acceleration until it collides  $t/T_{ref} = 0.9$ , then, the highest liquid energy peak is reached at  $t/T_{ref} = 1$ . [figure IV.2a]. After collision oscillations occur and a second energy peak is observed which corresponds to the rising structure [figure IV.1]. Small discrepancies are observed on the liquid kinetic energy evolution, our guess is that it is the action of the volume restriction.

To evaluate this hypothesis, the top/bottom interface evolution is analyzed against characteristic time, scaled by the initial free surface height [figure IV.2]. The free-falling droplet is observed through the top interface evolution until it reaches the free surface at  $t/T_{ref} = 0.9$ . Small structures are ejected from the splash that rises the top interface. At  $t/T_{ref} = 1.25$ , a discontinuity appears on the top interface evolution, it shows the action of the volume restriction. Indeed the use of the volume restriction is an inconsistency for mass conservation but it also affects the momentum conservation.

The bottom interface evolution is constant until the droplet reaches its vicinity, then it evolves and at  $t/T_{ref} \approx 2$ , a local minimum is observed. At this point a crater like shape is observed. This information is used as reference to compare ICM and Hybrid approach.



(a) Liquid kinetic energy evolution against characteristic time.



(b) ICM Top/Down interface position evolution against characteristic time.

Figure IV.2: 2D ICM splash reference results.

#### IV.1.2 Numerical configuration

Several factors influence Hybrid approach implementation and they can change simulation's results. The most important are the parametrization criteria and particle tracking method. Our goal is to achieve a transformation as transparent as possible without modifying Eulerian fields to ensure that the results depend only on the model. To quantify transformation influence, the following parameters are modified:

- the distance of transformation from droplet toward particle ( $\mathcal{L}_{D \rightarrow P}$ ),
- the distance of transformation from particle toward droplet ( $\mathcal{L}_{P \rightarrow D}$ ),

- the numerical resolution.

It is recalled that  $\mathcal{L}_{\mathcal{D} \rightarrow \mathcal{P}} > \mathcal{L}_{\mathcal{P} \rightarrow \mathcal{D}}$  to avoid successive transformations [section III.3]. It ensures a preferential direction of transformation, from droplet toward particle. The morphological criteria, *Flattening* and  $\Delta\tilde{S}$  are not studied since it has been done in section III.4. All particles approaches are used to study their influence on the results of the simulation with:

- the retraction at high Reynolds number (IBM),
- the filter size redistribution (Two-way),
- the correction on  $\mathcal{A}(u_{f@p})$  (3D).

The interpolated velocity correction are not studied in 2D since they are implemented for 3D drag force. Moreover, the One-way and Two-way approaches in 2D are studied with 3D correlation, the results are not strongly deviated from our reference since the simulation does not permit to reach particle's terminal velocity. When the Stokes equation is used to transport particle in 2D, it is known that an error is done and the results show it.

### One-way simulation

The parameters' variation in the study of the One-way method is done for:

- the numerical resolution:  $Nx = [16, 32]$ ,
- $\mathcal{L}_{\mathcal{D} \rightarrow \mathcal{P}} = [0.7125, 1.425, 2.85] \cdot R_p$ ,
- $\mathcal{L}_{\mathcal{P} \rightarrow \mathcal{D}} = [2., 4.] \cdot \Delta x$ .

The campaign of One-way simulation is listed in table IV.3.

Case	Num. Res. [Nx]	$d_p/\Delta x$ [-]	$\mathcal{L}_{\mathcal{D} \rightarrow \mathcal{P}} \times [\Delta x]$	$\mathcal{L}_{\mathcal{P} \rightarrow \mathcal{D}} [R_p]$	Drag Model
OW 16 D2 N.& S.	16	2.82	2	0.7125	<i>Sc.&amp;Nau.</i>
OW 16 D2 Sto.	16	2.82	2	0.7125	<i>Stokes</i>
OW 16 D4 N.& S.	16	2.82	4	1.425	<i>Sc.&amp;Nau.</i>
OW 16 D4 Sto.	16	2.82	4	1.425	<i>Stokes</i>
OW 32 D2 N.& S.	32	5.63	2	0.7125	<i>Sc.&amp;Nau.</i>
OW 32 D2 Sto.	32	5.63	2	0.7125	<i>Stokes</i>
OW 32 D4 N.& S.	32	5.63	4	1.425	<i>Sc.&amp;Nau.</i>
OW 32 D4 Sto.	32	5.63	4	1.425	<i>Stokes</i>

Table IV.3: List of simulation run with the One-way method for 2D/3D Splash.

### Two-way simulation

The parameters' variation in the study of the Two-way method is done for:

- the numerical resolution:  $Nx = [16, 32]$ ,
- $\mathcal{L}_{\mathcal{D} \rightarrow \mathcal{P}} = [0.7125, 1.425] \cdot R_p$ ,
- $\mathcal{L}_{\mathcal{P} \rightarrow \mathcal{D}} = [2., 4.] \cdot \Delta x$ ,
- filter length:  $\delta/d_p = [1., 1.75, 2.5, 3.25]$ ,
- averaged interpolation correction  $\mathcal{A}(\vec{u}_{f@p})$  (in 3D).

For this campaign, the drag expression is set to Schiller and Naumann correlation.

The motivation to vary the area of redistribution is because the distance of transformation can be smaller than the area of redistribution,  $\mathcal{L}_{\mathcal{P} \rightarrow \mathcal{D}} < \delta$ . It implies a redistribution of particles' momentum toward the liquid surface, thus its influences on simulations' results is of interest.

In section II.1.2 the necessity to remove the disturbance of particle on the interpolation of the velocity is introduced, and validated in section II.3 showing its benefits. We recall that since those corrections are implemented for spheres, they are only compared in 3D, they are:

- without correction (2D/3D),
- linear correction (3D) [Balachandar et al., 2019],
- averaged Wendland correction (3D) [Evrard et al., 2020].

It is recalled that using the averaged Wendland correction reduces the area of redistribution since  $\delta = \lambda \sqrt{2/9\pi}$ .

The simulations are the same in 2D/3D for the method without correction. Since simulations configuration are the same for each correction in 3D, only the campaign of simulations for Two-way method without correction in 3D is listed [table IV.4].

Case	Num. Res. [Nx]	$d_p/\Delta x$ [-]	$\mathcal{L}_{\mathcal{D} \rightarrow \mathcal{P}} \times [\Delta x]$	$\mathcal{L}_{\mathcal{P} \rightarrow \mathcal{D}}$ [ $R_p$ ]	Drag Model
TW 16 D2 $\delta = 1$ wo	16	2.82	2	0.7125	1. No Corr
TW 16 D2 $\delta = 1$ w Av.	16	2.82	2	0.7125	1. Av. Corr.
TW 16 D2 $\delta = 1$ w Lin.	16	2.82	2	0.7125	1. Lin. Corr.
TW 16 D2 $\delta = 1.75$ wo	16	2.82	2	0.7125	1.75 No Corr
TW 16 D2 $\delta = 2.5$ wo	16	2.82	2	0.7125	2.5 No Corr
TW 16 D2 $\delta = 3.25$ wo	16	2.82	2	0.7125	3.25 No Corr
TW 16 D4 $\delta = 1$ wo	16	2.82	4	1.425	1. No Corr
TW 16 D4 $\delta = 1.75$ wo	16	2.82	4	1.425	1.75 No Corr
TW 16 D4 $\delta = 2.5$ wo	16	2.82	4	1.425	2.5 No Corr
TW 16 D4 $\delta = 3.25$ wo	16	2.82	4	1.425	3.25 No Corr
TW 32 D2 $\delta = 1$ wo	32	5.63	4	1.425	1. No Corr
TW 32 D2 $\delta = 1.75$ wo	32	5.63	4	1.425	1.75 No Corr
TW 32 D2 $\delta = 2.5$ wo	32	5.63	4	1.425	2.5 No Corr
TW 32 D2 $\delta = 3.25$ wo	32	5.63	4	1.425	3.25 No Corr
TW 32 D4 $\delta = 1$ wo	32	5.63	4	1.425	1. No Corr
TW 32 D4 $\delta = 1.75$ wo	32	5.63	4	1.425	1.75 No Corr
TW 32 D4 $\delta = 2.5$ wo	32	5.63	4	1.425	2.5 No Corr
TW 32 D4 $\delta = 3.25$ wo	32	5.63	4	1.425	3.25 No Corr

Table IV.4: List of simulation run with Two-way approach, Splash 2D and 3D.

## IBM simulation

The parameters' variation in the study of the IBM is done for:

- the numerical resolution:  $Nx = [16, 32]$ ,
- $\mathcal{L}_{\mathcal{D} \rightarrow \mathcal{P}} = [0.7125, 1.425] \cdot R_p$ ,
- $\mathcal{L}_{\mathcal{P} \rightarrow \mathcal{D}} = [2., 4.] \cdot \Delta x$ ,
- radius retraction:  $|\vec{X}_p - \vec{X}_L| = R_p - 0.3 \times \Delta x$  or  $|\vec{X}_p - \vec{X}_L| = R_p$ .

The mesh generation is done analytically using equations II.32-II.33 from [Saff and Kuijlaars, 1997]. The IBM simulation campaign is listed [table IV.5].

Case	Num. Res. Nx	$d_p/\Delta x$ [-]	$\mathcal{L}_{\mathcal{P} \rightarrow \mathcal{D}} \times [\Delta x]$	$\mathcal{L}_{\mathcal{D} \rightarrow \mathcal{P}} \times [R_p]$	Retract.
IBM 16 D2 w Ret.	16	2.82	2	0.7125	.TRUE.
IBM 16 D2 wo Ret.	16	2.82	2	0.7125	.FALSE.
IBM 16 D4 w Ret.	16	2.82	4	1.425	.TRUE.
IBM 16 D4 wo Ret.	16	2.82	4	1.425	.FALSE.
IBM 32 D2 w Ret.	32	5.63	2	0.7125	.TRUE.
IBM 32 D2 wo Ret.	32	5.63	2	0.7125	.FALSE.
IBM 32 D4 w Ret.	32	5.63	4	1.425	.TRUE.
IBM 32 D4 wo Ret.	32	5.63	4	1.425	.FALSE.

Table IV.5: List of simulation run with the IBM, Splash 2D and 3D.

### IV.1.3 2D Results

The first stage of this analysis is based on the 2D splash. The interface evolution is studied through snapshots of the simulation to determine how transformation impacts the simulation. Then, a focus on the liquid kinetic energy is done, it permits to conclude on the use of Hybrid approach in 2D.

#### Global results

Since a wide amount of data has to be analyzed, the study is organized as follows:

- reference simulation (ICM 256<sup>2</sup>) compared to ICM 32<sup>2</sup>.
- Hybrid results qualitative analysis:
  - Lagrangian approach.
  - Numerical resolution.
  - Distance of transformation.
- ICM 32<sup>2</sup> compared to Hybrid 32<sup>2</sup> results.

Snapshots of the 32<sup>2</sup> simulations against ICM reference at five characteristic times;  $t/T_{ref} = [0, 0.5, 1.0, 1.8, 3.3]$  are used to illustrate our analysis [figure IV.3]. On these snapshots, the four main stages of the simulations are represented; the transformation toward particle, the collision, evolution after collision with crater creation and finally the rising liquid column. Since a large series of simulations' results are obtained, all results are not showed but they are all commented in this section.

#### Fine and coarse ICM results

The evolution of the splash for the two numerical resolutions is represented on figure IV.3 where the general physic of the splash is respected at low mesh resolution until the last snapshot;  $t/T_{ref} = 3.3$ . The droplet collides with the free surface pushing the liquid on the extremities of the domain. Then it oscillates and creates a rising column at the center of the box.

Some differences are observed due to the numerical resolution. The first difference is the time to reach the free surface, it was commented in [Zuzio et al., 2018] that the numerical resolution increased the droplet's free-falling velocity. In our results, it is also observed that the finer simulation reaches the free surface first, it explains the rim structures already ejected at  $t/T_{ref} = 1$  on ICM reference results.

Again, these figures show that the mass convergence can not be studied since the finer is the mesh, the smaller are the ejected droplets. It implies that the volume restriction is more often used at high resolution and leads to complex mass study analysis.

Last, it is seen that the crater depth is of the same order for both resolutions, a finer analysis is required since the resolved simulation evolves faster. The rising structure rises higher for the fine simulation, it is supposed that this is due to the increase of droplet's falling velocity.

## Hybrid qualitative analysis

The series of simulation for the One-way method showed that the drag correction was required to recover the physic of the splash in 2D. When the Stokes assumption is used to transport the particle, the drag force is strongly underestimated and particle's motion is accelerated, yielding to an overestimation of the momentum transfer at collision. The variation of filter length for the Two-way method and the radius's retraction for the IBM does not strongly modify the results in 2D. The quantitative analysis provides more information for both methods.

All simulations performed with  $Nx = 16$  and  $\mathcal{L}_{\mathcal{D} \rightarrow \mathcal{P}} = 4\Delta x$  do not transform the droplet into particle even though the distance between the two interfaces is higher. Except this configuration, all simulations transformed droplet toward particle and vice versa. It permits to observe that the distance parameter  $\mathcal{L}_{\mathcal{P} \rightarrow \mathcal{D}}$  influences simulation's outcomes. The closer results to the ICM reference simulation, for all particle approaches, were obtained with  $\mathcal{L}_{\mathcal{P} \rightarrow \mathcal{D}} = 4\Delta x$ .

Results obtained for the Hybrid approaches are displayed against ICM simulation for the same characteristic times [figure IV.3], using  $Nx = 32$  and  $\mathcal{L}_{\mathcal{P} \rightarrow \mathcal{D}} = 4\Delta x$ . Results are ordered as follows: ICM reference, ICM  $Nx = 32$ , IBM with radius retraction, Two-way with  $d_p/\delta = 2.5R_p$ , One-way with Schiller and Naumann drag correlation.

### ICM 32<sup>2</sup> vs Hybrid 32<sup>2</sup>:

The evolution of the interface for the three Hybrid approaches follows reference simulation. The physic of splash is recovered and the crater depth/rising structure height are of the same order of magnitude than ICM 32<sup>2</sup> simulation. It shows that the method used to update the Eulerian field for the two successive transformations is correctly implemented since reference is recovered, even for coarse reconstruction.

### One-way method

From the qualitative analysis it appears that the One-way results vary because of the distance of transformation and the drag force model. Now, the conservation of the momentum for the One-way method is analyzed. Similarly to the figures presented in introduction [figures IV.2b and IV.2], liquid kinetic energy evolution against the characteristic time is studied [figure IV.4a].

Since two successive transformations are obtained, the particle/droplet velocity evolution at transformation is also commented [figure IV.4b]. All simulations where transformation occurs with Schiller and Naumann correlation are showed, one simulation with Stokes motion is included. Those results are compared to the ICM simulation with mesh resolution  $Nx = [16, 32, 256]$  giving  $d_p/\Delta x = [2.8, 5.6, 45.1]$ .

Since the drag force computation is not accurate through Stokes motion for this configuration, a strong variation on the kinetic liquid energy appears. Thus, the first liquid energy peak's magnitude is overestimated due to the underestimation of the drag force.

The three One-way simulations including *S.&N.* drag correlation reach a different liquid kinetic energy peak magnitude, at  $t/T_{ref} = 1$  [figure IV.4a], which has repercussions on the surface oscillations. This difference is more important on the second peak since it modifies the oscillation regime. The configuration that has the wider distance of transformation is the closest to the ICM reference at same mesh resolution. It shows that the distance of transformation has an influence on the conservation of the momentum. Two reasons are possible, since the computation of the drag force is based on a sphere, the more time is spent through Lagrangian transport, the less accurate are the results. Next, transformation close to the interface modifies the simulation. Since  $\mathcal{L}_{\mathcal{D} \rightarrow \mathcal{P}} = \mathcal{L}_{\mathcal{P} \rightarrow \mathcal{D}} + 0.5\Delta x$ , the distance of transformation has two limits:

- upper limit because our goal is to transform under resolved droplets in particle as much as possible,
- lower limit since transformation must occur before reaching any interface to conserve the physic of the simulation.



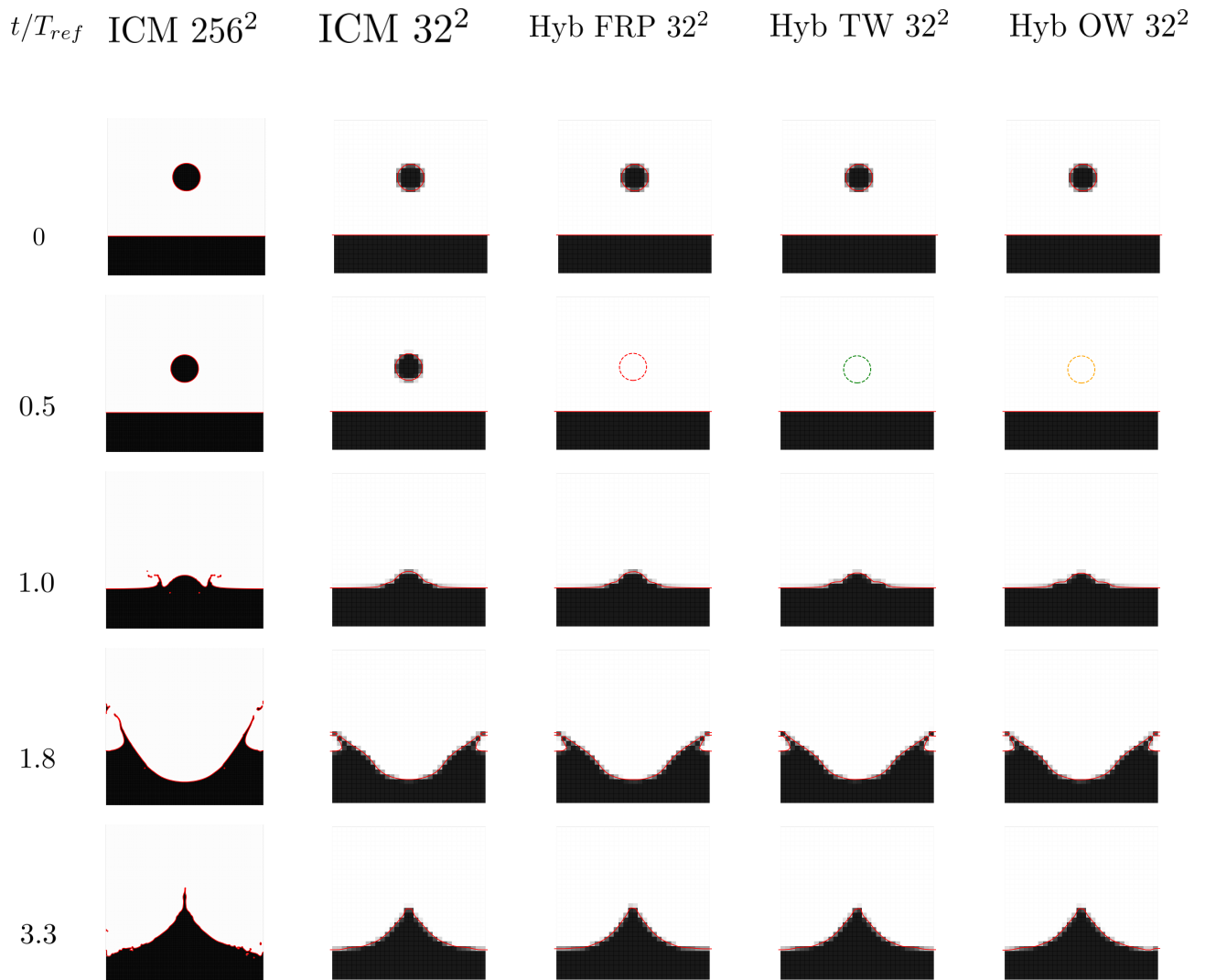


Figure IV.3: *Level-set* iso contour and VOF occupied cells, respectively in red and black showed for the 2D splash. From left to right: ICM  $256^2$ , ICM  $32^2$ , Hybrid IBM  $32^2$ , Hybrid Two-way  $32^2$ , Hybrid One-way  $32^2$ . From top row to bottom row:  $t/T_{ref} = [0, 0.5, 1.0, 1.8, 3.3]$  [–].

It will be further analyzed through 3D results.

Then the free-falling velocity evolution until droplet reaches the free surface is commented [figure IV.4b, droplet: discontinuous circle marker, particle: solid line with triangles]. The first zoomed area represents the velocity evolution at transformation: if the velocity evolution is not perturbed, the momentum is conserved. The particle in configuration OW 32 D4 Sto. strongly deviates after transformation which is due to the implemented model. Those results, added to the conservation of the momentum and interface evolution show that transformation from droplet to particle is not impacting the simulation.

For the reversed transformation, droplet's velocity evolution after transformation is not recovered when  $\mathcal{L}_{\mathcal{D} \rightarrow \mathcal{P}} = 2\Delta x$  because the detection algorithm does not differentiate it from the main surface. For the larger distance of transformation, a linear evolution is observed showing that the reverse transformation ensures momentum conservation.

## Two-way method

The conclusions hold for the One-way method are observed in these results. When  $\mathcal{L}_{\mathcal{P} \rightarrow \mathcal{D}} = 2\Delta x$ , an overestimation of the kinetic energy peak at  $t/T_{ref} = 1$  is seen [figure IV.5a]. The 3D results will give more insight on this event.

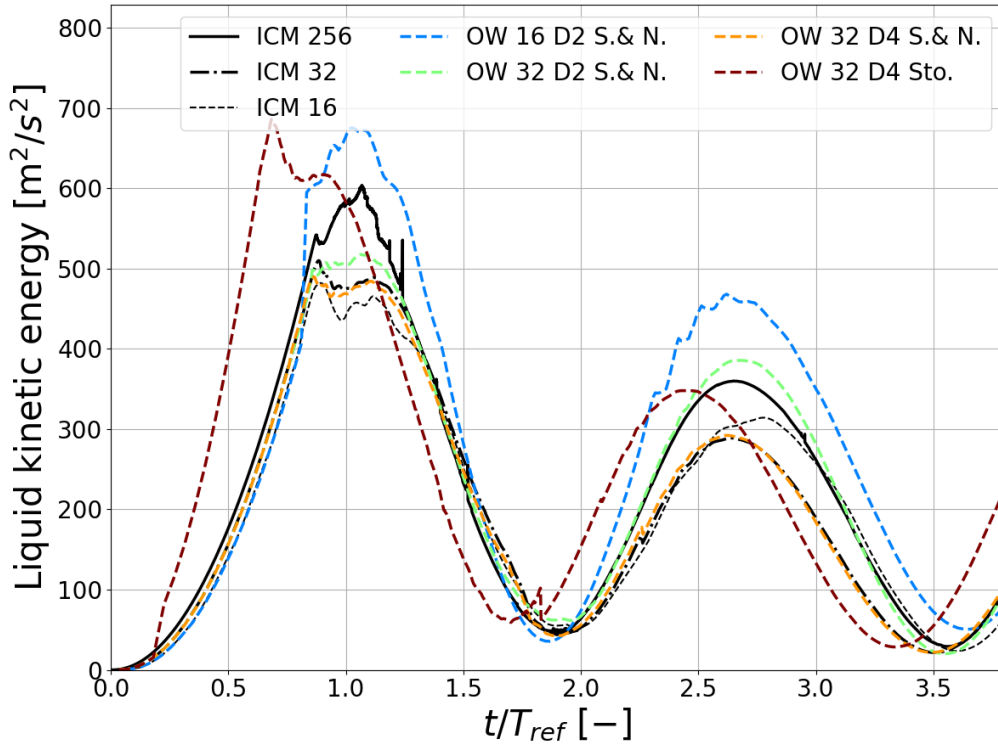
The second parameter of interest is the filter length. Its influence for the most accurate results, obtained at  $Nx = 32$  and  $\mathcal{L}_{\mathcal{P} \rightarrow \mathcal{D}} = 4\Delta x$ , are analyzed. For the larger filter size,  $\delta = 3.25R_p$ , the redistribution is done over  $4.6\Delta x$ . Thus, the particle's momentum redistribution area overlap the free surface. All results are converging toward the ICM32 simulation. A slight difference is observed which does not have any influence on the liquid kinetic energy evolution.

Then the free-falling droplet/particle velocity evolution is studied [figure IV.5b]. In this configuration, it is also observed that the numerical resolution does not modify prior observations' [Zuzio et al., 2018]. The transformation from droplet toward particle does not modify the linear velocity evolution. On the bottom zoomed area it appears that the second transformation occurs faster for the small filter length. For the Two-way method, it appears that the transformation does not influence the simulation but the transport of the particle does. An accurate model is important to ensure recovering the physic of the spray. On the other hand, large momentum redistribution does not modify the physic of the splash in 2D. It can be understood by the definition of the Gaussian function: the major part of particles' momentum is redistributed at the center of the particle. Then particles' momentum redistribution at the interface for the IBM simulation is studied to determine if it influences the simulation.

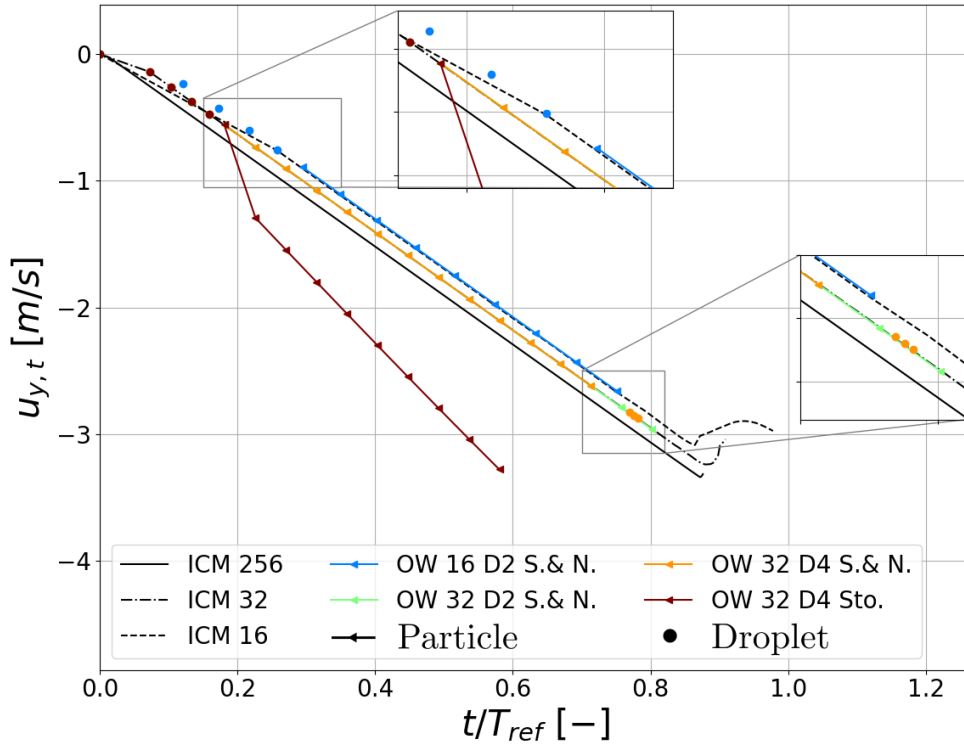
## IBM

IBM method does not imply any model for particle's transport, then, the 2D transport of the particle is representative of the physic. The results confirm our prior assumptions: the distance of transformation is a key criterion since the closer results to the reference are obtained when  $\mathcal{L}_{\mathcal{P} \rightarrow \mathcal{D}} = 4\Delta x$  [figure IV.6a]. A small overestimation of the energy peak is observed at  $t/T_{ref} = 1$ , it is supposed that the momentum's redistribution at particle's interface with IBM method influences the results. It must yield a modification of the bottom interface position. This assumption is studied plotting the top/bottom interface of the Hybrid approach, considering ICM results as reference [figure IV.7]. Since these results for other Hybrid approaches were not introduced, the description of the figure is done first, to go further on our hypothesis.

The three configurations are showed on these results, at  $Nx = 16$  the interface is slightly shifted during the transformation. The reason is that the *Level-set* is updated at transformation in the simulation. The use of the redistanciation permits shifting back the interface and to recover the position of the free surface. Again, a difference appears at the second transformation,  $t/T_{ref} = 0.8$ , when Eulerian fields are updated. However, this modification influences simulations' result since the interface is pushed down earlier than for ICM configuration at  $Nx = 16$ . It confirms the importance of transforming far from other interfaces since in this configuration, it yields to an overestimation of the crater depth.

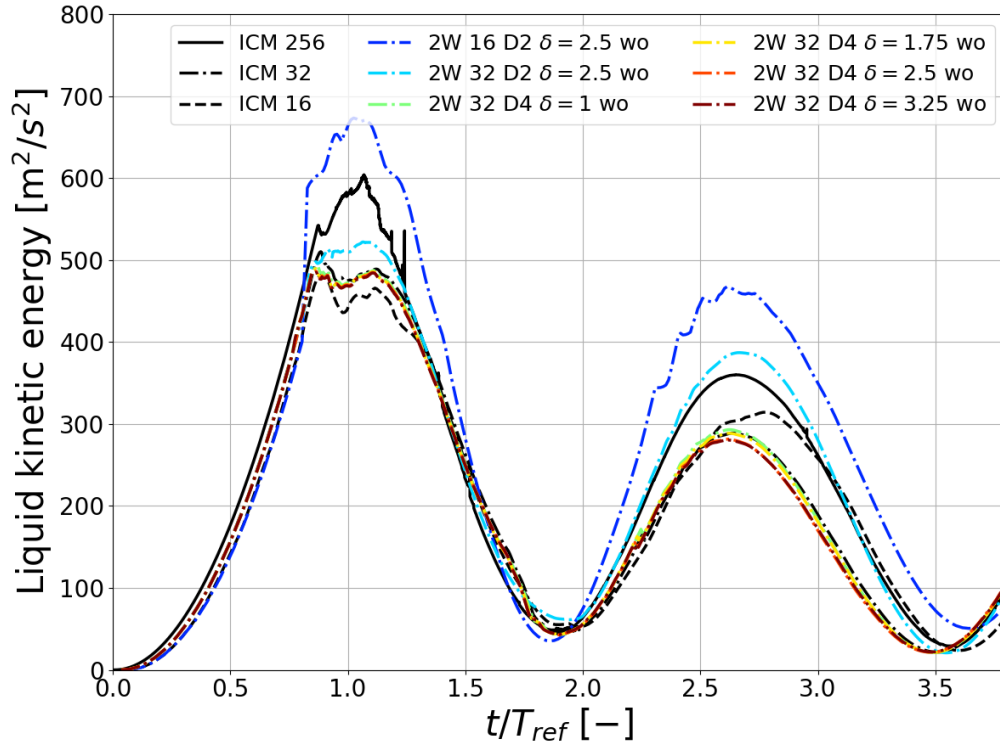


(a) Liquid kinetic energy evolution for  $Nx = [16, 32]$  against characteristic time. Particle and liquid cell momentum is considered for Hybrid approach.

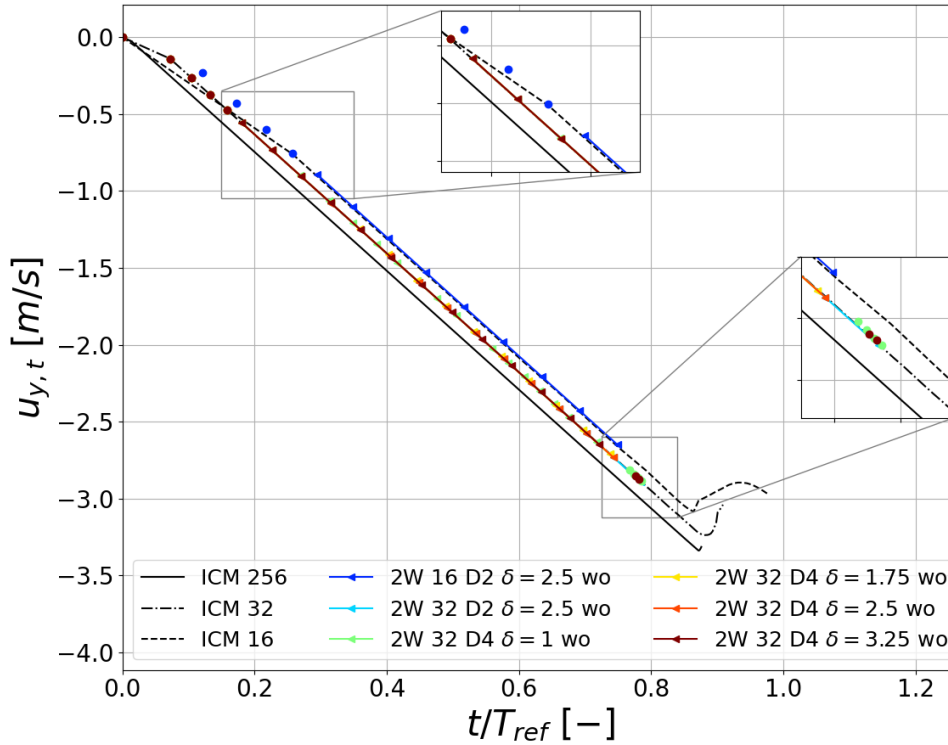


(b) Free-falling particle velocity for  $Nx = [16, 32]$  against characteristic time with zoom onto the two transformations. Droplets and particles represented by discontinuous circle marker and particles triangle marker on solid line for Hybrid approach.

Figure IV.4: Hybrid One-way 2D splash results.



(a) Kinetic energy evolution for  $Nx = [16, 32]$  against characteristic time. Particle and liquid cell momentum is considered for Hybrid approach.



(b) Free-falling particle velocity for  $Nx = [16, 32]$  against characteristic time with zoom onto the two transformations. Droplets and particles represented by discontinuous circle marker and particles triangle marker on solid line for Hybrid approach.

Figure IV.5: Hybrid Two-way 2D splash results.

For the resolution  $Nx = 32$ , differences are observed at  $t/T_{ref} = 3.25$  when the top interface rises. The closer simulation to the reference is obtained with configuration  $Nx = 32$  and  $\mathcal{L}_{\mathcal{P} \rightarrow \mathcal{D}} = 4\Delta x$ . For all configurations, at  $t/T_{ref} = 1$ , the results are close to the ICM simulation, the small differences of liquid peak energy are assumed to be a consequence of the Lagrangian approach. Moreover, no discontinuities are observed in particles/droplets velocity evolution at transformation [figure IV.6b].

### Hybrid approach quantitative comparison

To compare the results of each Hybrid approaches, the following information are extracted: the liquid kinetic energy peak and the crater depth for configuration  $Nx = 32$  and  $\mathcal{L}_{\mathcal{P} \rightarrow \mathcal{D}} = 4\Delta x$ . These results are scaled by the results for the reference and at same mesh resolution [table IV.6]. To facilitate the analysis, each value is colored as follow: green, black and red respectively for  $Error < 3\%$ ,  $3\% \leq Error \leq 10\%$  and  $10\% < Error$ .

First, the liquid kinetic energy peak is studied. The closer results to the ICM simulation at same mesh resolution are obtained with Hybrid IBM approach. It is not expected since the over all liquid kinetic energy evolution is the less accurate for this configuration [figure IV.6a]. The results obtained for Hybrid One-way and Two-way approaches are also close to the reference and remains below 4% of error. For the Two-way method, the smaller is the filter the closer to ICM 32 are the results and it is possible that the momentum redistribution modifies the droplet/free surface collision.

The crater depth analysis shows that all methods reproduce accurately the physic of the splash since they remain below 2% of error. It appears that the closer results to ICM 32 are obtained for the Hybrid Two-way approach. From those results, the filter length influence is not observed.

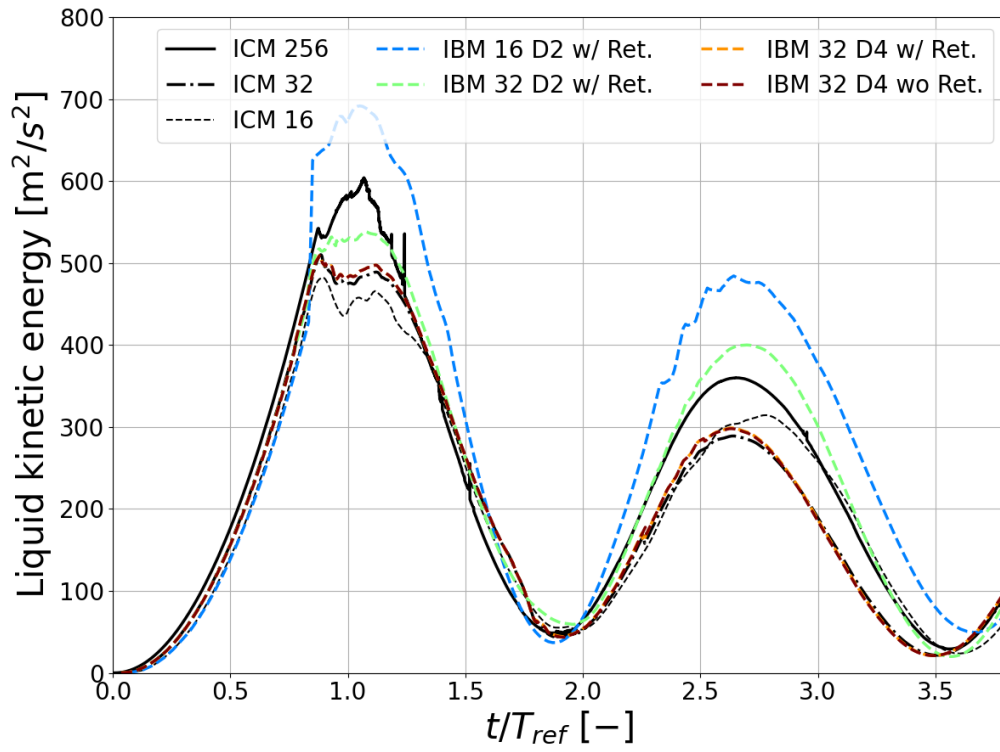
Case	$\frac{Ek_{liq,case}}{\bar{Ek}_{liq,ICM,Nx_{case}}}$	$\frac{\max(Ek_{liq,case})}{\max(Ek_{liq,ref})}$	$\frac{y_{crater,case}}{y_{crater,ICM,Nx_{case}}}$	$\frac{y_{crater,case}}{y_{crater,ref}}$
OW 32 D2 N.& S.	1.015	0.857	0.952	0.990
OW 32 D4 N.& S.	0.960	0.811	0.991	1.031
TW 32 D4 $\delta = 1$ . wo	0.967	0.817	0.992	1.032
TW 32 D4 $\delta = 1.75$ wo	0.960	0.810	0.998	1.038
TW 32 D4 $\delta = 2.5$ wo	0.953	0.805	1.002	1.042
TW 32 D4 $\delta = 3.25$ wo	0.950	0.803	0.997	1.037
IBM 32 D4 w Ret.	0.998	0.843	0.991	1.030
IBM 32 D4 wo Ret.	0.997	0.842	0.989	1.028

Table IV.6: Detailed analysis on the mass conservation, crater depth and first liquid kinetic energy peak ponderated by own mesh resolution and reference for the 2D splash. The red color indicates a deviation of more than 10% and the green color a deviation of less than 3%.

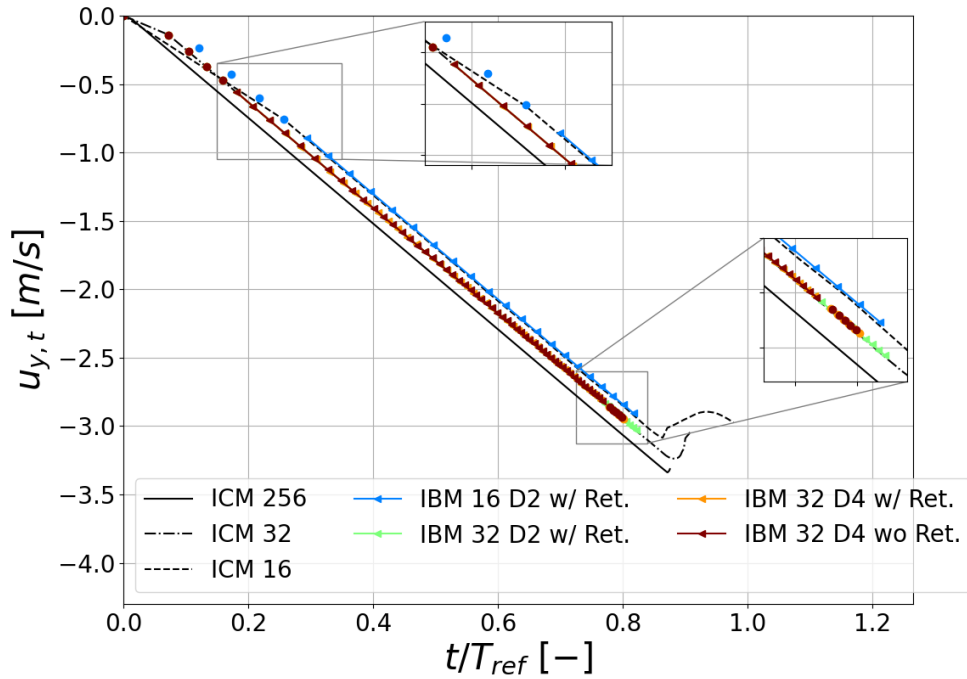
### Summary

In 2D, the method that seems to fit the most accurately the evolution of the splash are the One-way and Two-way methods. Since results are similar, it is better to use the One-way method for such under resolved configurations. It permits to avoid the influence of the redistribution of the energy into the liquid phase for the Two-way method. The IBM yields to an overestimation of the momentum due to its inaccurate transport which is probably due to the poor resolution.

It is observed that whatever the method, the process of transformation from droplet toward particle and vice versa does not affect the solution when the parametrization is well defined. Then, the distance of transformation in 2D is calculated on the radius of the particle. This distance must be always greater or equal to  $4\Delta x$ , and, the distance of transformation from droplet to particle must be always higher than the distance of transformation from particle to droplet. These observations are now analyzed for the 3D version of the splash simulation.



(a) Liquid kinetic energy evolution for  $Nx = [16, 32]$  against characteristic time. Particle and liquid cell momentum is considered for Hybrid approach.



(b) Free-falling particle velocity for  $Nx = [16, 32]$  against characteristic time with zoom onto the two transformations. Droplets and particles represented by discontinuous circle marker and particles triangle marker on solid line for Hybrid approach.

Figure IV.6: Hybrid IBM 2D splash results.

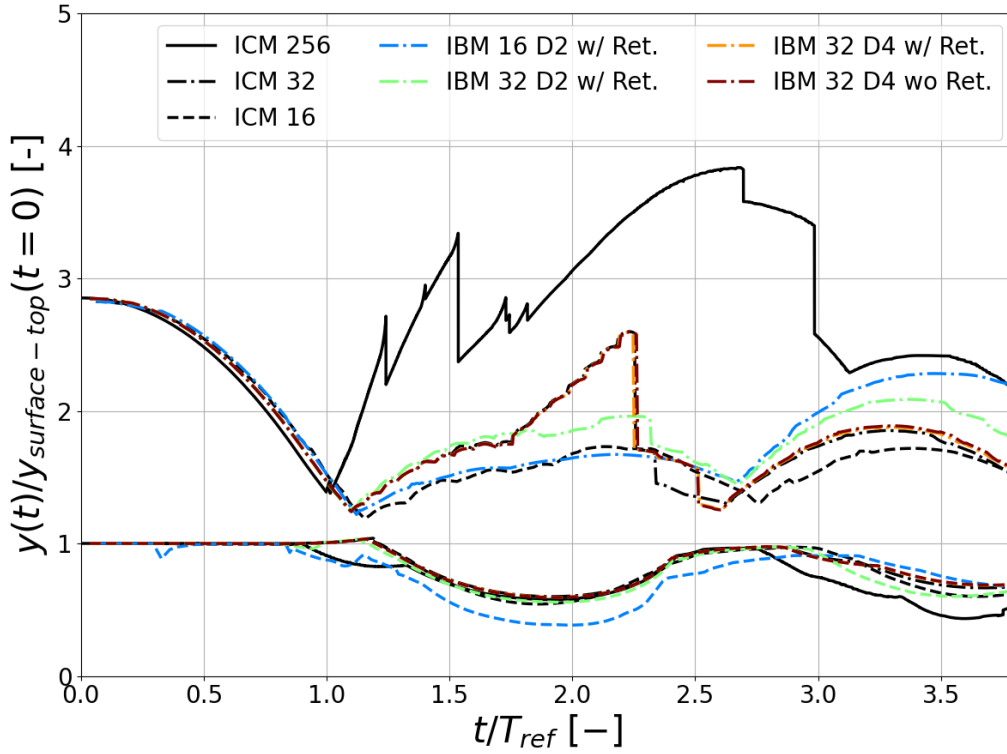


Figure IV.7: Interface evolution top/bottom for  $Nx = [16, 32]$  against characteristic time. Particle position is also considered for Hybrid Hybrid IBM 2D approach.

#### IV.1.4 3D Results

To comment the 3D splash, the same strategy is followed: first the global results with extraction of interface are studied, next results are detailed through liquid kinetic energy evolution and the top/bottom interface position analysis. Then, the Hybrid approaches are compared. It is recalled that in this section more tests are added for the Two-way method since we consider the linear [Balachandar et al., 2019] and averaged correction [Evrard et al., 2020]. Note also that the reference simulation is obtained for ICM  $Nx = 64$ . Finally, the 2D conclusions, on the distance's criterion influence and the most accurate Hybrid approach, are evaluated for the 3D.

##### Global results

Again, a large series of simulations are performed, and all results are not showed but they are all commented in this section. For instance, results obtained with IBM method are not presented since the method is not able to simulate high Reynolds numbers at low mesh resolution  $d_p/\Delta \approx 5$ . We observe that few iterations after transformation, an overestimation of the particles' momentum redistribution toward the Eulerian grid is observed, yielding to a crash of the simulation. To ensure that the cause of the crash was the IBM and not the 3D transformation toward particle, the splash simulation has been directly initialized with an IBM instead of ICM droplet. The overestimation of particles momentum is also observed permitting to ensure that the issue is coming from the IBM method and not the momentum's conservation at transformation.

The One-way results are more accurate with the Schiller and Naumann and Stokes correlation, but the gap between results is smaller with 3D simulations than 2D. The Two-way method has good results for all implementation; the direct interpolation without correction on the interpolated velocity, the linear interpolation correction and the Gaussian averaged correction.

From the evolution of the interface, it appears that the distance of transformation plays a role in 3D, again, and the results closer to the reference were obtained for the larger distance of transformation. The difference is showed later.

Five snapshots of the ICM 32, all Two-way 32 with  $\delta = 2.5R_p$ , and One-way with transformation's



distance,  $\mathcal{L}_{\mathcal{P} \rightarrow \mathcal{D}} = 4\Delta x$ , are showed [figure IV.8]. From the left to the right: ICM, Hybrid Two-way without correction in green, Hybrid Two-way Gaussian averaged correction in blue, Hybrid Two-way linear correction in red and One-way method in orange. The selected times are  $t/T_{ref} = [0, 0.9, 1.6, 2.6, 3.3]$ . The general physic of the splash is obtained for all configurations since the crater creation and the rising structure, respectively on third and fourth row, are well recovered.

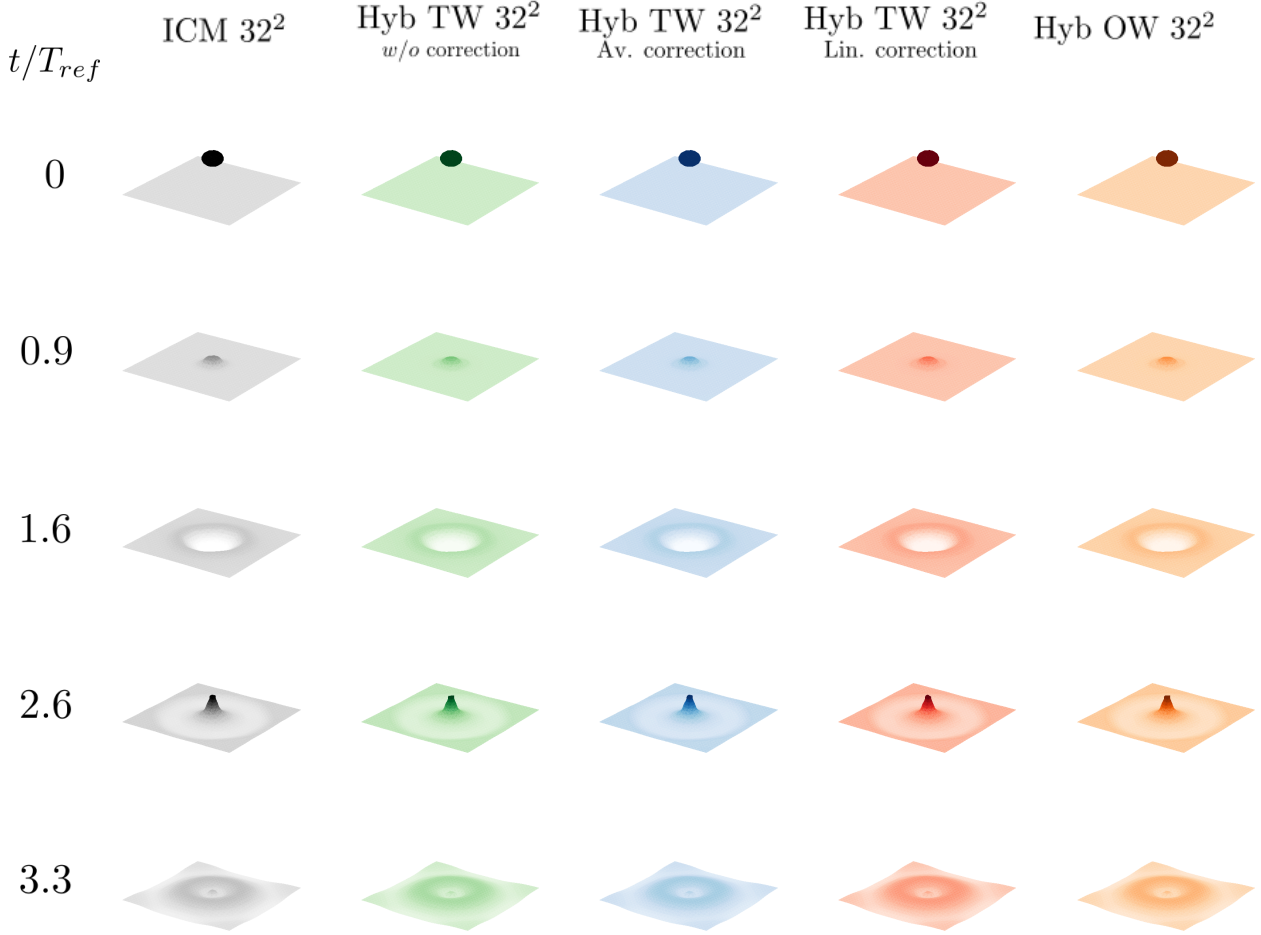


Figure IV.8: *Level-set* iso contour showed for the 3D splash. From left to right: ICM  $32^3$ , Hybrid Two-way without correction  $32^3$ , Hybrid Two-way Av. correction  $32^3$ , Hybrid Two-way Lin. correction  $32^3$ , Hybrid One-way  $32^3$ . From top row to bottom row:  $t/T_{ref} = [0, 0.9, 1.6, 2.6, 3.3]$  [–]

It is commented that a difference is observed when the distance of transformation is reduced. The results for the configuration Hybrid Two-way Av. correction  $32^3$  with  $\mathcal{L}_{\mathcal{P} \rightarrow \mathcal{D}} = 2\Delta x$  are showed for the time steps  $t/T_{ref} = [0.9, 1.1]$  [figure IV.9], right after coalescence. From these snapshots, it is possible to observe that the crater creation occurs differently, but it is impossible to say that it modifies the simulation's result. The difference is easier to observe studying the rising structure that appears after  $t/T_{ref} = 2.6$  [figure IV.8]. To highlight this discrepancy, five successive snapshots are extracted from configuration  $Nx = 32$  and  $\mathcal{L}_{\mathcal{P} \rightarrow \mathcal{D}} = 2\Delta x$  and  $Nx = 32$  and  $\mathcal{L}_{\mathcal{P} \rightarrow \mathcal{D}} = 4\Delta x$  at  $t/T_{ref} = [3.3, 3.5, 3.7, 3.9]$  [figure IV.10].

At  $t/T_{ref} = 3.3$ , the rising tip generates a small isolated droplet which is not observed on the ICM reference. This droplet is under resolved and it is transformed into particle at  $t/T_{ref} = 3.5$  avoiding volume restriction. The particle is transported with One-way approach because a threshold that transforms all small droplets, ( $d_p < 1.5\Delta x$ ), in One-way particle is implemented. Then gravity acts on its motion and particle reaches the oscillating surface which implies a transformation toward droplet. In this simulation, two Lagrangian approaches have been successfully used.

It is noted that if  $\mathcal{L}_{\mathcal{D} \rightarrow \mathcal{P}}$  is parametrized to  $4\Delta x$ , the under resolved droplet might be removed by the volume restriction algorithm before to be transformed. It shows the complexity to parametrize the





Figure IV.9: Snapshots of 3D Splash Hybrid Two-way Av. correction  $32^3$  with  $\mathcal{L}_{\mathcal{P} \rightarrow \mathcal{D}} = 2\Delta x$  after coalescence at  $t/T_{ref} = [0.9, 1.1]$ .

$\mathcal{L}_{\mathcal{P} \rightarrow \mathcal{D}}$  since the transformation must not occur too close to the interface, and, not too far since the under resolved droplets could vanish. One of the goal would be to remove the volume restriction algorithm, we comment it later in the manuscript [chapter V].

The next part of our analysis focuses on the influence of the correction onto the physic of the splash. Then the most accurate method is selected to study the filter's size influences on the simulation. The One-way method is added on the analysis of the filter size.

### Interpolated velocity correction influence

The selected results are the Two-way Hybrid approach parametrized to  $Nx = 32$  and  $\mathcal{L}_{\mathcal{P} \rightarrow \mathcal{D}} = 4\Delta x$  without correction, with linear correction, and with averaged correction [section II.1], against ICM references at  $Nx = [16, 32, 64]$ . The results obtained for  $Nx = 16$ ,  $\mathcal{L}_{\mathcal{P} \rightarrow \mathcal{D}} = 2\Delta x$  and  $Nx = 32$ ,  $\mathcal{L}_{\mathcal{P} \rightarrow \mathcal{D}} = 2\Delta x$  are presented in an indicative way. For this comparison, the filter's length is set to  $\delta = 2.5 \cdot d_p$ . The kinetic liquid energy against characterist time is first studied [figure IV.11a].

For the configuration of interest,  $Nx = 32$  and  $\mathcal{L}_{\mathcal{P} \rightarrow \mathcal{D}} = 4\Delta x$ , the first peak, at  $t/T_{ref} = 1.$ , is slightly underestimated by all methods. Thus, the influence of the correction is not clearly seen. We observe that surface oscillations are well recovered by all methods and the second maxima is reached at the same instant for all methods,  $t/T_{ref} = 1.8$ . The results for the short distance of transformation  $\mathcal{L}_{\mathcal{P} \rightarrow \mathcal{D}} = 2\Delta x$  deviate from the reference, a strong overestimation of the kinetic energy is observed. It is seen that the 3D method is more sensitive to the distance of transformation than 2D results.

Then, the top/bottom interface against characteristic time is studied [figure IV.11b]. The overall interface evolution follows the results obtained for ICM 32 and there are no modifications for the different Two-way corrections. From the liquid kinetic energy and interface evolution, it is complex to observe differences between methods. To go further on our analysis, the detail results on the first liquid knetic energy peak magnitude, crater depth and CPU time are studied [table IV.7].

Case	$\frac{Ek_{liq,case}}{Ek_{liq,ICM,Nx_{case}}}$	$\frac{\max(Ek_{liq,case})}{\max(Ek_{liq,ref})}$	$\frac{y_{crater,case}}{y_{crater,ICM,Nx_{case}}}$	$\frac{y_{crater,case}}{y_{crater,ref}}$	$\frac{t_{CPU,case}}{t_{CPU,ICM,Nx_{case}}}$
ICM M32	1.0	0.925	1.0	1.030	1.0
OW 32_D4 S.& N.	0.966	0.894	1.007	1.037	0.908
TW 32 D4 $\delta = 2.5$ wo	0.964	0.892	1.0124	1.0423	0.846
TW 32 D4 $\delta = 2.5$ w Av.	0.964	0.892	1.010	1.040	0.852
TW 32 D4 $\delta = 2.5$ w Lin.	0.962	0.890	1.018	1.048	0.832

Table IV.7: Detailed analysis on the first liquid kinetic energy peak, the crater depth, and CPU time ponderated by own mesh resolution and reference for the 3D splash. The red color indicates a deviation of more than 10% and the green color a deviation of less than 3%.

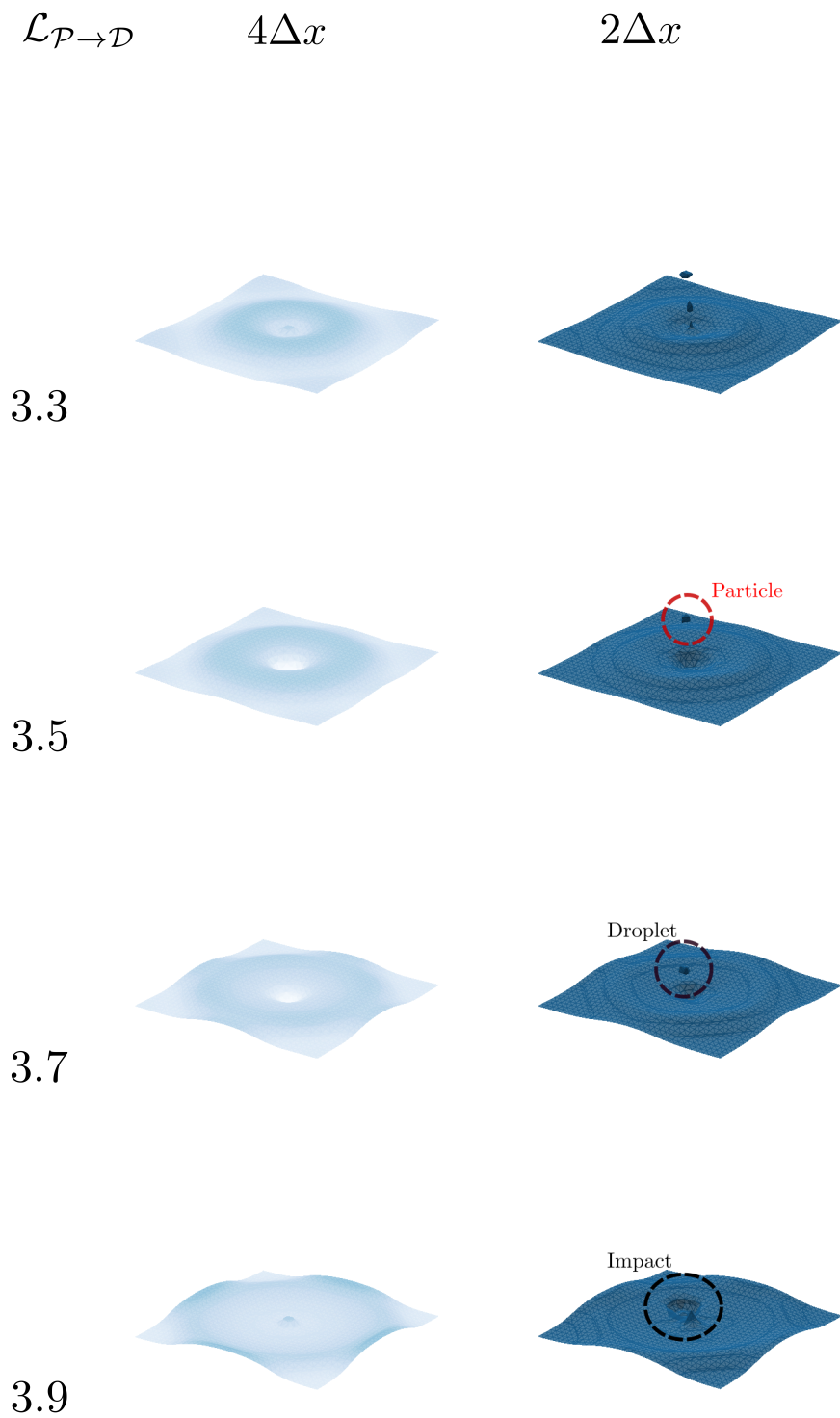


Figure IV.10: Snapshots of 3D Splash for configuration  $Nx = 32$   $\mathcal{L}_{\mathcal{P} \rightarrow \mathcal{D}} = 4\Delta x$  on the left and  $\mathcal{L}_{\mathcal{P} \rightarrow \mathcal{D}} = 2\Delta x$  on the right at  $t/T_{ref} = [3.3, 3.5, 3.7, 3.9]$ .

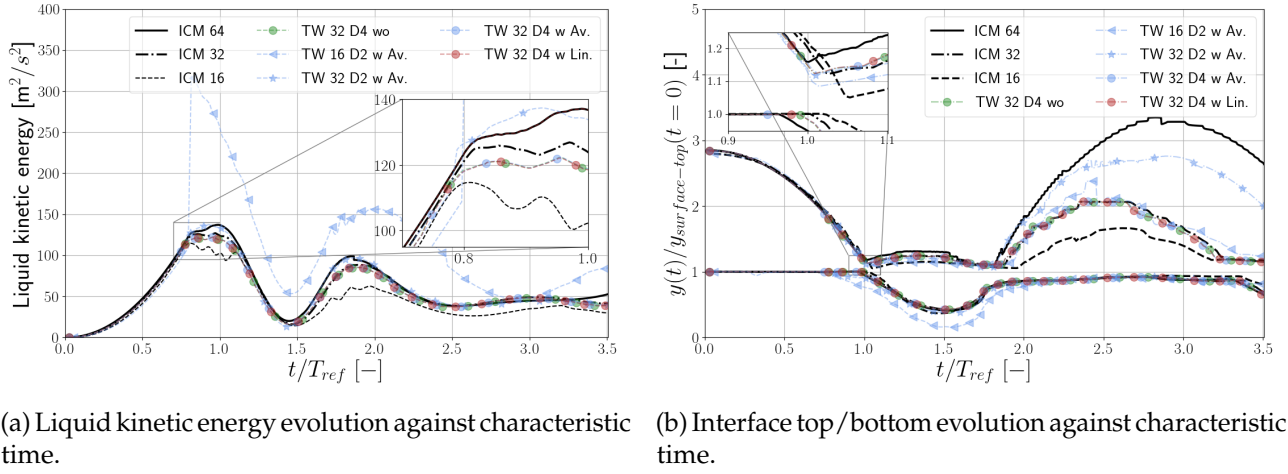


Figure IV.11: Two-way Hybrid without correction (green), with averaged correction (blue) and linear correction (red) with  $\delta = 2.5 \cdot R_p$  and ICM references with parameters set to  $Nx = 32$  and  $\mathcal{L}_{\mathcal{P} \rightarrow \mathcal{D}} = 4\Delta x$ . Two-way averaged correction results are included for  $Nx = 16$ ,  $\mathcal{L}_{\mathcal{P} \rightarrow \mathcal{D}} = 2\Delta x$  and  $Nx = 32$ ,  $\mathcal{L}_{\mathcal{P} \rightarrow \mathcal{D}} = 2\Delta x$ .

As expected the differences on the results are relatively small for the kinetic energy and crater depth with respect to the ICM at same mesh resolution. The min/max error are respectively of 3.2%/3.8% and 0.7%/1.2% showing that for this test case it is complex to discriminate a Two-way method. Moreover, it seems that the correction is not influencing the outcomes of the simulation. Our guess is that this is because the gravitational acceleration is dominant in this configuration, and that the terminal velocity is not reached.

It is observed that the CPU time consumption is reduced using Hybrid approach. The reason is that when the droplet is transformed into particle, whatever the approach is used, the CFL is less restrictive since the free surface at the bottom of the box does not evolve. To validate this assumption, the time step is plotted against the characteristic time for all configuration presented in table IV.7 [figure IV.12]. It is observed that during the time that the droplet is transported using Lagrangian algorithm, the time step is almost four times higher. At the instant of reversed transformation, particle toward droplet at  $t/T_{ref} = 0.7$ , the time step decreases recovering the order of the ICM simulation. These results are encouraging to use this method.

### Two-way filter size influence

The filter's length influence is studied using the Hybrid Two-way simulation with averaged interpolation correction, with size  $\delta = [1.0, 1.75, 2.5, 3.5] \cdot R_p$  and One-way method against ICM reference. The selected configuration is  $Nx = 32$  and  $\mathcal{L}_{\mathcal{P} \rightarrow \mathcal{D}} = 4\Delta x$ . First, the liquid kinetic energy evolution is studied [figure IV.13].

These results show that the smallest filter size,  $\delta = 1.0R_p$ , does not transport accurately the particle, see the high increase in liquid kinetic energy evolution. It yields to an under estimation of the energy peak after transformation and shows the influence of the filter size on the physic of the splash for this Hybrid approach. For results with  $\delta > 1.0R_p$  and One-way method, the physic of the splash is well recovered, we observe a convergence toward the liquid kinetic energy peak value. This value is lower than the value of ICM 32 and increasing the filter size will not permit to converge toward it since it appears that the highest peak is obtained for  $\delta = 1.75R_p$ . Moreover, it is observed that when the physic of the splash is respected, the filter size redistribution does not strongly modify the results. The study of the interface position does not modify those conclusions and are not studied in this section.

### IV.1.5 Summary

The results obtained for the 2D and 3D splash simulations showed that the most convenient method to transport particles is the Two-way method. Generally, the methods have been able to recover

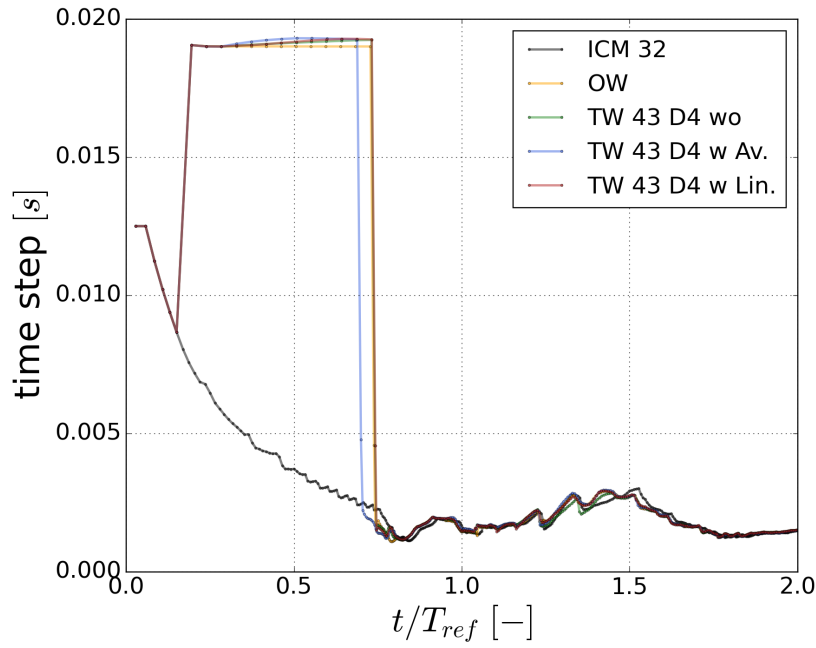


Figure IV.12: Time step evolution against characteristic time for reference simulation listed in table IV.7.

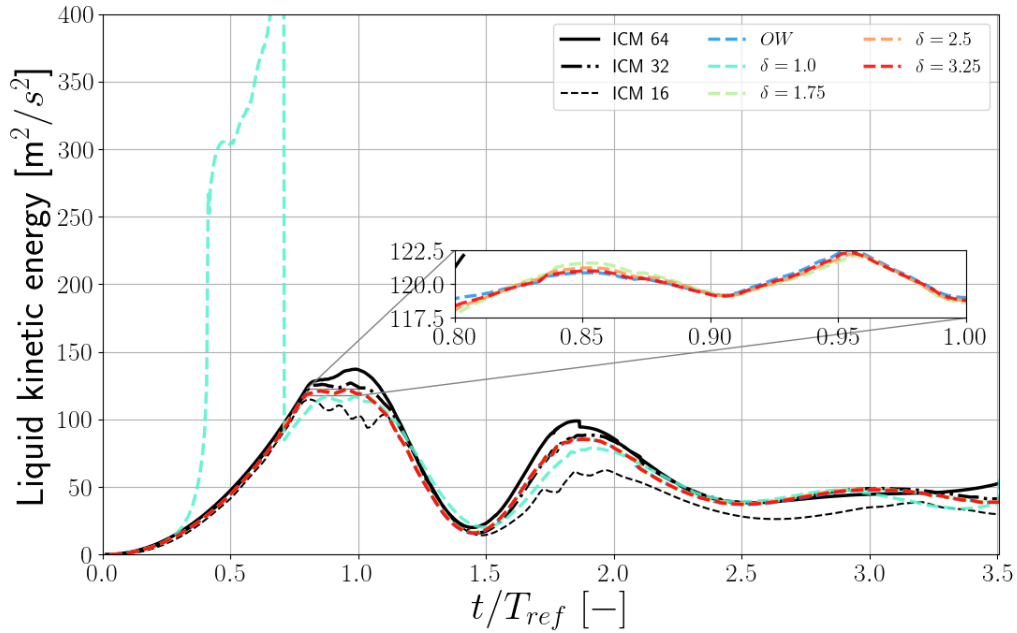


Figure IV.13: Liquid kinetic energy evolution against characteristic time for Two-way Hybrid with averaged interpolation correction results for  $\delta = [0., 1.0, 1.75, 2.5, 3.5] \cdot R_p$  and ICM references with parameters set to  $Nx = 32$  and  $\mathcal{L}_{\mathcal{P} \rightarrow \mathcal{D}} = 4\Delta x$ .

the physic of the simulation for a relatively complex test case. From the results of the free-falling sedimented particle [section II.4], we favor the Two-way method with averaged correction even though strong differences between implementations have not been observed on this simulation. Unfortunately, the results were promising for the IBM method in 2D but the 3D lacks of stability. More developments are required to improve this method for poorly resolved droplets.

The importance of the parametrization has been observed with a focus on the distance of transformation criteria. The conclusion is that the transformation from droplet toward particle and vice versa must respect a certain distance because when the transformation is relatively close to the interface, the reconstruction of the area influences locally the evolution of the simulation. This modification yields to a loss of the physic of the simulation, in 2D and 3D. See for example the results obtained when the distance of transformation was set to 2 cells. A balance must be found in order to avoid Eulerian fields modification meanwhile enhancing transformation from droplet toward particle before volume resitraction is used.

One of our goal was also to evaluate momentum's redistribution toward the free surface because it can influence the results of the simulation. In our study, no modifications were observed due to the liquid redistribution and more tests are required to study its influence.

Finally, the computational time is improved using the Hybrid method and it is eventually resulting from a less restrictive CFL because the under resolved interface is no longer transported.

## IV.2 Plateau-Rayleigh instability of a round liquid jet

The Plateau-Rayleigh instability is set up to observe a main isolated droplet, ideal to represent transformations in the primary atomization area. Due to breakup, surface oscillation are observed until droplet converges toward its spherical shape [figure IV.14]. This test case is ideal because we can show the advantages and drawbacks of defined morphological criteria since droplets regime evolves [section III.4]. This analysis is coupled with the introduction of a physical criterion based on the inside droplet velocity field. Then, ICM and Hybrid approaches influence are compared on the outcome of the simulation.

The first analysis is performed on a refined Plateau-Rayleigh atomization simulation in a large domain in order to observe droplets' shape evolution until it reaches a sperical state. A pattern similar to the results observed on the Lamb oscillatory droplet is observed [section III.4]. The goal is to show the weaknesses of morphological parameters while introducing our reflections on the construction of a physical parameter inspired from shear breakup modelling [section I.1.3]. Then, the same configuration is studied with coarser mesh to compare ICM coarse results and Hybrid approaches against the refined simulation, considered as reference.

The section is organized as follows, the details of the physical and numerical configuration are given first. Next, morphological analysis results are presented. Finally, the results obtained for ICM and Hybrid methods against highly refined ICM simulation are commented.

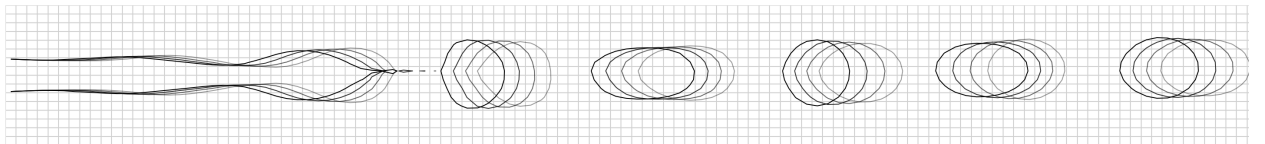


Figure IV.14: Illustration of the Plateau-Rayleigh atomization breakup and morphological evolution of the droplet.

### IV.2.1 Plateau-Rayleigh configuration

This study follows the work of [Moallemi et al., 2016, Denner et al., 2017] where the configuration is thoroughly detailed. The liquid jet is atomized along  $x$  direction inside a domain of size  $Lx = 7.0 \times Ly$  and  $Ly = Lz$ , with  $D_{inj} = \frac{Ly}{8}$ . In this configuration, the domain length is increased, 1.4 times reference

[Moallemi et al., 2016, Denner et al., 2017], to study droplets' morphological evolution and to ensure that the filter of the Hybrid Two-way approach is entirely redistributed inside the domain. Initial parameters are resumed below:

Domain Size [m]	$\vec{x}_{cyl,init}$ [m]	Diameter [m]
$[14. \cdot 10^{-3}, 2. \cdot 10^{-3}, 2. \cdot 10^{-3}]$	$[:, Ly/2., Lz/2.]$	$\frac{Ly}{8} = 2.5 \cdot 10^{-4}$

Table IV.8: Plateau-Rayleigh atomization's computational domain initialization.

The physical parameters used for both phases, liquid (droplet) and gas (carrier) are referred in the table IV.9 where the gravity is set in the direction of atomization. Dimensionless number are  $We = \frac{\rho_{liq} U_0^2 r_0}{\sigma} = 6.829$  and  $Oh = \frac{\mu}{\sqrt{\rho_{liq} \sigma r_0}} = 9.44 \cdot 10^{-3}$ , showing that the dominant breakup regime is due to the Plateau-Rayleigh instability.

Radius [m]	$\rho_l$ [kg.m <sup>-3</sup> ]	$\mu_l$ [kg.m <sup>-1</sup> .s <sup>-1</sup> ]	$\rho_g$ [kg.m <sup>-3</sup> ]	$\mu_g$ [kg.m <sup>-1</sup> .s <sup>-1</sup> ]	$\vec{g}$ [m.s <sup>-2</sup> ]	$\sigma$ [kg.s <sup>-2</sup> ]
$Ly/8.$	997.0	$9.0 \cdot 10^{-4}$	1.18	$1.85 \cdot 10^{-5}$	9.81, 0, 0	0.073

Table IV.9: Plateau-Rayleigh atomization's physical properties.

The perturbation to generate Plateau-Rayleigh instability is implemented through the liquid cylinder velocity profile. First, the velocity field is initialized inside the liquid cylinder along x-component, this is the initial velocity  $U_0 = 2$  [m.s<sup>-1</sup>]. Then, the perturbation is included inside a sinusoidal velocity profile on the injection boundary condition:

$$U_{inlet}(t) = U_0 \left[ 1 + \delta'_0 \sin \left( \frac{2\kappa U_0 t}{D_{inj}} \right) \right]. \quad (IV.1)$$

In this equation the initial dimensionless deformation amplitude is expressed as  $\delta'_0$ , set to  $\delta'_0 = 0.08$ , obtained from a derivation of the diameter's perturbation:

$$\eta'_0 = 2 \times \epsilon_0 / D_{inj},$$

with  $\eta'_0$  the dimensionless disturbance and  $\epsilon_0$  the radial disturbance [Moallemi et al., 2016]. The initial diameter is  $D_{inj}$  and is equivalent to  $\frac{Ly}{8}$ . The wavelength is set to  $\kappa = 0.697$  in order to recover the most unstable mode that leads to only one main droplet. It is recalled that injection is done in quiescent air, computational domain, velocity profile and boundary conditions are schemed on figure IV.15.

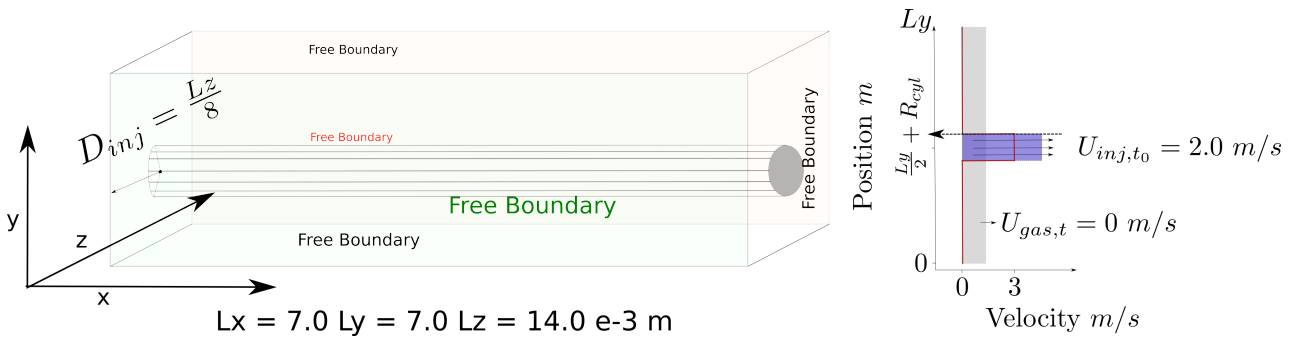


Figure IV.15: Computational domain, velocity profile and boundary conditions of the Plateau-Rayleigh atomization configuration.

## IV.2.2 Numerical configuration

### Campaign of simulations

As introduced, two grid sizes are used for this study, one fine enough to be considered as reference, describing accurately the physic of the instability. A second, considered coarse, to study transformation

from droplet toward particle in the Hybrid framework. The latter is configured to generate isolated droplets in the *transformable size* range [section II.4], approximately  $\frac{d_d}{\Delta x} \approx 5$ . Through linear analysis, the ideal numerical resolution for the liquid jet is:  $D_{inj} = d_d/1.89 = 2.65\Delta x$ . The challenge is to represent the physic of the instability at such small number of cells across injection diameter. For this numerical resolution, it was not possible to observe the instability grows, so the coarse resolution is set to  $D_{inj} = 3\Delta x$ . The expected droplets size is of the order of  $\frac{d_d}{\Delta x} \approx 5.7$  cells across the diameter, thus using the Hybrid approach remains coherent. The simulations are listed below.

Method	Eul <sub>fine</sub>	Eul <sub>coarse</sub>	Hyb. One-way	Hyb. Two-way
[Nx;Ny;Nz]	[448, 64, 64]	[168, 24, 24]	[168, 24, 24]	[168, 24, 24]
$\Delta x$ [m]	$3.13 \cdot 10^{-5}$	$8.33 \cdot 10^{-5}$	$8.33 \cdot 10^{-5}$	$8.33 \cdot 10^{-5}$
$D_{cylinder}/\Delta x$ [–]	8.0	3.0	3.0	3.0

Table IV.10: Simulations performed for Plateau-Rayleigh instability study, in red reference from refined ICM.

For the fine grid, ejected droplets have approximately  $15\Delta x$  cells across the diameter, it permits a detailed morphological and physical analysis.

### Hybrid method parametrization

The conditions of transformation toward particles are first described, then, the Lagrangian tracking model.

We commented the complexity to find an equilibrium for the distance criteria,  $\mathcal{L}_{\mathcal{P} \rightarrow \mathcal{D}}$  and  $\mathcal{L}_{\mathcal{D} \rightarrow \mathcal{P}}$ , [section IV.1]. Ideally, they might be set to  $\mathcal{L}_{\mathcal{D} \rightarrow \mathcal{P}} = 3 \times R_d$  and  $\mathcal{L}_{\mathcal{P} \rightarrow \mathcal{D}} = 0.5 \times \mathcal{L}_{\mathcal{D} \rightarrow \mathcal{P}}$ . In this simulation, the distance between isolated droplets is of the order of the ideal threshold. Thus, to ensure transformations from droplets toward particles, distance criteria are set to  $\mathcal{L}_{\mathcal{D} \rightarrow \mathcal{P}} = 1.5 \times R_d$  and  $\mathcal{L}_{\mathcal{P} \rightarrow \mathcal{D}} = 0.5 \times \mathcal{L}_{\mathcal{D} \rightarrow \mathcal{P}}$ . Morphological criteria have been conserved relatively high in order to avoid early transformations; *Flattening* > 0.92 and  $\Delta \tilde{S} > 0.95$ . To ensure that all droplets are transformed into particles, the numerical resolution threshold is set to  $8.5\Delta x$ .

The two Hybrid approaches, using respectively One-way and Two-way methods, are then detailed. The One-way method follows motion equation [equation II.10]. The Two-way method is used considering correction on interpolated velocity  $\vec{u}_{f@p}$ , implying  $\delta = \sqrt{2/9\pi}\lambda$ . The interpolation area is set to  $\lambda = 2.5R_p$ . For both Hybrid approaches, ICM droplets with a diameter smaller than a threshold,  $d_d/\Delta x < 1.$ , are transformed into point particle without checking morphological transformation criteria.

### IV.2.3 Results

The goal of this simulation is to generate an isolated droplet transformed in particle. This droplet oscillates until it reaches a spherical stable shape. The morphological evolution is expected to follow a prolate/oblate shape variation passing by spherical state. In Hybrid approach, the transformation of a droplet toward particle is considered *on the fly* when criteria are validated, even though few iterations later they are no longer validated. The motivation to avoid using history of droplets' motion is the complexity to track and identify at each iteration all droplets, moreover, it has a relatively high computational cost [section III.2]. Then, an *on the fly* physical criterion, which does not depend on the morphological shape of the droplet, is studied.

Our aim is to work on the velocity field inside the droplet, accessible through the tagged field [section III.2]. Two criteria have been proposed, the first one uses the difference between the velocity of the droplet and the maximum velocity at its interface [Renardy, 2008]. The results that have been reached in this analysis were not satisfactory, and are not presented. The second criterion is based on the dispersion of velocity inside the droplet, since interesting results have been obtained, the methodology is described below.



As commented, the second part of this section focuses on the Hybrid approaches vs ICM results. Following the methodology detailed in chapter III, Eulerian fields are updated to ensure mass/momentum conservation at each transformation. Since the distance of transformation is reduced in this study, near breakup area statistics such as averaged droplets' size and breakup length are studied to quantify transformation's influence. Then, statistics on the dispersed area such as particles/droplets velocity/position motion are compared to conclude on the Hybrid approach that is used.

## Morphological analysis

The results of the refined simulation are stored at constant time step, large enough to consider all droplets independent, a total of 2,000 droplets is used to construct those statistics. The used morphological criteria are *Flattening* and  $\Delta\tilde{S}$  [section III.4] and a convergence toward sphere is expecting downstream to the jet. It is recalled that their values for a sphere are *Flattening* = 1 and  $\Delta\tilde{S} = 1$ . They are not obtained since a small error is included, below 0.5% for this resolution [section III.4], in the computation of length and surface quantities, which is passed on morphological criteria computation.

The evolution of these criteria is studied through their distance from the injector (along x-component), it is equivalent to their time spent in the domain ( $t = \frac{U_{inj}}{Lx} = 7 \cdot 10^{-3}$  [s]). Since droplets size and velocity have an influence on morphological evolution, those information are considered scaled by dimensionless velocity,  $u_{d,x}/V_{inj}$  and numerical size  $d_d/\Delta x$ .

### Shape evolution :

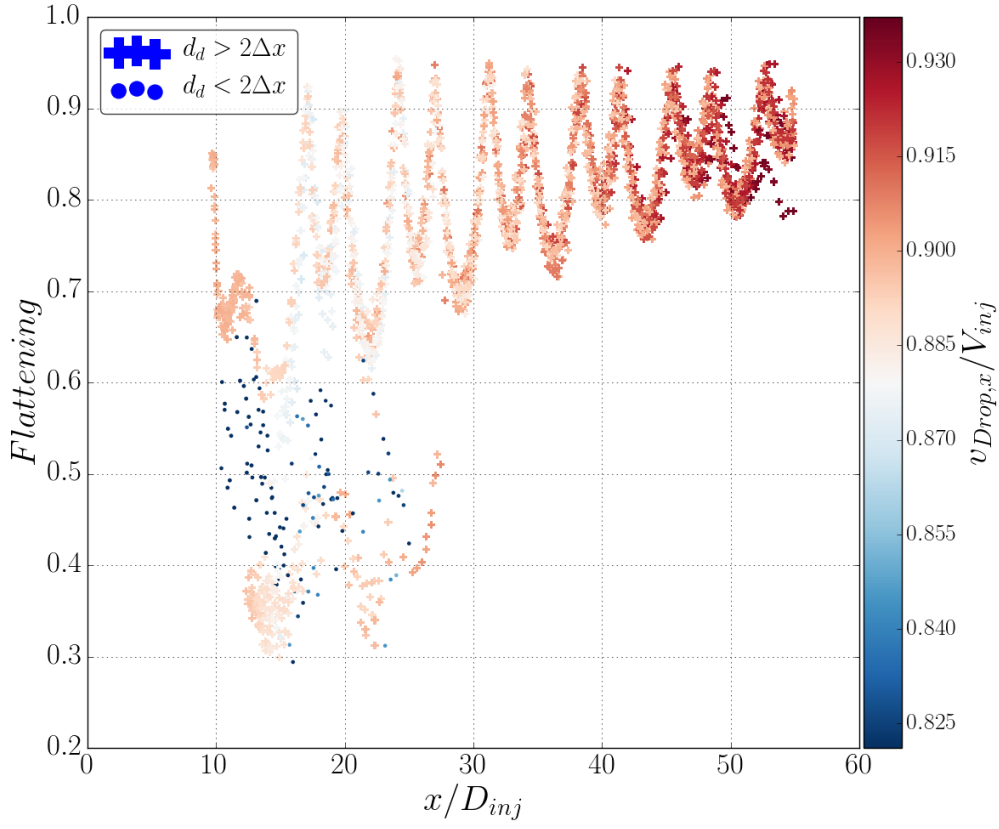
Droplets morphological evolution, respectively *Flattening* [figure IV.16a] and  $\Delta\tilde{S}$  [figure IV.16b], against their dimensionless position are studied. A color map is used to represent the dimensionless velocity and the marker style represents the dimensionless droplet size scaled by the mesh length. It shows two classes of droplets that are called in this section the *small* droplets and main resolved droplets. Since small droplets, (circle marker), vanish above  $x/D_{inj} = 30$ , due to coalescence with bigger droplets, our study focuses on the resolved droplets.

The *Flattening* evolution describes an oscillatory behavior. Near the breakup area we observe a wide variation of *Flattening* because some droplets coalesce with small droplets. This variation stops after  $x/D_{inj} > 30$ , then its value varies on the range  $\approx 0.7 - 0.95$ . It shows that the surface oscillations decrease downstream to the jet, and that the droplet can be considered as converging toward sphere. We also observe droplets near injector, for example at  $x/D_{inj} \approx 18$ , that validate morphological criteria of transformation since *Flattening*  $\approx 0.93$ . An early transformation, close to the breakup area, leads to two consecutive issues. First, it confirms the weakness of *on the fly* morphological criteria. At this stage, the droplet is spherical and validates the transformation hypothesis meanwhile it is far from being converged toward spherical shape, see its evolution downstream to the jet [figure IV.16a]. Then, a transformation close to the breakup area appears, it can modify breakup phenomenon, and shows the importance to coupled morphological information with other criteria. Those concerns are later discussed.

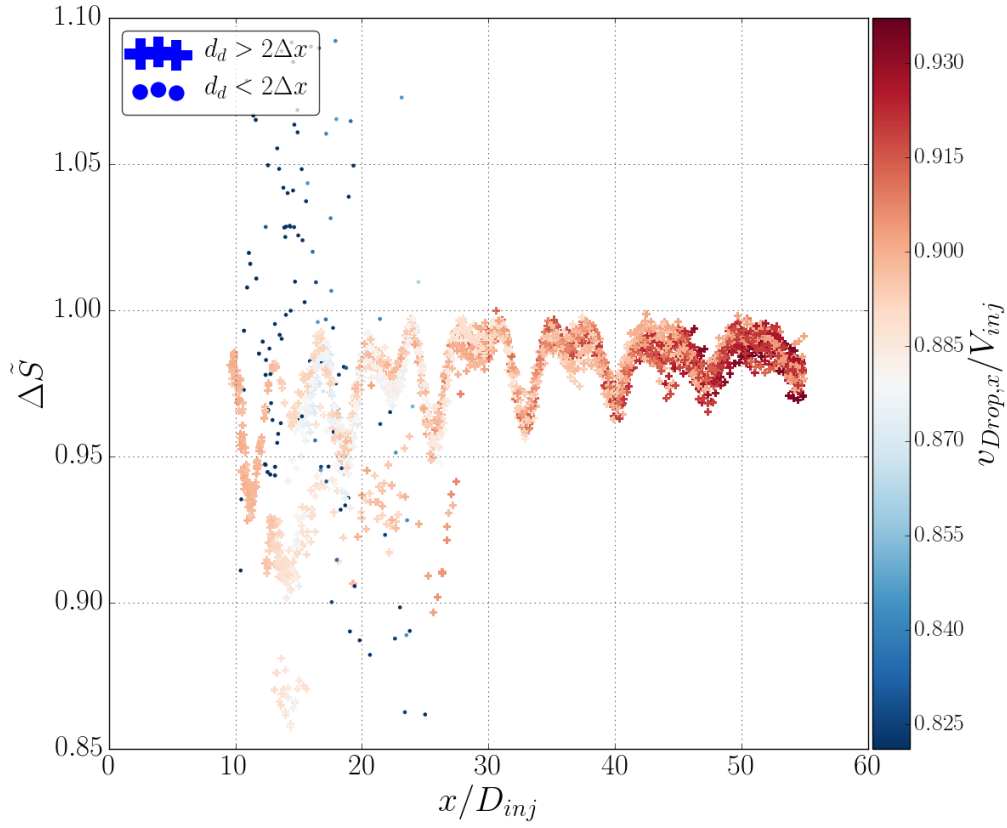
The criterion  $\Delta\tilde{S}$  shows that the surface of the small droplets is not accurately computed since it overcomes 1, impossible from our implementation. This error is understood through poor numerical resolution, it is supposed that a cluster of small droplets are identified through the detection algorithm and might not be considered in this analysis [section III.4]. This has not been observed for *Flattening*, and it shows the importance of coupling morphological information. For resolved droplets, this criterion varies from  $0.85 < \Delta\tilde{S} < 0.98$  in the vicinity of the breakup length. Then, oscillations are observed along the position and it decreases downstream to the jet converging toward  $\Delta\tilde{S} \rightarrow 0.98 \approx 1$ .

For both criteria, similar oscillations are observed and we define them using local minimums to compare the information that they give on droplets morphological state. This period is presented for the *Flattening* evolution, for example on the range  $x/D_{inj} = 36$  to  $x/D_{inj} = 43$  where two local minimums are observed [figure IV.16a]. This range of study is selected because small droplets are no longer in droplets' vicinity. The morphological evolution for both parameters on this range is resumed [table IV.13].





(a)



(b)

Figure IV.16: Droplets morphological evolution against the distance to the injector, *Flattening* [figure IV.16a] and  $\Delta\tilde{S}$  [figure IV.16b]. Color map represents the ratio between the velocity of the droplet along  $x$  and the velocity of injection  $u_{drop,x}/V_{inj}$ . The size of the marker represents the number of cells across the diameter.

$x/D_{inj} [-]$	36	38	40	41	43
$Flattening [-]$	0.72	0.94	0.78	0.94	0.76
$\Delta\tilde{S} [-]$	0.985	0.995	0.96	0.995	0.985

Table IV.11: Droplets morphological evolution on the range  $x/D_{inj} = 36$  to  $43 [-]$  for  $Flattening$  and  $\Delta\tilde{S}$  morphological criteria.

For both criteria, the local maximums are reached at the same distance to the injector;  $x/D_{inj} = [38, 41]$ , it converges toward a spherical shape. The extreme minimum values are not reached at the same distance from the injector and it shows that the two morphological criteria do not give the same information for those spheroids. This difference is due to the use of distance information to construct the  $Flattening$  while  $\Delta\tilde{S}$  is constructed through surface information.

The  $Flattening$  considers only the smallest/biggest distances from droplets' gravity center to its interface, respectively  $a > b$ . In spheroid description, a third dimension is required to discriminate between oblate,  $a = c$ , or prolate  $a = b$  [section III.4]. Then, this criterion cannot give this information.

From the construction of  $\Delta\tilde{S}$ , the discrimination can be recovered since  $S_{Oblate} < S_{Prolate}$ . It gives the following classification for the surface criterion:  $\Delta\tilde{S}_{Oblate} < \Delta\tilde{S}_{Prolate} < \Delta\tilde{S}_{Sphere}$  since the volume is constant. It is possible to define that the droplets' morphological evolution follows the pattern oblate-sphere-prolate-sphere-oblate.

So far, it is observed that coupling morphological information enhances the discrimination of under resolved structures. The droplets shape evolution is accurately described through our criteria, describing the prolate/oblate oscillatory regimes. Nevertheless, the morphological information are not sufficient to determine if a droplet has reached a stable spherical shape, see the peak at  $x/D_{inj} = 18$

During the transport of the droplet we commented that its shape evolves in a oblate-sphere-prolate-sphere-oblate pattern. For simplicity, the oscillatory regime will refer to that pattern in the present section. During these modifications, the velocity of the droplet evolves, converging toward the velocity of injection downstream to the jet [figure IV.16]. For example, at  $30 < x/D_{inj} < 40$ , the range of velocities varies from  $0.885 \times v_{Drop,x}/V_{inj}$  to  $0.92 \times v_{Drop,x}/V_{inj} [-]$ . Our hypothesis is to study the velocity field inside in order to provide an information of the future droplets' shape evolution. This strategy is described below, the first step is the analysis of the extracted velocity field, then, the criterion construction and finally its comparison against morphological criteria.

Velocity field extraction is done using the Cartesian grid, cells belonging to the droplet are extracted (identified with tagging algorithm and  $VoF$  field, and we compute the histogram of velocities among each x-y-z component. From these histograms we extract the mean, standard deviation and skewness among each x-y-z component, respectively  $\mu(v_{Drop})$ ,  $\sigma(v_{Drop})$  and  $(\mu - v)/\sigma(v_{Drop})$ . As reference, the velocity of the droplets extracted from *Archer* is given.

The methodology is presented on a representative time step where the oscillatory shape evolution is visible [figure IV.17]. It appears that the flow in droplet vicinity evolves along the jet, downstream to the jet, an uniform flow due to gravitational acceleration is observed. Near breaking area, the velocity around the droplet is not uniform, for example droplet number 2 where a low velocity magnitude is located below it. An influence of the outside velocity profile inside the droplet is expected.

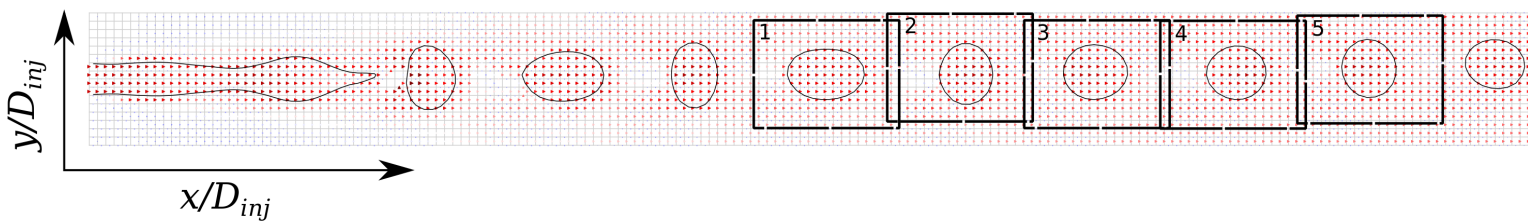


Figure IV.17: 2D velocity field with *Level-set* iso contour (black) of Plateau-Rayleigh instability simulation.

The five highlighted droplets showing oscillatory regime [figure IV.17] are used. Their inside flow is extracted and analyzed through an histogram description for each component [figure IV.18]. These histograms are computed with approximately  $\frac{4\pi}{3}(R_p/\Delta x \approx 7.5)^3 \approx 1400$  cells per droplet in each direction. For each component, a unimodal distribution is observed, the peaks are evolving toward the velocity of injection for the x-component and toward zero for other directions. The distributions are not symmetric and their tails are not always located at the same position, it is expected to observe a pattern from the standard deviation/skewness. These information are resumed in the table IV.13.

Droplet	1 - Oblate	2 - Sphere	3 - Prolate	4 - Sphere	5 - Oblate
<i>Flattening</i> [–]	0.663	0.854	0.825	0.857	0.9
$\Delta\tilde{S}$ [–]	0.974	0.978	0.991	0.996	0.986
<b>x-component</b>					
$v_{Drop,x}$ [ $m.s^{-1}$ ]	1.7533	1.7996	1.7829	1.8171	1.8078
$\mu(v_{Drop,x})$ [ $m.s^{-1}$ ]	1.6843	1.7330	1.7104	1.7430	1.7369
$\sigma(v_{Drop,x})$ [ $m.s^{-1}$ ]	0.1564	0.2015	0.1631	0.2164	0.1565
$(\mu - v)/\sigma(v_{Drop,x})$ [–]	-0.207	0.105	0.296	0.078	0.257
<b>y-component</b>					
$v_{Drop,y}$ [ $m.s^{-1}$ ]	0.0161	0.0123	0.0182	0.0119	0.0211
$\mu(v_{Drop,y})$ [ $m.s^{-1}$ ]	0.0107	0.0114	0.0204	0.0118	0.0225
$\sigma(v_{Drop,y})$ [ $m.s^{-1}$ ]	0.0795	0.1208	0.0864	0.0999	0.0882
$(\mu - v)/\sigma(v_{Drop,y})$ [–]	-0.075	-0.031	-0.023	-0.117	-0.085
<b>z-component</b>					
$v_{Drop,z}$ [ $m.s^{-1}$ ]	0.0076	0.0157	0.0145	0.0240	0.0181
$\mu(v_{Drop,z})$ [ $m.s^{-1}$ ]	0.0044	0.0160	0.0151	0.0287	0.0236
$\sigma(v_{Drop,z})$ [ $m.s^{-1}$ ]	0.0658	0.1208	0.0859	0.1063	0.0922
$(\mu - v)/\sigma(v_{Drop,z})$ [–]	0.026	-0.013	-0.030	-0.055	0.0138

Table IV.12: *Flattening*,  $\Delta\tilde{S}$ , *Archer* velocity, histogram's mean, standard deviation and skewness [figure IV.18] from the five successive droplets [figure IV.17].

First, it is observed that *Archer* droplets velocities and the mean of histograms are different. The reason is that droplets' velocity is weighed by the volume fraction, nevertheless, the difference remains relatively small, for example  $v_{1,x} = 1.04 \times \mu(v_{1,x})$ . These errors are considered and accepted in our analysis. Although, histograms' skewness evolves with respect to droplets' location, but a clear tendency is not observed so we do not comment those results.

The series of histograms following x-component is considered. A velocity variation appears inside the droplets, in the range 1 – 2.5 [ $m.s^{-1}$ ]. The wider variation is observed for the droplets 2 and 4 [table IV.13], it is identified as the stage when droplets are considered as spheres. It yields to the higher standard deviations values, respectively  $\sigma(v_{2,x}) = 0.2015$  [ $m.s^{-1}$ ] and  $\sigma(v_{4,x}) = 0.2164$  [ $m.s^{-1}$ ]. The smaller *Flattening* values, droplet 1, has the smaller dispersion of velocity:  $\sigma(v_{1,x}) = 0.1564$  [ $m.s^{-1}$ ]. The last droplet is ambiguous since we have an increase of its *Flattening* and a decrease of its surface variation  $\Delta\tilde{S}$ , it is not commented. From the x-component analysis, it is observed that the standard deviation evolves with the flow inside the droplet. We suppose that a complementarity can be observed in our analysis coupling the velocity dispersion and the morphological criteria.

Observations are similar for y-z directions since we have a symmetry along x component, the conclusions are similar. A trend is observed for the standard deviation similar to the one for x direction, maximal values are reached for droplets 2 and 4. It confirms that coupling this information with morphological criteria can give more insight about droplets' state. The standard deviation magnitude evolution against its distance to the injector is studied for our sample of droplets [figure IV.19]. Each velocity field components are used to compute it:

$$|\sigma(v_{Drop})| = \sqrt{\sigma(v_{Drop,x})^2 + \sigma(v_{Drop,y})^2 + \sigma(v_{Drop,z})^2}$$

An evolution similar to the *Flattening* oscillatory regime appears, and a convergence toward  $|\sigma(v_{Drop})| \approx 0.3 - 0.4 [m.s^{-1}]$  is reached at  $x/D_{inj} = 45$ . The higher magnitude is obtained near the injector, at droplets' generation. In this area, it is recalled that small droplets coalesce with resolved droplets, it is possible to have a perturbation of the velocity field due to such events, complicating comments.

Above  $x/D_{inj} > 22$ , the oscillatory regimes is clearly observed [figure IV.16]. For example on the range  $36 < x/D_{inj} < 43$ , the local minimums are recovered:  $|\sigma(v_{Drop})| = [0.25, 0.27] [m.s^{-1}]$ . Following the velocity field analysis of the five droplets [figure IV.17], the complexity to determine a correlation between morphological criteria and velocity dispersion was commented since they exhibit a different convergence. However, same oscillatory regime is observed on the same period, it is supposed that a correlation between the shape of the droplet and the velocity dispersion exists. Eventually, the wider is the dispersion, the flattened is the droplet and vice versa.

To evaluate our hypothesis, morphological criteria, *Flattening* [figure IV.20a] and  $\Delta\tilde{S}$  [figure IV.20b], are colored by the standard deviation. Since oscillatory regime is reached for the same period, its evolution is compared on the range  $x/D_{inj} = [36 : 43]$ , morphological information are resumed in table IV.13. The evolution for the standard deviation is listed in table IV.13.

Shape	Oblate	Sphere	Prolate	Sphere	Oblate
$x/D_{inj} [-]$	36	38	40	41	43
$ \sigma(v_{Drop})  [m.s^{-1}]$	0.25	0.38	0.285	0.415	0.275

Table IV.13: Droplets standard deviation,  $|\sigma(v_{Drop})|$ , evolution on the range  $x/D_{inj} = 36$  to 43.

It is recalled that the oscillatory regime follows oblate-sphere-prolate-sphere-oblate evolution. Our analysis is first focused on the *Flattening* [figure IV.20a]. The first stage, from  $x/D_{inj} = 36$  to  $x/D_{inj} = 38$  (oblate toward sphere), shows an increase of velocity dispersion, the flow inside the droplet evolves. At  $x/D_{inj} = 38$ , the *Flattening* reaches its maximum resulting in a decrease of the dispersion inside the droplet.

The second stage, from  $x/D_{inj} = 38$  to  $x/D_{inj} = 40$  (sphere toward prolate), does not show a clear evolution of the standard deviation. From  $x/D_{inj} = 40$  toward  $x/D_{inj} = 41$ , the spherical shape is recovered and it is expected to observe an uniformization of the flow field inside the droplet, similarly to the range  $x/D_{inj} = 36$  to  $x/D_{inj} = 38$ . However, the opposite appears: the dispersion inside the droplet increases to reach its local maximum:  $|\sigma(v_{Drop})| = 0.415 [m.s^{-1}]$ . At the end of the oscillatory regime, the *Flattening* decreases to go from sphere toward oblate, the velocity dispersion decreases too.

The surface criterion [figure IV.20b], shows on this period two strong variations on the range sphere-prolate-sphere at  $x/D_{inj} = [38 - 40 - 41]$ . Again, on this range the maximum for the velocity dispersion is recovered. From our results, it is observed that when droplets are in oblate shape, the standard deviation is the smaller, when they are in prolate shape, the standard deviation reaches its maximum. A transitory regime is observed for the sphere shapes. Our guess is that velocity field in the droplet is more homogeneous when the droplet is elongated perpendicularly to the direction of injection. In prolate shape, droplets are elongated in the direction of injection, the inside velocity field is less homogeneous. It is supposed that since more energy is required to go from sphere to prolate than sphere to oblate, it yields to a higher perturbation of the velocity field inside the droplets.

Finally, it is complex to comment on the implementation of a criterion based on the velocity field in the droplet using the standard deviation. The reason is that when a droplet is randomly extracted from the series of data, it is not possible to determine the shape of the droplet and its future evolution *on the fly*. The reason is the lack of scaling laws determining what is the expected standard deviation inside a stable droplets. Nevertheless, combined to the morphological information, it provides an interesting overview for the droplets' morphological evolution.

### Summary :

To conclude, morphological criteria describe accurately the evolution of the droplet and gives a good description of its state. Moreover, their use shows a weakness of the Hybrid approach: it is

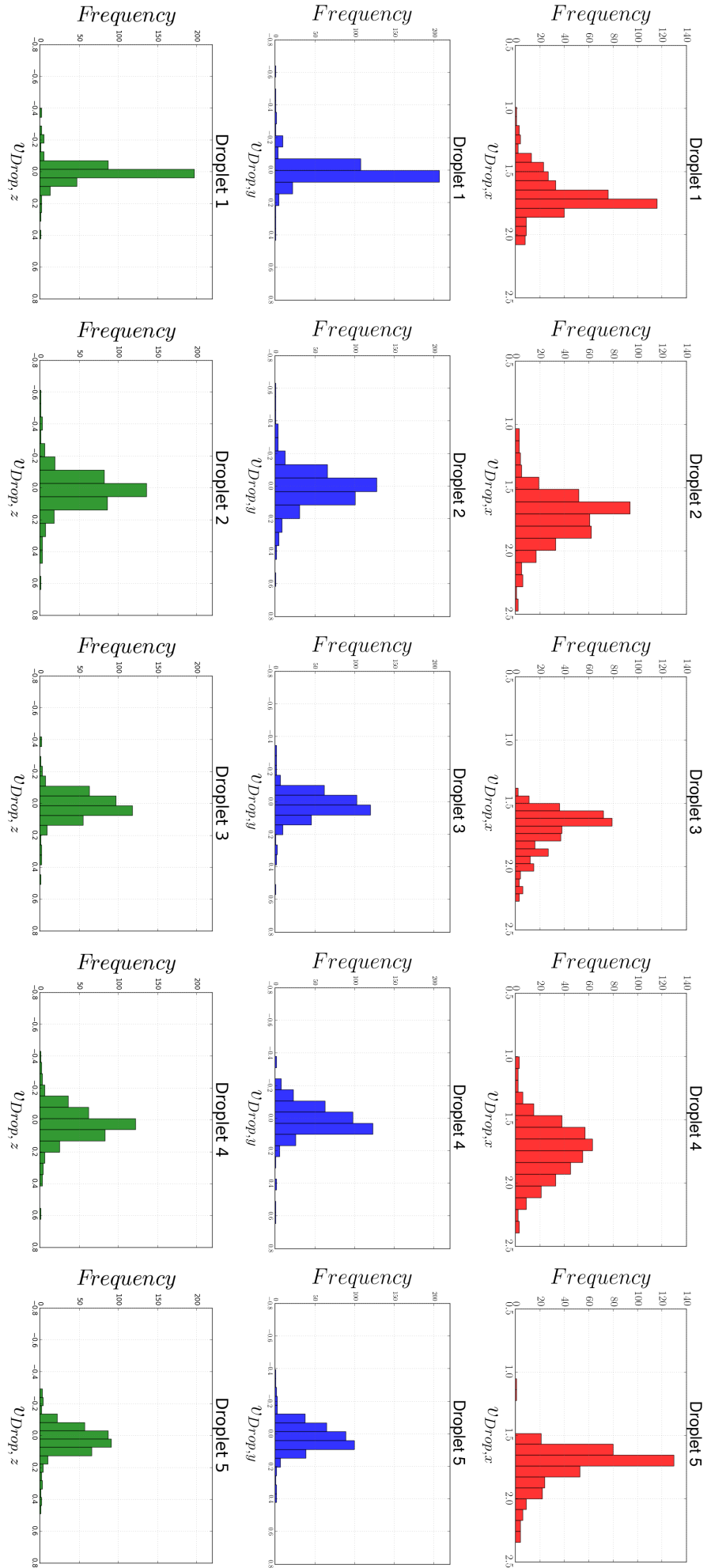


Figure IV.18: Five droplets representing oscillatory regime selected from figure IV.17. Extracted velocity histograms are shown for each x-y-z component (top to bottom). *Archer* droplet's velocity, mean velocity, standard deviation and skewness given in table IV.13.

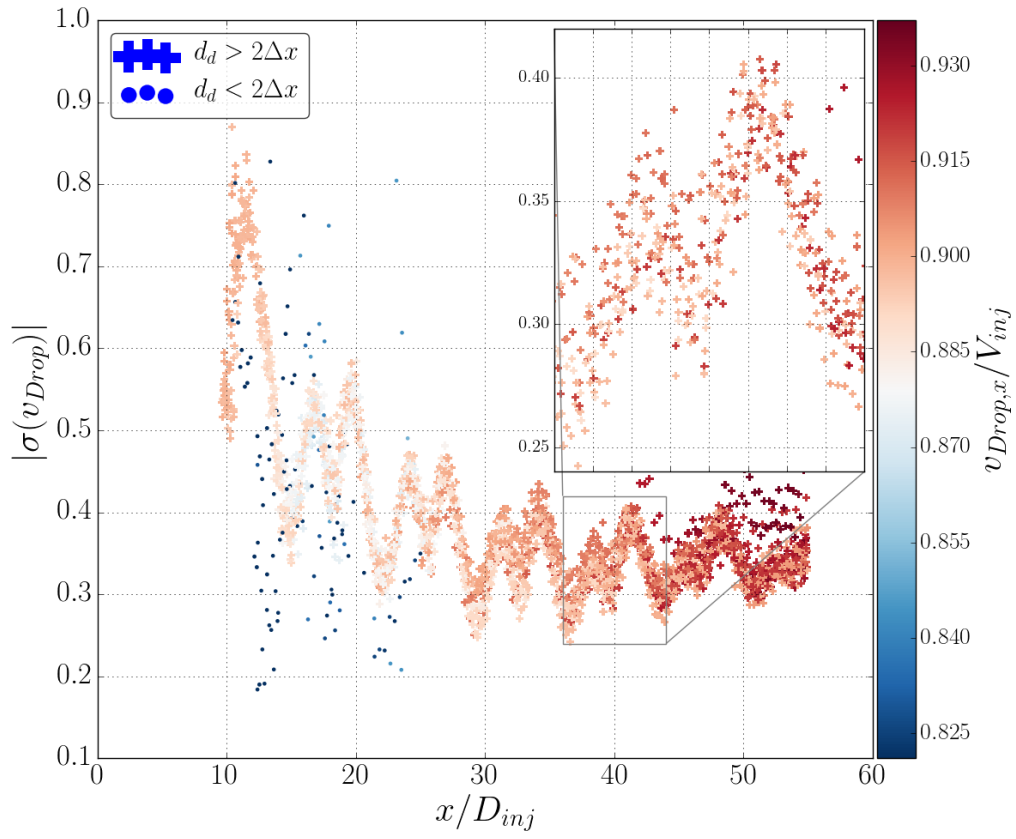
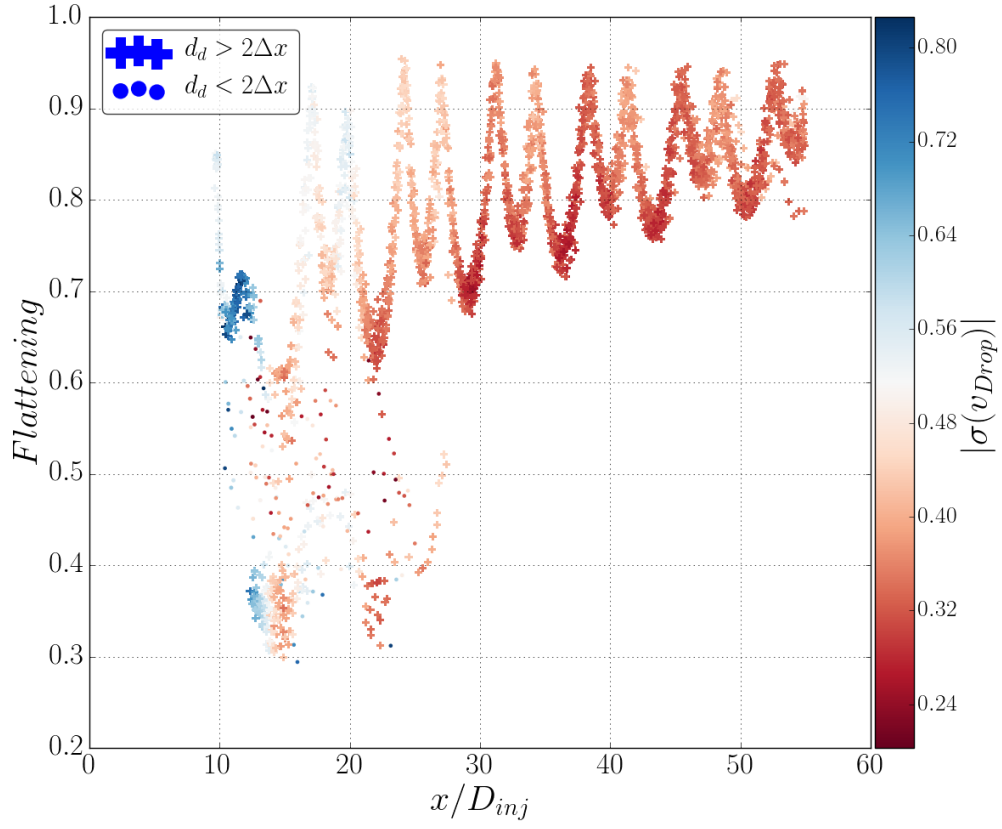
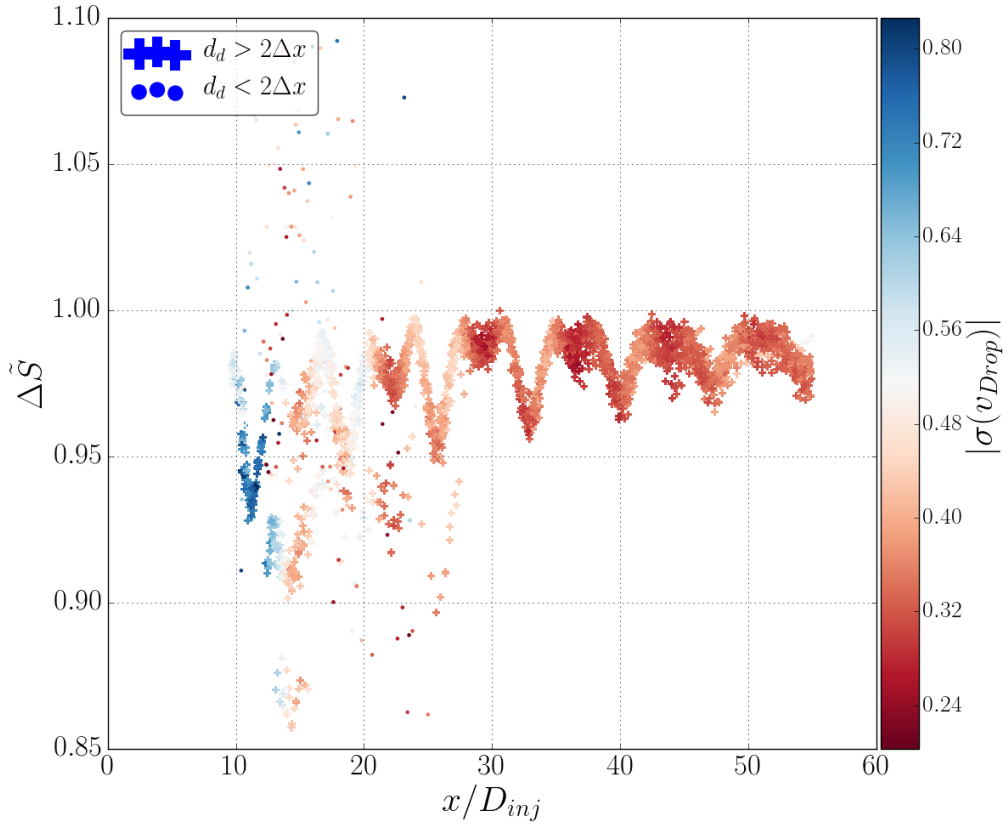


Figure IV.19: Magnitude of the standard deviation evolution against the distance to the injector. The color map represents the ratio between the velocity of the droplet along x and the velocity of injection  $u_{drop,x}/V_{inj}$ . The size of the marker represents the number of cells across the diameter.



(a)



(b)

Figure IV.20: Droplets morphological evolution against the distance to the injector, on the left *Flattening*, on the right  $\Delta\tilde{S}$ . The color map represents the droplets' velocity field standard deviation magnitude calculated  $|\sigma(U_{Drop})| = \sqrt{\sigma(U_{Drop,x})^2 + \sigma(U_{Drop,y})^2 + \sigma(U_{Drop,z})^2}$ . The size of the marker represents the number of cells across the diameter.

impossible to determine *on the fly* for this academic case if a droplet has reached the spherical stable shape. In order to improve the selection of droplets candidate to transformation, an analysis based on the velocity field inside the droplet has been implemented.

That analysis is coherent with the droplets' morphological evolution and reaches a convergence when droplets stabilize. However, it has the same drawback than the geometric parameters: it is impossible to determine the future evolution of the droplets with only one iteration.

Two solutions are possible, the first one is to perform a deeper analysis of this simulation with fluid properties and Reynolds number variation in an infinite domain length in order to ensure that the stable spherical shape is reached. It could permit to define empirically a standard deviation for a spherical droplet in various fluid configurations.

The second is to implement a criterion that uses droplets' history. It has already been considered in SBM model [Chen et al., 1998] and must be implemented in *Archer* in future developments.

The next step is to compare the results for the Hybrid and ICM methods against analytical solutions when it exists and ICM refined simulation.

### Hybrid approach analysis

The goals of this comparison are to determine the influence of the Hybrid approach for transformation close to breakup area. It was observed that transformation from particle toward droplet near interface modifies the physic of the simulation [section IV.1]. Here, we emphasize on the transformation from droplet toward particle. Two particle tracking approaches are compared with fixed transformation criteria [subsection IV.2.2].

To illustrate the differences between the three simulations [table IV.10], their velocity fields are studied for a given snapshot,  $t = 4.3 \cdot 10^{-3}$  [s], giving enough time to observe the influence of the Hybrid approach. As reference, the ICM refine simulation field is shown. Velocity slices along  $x$ - $z$  direction at liquid cylinder's center are presented [figure IV.21], the velocity magnitude scale has been conserved constant for all snapshots. The droplets/particles' interfaces are respectively represented in white/colors. From top to bottom we display the results of the ICM fine/Hybrid One-way approach/Hybrid Two-way approach and ICM coarse.

First, using coarser mesh modifies the transverse droplets' motion, it appears on all configuration that droplets' center is no longer aligned on  $[Ly/2; Lz/2]$  downstream to the jet. Then, it is not expected to recover the droplets' distribution of the reference simulation [top figure IV.21]. Although a specific velocity pattern is observed on the reference simulation, the velocity reaches its maximum inside droplets and minimum are obtained in between. Even though ICM coarse simulation is less resolved and droplets are no longer aligned, a velocity variation appears in droplets vicinity, similar to the finer simulation.

On the other hand, both Hybrid approaches do not recover this specific velocity pattern. Our guess is that two main factors can explain it: the velocity field is updated after transformation and particles/carrier interactions are different than droplets/carrier's one. The influence of the Hybrid is more significant with the One-way approach, when we observe the area downstream to the jet. Since there are no momentum's redistribution, the carrier magnitude velocity is smaller than the ICM coarse simulation.

The Hybrid Two-way results are different since momentum's redistribution is included, nevertheless, the ICM velocity field is not recovered. The influence of the velocity update after transformation is studied later.

Until  $x/D_{inj} = 30$ , the droplets' position are similar for coarse simulations. Above this range, differences are observed between Hybrid and ICM simulation which are due to the transport used. Surprisingly, it appears that a droplet transformed into particle for Hybrid Two-way simulation is not for the Hybrid One-way's simulation. It is possible that the early transformation and redistribution of the particles' momentum modify the physic of the primary atomization. This assumption is studied through theoretical Plateau-Rayleigh analysis. Moreover, a droplet remains untransformed in between particles, it is due to the restrictive morphological criteria of transformation (see the droplets' tail).

To quantify the influence of the Hybrid approach on the physic of the instability, the comparison of averaged breakup length, droplet's diameter, droplet/particle velocity for all configurations against



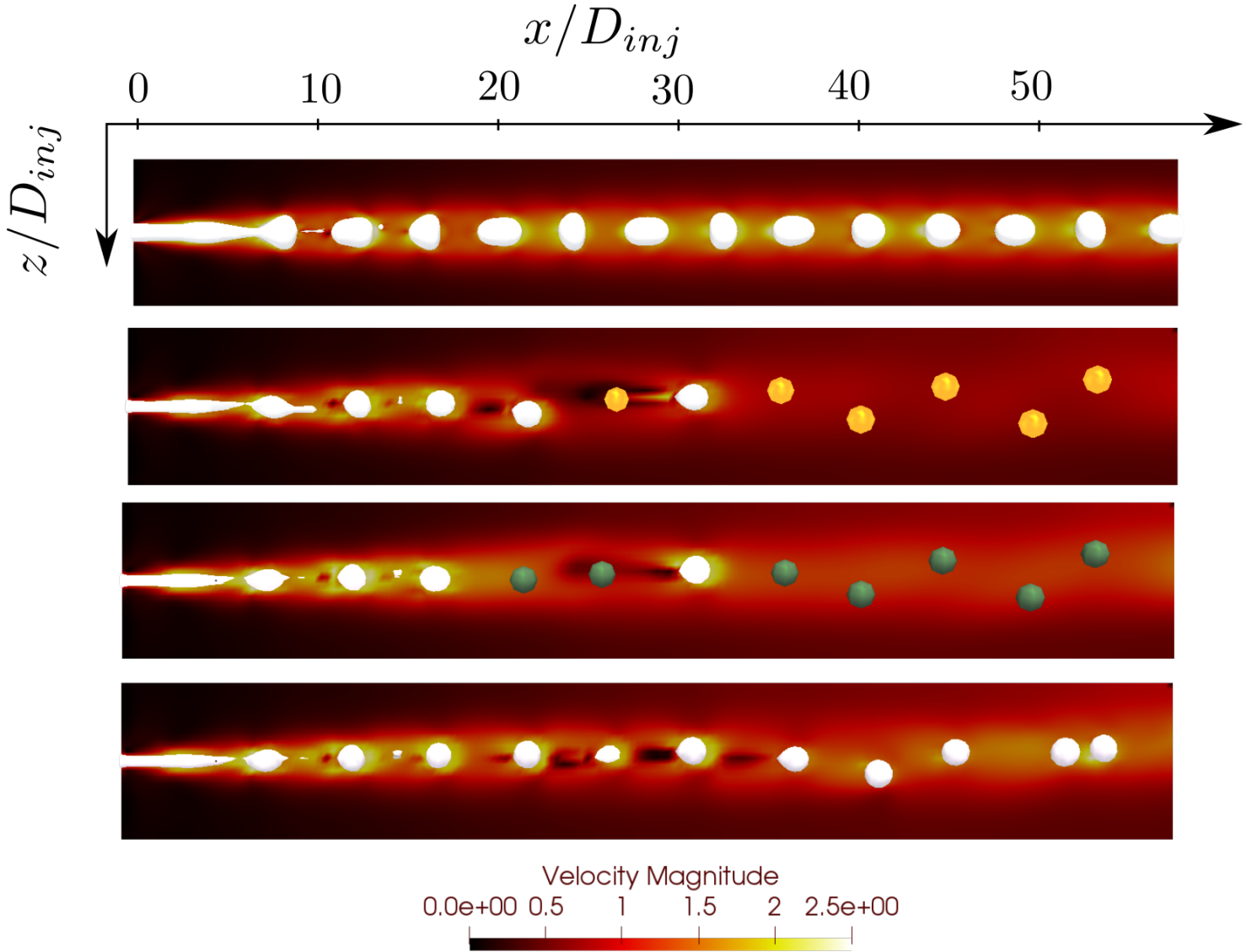


Figure IV.21: Snapshot of the velocity field at the same time step for, from top to bottom: fine ICM, Hybrid One-way, Hybrid Two-way and coarse ICM simulations. Colormap is used to represent velocity field magnitude with same values for each snapshots. The *Level-set* iso contour are shown in white and the particles interface in green (Two-way) and orange (One-way).

refined simulation is studied. The linear analysis of the Plateau-Rayleigh atomization permits to determine analytically the breakup length and the size of the droplet with respect to the diameter. This analysis for this academic case is detailed in Moallemi [Moallemi et al., 2016]. For this configuration, it gives a breakup length of  $L_b = 8.578 \cdot D_{inj}$  [equation IV.2]. From linear analysis we also obtain expected droplet's diameter  $d_d = 1.89 \cdot D_{inj} = 5.7\Delta x$ .

$$L_b = \frac{U_0}{q} \cdot \ln\left(\frac{2}{3\delta'_0}\right) \quad \text{with} \quad \omega = q \cdot \sqrt{\frac{D_{inj}^3 \rho_l}{8\sigma}} \quad \text{and} \quad w = 2\pi \quad (\text{IV.2})$$

The breakup length is obtained through the reconstruction of the liquid core. It is done averaging VoF Eulerian field for several time steps. Then, the limits of the liquid core gives the estimated breakup length distance along the direction of injection, x-component. The droplets size is obtained averaging all droplets with  $d_d/\Delta x > 1.5$ , located at a distance higher than  $1.5 \times L_b$  from the injector. Small droplets are filtered,  $d_d \approx \Delta x$ , since they were not observed in literature results [Denner et al., 2017], they are treated as numerical errors due to the mesh resolution since their diameters are equivalent to the mesh size in all simulations. To compute the average velocity, we consider all particles/droplets located above  $x_d/D_{inj} > 35$ , results for all configurations are listed in table IV.14.

Stats	ICM refine	ICM Coarse	Hybrid Two-way	Hybrid One-way
$\frac{ L_b - L_{B,Analytical} }{L_{B,Analytical}} \cdot 100$ [%]	2.37%	12.25%	12.5%	12.5%
$\langle D_{drop} \rangle / D_{inj}$ [–]	1.87	1.54	1.52	1.50
$\langle  V_{drop}  \rangle$ [ $m.s^{-1}$ ]	1.78	1.98	1.96	1.93

Table IV.14: Breakup length, averaged droplet size and averaged velocity magnitude of the droplets/-particles for the ICM refined, coarse, Hybrid Two-way and Hybrid One-way simulations.

The results obtained for the refined simulation, breakup length and droplets' diameter, are the closest to the analytical solution, which is expected. It confirms that we can consider them as reference. In coarse ICM, the ejected droplets are 0.81 times smaller than the size expected from analytical solution, it is not surprising since the simulation is coarser, see the difference of accuracy in breaking length estimation.

The comparison between ICM coarse and Hybrid configurations shows that we converge toward the same droplets diameter. It is observed that the Hybrid approach does not modify the liquid jet breakup length, we suppose that transformations occur far enough from the breakup area. This assumption is analyzed later displaying a transformation map.

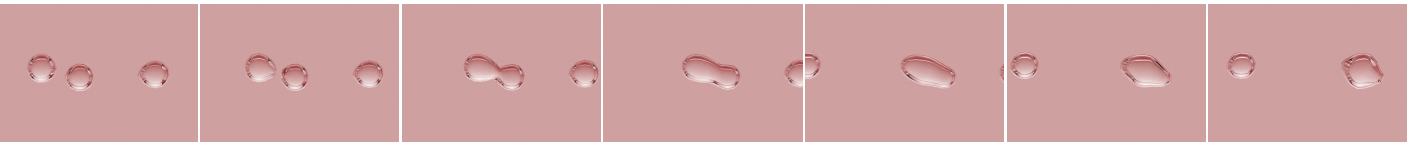


Figure IV.22: Successive snapshots from coarse ICM simulation showing coalescence event downstream to the jet, image centered on  $x/D_{inj} \approx 45$ .

It appears that the droplets' velocities are overestimated in all configurations, in the worst scenario, ICM coarse results, an increase of 1.1 times the ICM refine results is observed. It yields to coalescence events of same size droplets downstream to the jet [figure IV.22]. These events, that would have been treated as collisions [section III.7], were not observed in the Hybrid simulation. Our guess is that these events are created because of a poor numerical resolution of the interface in droplets transport.

It has been observed that small droplets resulting from breakup are created [figure IV.21]. These droplets are transformed toward particles in Hybrid simulations and collisions occur downstream to the jet. This transformation, even though these droplets creation is arguable, avoids the volume restriction that can be observed with ICM coarse simulation [figure IV.23]. Those events are not dominant in the Plateau-Rayleigh atomization study. From the Hybrid results, we can say that both approaches recover the physics of the simulation obtained through ICM method, at same resolution.

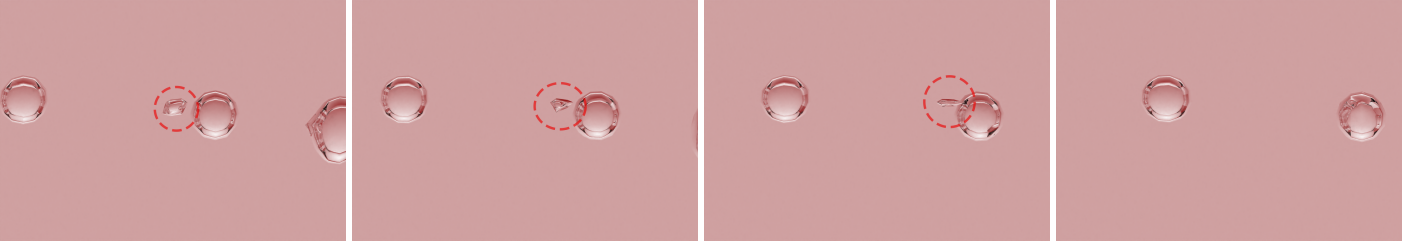


Figure IV.23: Successive snapshots from coarse ICM simulation showing volume restriction on under resolved droplet downstream to the jet, image center is approxiamtely  $x/D_{inj} = 45$ .

The transformation area, from droplets toward particles, is studied for Hybrid approaches among x-y direction [figure IV.24]. The oscillatory maximum regimes are plotted when *Flattening* is at its maximums, (when spheres shape are reached on the reference ICM refined simulation [figure IV.16]), the analytical breakup length is also added. The transformation are expected to be near maximums spheres values.

Most of the droplets are transformed in the range  $16 < x/D_{inj} < 31$  which is relatively close to the breakup area, there are no clear differences between Hybrid approaches. It shows the importance to introduce a criterion that can discriminate morphological criteria since these droplets are far from a terminal spherical shape [figure IV.20]. Notably, droplets are not transformed in the expected areas, we suppose that the differences observed between coarse and refined simulations influence the droplets oscillatory regime [table IV.14]. These results show that some transformations from droplets toward particles appear near breakup area, these early transformations do not modify the physic of the simulation.

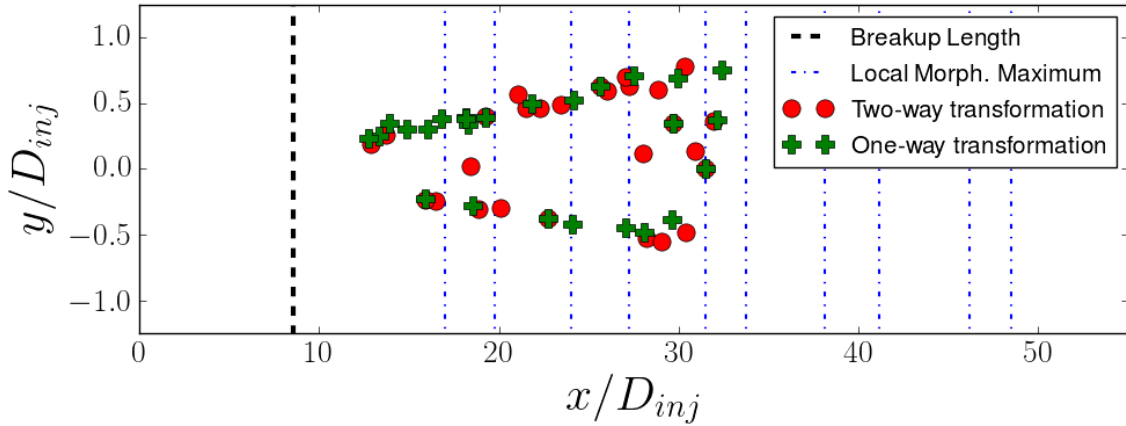


Figure IV.24: Map of droplets transformed into particles, represented along x-y axis.

The averaged droplets/particles velocity does not show differences between the simulations even though the transport is different. The droplets oscillate while particles do not reproduce this behavior, they are only transported under gravitational acceleration. This difference is observed on the position evolution of droplets/particles among x-y components [figure IV.25]. For Hybrid approaches, it is observed that the further from the injection area is the particle, the further it is from the cylinder's center ( $y/D_{inj} = 0$ ). The reason is that particles conserve droplets' motion when transformed but cannot reproduce oscillatory motion along x-axis. Then, most of those particles evolve linearly toward extremities of the simulation's domain while droplets are concentrated near  $y/D_{inj} \approx 0$ , downstream to the jet,  $x/D_{inj} = 35$ .

Since particles have a linear transport, it is expected to observe a linear evolution of the velocity along x direction, scaled by the velocity of injection [figure IV.26]. Some information for droplets evolution are lost for ICM coarse simulation, for example at  $[x/D_{inj}; U_x/D_{inj}] = [26; 0.86]$ , this is due to coalescence events [figure IV.22]. Two clear regimes for all simulation are observed, a linear and oscillatory velocity evolution. The linear evolution does not appear in ICM coarse simulation since

this is typical from the particle transport. It shows that Hybrid approach cannot reproduce entirely the physic of the droplet when it transports it, which is expected.

Yet, another phenomenon reduces the probability to observe droplets velocity evolution for Hybrid approaches: at transformation, the velocity field is updated [section III.6]. Eventually, the specific velocity pattern observed in, and around droplets is lost, (i.e. low velocity around and high velocity inside), [figure IV.17]). The Eulerian velocity field magnitude along x-component at cylinder center is extracted, and analyzed before/after successive droplets toward particles transformation. This is done for Hybrid One-way results to avoid fluid's velocity perturbation.

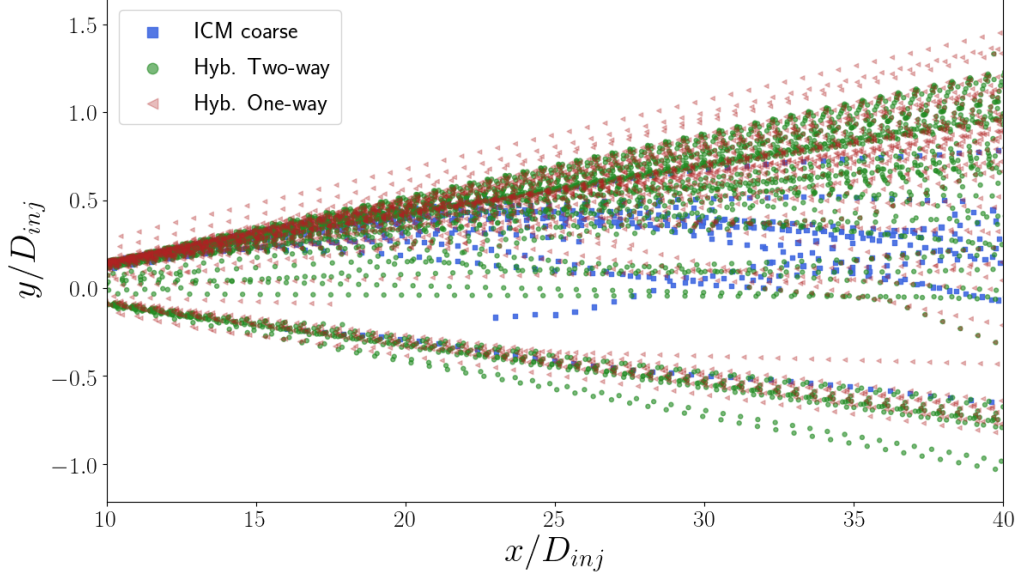


Figure IV.25: Droplets/particles x-y position evolution scaled by injector diameter. In blue ICM coarse, green Hyb. Two-way and red Hyb. One-way.

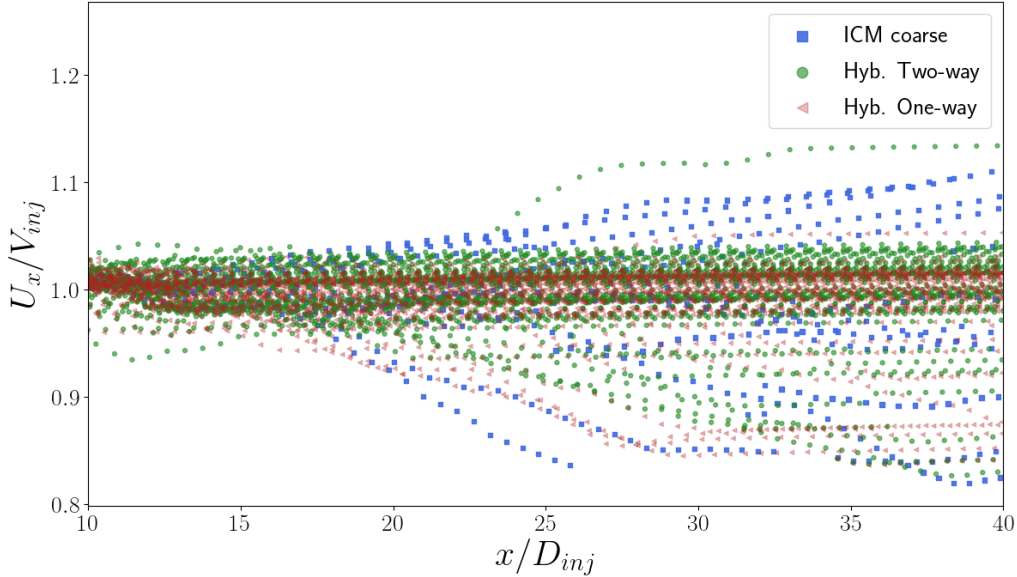
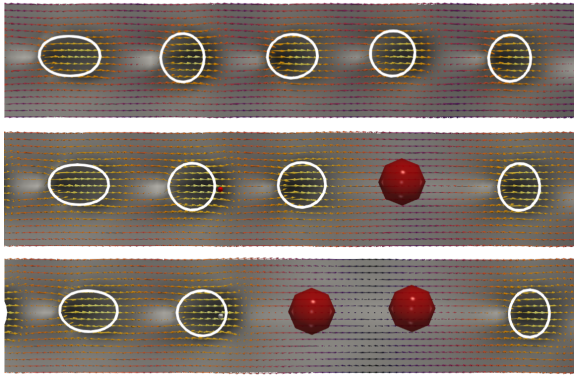


Figure IV.26: Droplets/particles velocity evolution scaled by injection velocity against distance to injector along x-component. In blue ICM coarse, green Hyb. Two-way and red Hyb. One-way.

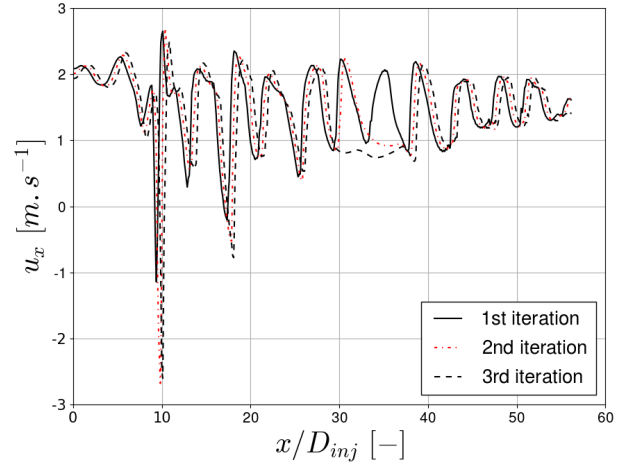
The global evolution of the velocity field is presented for three successive snapshots,  $t = [2.5, 3.0, 3.5] \cdot 10^{-4}$  [s], extracted from Hybrid One-way results [figure IV.27a]. At  $t = 2.5 \cdot 10^{-4}$  [s], only droplets are present in the domain and the velocity profile is similar to the one commented before: the two velocities areas are observed for all droplets. Then, the fourth droplet validates the

criteria of transformation, on the second line, it is represented as a particle. To ensure momentum conservation, the velocity around the particle is updated defining a box around the droplet. Since liquid jet is broken in quiescent gas, the velocity field at the position of the particle is strongly modified: at particle's position there are no more velocity oscillations back and near particle. Transformation is shown on the second row of figure IV.27a. Then, a second transformation is observed on the third line.

The magnitude of the velocity along x-component is extracted along liquid jet's cylinder center ( $y = Ly/2, z = Lz/2$ ) [figure IV.27b]. The first iteration evolves with respect to droplets' location recovering the pattern commented before [figure IV.17]. The second iteration shows a linearization of the velocity field on the range  $x/D_{inj} \approx 33 - 36$ , the velocity goes from a maximum value in this area of  $2.1 [m.s^{-1}]$  toward  $\approx 1.0 [m.s^{-1}]$ . The third iteration also modifies the velocity field and it shows that in two time steps, the physic of the Plateau-Rayleigh atomization is modified in the dispersed area.



(a) Slice of velocity along x-y direction with arrow glyph showing the velocity evolution around the droplets/particles for the Hybrid One-way coarse simulation. Iso contour of droplets in white and particles in red. Time steps from top to bottom:  $t = [2.5, 3.0, 3.5] \cdot 10^{-4} [s]$ .



(b) Velocity profile along direction of injection with at  $y = z = Ly/2$  for three consecutive time steps  $t = [2.5, 3.0, 3.5] \cdot 10^{-4} [s]$  extracted from the Hybrid One-way approach.

Figure IV.27

#### IV.2.4 Summary

In the Plateau-Rayleigh instability of a round liquid jet analysis, the Hybrid approach has been successfully applied with two methods of particle's transport, with and without particles' momentum redistribution. Global statistics were not modified by its use, and the transport of under resolved droplets downstream to the jet were similar. However, it is noticed that the droplets oscillatory motion is lost.

This analysis where oscillatory droplets motion is observed permits to discriminate morphological criteria since they are not sufficient to avoid early transformations. A solution is to increase the distance of transformation,  $\mathcal{L}_{D \rightarrow P}$ , to restrain transformation in the primary atomization area that can modify the physic of the simulation [section IV.1]. The other solution is to develop physical criteria that are not correlated with the morphological analysis.

A criterion based on the velocity field inside the droplet has been introduced. Its results were following the prolate/oblate evolution of the droplets but did not permit to determine if droplets converged toward spherical stable shape on the fly. More simulations are needed to improve this criterion varying the physical parameters of the simulation. Generating a wide database on this specific test case might be a good methodology to introduce machine learning in droplet breakup analysis.

Finally, small droplets have been observed near the breakup area. They have been successfully transformed into particles, and, reversed transformations have been observed where the particles coalesce with the main droplets. It justifies the importance of the Hybrid coupling to transport the



small droplets because those droplets are removed from the simulation with classic method.

### IV.3 Decaying Homogeneous Isotropic Turbulence

The Hybrid approach has been applied to classical academic cases showing its advantages and drawbacks against classic ICM simulations. Here, under resolved droplets are immersed in a Decaying Homogeneous Isotropic Turbulence (D-HIT) at low Reynolds number. The D-HIT is studied to avoid the influence of the forcing over droplets/particles that are treated differently, the details of the HIT generation are given. This study is more exploratory since there are no reference solution. In the present section, there are two clear objectives: the first one is to propose physical criterion to couple with morphological criteria. Following the breakup modeling review [subsection I.1.4], a Weber number based on turbulent fluctuations at droplets' interface is implemented [Perlekar et al., 2012]. The second goal is to study the behavior of the Hybrid approach against ICM simulation in such flows that are usually found downstream to the injector in diluted turbulent flows. It is expected to obtain more information about the influence of the method on small droplets transport in two-phase flow atomization.

#### IV.3.1 Decaying Homogeneous Isotropic Turbulence configuration

Several approaches have been used to maintain a forced turbulence with two phases [Duret et al., 2012, Trontin et al., 2010, Perlekar et al., 2012], however, due to the complexity to understand energy transfer in subscales of the flow and our interest onto this range,  $d_p/\Delta x \approx 4$ , the decaying turbulence is selected, where energy transfers can be studied [Dodd and Ferrante, 2016]. Thus, the flow has to be initially forced and the methodology to release droplets without forcing scheme inside the liquid part is described in the present section.

The first stage is the generation of the turbulent flow, using a turbulent forcing scheme. The forcing scheme that has been used to generate the turbulent flow is described in the work of [Rosales and Meneveau, 2005] and later used in *Archer* [Duret et al., 2012, Canu et al., 2018] in a configuration  $Nx^3 = 128^3$  and  $Nx^3 = 256^3$ . In this study, we perform the simulation using  $Nx^3 = 128^3$  cells. To reach a converged turbulent flow, the forcing is maintained during 5 turns over time,  $5 \cdot T_e$  with  $T_e = \frac{\Lambda}{\bar{u}'} [s]$  with  $\Lambda [m]$  the Taylor macro scale set to half box size and  $\bar{u}' [m.s^{-1}]$  the characteristic velocity [figure IV.28]. The second stage is to add evenly distributed fixed resolved particles inside the field conserving the forcing to adapt the flow at their interface, during 2 eddy turn over time. Special care is hold onto the convergence toward the kinetic turbulent energy,  $\bar{k}_c$ , after particles' introduction. Next the forcing scheme is turned off, the resolved particles are transformed into droplets updating their velocity field [section III.6], which corresponds to the third stage [figure IV.28]. From this point, the comparison between under resolved ICM and Hybrid approaches begins over three realisations for each to converge statistics. The configuration of the Hybrid approaches, One-way and Two-way, are the same as those described in subsection IV.2.2 with the same criteria of transformation. Since we are in dilute flow, the distance criterion can be conserved relatively low.

The turbulent flow is initialized in a cubic box of numerical resolution  $Nx \times Ny \times Nz = 128^3$  cells. The box length is  $L = 1.5 \cdot 10^{-4} [m]$ , and the mean kinetic energy is  $\bar{k}_c = 3.6 [m^2.s^{-2}]$ , generating an inertial Reynolds number of  $Re_\lambda = 37.77$ .

The parametrization of both phases is done following fluid properties found in atomization. Stokes number based on the initial eddy turnover time is selected close to 1 in order to have interaction between both phases, set to  $St = \frac{\tau_p}{T_e} = \frac{\rho_l d_p^2}{18\mu_g} \cdot \frac{\bar{u}'}{L_c} \approx 2.45$ . The characteristic length  $L_c$  represents biggest eddies diameter, it is set to half box size. The characteristic velocity is  $\bar{u}' = \sqrt{\frac{2}{3}\bar{k}_c}$ , from the turbulent flow initialization it is observed that  $\bar{u}'$  is 1.3 times higher than the expected one from the forcing scheme initialization. This observation does not modify our observations for this study. A droplet based Weber number that avoids droplet breakup has been chosen:  $We_d = \frac{\rho_l d_p (\bar{u}')^2}{\sigma} \rightarrow 1$ , it permits to

use the Hybrid approach validating morphological criteria. In order to reduce coalescence events, the number of droplets,  $N_d$ , is conserved relatively low, and the volume fraction is set to  $\alpha = \frac{N_d 4/3 \pi R_d^3}{L^3} = 0.1$ . The characteristic number droplets' collision time is set to  $\tau_c = 16 N_d R_d^2 \sqrt{\pi(\overline{u'})^2}$ . Physical properties of the simulation are resumed in the table below:

$\rho_l [\frac{kg}{m^3}]$	$\rho_g [\frac{kg}{m^3}]$	$\mu_l [\frac{kg}{m.s}]$	$\mu_g [\frac{kg}{m.s}]$	$\sigma [\frac{kg}{s^2}]$	$L [m]$	$\Delta x [-]$	$R_d [m]$	$R_d / \Delta x [-]$
1945.0	65.0	$5.650 \cdot 10^{-4}$	$1.879 \cdot 10^{-5}$	$1.35 \cdot 10^{-2}$	$1.5 \cdot 10^{-4}$	$1.172 \cdot 10^{-6}$	$2.344 \cdot 10^{-6}$	2

Table IV.15: Physical phases configuration for D-HIT study.

Giving the following characteristic numbers:

$Re_\lambda [-]$	$\lambda [m]$	$\alpha [-]$	$N_d [-]$	$We_d [-]$	$T_e [s]$	$\tau_p [s]$	$\tau_c [s]$	$St [-]$	$\bar{k}_c [\frac{m^2}{s^2}]$
37.77	$7.064 \cdot 10^{-6}$	0.10	64	1.60	$4.885 \cdot 10^{-5}$	$1.25 \cdot 10^{-4}$	$1.5 \cdot 10^{-8}$	2.58	3.6

Table IV.16: Characteristic number for D-HIT study.

Even though the simulation is configured to avoid coalescence or collisions for Hybrid approaches, these events appear. As a main indication, the number of droplets in the ICM simulation is reduced during the simulation by 20%. When the droplets coalesce, they are removed from the statistics.

### IV.3.2 Results

The analysis of this study is conducted as follows: first the ICM morphological analysis coupled with a physical criterion [Perlekar et al., 2012]. Next, the comparison between Hybrid approaches and ICM until kinetic turbulent energy is halved.

#### Morphological analysis

As mentionned in prior analysis, the choice to describe the droplets' morphological evolution is done through the *Flattening* and surface variation  $\Delta\tilde{S}$  criteria [section III.4]. A morphological cartography is presented with *Flattening* against  $\Delta\tilde{S}$  considering droplets when released  $(t - t_{ref})/T_e > 0$  [figure IV.29c]. Two colors are used to differentiate droplets through a volume threshold: droplets with a volume increase, i.e. more than 1.05 times initial one, are identified in red, others in black. This simple color change shows coalescence events and it is briefly detailed.

Two populations of droplets are observed, droplets remaining inside the area where transformation criteria are validated (top right area with *Flattening* > 0.65 and  $\Delta\tilde{S}$  > 0.8), and droplets moving

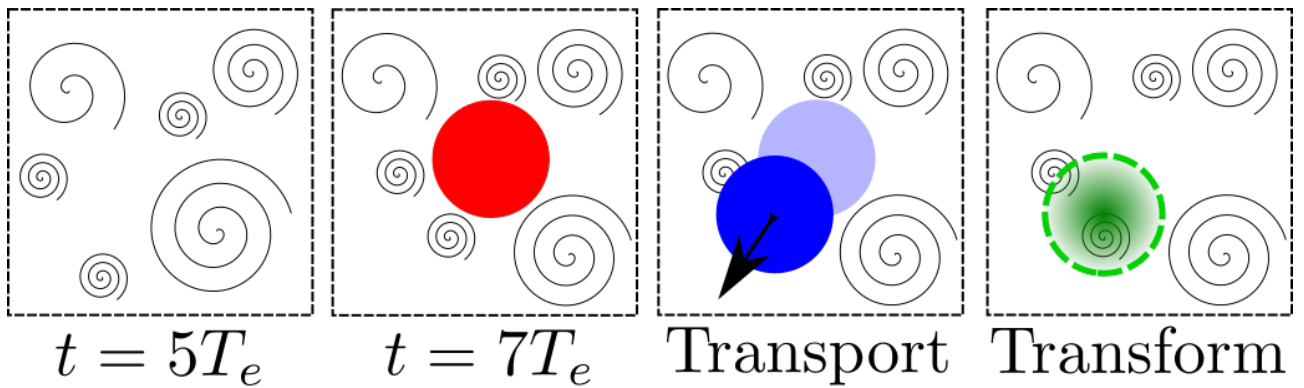


Figure IV.28: HIT flow generation around droplets, step 1: turbulent production, step 2: flow adaptation around fixed IBM, step 3: rewriting of the velocity flow in the droplet, step 4: freely moving droplet in the box and transform in particle when validates criteria.

toward low *Flattening* values. The second population represents droplets that are currently coalescing which explains the low value of *Flattening*. A variation of a surface criterion, although less wide, also appears. After coalescence, droplets recover their initial spherical shape since several droplets with  $Vol_{Drop} > 1.05 \times Vol_{Drop,init}$ , are observed in the zoomed area. Even though shape modifications due to coalescence events appear, the spherical shape is recovered fast, showing that the simulation has been correctly defined to ensure accurate transformation from droplets toward particles.

The other goal of our analysis is to study the evolution of a physical criterion to enhance droplets breakup analysis. The physical introduced criterion is inspired from [Perlekar et al., 2012], already validated for highly resolved simulations of breaking droplet in forced HIT, define as:

$$We^* = \frac{\rho_l \max(\delta u_d)^2 d_d}{\sigma}, \quad (IV.3)$$

with  $\max(\delta u_d)$  the maximum velocity difference between droplet's velocity magnitude and velocity at its interface. To compute this difference, the interface magnitude velocity is centered in each cells containing droplets' interface, and the maximum difference with droplets' velocity magnitude is obtained with:  $\max(\delta u_d) = \max(u_\Gamma - u_d)$ , with  $\Gamma$  to define cells at interface. The Weber number evolution is averaged among all droplets against characteristic time and compared to the morphological criteria [figures IV.29a and IV.29b]. To avoid noise, droplets with volume exceeding 1.05 times initial volume, i.e. coalescing/coalesced droplets, are removed. The definition of this Weber number is strongly related to the number of cells across the diameter, since the less cells are located inside the droplets, the higher is the probability to find a surface velocity close to the droplets' one. However, we expect to observe velocity fluctuation due to droplets-carrier phases interactions which can provide fluctuations of this Weber number, that might be correlated to an evolution of droplets' morphology.

It is noted that even though the initialization of the flow is set up to avoid strong shear at the droplets' interface, the morphological criteria are not beginning exactly at  $Flattening \rightarrow 1$  and  $\Delta\tilde{S} \rightarrow 1$ . The reason why is that the flow velocity perturbs droplets at start through a fluctuation of velocity at their interfaces [figure IV.30]. The less spherical droplet has a strong velocity variations on its extremities, explaining shape modifications.

For both morphological criteria, an increase of values is observed until  $(t - t_{ref})/T_e = 0.6$ , it is supposed that droplets are adapting to the initial shear observed at their interfaces [figure IV.30]. Since similar patterns are observed for both morphological criteria, the focus is hold on the *Flattening* analysis [figure IV.29a], because variations are wide. When the peak is reached, averaged *Flattening* slightly decreases until  $(t - t_{ref})/T_e = 1.2$  to finally remains in the range  $Flattening = 0.88$  after  $(t - t_{ref})/T_e = 1.5$ . It corresponds approximately to the area where more than half of the kinetic turbulent energy has been dissipated.

For the characteristic Weber number study, it appears that at droplets release its value increases under droplets motion, we suppose that this is due to velocity fluctuations at their interfaces [figure IV.30]. One eddy turn over later, energy decays is more influent in the box and the characteristic Weber number decreases along time until reaching a plateau,  $We^* = 2$ . Since its computation is based on the difference of magnitude between droplets velocity and its peak at interface, it is supposed that when the energy within the box decays, the Weber number decreased. We expect to observe a convergence toward 0 after several eddy turnover times, this is not the goal of the simulation since this criterion has been already extensively studied [Perlekar et al., 2012] and the simulation cost would have been non necessarily expensive. Similarly to the criterion computed from the velocity field inside the droplet [section IV.2], more tests would be required to determine the range under the which the droplets converged toward a stable shape.

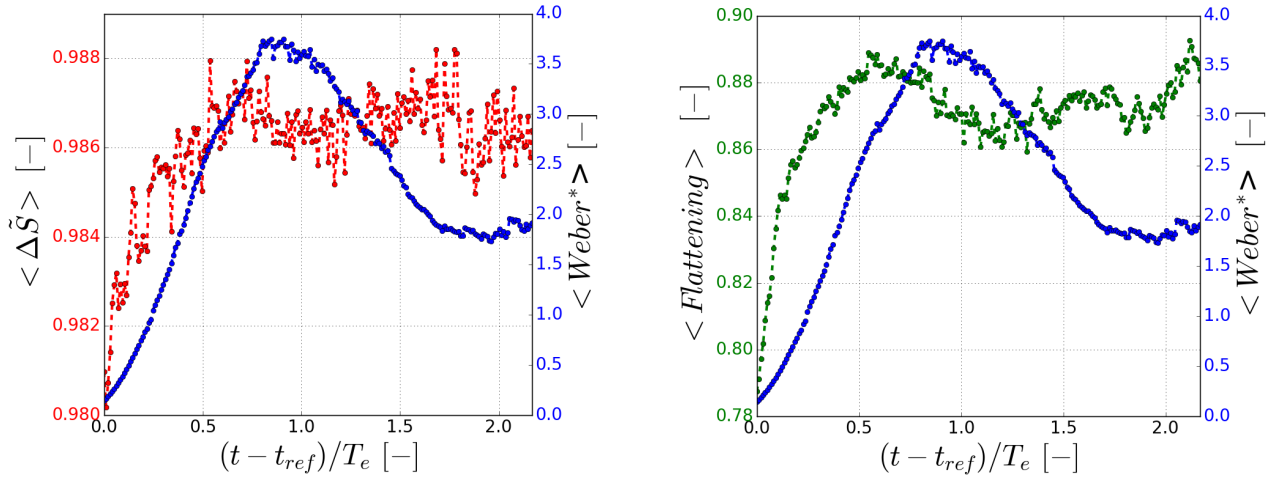
It is encouraging to observe two clear tendencies from those under resolved droplets analysis when the energy decays, the convergence toward high morphological values and the decrease of the characteristic Weber number after a clear peak. Moreover, the range of characteristic Weber number observed in our analysis is coherent with the work of [Perlekar et al., 2012], where they observed a variation on the range  $We = 0 - 8$  for droplets immersed in HIT.



## ICM-Hybrid comparison

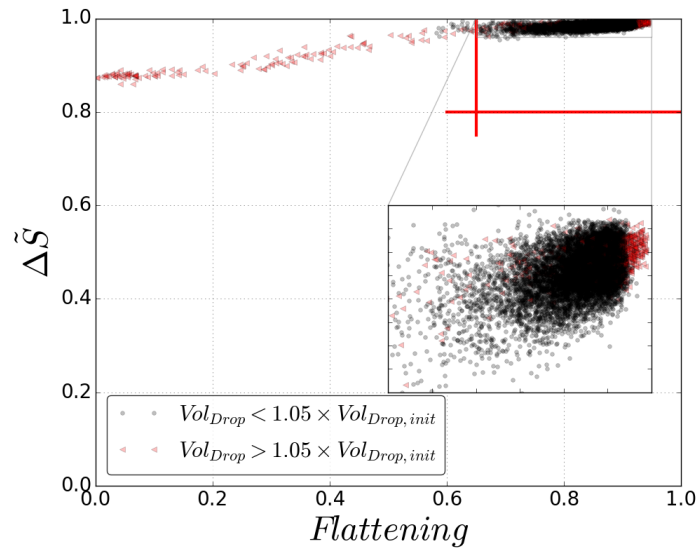
At transformation from under resolved droplets toward particles, the velocity field is updated on two droplet's diameter [section III.6]. To quantify the influence of velocity update, the initial spectra, common to all simulations before transformation (black solid line), is compared to spectra after transformation at  $(t - t_{trans})/T_e = 0.01$  (solid line) and after one eddy turnover  $(t - t_{trans})/T_e = 1$ . (dashed line) [figure IV.31]. Important length are given on this figure such as two droplet diameters, one droplet diameter and the Kolmogorov length scale, respectively  $1/2D_d$ ,  $1/D_d$ , and  $1/\eta_k$ . There are several strategies to compute the Kolmogorov length scale:

- calculated through turbulence length scale and Reynolds number,
- calculated afterward through dissipation,
- calculated afterward through structure functions.



(a) Evolution of averaged  $\Delta\tilde{S}$  and  $We^*$  against characteristic time.

(b) Evolution of averaged  $Flattening$  and  $We^*$  against characteristic time.



(c) Droplets' morphological cartography coupling length and surface criteria.

Figure IV.29

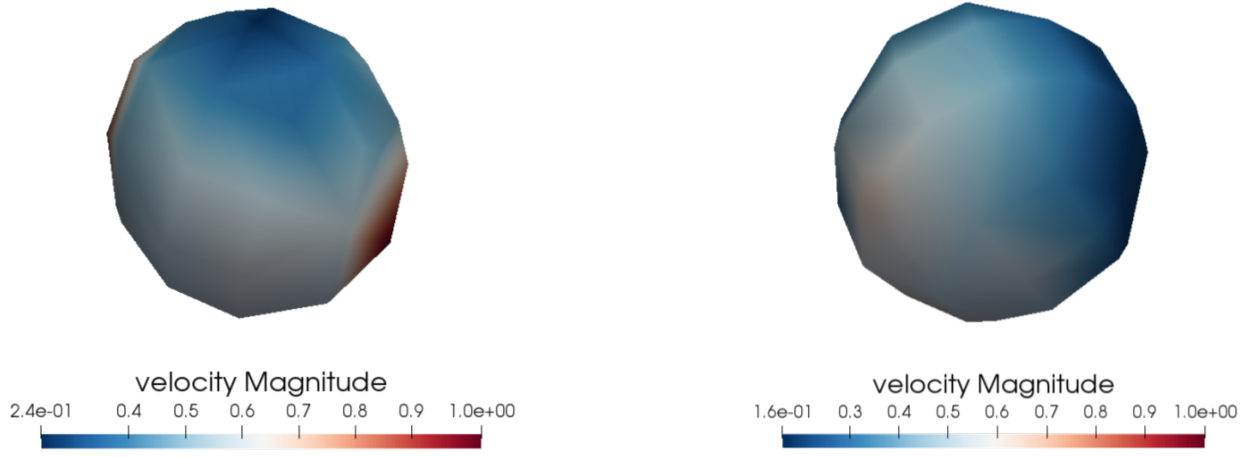


Figure IV.30: Two droplets extracted from ICM simulation when released in the D-HIT, on the right low *Flattening* value, on the right, high *Flattening* value. The magnitude velocity on the *Level-set* at  $\phi(\vec{x}) = 0$  is represented.

In here, we follow the work of [Duret et al., 2012] to obtain the Kolmogorov length scale, obtained with the following equation:

$$\eta_k = L_c \times \left[ \frac{L_c \overline{u'}}{v_g} \right]^{4/3}. \quad (\text{IV.4})$$

Large structures, ( $< \frac{1}{2D_d}$ ), are first analyzed and it appears that after transformation, the large scales of turbulence are not modified, see the range  $k = [4 \cdot 10^4, \frac{1}{D_d}]$ . At droplets' diameter length scale, Hybrid spectra decreases faster than the ICM's one. This is due to the velocity field update. Since this update is done at droplets scales, it only influences the smallest scales of the turbulence.

Then the comparison is done for ICM/Hybrid approaches one eddy turnover time after transformation (dashed lines). Again, the the largest structures of the turbulence are of the same order, the general flow motion patterns are conserved. It was noticed right after transformation that droplets' length scale turbulent energy magnitude was higher for ICM simulation, same results are observed. Our guess is that this is no longer because of the update of velocity field, this is due to the droplets' energy contribution. It was commented that resolved droplets/resolved particles increase turbulent two-phase flow energy spectra on their diameter length scales [Dodd and Ferrante, 2016, Brändle de Motta et al., 2019]. Then, it explains the difference between ICM and Hybrid One-way approach since the latter is considered similar to single phase flow.

However, a difference of energy between both Hybrid approaches was expected since Hybrid Two-way considers momentum's redistribution. It is supposed that the case is too dilute to observe particles' influence on the two-phase flow spectra [Rosa et al., 2020]. Finally, general flow motion is well recovered after transformation, and only small scales of turbulence are modified by velocity update. The next part of the present analysis focuses on global statistics,  $V_{RMS}$  and position dispersion, to determine the influence of the velocity update/transport methods on droplets/particles motion.

The averaged root mean square velocity evolution,  $V_{RMS}(t)$ , is obtained through:

$$V_{RMS}(t) = \frac{1}{N_d} \sqrt{\left[ \sum_{i=1}^{N_p} |\vec{u}_i(t)| \right]^2},$$

scaled by the initial characteristic velocity of the flow;  $u'(t_{ref}) = 2.2 [m.s^{-1}]$ . The comparison starts at one time step before transformation,  $t_{ref}$ , to start exactly from the same information, and evolves against characteristic time until initial energy is halved [figure IV.32a]. Since droplets/particles are initialized at rest, their evolution starts from  $V_{RMS} \approx 0$ . Quickly, two clear regimes are observed, differentiated by the methods. ICM results increase until a peak is reached at  $(t - t_{ref})/T_e = 0.95$ ,

then a decrease is observed due to energy dissipation in the box. Both Hybrid methods results are similar, a peak is reached later in the simulation, approximately at  $(t - t_{ref})/T_e = 1.4$ , and then similar decrease is observed. The main difference is the magnitude of the peak, ICM method reaches twice Hybrid approaches peaks' magnitudes, and almost two times before. Our understanding of these results is that the motion of particles is more linear since they are less inertial than droplets. From those results, particles/droplets are expected to evolve differently in the simulation. This analysis is pursued through droplets/particles dispersion evolution.

The position before transformation is used as reference and the dispersion is computed using:

$$| \vec{X}_p(t) - \vec{X}_p(t_{ref}) | = \frac{1}{N_d} \sqrt{\left[ \sum_{i=1}^{N_p} | \vec{X}_i(t) - \vec{X}_i(t_{ref}) | \right]^2},$$

and studied with its evolution against time [figure IV.32b].

Until  $(t - t_{ref})/T_e \approx 0.2$ , it appears that particles are more dispersed from their initial position than droplets. Few time steps later, after  $(t - t_{ref})/T_e = 0.4$ , a similar linear evolution is obtained for all configurations. Prior analysis [figure IV.32a] showed similarities between Hybrid approaches, the dispersion evolution shows that at  $(t - t_{ref})/T_e = 0.8$ , a different evolution appears. The Hybrid Two-way approach appears more dispersed than One-way approach, we suppose that two stages are observed at droplets/particles release. First, the start of the dispersion can be different between Hybrid/ICM because the velocity field is updated. Moreover, we have to account for droplets' inertia since their interface is entirely resolved, energy transfers occur at their scale that can slightly slow down their dispersion. After several iterations, we recover the same flow topology since bigger scales transfer eddies energy, thus in the second stage of this analysis, the differences are caused by the transport method.

To go further on those assumptions, 4 droplets initialized at the same positions are extracted from each simulations' results to show the two different patterns observed: differences observed from the

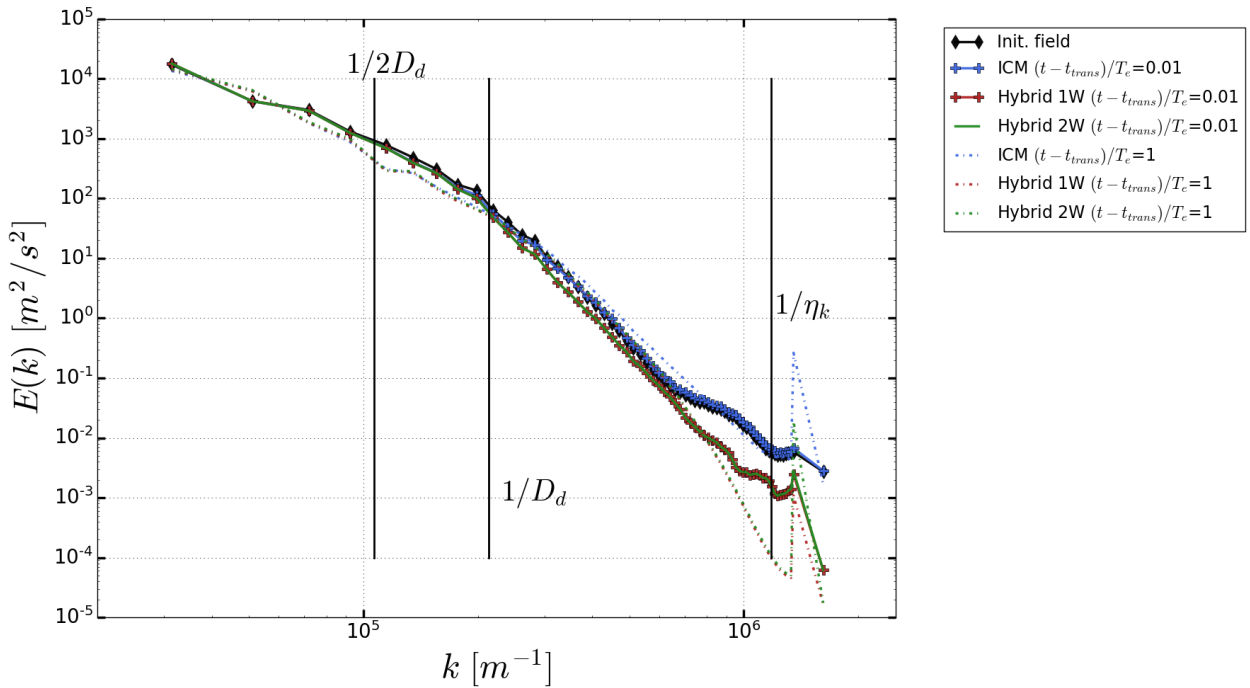


Figure IV.31: Spectra comparison before transformation (solid black line with diamond markers), after transformation at  $(t - t_{trans})/T_e = 0.01$  (solid line with cross markers except for Hyb. 2W that overlaps Hyb. 1W) and after one eddy turnover  $(t - t_{trans})/T_e = 1$ . (dashed line). ICM, Hybrid One-way and Hybrid Two-way are respectively represented in blue, red and green. Droplets diameter and area of reconstruction, respectively  $D_d = (d_d)^{-1}$  and  $2D_d = (2d_d)^{-1}$  are given on the figure.

beginning of the simulation and differences observed later in the simulation. The position evolution during  $1.6T_e$  is plotted on 3D axis (x-y-z), and its evolution over each direction, (x-y/x-z/y-z), on characteristic axis,  $X^* = |X_p(t) - X_p(t_{ref})|/Lx$ , simultaneously for all methods (ICM blue, Hyb. One-way red, Hyb Two-way green) is projected [figure IV.33]. The first row represents droplets/particles where differences are observed at the beginning of its evolution, the second row shows differences due to the method.

On the first row, it appears that the droplets/particles are sustained at their initial location since we observe several iterations near the initial location. Then, two trajectories are clearly observed and we use results from top left figure IV.33 to comment it. ICM droplet evolves toward  $[X^+; Y^-]$  meanwhile particles are evolving toward  $[X^-; Y^+]$ . Later, particles are evolving in the trajectory of the droplet. To our understanding, the initial velocity update influences particles' propagation in this case. Later, the method influence droplets/particles' trajectory, observed on top right figure IV.33.

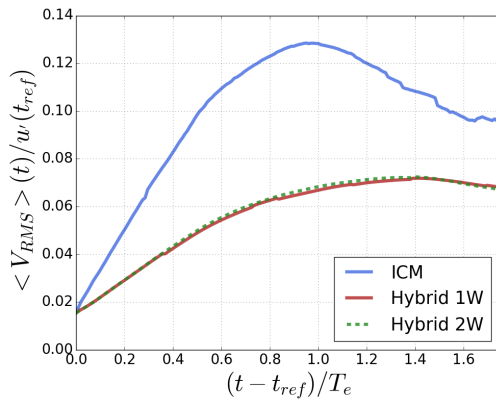
This pattern is easier to observe on the second series of results [bottom figures IV.33], we observe that the initial evolution of droplets/particles is slightly similar, they evolve in the same direction. After some iterations, the method influences the motion of the immersed structures which is clearly observed on bottom left figure IV.33. A rotation is observed for Hybrid approaches, it is supposed that the particles are following an eddy motion. On the other hand, the ICM droplet follows a linear evolution, see the projection on the  $X^*$  axis. Another shift is observed few iterations later, the Hybrid One-way method changes of direction while the Two-way method keeps evolving linearly. Again, it is supposed that the One-way method follows an eddy while the Two-way has probably more inertia. On bottom right figure IV.33, the methods follow the same trajectory at start and some iterations later, the trajectories slightly deviate since Hybrid approaches evolve toward  $Y^-$  and ICM toward  $Y^+$ .

From these results, it is assumed that updating the velocity field after transformation influences initial condition (first row vs second row). Then, the more the simulation evolves, the more the method used to transport droplets/particles influences simulations' results.

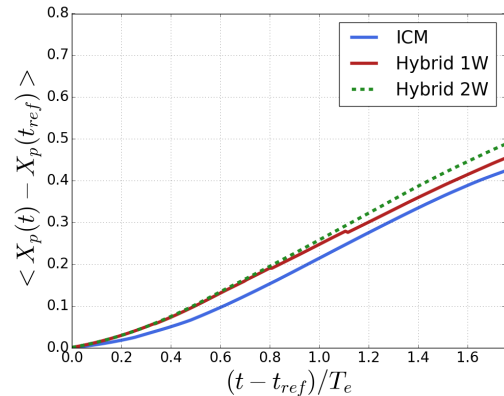
### IV.3.3 Summary

In this exploratory study, first a physical criterion is used to determine the probability of droplets to break [Perlekar et al., 2012] to improve transformation criteria, second a comparison of droplets/particles motion after transformation in the decaying flow is done.

The morphological criteria are well defined for this analysis, and are able to detect coalescence of droplets in the decaying flow. Since this study might represents the flow motion downstream to the jet, the accurate definition of criteria is emphasized since it ensures accurate transformation in the dispersed area. Nevertheless, it is recalled that in primary atomization, those criteria are still unsatisfactory and must be coupled with distance or physical criteria [section IV.2].



(a) Mean RMS velocity evolution against characteristic time for ICM in blue and Hybrid method in red.



(b) Mean position evolution against characteristic time for ICM in blue and Hybrid method in red.

Figure IV.32

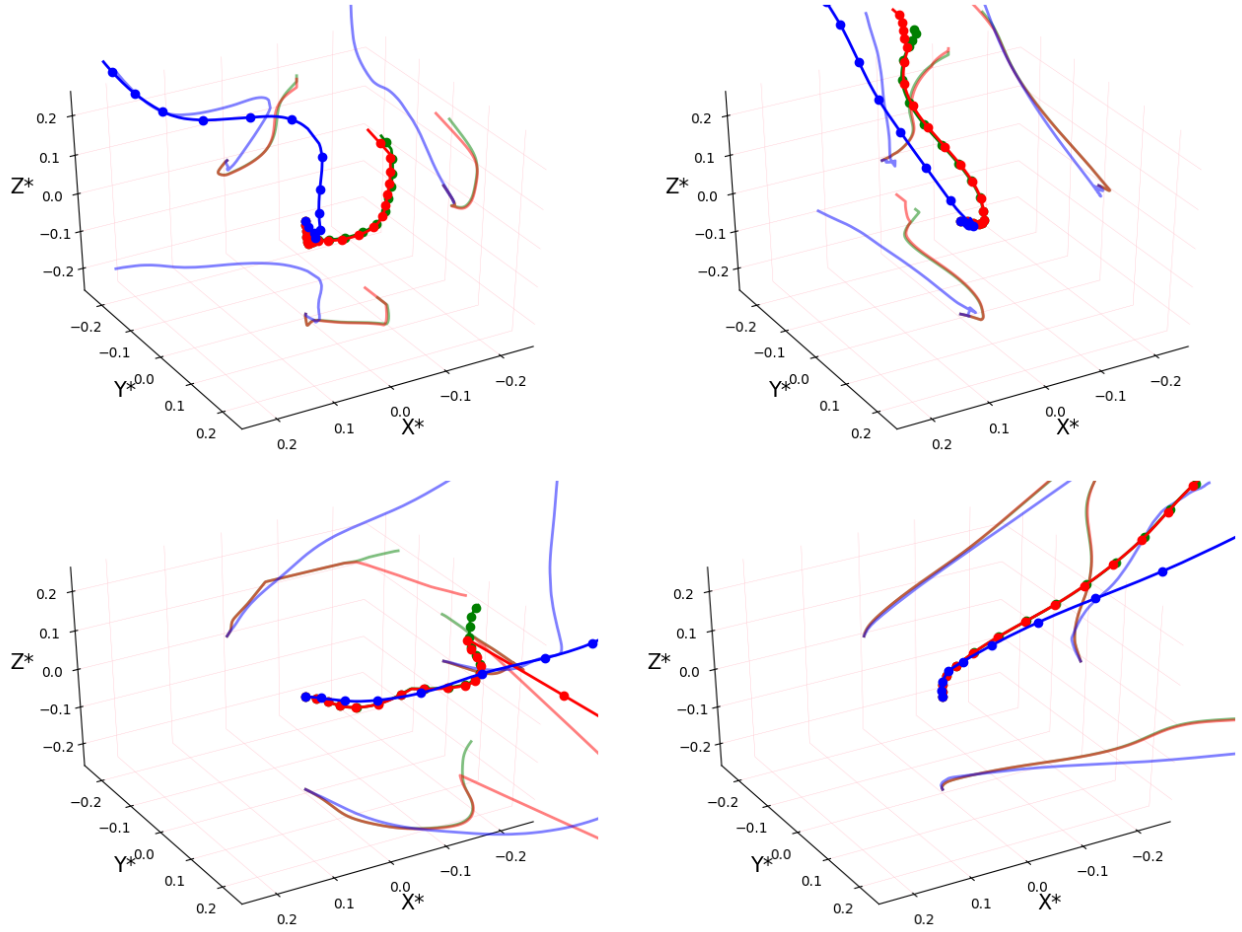


Figure IV.33: Particles/Droplets position evolution against reference position before transformation for ICM (blue), Hybrid One-way (red) and Hybrid Two-way (green) results over  $1.6T_e$ . The projection of the position evolution is done over each x-y-z components on characteristic axis  $X^* = |X_p(t) - X_p(t_{ref})|/Lx$ .

On this specific matter, it was observed that a physical criterion based on turbulent velocity fluctuation at droplets' interface gave interesting results [Perlekar et al., 2012]. This criterion based on the velocity shows similar behavior that the morphological criteria [section III.4]. Future work have to clarify the advantages of this criteria and its range of application.

The second part of this analysis showed that transforming an under resolved droplet into particle modifies only the small scales of the turbulent flow, i.e. droplets' diameter length. Later after the transformation, the spectra of the ICM simulation is coherent with the literature: a production from the surface droplets' energy increased the spectra at diameters length. In the other hand, the Hybrid Two-way approach did not recover results from the literature [Rosa et al., 2020], it is supposed that the simulation is too dilute. Finally, the main flow characteristics are not the transformation and after several iterations, the influence of the velocity update onto the subscales is vanished.

The influence of the transformation on the trajectory is observed on the first iterations of the simulation and shows that the particles/droplets evolution can differ. But, generally the patterns are similar and the method of transport is more and more important after some iterations. The Hybrid method's influence does not perturb the flow motion but locally modifies the trajectory of particles/droplets. A deeper comparison on a realistic application on velocity/position evolution for ICM/Hybrid method must be done to quantify the influence of this transformation. That is the purpose of the next chapter that focuses on a turbulent round liquid jet atomized in a crossflow.

---

## Study of Jet in crossflow atomization

---

*In this chapter the Hybrid approach is applied to realistic application. The atomization configuration is a crossflow simulation that is ideal for our study since we observe a wide generation of droplets in the secondary atomization area. Since we focus on the Hybrid approach, we study this application using under resolved DNS simulation. It permits to perform this simulation varying the criteria of transformation and to compare it to the full ICM equivalent simulation. Then, we perform the simulation without volume restriction since we expect to transform the small droplets before they vanish. Finally, we comment the computational cost using the Hybrid approach.*

### Contents

---

V.1	Configuration setup . . . . .	177
V.2	Physical results . . . . .	179
V.2.1	ICM results . . . . .	179
V.2.2	Hybrid approach . . . . .	185
V.2.3	Configuration comparisons . . . . .	201
V.3	Computational cost of simulation . . . . .	204

---

## V.1 Configuration setup

In this section we describe the studied application to apply the Hybrid approach. First, a brief overview of the physical specificities of the configuration is done. Next, we introduce the physical and numerical configurations. Finally, we describe the Hybrid method that we applied to the jet analysis.

The jet in crossflow is relevant to many applications and has been studied extensively varying injection parameters to target several applications such as fuel or dilution air injection in gas turbine engines, and rocket vehicles [Karagozian, 2010]. Some studies have focused on liquid jet injection conditions [Stenzler et al., 2006], others on drop breakup mechanisms [Ng et al., 2008], or on the crossflow carrier regime's influence, varying from laminar to turbulent [Broumand et al., 2019]. In our studies of the dispersed phase, it is pertinent to study crossflow's influence on the dominant breakup mechanisms, bag breakup or elongated breakup [Ng et al., 2008]. Within the wide varieties of investigations, we decided to focus on a configuration intensively studied, experimentally, theoretically and numerically, among past years: liquid turbulent jet injection inside uniform carrier crossflow. This configuration is challenging studying since it involves high momentum ratio and a creation of several droplets' sizes [Aalburg et al., 2005]. Thus, it makes it ideal to apply and compare Hybrid approach against literature [Brown and McDonnell, 2006, Herrmann, 2010b] and our own ICM solver [Mukundan et al., 2020].

The computational domain length centered on the injection hole,  $D_{inj}$ , is  $[Lx, Ly, Lz] = [-10 \times D_{inj} : 30 \times D_{inj}, -5 \times D_{inj} : 5 \times D_{inj}, 0 : 20 \times D_{inj}]$ . This domain is smaller than experiment [Brown and McDonnell, 2006] but provides enough space to observe primary breakup atomization and small droplets transport [Herrmann, 2010b, Xiao et al., 2016]. Liquid turbulence is modeled by turbulent pipe flow velocity profile at the injection using filter based turbulent data generation [Klein et al., 2003]. The physical quantities of the liquid and gas phases and boundary conditions are showed [figure V.1] taken from [Herrmann, 2010b, Mukundan et al., 2020], and listed in table V.1.

$D_{inj}$ [m]	$U_j$ [m.s <sup>-1</sup> ]	$\rho_l$ [kg.m <sup>-3</sup> ]	$\mu_l$ [kg.m <sup>-1</sup> .s <sup>-1</sup> ]
$1.3 \cdot 10^{-3}$	97.84	12.25	$1.11 \cdot 10^{-4}$
$U_c$ [m.s <sup>-1</sup> ]	$\rho_g$ [kg.m <sup>-3</sup> ]	$\mu_g$ [kg.m <sup>-1</sup> .s <sup>-1</sup> ]	$\sigma$ [kg.m <sup>-2</sup> .s <sup>-2</sup> ]
120.4	1.225	$1.82 \cdot 10^{-5}$	0.07

Table V.1: Crossflow atomization's physical properties.

It gives the characteristic numbers listed in [table V.2].

$\rho^*$	M	We <sub>j</sub>	Re <sub>j</sub>	We <sub>c</sub>	Re <sub>c</sub>
10	6.6	2178	14,079	330	10,652

Table V.2: Crossflow atomization's characteristic dimensionless numbers.

The computational domain is resolved by  $16.7 \cdot 10^6$  cells giving 14.5 cells across the diameter of injection. It is observed in [Herrmann, 2010b] that this numerical study requires a wide amount of cells across injection diameter to be converged, and, in his work, 64 cells across the diameter were not sufficient. Here, we aim to study the influence of the Hybrid approach, and we conserve the numerical resolution relatively low to perform series of simulations. The first part of our study is then dedicated to the analysis of purely ICM simulation in order to show that the biggest scales of the simulation are recovered. It permits to justify our analysis even though numerical resolution is low.

The second part of our study focuses on the Hybrid approach influence is on the simulation's results. The main goals of the approach are to avoid numerical instabilities of the method through the use of Lagrangian particle transport and to improve statistics on the dispersed area. In *Archer*, the dispersed area often leads to numerical instabilities through the transport of small structures with high density ratio, a volume restriction has been implemented to solve it [section I.5]. Two simulations are performed without volume restriction, with full ICM and Hybrid approach (the low density ratio reduces numerical instabilities' probability due to the small under resolved structures). Implicit goals



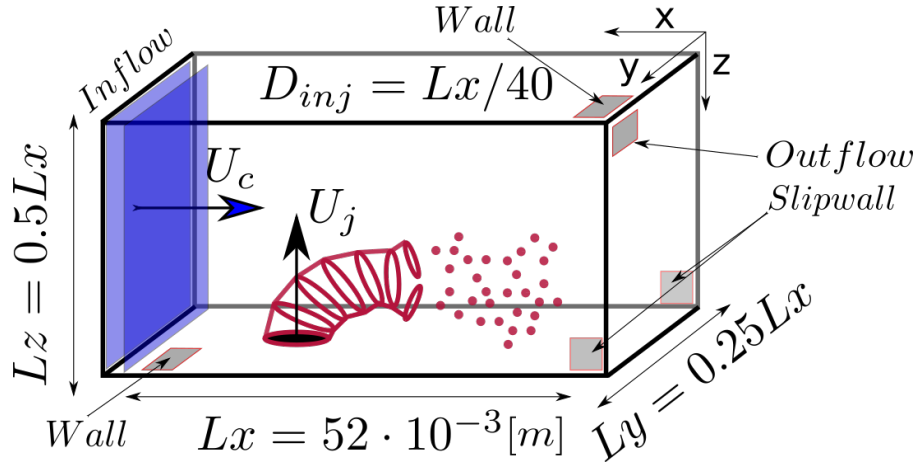


Figure V.1: Crossflow physical configuration description.

are to reduce the computational time of the method and in shortcoming, avoid the use of the volume restriction.

Both ICM simulations are compared to their equivalent Hybrid approach. The distance criteria is fixed for all Hybrid simulations, and we conserve it relatively high following our prior results [section IV.1]. From our morphological analysis [section III.4], we define length criterion  $Flattening = 0.65$  and surface criterion  $\Delta\tilde{S} = 0.95$ . The Plateau-Rayleigh analysis showed that fixing  $Flattening$  can have a strong influence on the outcome of the simulation [section IV.2]. A simulation with a variation of this parameter, selecting  $Flattening = 0.85$ , is performed to study its influence in realistic application where a wide panel of structures is observed.

Another topic of interest is the influence of the particles' momentum redistribution. In prior studies, differences between Two-way and One-way have been observed, but were not determinant in the evolution of the simulation [section IV.3 and IV.2]. The crossflow atomization creates several droplets that are here transported with Lagrangian methods, their evolution is compared to go further on our analysis.

Last, to avoid highly under resolved structures to be removed from the simulation, a threshold is set,  $d_{eq}/\Delta x < 2$ , below the which morphological aspect is no longer studied. The influence of this parameter is studied decreasing this threshold to  $d_{eq}/\Delta x < 1.5$ .

Below we list the simulation set up that we implemented in order to conclude on the benefits of the Hybrid approach to transport under resolved droplets:  $\mathcal{L}_{\mathcal{D} \rightarrow \mathcal{P}} = \max(4.5\Delta x, 3R_p)$  and  $\mathcal{L}_{\mathcal{P} \rightarrow \mathcal{D}} = \max(4\Delta x, 0.5\mathcal{L}_{\mathcal{D} \rightarrow \mathcal{P}})$ . In this study we use a reference time based on droplets' residence time in the combustion chamber, computed from the crossflow velocity,  $t^* = U_c/(0.75Lx) \approx 3.5 \cdot 10^{-4} [s]$ , we store data every  $0.0625 \times t^*$  and simulate  $4 \times t^*$  when convergence is reached.

Case study	Method	Vol. Rest.	Flattening [-]	$\Delta\tilde{S} [-]$	Threshold [ $\Delta x$ ]	$\mathcal{L}_{\mathcal{D} \rightarrow \mathcal{P}} \times [R_p]$
Case 1	ICM	True	-	-	-	-
Case 2	ICM	False	-	-	-	-
Case 3	Hyb. One-way	True	0.65	0.95	2.	3.
Case 4	Hyb. One-way	True	0.85	0.95	2.	3.
Case 5	Hyb. One-way	False	0.65	0.95	2.	3.
Case 6	Hyb. Two-way	True	0.65	0.95	2.	3.
Case 7	Hyb. One-way	True	0.65	0.95	1.5	3.

Table V.3: Crossflow atomization's numerical simulation configurations.

## V.2 Physical results

In this section we first compare the largest scales of ICM results, *Case 1*, against literature to ensure that we are representative of the atomization process. It consists in the comparison of droplet's size diameter and velocity distributions against reference [Herrmann, 2010b]. Our focus on droplets is natural since our application aims to improve their treatment in the dispersed area. We use the opportunity that gives the detection algorithm to study the morphological distribution of droplets in atomized jet, we develop an analytical relation to discriminate prolate/oblate based on their surface and flattening information. Then, we compare ICM results toward Hybrid results.

### V.2.1 ICM results

We first provide two snapshots of atomized jet in crossflow with a bottom and side view [figure V.2]. On this snapshot, we see that the aerodynamic force bends the jet following prior observations [Stenzler et al., 2006, Wu et al., 1997, Song et al., 2014], we will not go further on the penetration's length analysis since it has been studied with *Archer* in [Mukundan et al., 2020]. Since turbulent velocity field is used to inject liquid jet, we have two complex phenomena that lead to small droplets' creation: droplets detached from the liquid core that are transported behind it, often found under the jet bending, and droplets created from the top liquid core breakup, often found above the jet bending or in its following. Since the liquid core is an obstacle to the crossflow, it creates a turbulent wake behind it which produces a recirculation area, several droplets can be evolving in the opposite crossflow or liquid jet injection directions when located in this area. This is more common for droplets detached from the liquid core.

With respect to the literature [Herrmann, 2010b, Mukundan et al., 2020, Xiao et al., 2016], fewer droplets are present in our configuration. This is due to the poor numerical resolution, three times coarser than the reference used to comment our results [Herrmann, 2010b]. On this specific time step, approximately 1000 droplets were identified through our detection algorithm. After a transitory time, the number of droplets in the domain remains relatively constant. The analysis here are done after this time is reached, we fix it at  $t > 4 \times t^*$ . We suppose that it is sufficient to apply the Hybrid method and compare methods' influence on under resolved droplets.



Figure V.2: [Side/top snapshots ICM converged crossflow simulation.

### Droplets distribution

Our first interest is to compare droplets evolution with respect to a detailed reference [Herrmann, 2010b], first we study droplets' size distribution. Approximately 200,000 droplets are used, we filter droplets below  $d_d/\Delta x = 2.5$  and above  $d_d/\Delta x = 9.$ , resulting into 120,000 droplets split into 20 logspace bins. We show our droplets' size distribution [figure V.3a], and the reference from refined simulation [Herrmann, 2010b] [figure V.3b] (Two density ratios are showed on the reference, we only compare to the black circles reference: same density ratio). We consider that the main phenomenon leading to breakup and small droplet's creation are recovered even at low numerical resolution.

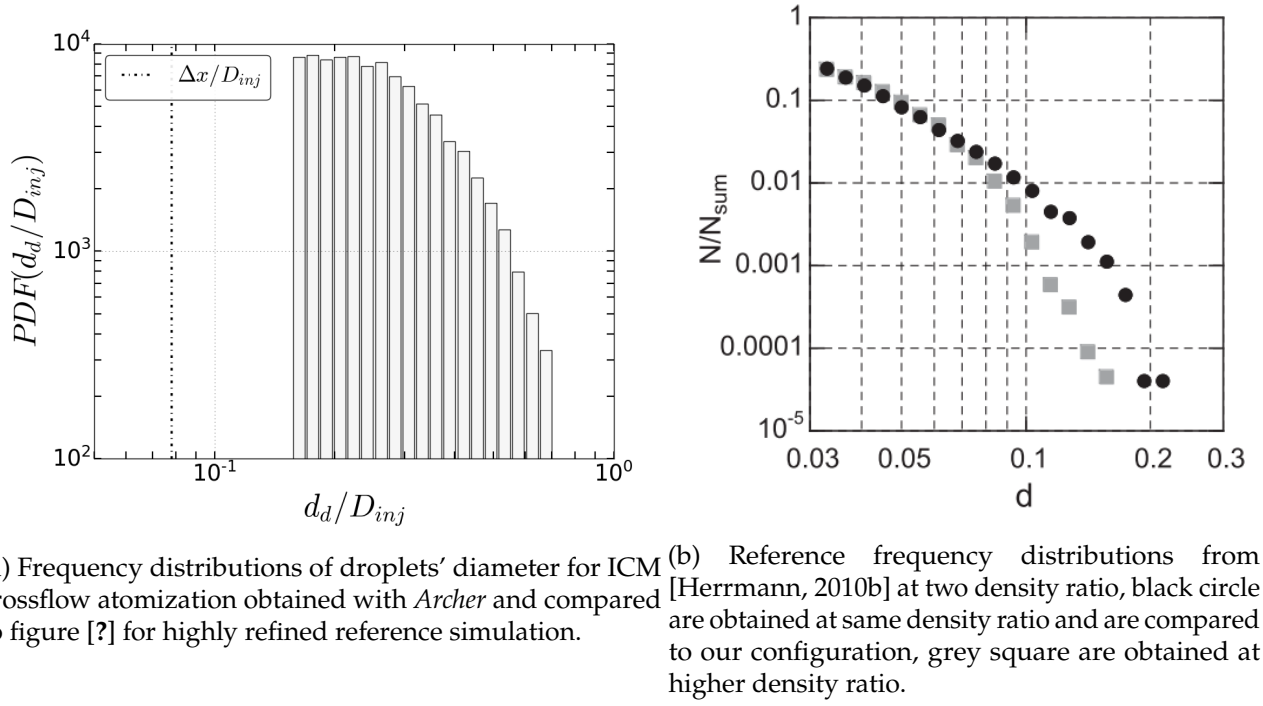


Figure V.3

The three components droplets' velocity distribution for six classes of droplets are compared, splitting it through log scale diameter distribution, going from  $d_0$  to  $d_5$ . The droplets that are considered in this study are of the size  $2 < d_d/\Delta x < 9$ , inspired of the reference [Herrmann, 2010b]. Since our numerical resolution is poorer, we estimate that we are representative of medium droplets but not small droplets. The following classes are obtained using  $d_X = d_d/\Delta x$ :

$d_0$	$d_1$	$d_2$	$d_3$	$d_4$	$d_5$
$2. < d_X < 2.57$	$d_X < 3.30$	$d_X < 4.24$	$d_X < 5.45$	$d_X < 7.0$	$d_X < 9$

Table V.4: Crossflow atomization's numerical liquid core/droplets/particles distribution.

For each class of droplets, the distribution is split into 20 equally sized bins from minimum and maximum velocities. In these 6 classes, more than 5,000 droplets are present at least, which ensures a reliable representation of the velocity dispersion. Here, the studied classes of droplets, (black square), are the one that can be compared to the reference (red circle).

First, the velocity distribution in the direction of the crossflow scaled by the injection crossflow velocity,  $u_p/U_c$ , is analyzed. The two classes of droplets are  $d_0$  [figure V.4a], and  $d_4$  [figure V.4b], that represents smallest and medium droplets. The resolution in [Herrmann, 2010b] is 4 times finer than our under resolved method. For the small droplets, the under resolution has here a strong impact since we observe a bigger population near  $u_p/U_c = 1$ . Our guess is that the flow downstream to the jet is less perturbed by the presence of droplets since we have fewer droplets than the reference's simulation. Since fewer droplets are created, it is supposed that fewer vortices are produced which are the reason why droplets deviate since their Stokes number is considered small [Herrmann, 2010b, Jazi, 2014]. For medium droplets, it appears that our distribution is coherent with the reference since they both converge toward unity. So far, it is a known result since it was already commented for experimental studies [Wu et al., 1997, ELShamy, 2007]. It appears that droplets with a higher velocity than the crossflow injection velocity are found, this is due to the y-boundary conditions that are used in this configuration, symmetrical that create a pseudo venturi effect.

Then, we scale droplets' velocities in liquid jet atomization direction by the liquid injection's velocity,  $v_p/U_j$ , for small droplets  $d_0$  [figure V.5a], and medium droplets  $d_3$  [figure V.5b]. In this configuration, a turbulent wake is produced behind the injected jet due to crossflow, it yields to a

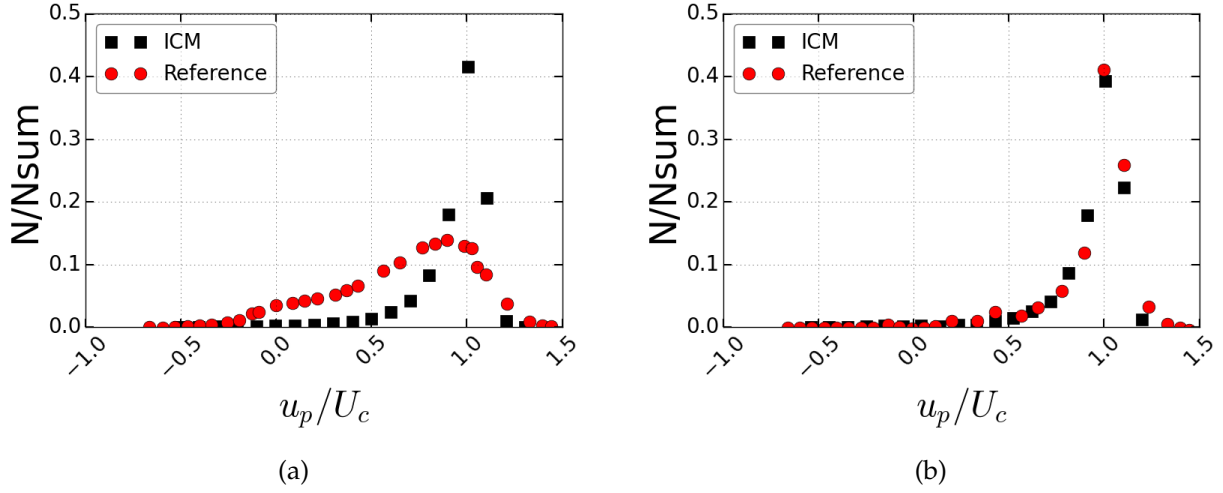


Figure V.4: Velocity distribution in the direction of the crossflow scaled by crossflow injection velocity for smallest class of droplets  $d_0$  [figure V.4a], and medium droplets  $d_4$  [figure V.4b] compared to reference's results [Herrmann, 2010b].

recirculation area that can transport droplets in the opposite injection direction [Herrmann, 2010b], i.e.  $v_p < 0$ . This phenomenon slightly influence droplets' evolution since they converge toward  $v_p/U_j = 0$ .

Results for the smallest droplets show that we underestimate the velocity dispersion, it is supposed that this is due to the numerical resolution since the smallest droplet size in our numerical study remains larger than the refined reference. It yields to a shift of the highest velocity probability, closer to  $v_p/U_j = 0$ . The distribution of medium droplets, with a peak at  $v_p/U_j = 0$ , is again closer to the reference, but we underestimate the wide dispersion of velocities.

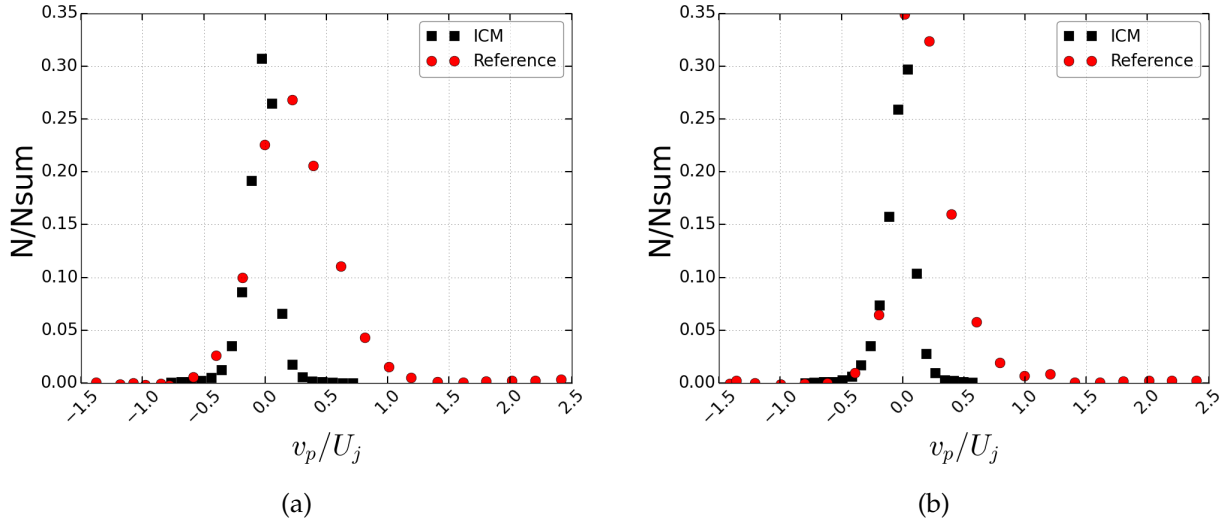


Figure V.5: Velocity distribution in the jet injection direction scaled by liquid jet injection velocity for smallest class of droplets  $d_0$  [figure V.5a], and medium droplets  $d_3$  [figure V.5b] compared to reference's results [Herrmann, 2010b].

Finally, we study the transverse droplets' velocities direction scaled by the crossflow velocity,  $w_p/U_c$ , for droplets  $d_0$  [figure V.6a], and medium droplets  $d_3$  [figure V.6b]. We recover the symmetric distribution centered on  $w_p/U_c = 0$  observed by the reference, the main difference is that our results tend to overestimate the droplets' concentration on  $w_p/U_c = 0$  for small and large droplets [figure V.6]. In other words, the spray spreading is less important in our case.

We observe that for small droplets, we underestimate the dispersion of velocities, we suppose that this is because the same length scales are not resolved, i.e. the higher resolution of the reference permits to have a wider representation of droplets scales meanwhile we are restrained by our resolution, which

explains similarities between medium and small droplets. For medium droplets, our description of droplets' motion is converging toward the reference's results, and we expect to describe accurately these scales of atomization. Since these small droplets are going to be transported with Lagrangian algorithm, we expect to observe a change in the  $d_0$  velocities distributions. These results are compared later in the present section.

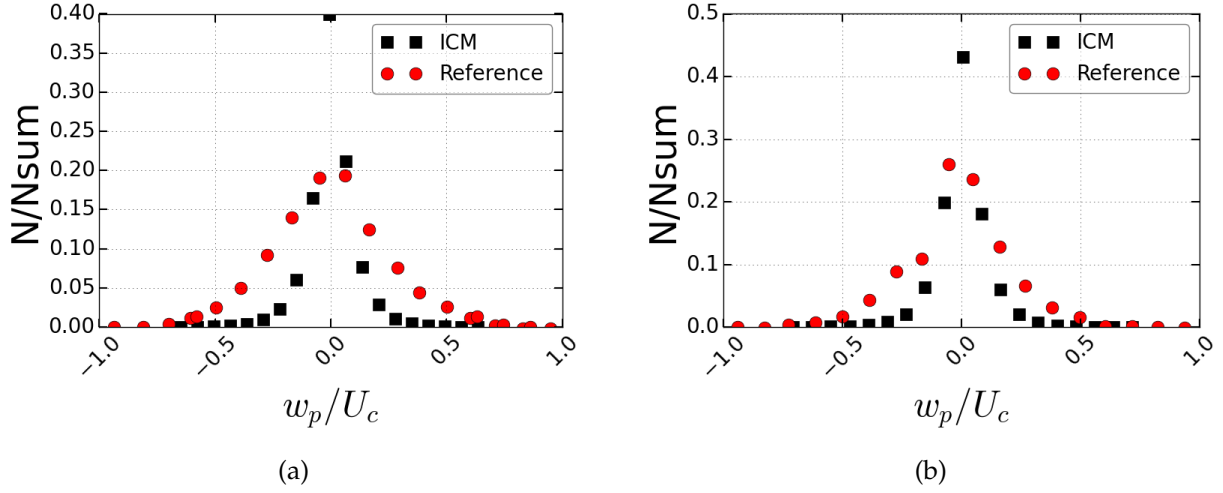


Figure V.6: Transverse velocity distribution scaled by crossflow injection velocity for smallest class of droplets  $d_0$  [figure V.25a], and medium droplets  $d_3$  [figure V.25b] compared to reference's results [Herrmann, 2010b].

From the velocity dispersion analysis, droplets follow the crossflow velocity injection with a small dispersion among transverse directions. Droplets' position evolution (in blue), inside the simulation domain is plotted in 3D axis [figure V.10]. Each axis has the 2D projection of droplets' position evolution (in gray). As commented, droplets evolve in the crossflow (along x-component) direction. Most of the transverse variation are observed near the breakup area:  $x/D_{inj} \approx [0 : 5]$ , where the flow motion is perturbed by the liquid jet presence. Near breakup area, some droplets trapped in recirculations area are observed, but from this figure, it is complex to evaluate, it is detailed later in the manuscript.

### Morphological analysis

The morphological analysis is commented for droplets, filtering droplets below  $d_d < \Delta x$  to avoid any noise in our analysis [section III.4] using surface criterion  $\Delta\tilde{S}$ . This criterion is chosen because it can discriminate complex shapes. The evolution of  $\Delta\tilde{S}$  against droplets' position with a color map scaled on droplets' velocity against crossflow velocity is showed [figure V.9a]. First, a group of markers is located near the injector  $x/D_{inj} < 5$  and  $\Delta\tilde{S} < 0.4$ , these markers represent the liquid core and are not relevant to our study. The droplets closer to breakup area have a wider surface variation, from  $\Delta\tilde{S} = 0.2$  to  $0.95$ , than droplets downstream to the jet, for example at  $x/D_{inj} = 25$  where  $\Delta\tilde{S}$  varies from  $0.5$  to  $1$ . It shows an expected pattern: the further are droplets from breakup area the more spherical they are. However, no clear pattern is observed with droplets' velocity.

Since we have the opportunity to identify and study each atomized droplets, we represent the morphological evolution at three distances from the diameter of injection;  $x_d/D_{inj} = 5$ ,  $x_d/D_{inj} = 10$ , and  $x_d/D_{inj} = 20$  [respectively figures V.8a, V.8b and V.8c]. We account for droplets with a numerical resolution below 4 cells across diameter candidate to Lagrangian transport that are identified in red on these figures. We recall that these droplets are the ones analyzed by the transformation criteria.

Under the assumption of a spheroidal shape, the two criteria can be related [equations V.1 and V.2] to determine if droplets evolve following an oblate or prolate shape. These relations are analyzed in a communication being written [Chéron et al., 2020]. They provide the analytical relation between the shape parameters for prolate and oblate spheroids, following similar development for 2D ellipsoidal shape analysis [Malot and Blaisot, 2000, Yon and Blaisot, 2004].



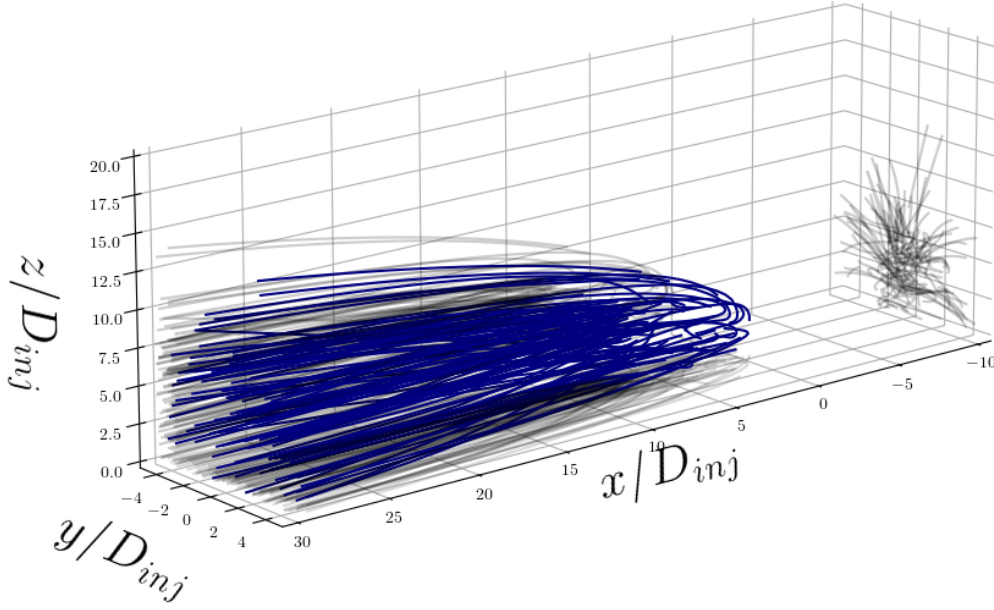


Figure V.7: Droplets 3D trajectory in the domain [figure V.1], in blue the 3D evolution and in gray the projection among each plane.

$$\Delta\tilde{S}_{prol}(Fla) = \frac{2(Fla)^{-2/3}}{1 + \frac{\arcsin(\sqrt{1-(Fla)^2})}{(Fla)\sqrt{1-(Fla)^2}}}, \quad (V.1)$$

$$\Delta\tilde{S}_{obl}(Fla) = \frac{2(Fla)^{2/3}}{1 + \frac{(Fla)^2}{\sqrt{1-(Fla)^2}} \operatorname{arctanh}\left(\sqrt{1-(Fla)^2}\right)}. \quad (V.2)$$

From these results, we observed that we have more droplets downstream to the jet, showing that breakup keeps occurring along the droplets' evolution. For these three graphs, most of the droplets are located above the analytical relation  $\Delta\tilde{S}_{prol}(Fla)$  showing a higher representation of elongated droplets in our simulation. We suppose that this is due to the dominant crossflow injection velocity as we observed that droplets' velocities distribution converged to unity for  $u_p/U_c$  [figures V.21a and V.21b]. Moreover, experimental studies of turbulent round jet atomization in crossflow [Broumand et al., 2019, Ng et al., 2008], (at higher momentum ratio  $M = [16.5 - 172]$ ) highlighted that the higher is the momentum ratio, the higher is the probability to observe bag breakup, dominant for oblate shapes. Thus, to confirm our observations, turbulent crossflow velocity injection is required to confirm experimental analysis.

In the prior chapter, two physical criteria, fluctuation Weber number  $We^*$  and droplets' inside velocities' dispersion  $|\sigma(v_{Drop})|$ , have been introduced to study droplets' morphological evolution in a Plateau-Rayleigh injection [section IV.2] and a D-HIT [section IV.3]. To follow our analysis, their computation is applied to the jet analysis. The results obtained for the Weber number based on the fluctuation at droplets' interface were not satisfying. Since its definition is based on HIT flows assumption, we consider that its use should be restricted to highly developed turbulence. Turbulence was observed downstream to the jet, but we suppose that numerical resolution restrained its full development that would improve the results.

On the other hand, the velocity inside droplets,  $|\sigma(v_{Drop})|$  showed better results for this analysis. Following prior methodology [section IV.2], results are showed against the distance of the injection and colored with droplets' velocity scaled by crossflow velocity. With respect to what was observed in the Plateau-Rayleigh analysis, observed values are much higher in this configuration. A decrease is

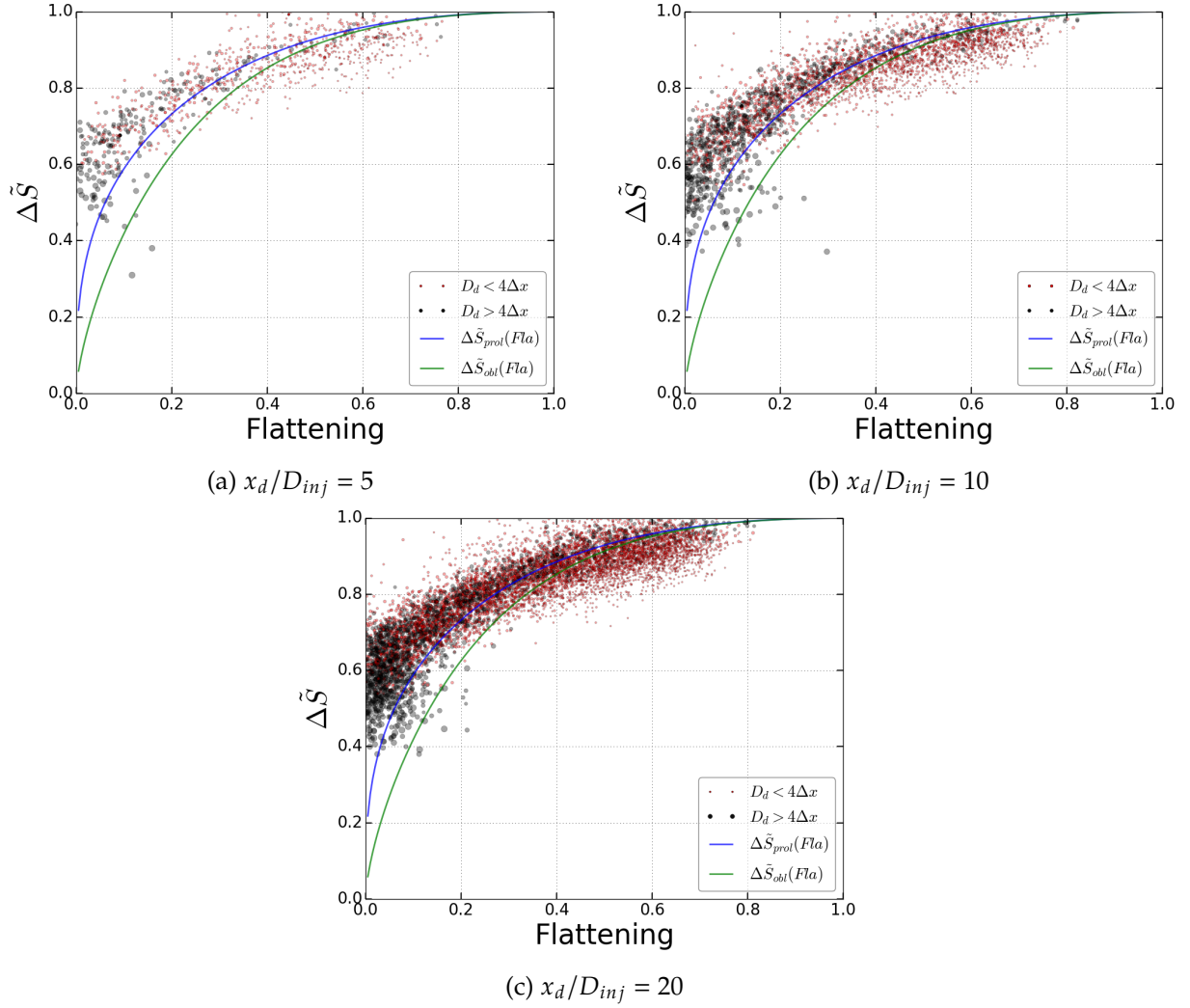
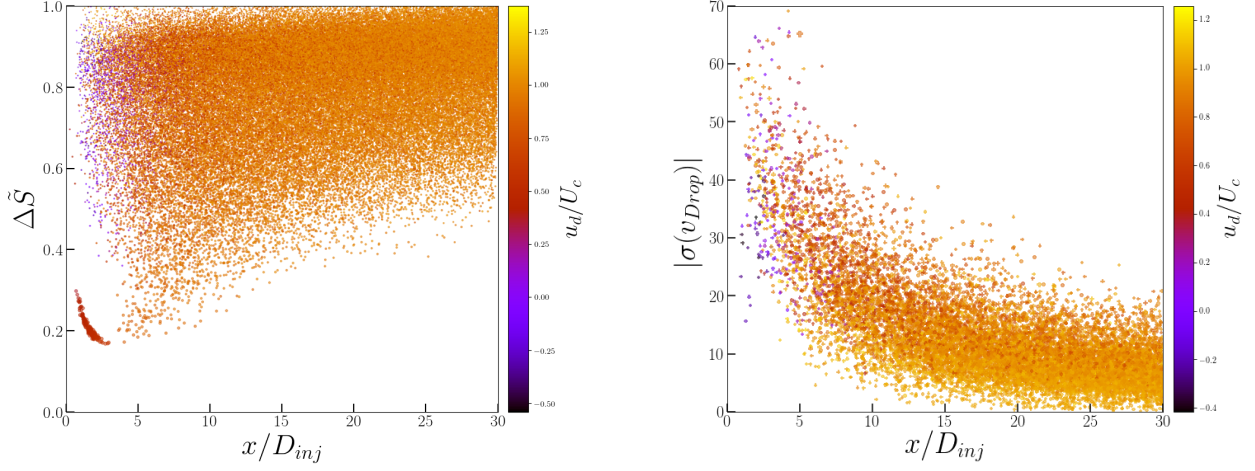


Figure V.8: Morphological droplets' distribution at  $x_d/D_{inj} = 5$  [figure V.8a],  $x_d/D_{inj} = 10$  [figure V.8b], and  $x_d/D_{inj} = 20$  [figure V.8c]. Droplets considered under resolved, below  $d_d/\Delta x < 4$ , in red, others in black. Analytical surface criterion evolution against flattening for prolate shape, in blue, and oblate shape, in green, plotted in solid line.

observed, it is understood by the strong initial shape deformation [figure V.9a], then, downstream to the jet these droplets recover a shape converging to sphericity evolving at a velocity near crossflow velocity [figure V.4] with a low slip velocity. Our guess is that this criterion is coherent in its prediction of droplets' shape evolution because a convergence similar to the one observed for  $\Delta\tilde{S}vsx/D_{inj}$  is observed.



(a) Surface criterion  $\Delta\tilde{S}$ , against distance of injector  $x/D_{inj}$ . Color map represents droplets velocity in the crossflow direction scaled by crossflow velocity.

(b) Dispersion of the velocity field inside droplets  $|\sigma(v_{Drop})|$ , against distance of injector  $x/D_{inj}$ . Color map represents droplets velocity in the crossflow direction scaled by crossflow velocity.

Figure V.9

## V.2.2 Hybrid approach

The Hybrid approach is now analyzed. The Hybrid parameters are modified to compare their influence against ICM results [table V.3], and the simulations are performed during 4 characteristic time ( $t^* = \frac{U_c}{0.75 \times Lx}$ ) on the same mesh resolution as the ICM one. Parameters of interest are the morphological criteria, the particle tracking algorithm and the threshold under the which morphological criteria are no longer checked to validate transformation. Moreover, the numerical solver *Archer* showed that a volume restriction is implemented to avoid numerical instabilities. Earlier, its use was commented on the 2D/3D splash [section IV.1] and Plateau-Rayleigh instability [section IV.2]. In this application, we compare ICM method with and without volume restriction, respectively case 1 and case 2. The Hybrid method is also used without volume restriction and compared to other simulations.

The results are introduced using global statistics such as the volume occupied for each phase in the simulation. Snapshots of the simulation allow us to go further on the representation of the Hybrid approach with respect to classic ICM. From these 7 cases, 3 main studies are considered.

1. The influence of the morphological criteria on the distance of transformation is studied, case 3 and case 4. This analysis is coupled with a novel definition of the *area of primary atomization* obtained through entropy computation [Blaisot et al., 2019]. The droplets/particles diameter probability distribution are also compared for both simulations at 5, 10 and 20 diameters of injection.
2. Simulations with and without volume restriction, case 1 and 2, are then compared through the droplets/particles' diameter probability function. A particular interest is hold on the area where the smallest droplets are found. Then, the Hybrid method is applied on the crossflow atomization without volume restriction, case 5.
3. The influence of the particle tracking algorithm, respectively One-way and Two-way are discussed through the analysis of the velocity probability density function for two sizes of droplets, cases 1,



3 and 6. An approximated Weber number based on crossflow injection velocity is defined in order to compare droplets/particles evolution.

Finally, the relevant droplets' distribution are plotted for all simulations following methodology presented for the ICM analysis [figure V.3a]. This distribution permits concluding on the modification implied by the use of a Hybrid method in two-phase flow atomization.

### Global results

The use of the Hybrid approach modifies structures found in the simulation. In the overall simulations, three kinds can be identified; the liquid core, the dispersed droplets and the particles. The three phases are identified through the detection algorithm, the liquid core is identified because of its location and its volume which is the higher in the simulation. The dispersed phase is identified as other identified structures with the detection algorithm. Their values are obtained through an averaging over the entire series of data that are stored during our analysis.

Its use leads to a strong variation in the quantity of droplets transported by ICM method [figure V.10]. Table V.5 resumes the quantity of volume transported by particle tracking method, see below:

Case study	Method	Liq. Vol. Liquid Core [%]	Liq. Vol. Droplets [%]	Liq. Vol. Particles [%]
Case 1	ICM	36.76	63.23	-
Case 2	ICM	33.48	66.52	-
Case 3	Hyb. One-way	32.05	35.58	32.37
Case 4	Hyb. One-way	32.04	35.31	32.64
Case 5	Hyb. One-way	33.28	64.03	2.69
Case 6	Hyb. Two-way	35.54	34.68	29.78
Case 7	Hyb. One-way	34.65	48.03	17.32

Table V.5: Crossflow atomization's numerical liquid core/droplets/particles distribution performed with *Archer* at same mesh resolution:  $512 \times 128 \times 256 \Delta x$ .

The two first simulations, cases 1 and 2 are the results with and without volume restriction. The percentage of liquid on the core is slightly larger with restriction. This is because small structures are not removed, then droplets' volume fraction will increase against time in a nonphysical way [see the discussion I.5]. The study of the droplets' diameter PDF presented later must provide more information about this point. It is observed that most of the simulation are performed with a One-way Hybrid coupling. The motivation is that the computational time of the One-way coupling is more advantageous to perform this study regarding the numerical analysis performed later in the manuscript [section V.3].

From the ICM case 1 toward the Hybrid One-way case 3, approximately half of the volume represented by droplets' has been transformed into particles. The area of transformation is of interest for this study since we expect to find more and more particles downstream to the jet [figure V.10]. Even though morphological criteria of transformation are more restrictive in case 4, the volume distribution is similar to case 3 with a third for the liquid core, droplets and particles. Again, the distance of transformation for droplets in the range  $2 < d_d/\Delta x < 4$  is of interest for this study.

The only difference between cases 1, 3 and 6 is the tracking method. The liquid volume in the core is similar. We suppose that the main difference is observed on droplets/particles velocities, analyzed later.

An important parameter appears from this volume distribution that was not commented before, the threshold under the which morphological criteria are no longer checked. The comparison between case 3 and 7 shows that the amount of transformed droplets drastically decreased since the transformation is more restrictive. It shows the importance of transformation criteria and open the questions of the arguability of a criterion that no longer checked sphericity.

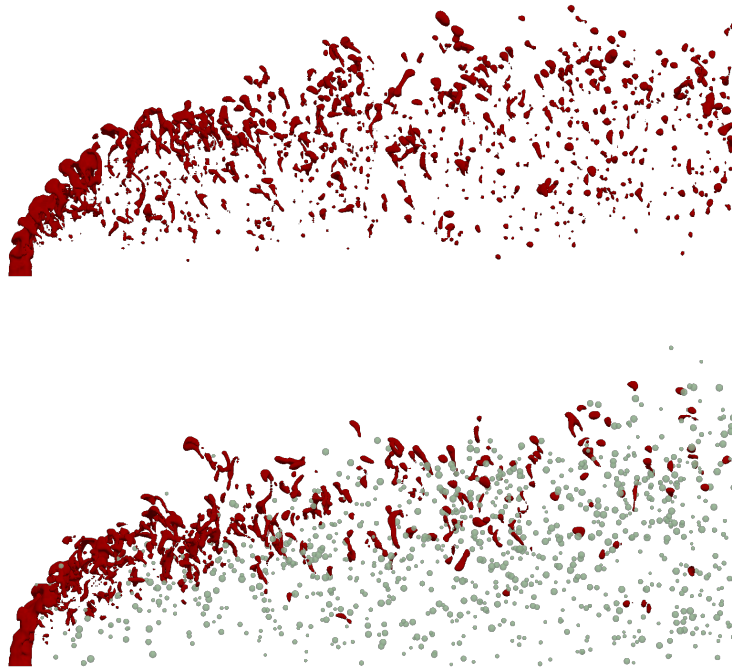


Figure V.10: Snapshots of crossflow side view simulation, top ICM (case 1), bottom Hyb. One-way with low Flattening criteria (case 3).

### Morphological criteria influence

From the volume splitting [table V.5], no differences are observed between case 3 and case 4, where, to recall, the Flattening is increased from  $Flattening = 0.65$  to  $0.85$ . The area of transition from droplets toward particles is first studied and compared to the reference's results [Herrmann, 2010b]. In his work, no distance criterion is used and transformations occur close to the injection, approximately  $x/D_{inj} = 0.5$ .

In our configuration, the transformation area for both configurations, case 3 (yellow triangle) and case 4 (blue circle), where droplets are transformed to particles, are overlapping for the side/top view and no clear differences are observed [figure V.11]. It is noted that preferential areas of transformation are observed (see darker areas, for example at  $x/D_{inj} = [5.5; 7.5]$  [right figure V.11]). To understand these areas, a deep analysis will be done in the future. A first step toward it is the study of the entropy to determine if transformations occur near to the primary atomization area. On our results, we do not observe near injector's hole,  $x/D_{inj} = 0.5$ , meanwhile it is clearly observed on the reference results, generally, transformations occur further. Two reasons can explain this modification: more restrictive transformations since no explicit distance criteria are used in his configuration (the detection algorithm acts as a distance criterion in his simulation, whenever a droplet is identified, it can be transformed) or the numerical resolution that is finer in the reference simulation [Herrmann, 2010b].

It is noted that transformations from particle toward droplet can strongly disturb the physical analysis, observed for transformation near interface (few meshes) [section IV.1]. To avoid them, we recall that distances are conserved relatively high ( $\mathcal{L}_{\mathcal{D} \rightarrow \mathcal{P}} = \max(4.5\Delta x, 3R_p)$ ). It is possible that these restrictions are not sufficient and transformation can occur in near breakup area.

To study the probability of such event, we define a zone representing primary atomization area using an entropy-based probability function [Blaisot and Yon, 2004, Blaisot et al., 2019], defined as follows:

$$E = \frac{-\sum_S p_S \ln(p_S)}{\ln(3)}, \quad (V.3)$$

where  $S$  represents the state into the which the studied area is identified and  $p_S$  the probability of

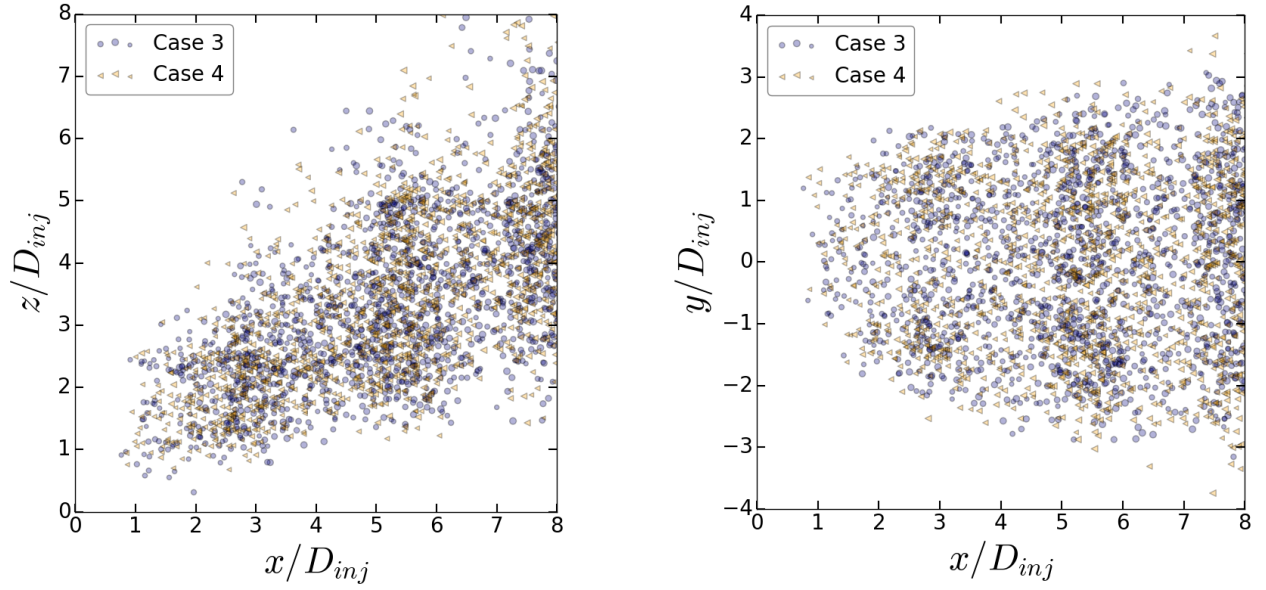


Figure V.11: Transformation from droplets to particle in crossflow atomization study for cases 3 (purple circle) and 4 (yellow triangle), side and top views.

occurrence of these states. Three states are defined: the liquid core, the dispersed phase identified as droplets and the carrier phase. The probability of occurrence of each state is computed over series of extracted 3D field from case 1 simulation. From the three-state conditions, entropy discretize the number of states seen per cell among the time. For example, a cell upward the jet always contains carrier phase, at the end of the post processing we find a probability of 1 to find carrier phase in the cell and 0 for other states. Then, then entropy computed in this cell is  $E = \ln(1)/\ln(3) = 0$ .

In the domain, there are some areas where only one state is identified, for example upstream the jet in the crossflow injection area. These areas are identified with a zero value since only one state is identified. On the other hand, the primary atomization area is defined as the area where the probability to find the three states is the highest, i.e. liquid core, dispersed and carrier phase. We can define a threshold where the probability is higher than the probability to find more than two states, defined as:

$$E_3 = \frac{\ln(2)}{\ln(3)} = 0.631,$$

to represent the limits of the primary atomization area [Blaisot et al., 2019].

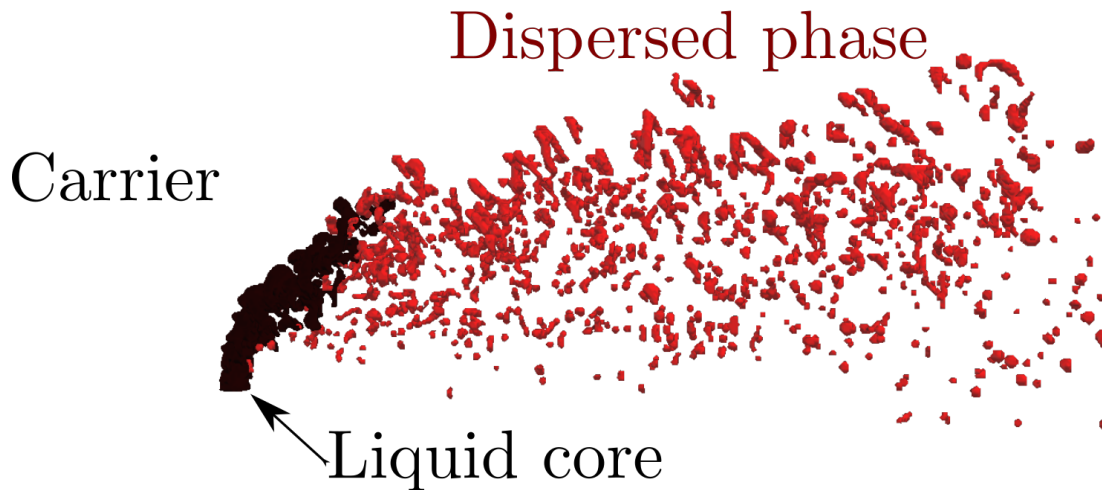


Figure V.12: Crossflow *VoF* extraction using spatial (along *y*) and temporal averaging to construct entropy map.

To define the three state fields, detection algorithm and the  $VoF$  field are coupled. The  $VoF$  gives the entire representation of the volume occupied by the liquid phase and the detection algorithm can split these structures. From the  $VoF$ , the carrier phase is directly identified when  $\alpha = 0$  showed in white for clarity [figure V.12]. However, we have to split the liquid phase into two states, liquid core and dispersed phase. To do so, the detection algorithm is used, the liquid core is identified as the structure with the higher volume and the closer to the injector [table V.5], giving a field binarized with 1-value on its position. We multiply this field by the  $VoF$  giving us the liquid core position on the Cartesian grid, showed in black [figure V.12]. The same procedure is used to recover the dispersed phase since we identify it as all liquid structures that do not belong to the liquid core, showed in red [figure V.12].

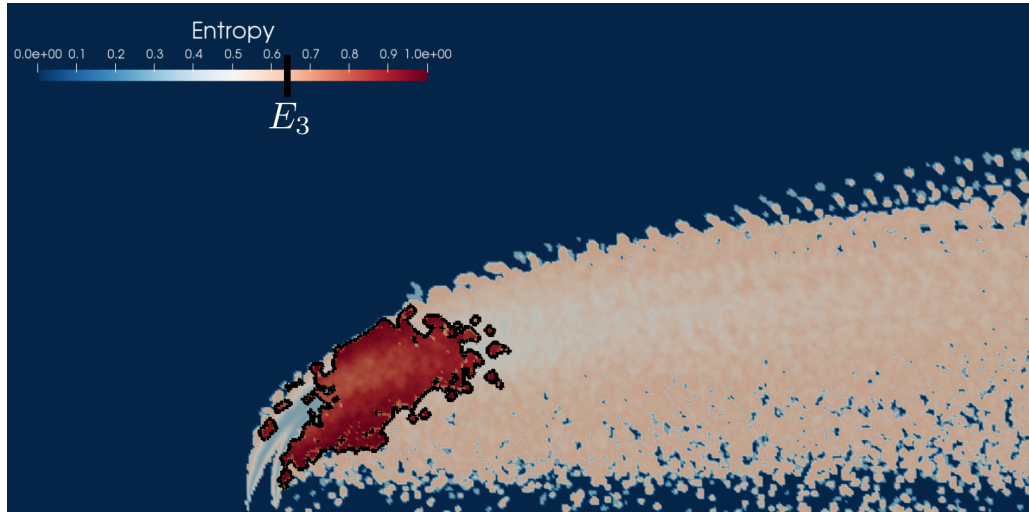


Figure V.13: Slice view of figure V.14 among  $x$ - $z$  centered on  $y$  (center of the liquid jet), showing primary atomization area in red through the entropy definition [equation V.3]. A contour is added to show the two states probability at  $E = 0.631$ .

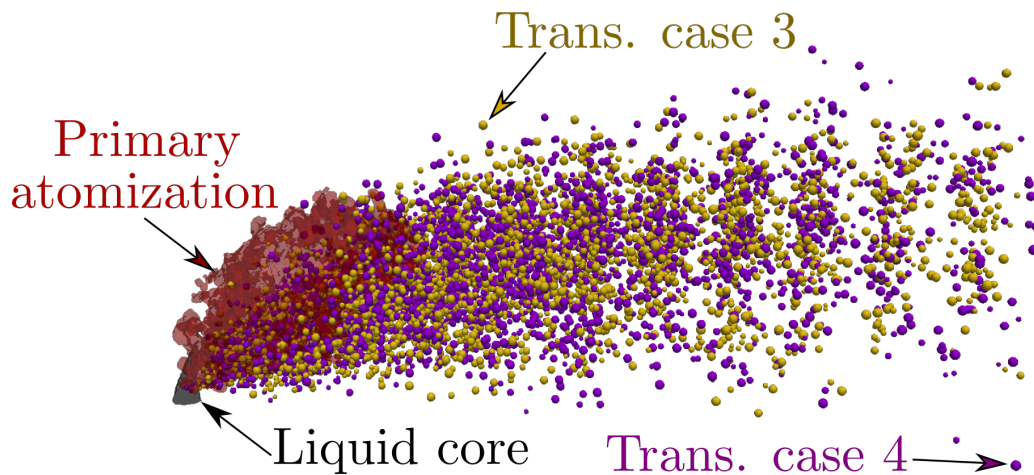


Figure V.14: 3D view of the definition of the primary atomization area (isocontour in red where  $E > 0.631$ ) through the entropy definition [equation V.3]. In black the liquid core is showed and droplets toward particles transformations locations are showed respectively in yellow and purple for cases 3 and 4.

Applying entropy definition over the temporal average of the three states probability [equation V.3], the 3D entropy map is obtained. A side view,  $x - z$  direction with  $y$  centered on liquid jet center, is proposed [figure V.13]. We can identify the areas where the probability to find only one

state are clearly see since the color map converges toward 0. For example the carrier phase observed before the jet and on the top area of the figure. A much more interesting area is recovered using the entropy, the identification of the liquid core (bottom left). Several applications require deep knowledge of the liquid jet bending [Wu et al., 1997, Stenzler et al., 2006] or the liquid jet penetration [Brown and McDonnell, 2006]. In numerical simulation, averaging Eulerian fields is a global strategy, whatever the *Level-set* field [Herrmann, 2010b] or the *VoF* field are considered [Mukundan et al., 2020]. Using entropy permits to exactly define the probability to find the liquid core state, comparing its results with classical algorithm might provide a variation of these quantities and can be considered in future jet studies.

Our interest lies in the area where the probability to find more than one state occurs. To understand the evolution of the entropy, we present the state evolution near liquid core identification. It appears that three clear cones are observed, the first one identifies the liquid core with  $E = 0$ . The second cone, next to the liquid core, has an entropy of approximately  $E = 0.5$ , in light orange. We understand this value by the high probability to find the liquid core state and the carrier phase. Moving away from this zone, we observe the presence of a third cone with an entropy value of approximately  $E = 0.3$ , in light blue. We understand this value by the lower probability to find the liquid core and the carrier phase at this distance of the injector. Near these cones, a small red area is represented on the top left of the jet injection, which is not expected. To our understanding, we consider that the detection algorithm can identify this area as dispersed meanwhile it should belong to the liquid core. Downstream to the jet, some discontinuities are observed in the Entropy map. From private communications with J.B. Blaisot, it seems that the strategy that we selected to conduct the entropy analysis is not optimal since we should have used decorrelated random images, at least every characteristic time. Indeed, it is complex to render such images since it would consist of approximately 250 box time.

Nevertheless, we consider that our area of interest is well defined since we clearly observe a wide red area in the near vicinity of the breakup area. This area, delimited by the iso contour at  $E = \ln(2)/\ln(3)$ , represents the primary atomiaation area since this is the area where we find the highest probability to identify the liquid core, the dispersed phase and the carrier phase [figure V.12]. Our interest is to determine if droplets are transformed toward particles in this area. The 3D rendering of the entropy map is then studied [figure V.14]. Only droplets transformed in the range  $2 < d_d/\Delta x < 4$  are represented on this map to be consistent with our prior methodology to construct [figure V.11]. Results are displayed for case 3 (yellow spheres) and case 4 (purple spheres) and we do not differentiate cases 3 and 4 in our observations since transformations occur in similar areas.

Again, we represent the liquid core (in black) and the primary atomization (in red). On these fields, the position where droplets are transformed into particles are added, respectively in yellow and purple for cases 3 and 4. Globally, the transformations occur at the same location and the further we are from the injector's hole, the less transformations are observed. This is desired since we want to transform droplets as far as we leave the primary atomization area. On the other hand, we observe that several early transformations are observed. We computed the number of these transformations that occur inside of the primary atomization area, we obtain respectively 15.7% and 17.8% of the tranformations for cases 3 and 4 [figure V.14]. The next study focuses on the analysis of the droplets' distribution at several radii distances from the injector to understand the influence of this variation.

To go further on the relative influence of morphological criteria observed on droplets toward particles transformations analysis, we study droplets/particles' diameter distribution at several distances of the injection;  $x/D_{inj} = [5; 10; 20]$  [figure V.15]. To construct these distributions, the methodology for case 1 distribution [figure V.3a] is used without filtering small droplets. We recall that the bins are shared between graphs and are found exactly at the same  $d_d/\Delta x$ . Objects are considered only when they are identified at  $x/D_{inj} \pm 0.05 \times x/D_{inj}$  before and after the distance of study, for example  $x/D_{inj} = 5$  gives a range of study of  $x/D_{inj} = [4.95 : 5.05]$ . Two diameters have to be considered on these distributions, first,  $d_d/\Delta x = 4$  where transformations begin and  $d_d/\Delta x = 2$  where morphological criteria are no longer used. We represent the droplets and particles on the same distribution, to split them we represent particles with hashed area and droplets with filled area.

At  $x/D_{inj} = 5$  [figure V.15a], differences are observed for the quantity of particles per diameter. Droplets distributions are similar and differences are only observed for particles' distributions. Case

4 shows distribution variation near  $d_d/\Delta x = 2$ , clearly, the bin right above this limit has a harsh modification. We understand this modification since below  $d_d/\Delta x = 2$ , morphological criteria are no longer used. Below this limit, the probability to find particles is higher in case 4, showing that the criteria of transformation have an influence. Downstream to the jet, this influence is limited seeing how close the distributions are at  $x/D_{inj} = [10; 20]$  [figures V.15b and V.15c]. The discontinuity observed near  $d_d/\Delta x = 2$  is no longer observed showing that the further we are from the injection area the lower is the influence of morphological criteria.

### Volume restriction

To recall the reader, the goal of the volume restriction is to avoid numerical instabilities due to interface normal inversion and local velocity acceleration due to poor numerical resolution for small structures. The advantage of the subsonic crossflow application is the low density ratio,  $\rho^* = 10$ , which reduces the probability to observe these structures. Then, conserving highly under resolved structures do not modify the physic of the solution.

Comparing the iso contour at  $\phi = 0$  for cases 1 and 2 [top figure V.10 and top figure V.17], it appears that the area covered by the liquid volume fraction is wider without volume restriction. Using only the description given by the *Level-set* is an under estimation of the total volume downstream to the jet since a cell can contain a volume fraction higher than 0 with a negative *Level-set* sign function [section I.5]. Then, a threshold is applied on the *VoF*,  $\alpha > 1 \cdot 10^{-2}$  to represent all cells containing more than this value of liquid volume fraction. Indeed, the smallest structures are not represented by the *Level-set* function since it gives a negative sign for these scales. On this specific snapshot, we observe that the total liquid volume identified with the *VoF* is 1.09 times higher than the one identified with *Level-set* function.

We study the influence of the volume restriction on the droplets' size distribution. Then, the Hybrid approach is applied without volume restriction and we comment the results.

The PDF are constructed following the methodology presented in case 1 vs reference comparison [figure V.3a] with a filter for structures smaller than  $d_d/\Delta x < 1 \cdot 10^{-1}$ , i.e. bins are shared for the two simulations and start at smallest diameter of the without restriction simulation. We recall that the diameter is computed from the volume belonging to one structure. To comment the evolution of the restriction with respect to the distance to the injector, three distances are selected to construct the PDF:  $x/D_{inj} = [5; 10; 20]$  following the methodology developed for morphological criteria study [figure V.15].

At  $x/D_{inj} = 5$ , the smallest diameter in case 1 is at  $d_d/\Delta x = 1.5$  where a clear-cut is observed [figure V.18a]. On the other side of the distribution, we recover the results presented before [subsection V.2.1]. On this distribution, the higher size is at  $d_d/\Delta x \approx 2.5$ .

Without volume restriction, structures are identified below the mesh size, a discontinuity is observed at  $d_d/\Delta x = 0.4$ , then, a cut is observed at  $d_d/\Delta x = 0.3$ . It is complex to comment on the reason why the discontinuity appears exactly at this location from these under resolved structures. Moreover, we comment that small droplets were observed below the range chosen for the PDF, until  $d_d/\Delta x = 0.03$ , we chose to not represent them to have a coherence when comparing both distributions with the same bins. Finally, the distribution without volume restriction recover the same structure as the simulation with restriction even though case 1 have a bigger droplets' representation. It shows that the volume restriction only influences the small scales and it gives an idea of the quantity of liquid volume that is removed from the crossflow.

At  $x/D_{inj} = 10$ , the highest probability are found in the same range for both distributions [figure V.18b]. A distribution similar to the one observed for the  $x/D_{inj} = 5$  configuration is obtained for case 1. On the other hand, case 2 recover a distribution more homogeneous since the discontinuity is no longer observed at  $d_d/\Delta x = 0.4$ . We recall that structures smaller are recovered below our threshold. For the biggest droplets, above  $d_d/\Delta x > 7$ , we observe that they are recovered on this distribution, not observed at  $x/D_{inj} = 5$  for this configuration.

At  $x/D_{inj} = 20$ , for case 1, the probability to find droplets with a diameter equivalent to  $d_d/\Delta x = 1.5$  dropped from  $10^{-2}$  to  $3 \cdot 10^{-3}$ , it is supposed that this is the action of the volume restriction [figure V.18c]. It strongly modifies the PDF representation, but in the total volume of the simulation these



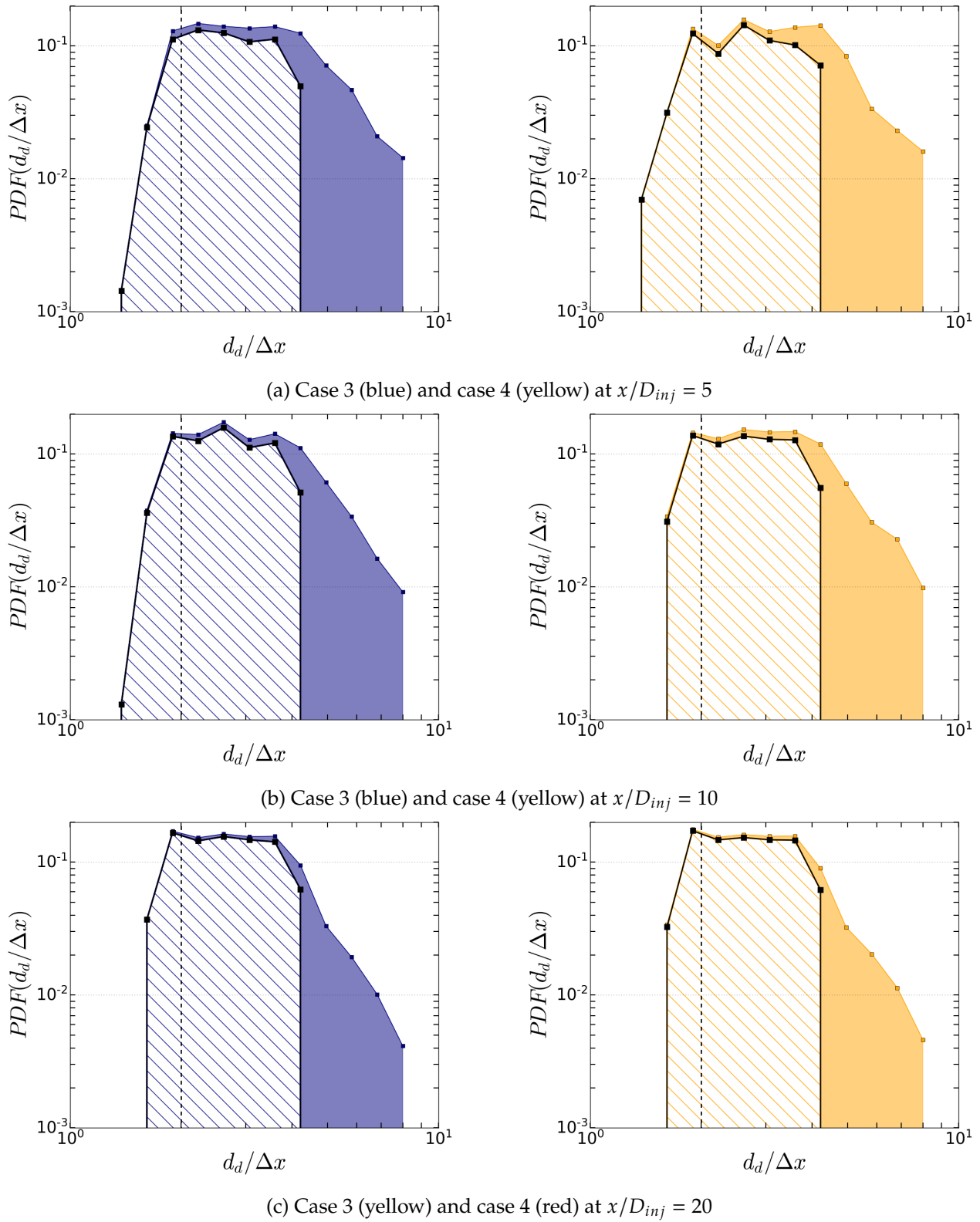


Figure V.15: Probability density function of diameter distribution scaled by mesh size. Results showed are for the Case 3 (blue) and Case 4 (yellow) at  $x/D_{inj} = [5, 10, 20]$  [figures V.15a, V.15b and V.15c]. Filled areas represent ICM droplets, hatched areas represent particles.

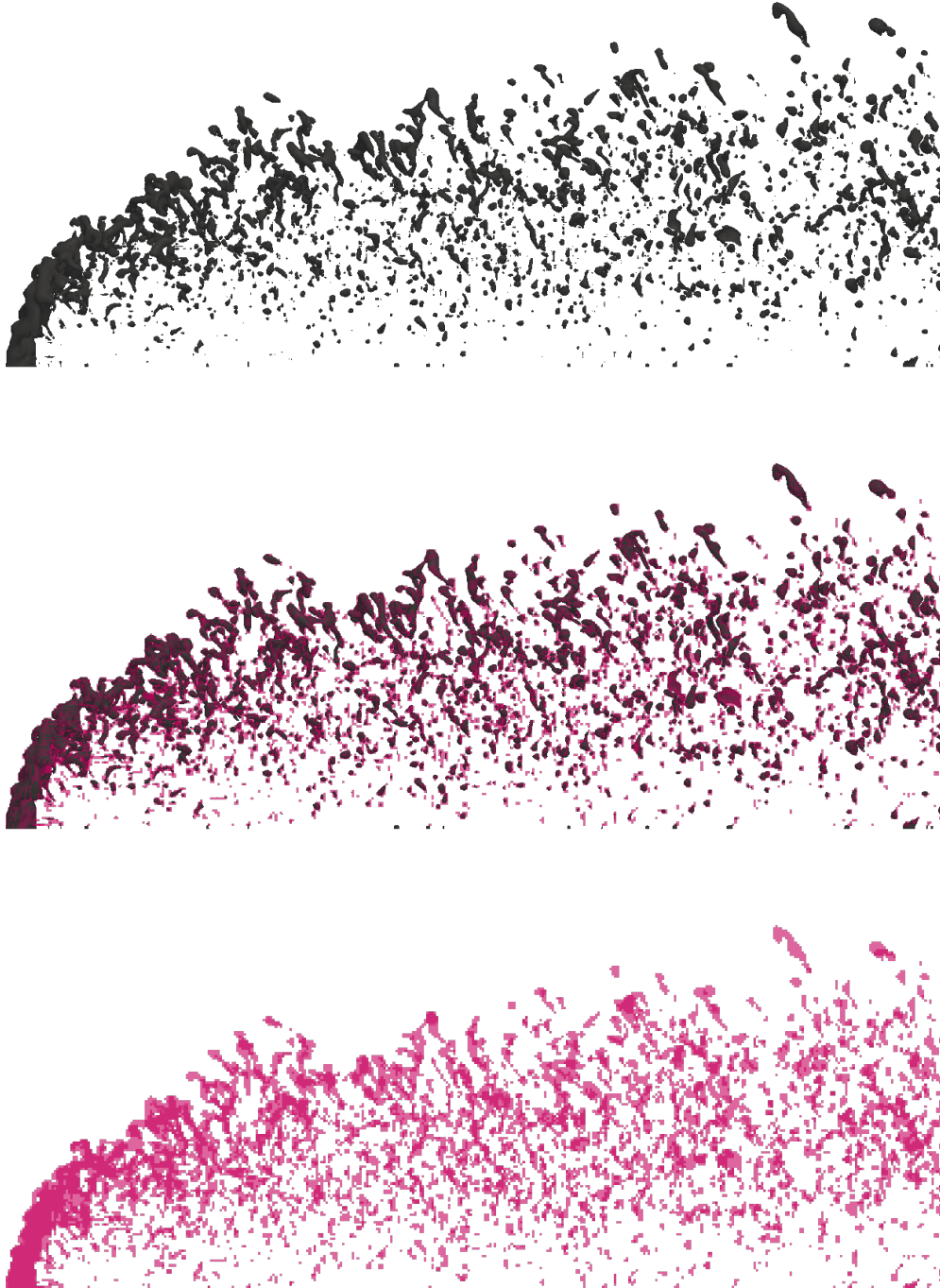


Figure V.16: Side view snapshots of crossflow simulation without volume restriction ICM (case 2), top *Level-set* contour at  $\phi = 0$ , bottom contour based on  $VoF > 10^{-3}$ , centered *Level-set* + *VoF* fields.



structures represent 0.67% of the total liquid volume which is relatively low. Indeed, the droplets with an equivalent diameter equal to  $d_d/\Delta x = 1.5$  are not removed from the simulation, the process is more complex and involve normal inversion in interface transport which breaks droplets, then, when the droplets are no longer identified with its *Level-set* information, it is removed [figure IV.23]. We can observe it on the representation of the *VoF* and *Level-set* fields for the crossflow snapshot. Near the injection's hole, we observe that a *VoF* structure is joined to the bottom of the liquid core [bottom figure V.17]. This structure is not identified with the *Level-set* function [bottom figure V.17], since we modified the detection algorithm to avoid the *Level-set* correction, we are sure that more structures of different shapes are identified in case 2, leading to this higher estimation of small structures (this difference of liquid volume fraction identification ensures that 100% of the liquid is identified in case 2, in case 1 we averaged the ratio liquid structures identified by detection algorithm and total liquid structures in the simulation, we have an underestimation of the total volume of  $10^{-5}\%$ ).

For case 2, the distribution is shifted toward bigger droplets since the minimum is obtained at  $d_d/\Delta x = 0.4$ . The difference is not due to the PDF representation since the same bins are used. Our assumption is that the smaller structures are no longer transported and a clustering occur in the simulation, called a frozen liquid structure. According to our observations and the increase in volume in the simulation, it is more likely that this is due to an accumulation of drops. We prefer to remain cautious on these observations due to the unpredictability of these structures representing a few percentages of mesh. The main conclusion is that a liquid volume fraction is removed from the simulation and using the Hybrid approach without volume restriction could improve the mass conservation on such simulation.

The Hybrid approach is applied on already converged crossflow without volume restriction (case 2  $\rightarrow$  case 5). A snapshot of the simulation is provided showing particles in black [figure V.17] after one characteristic time ( $t^* = \frac{U_c}{0.75 \times L_x}$ ). Small particles are observed, of the order of  $d_p/\Delta x = 10^{-2}$ , showing that the smallest structures are transported with Lagrangian tracking, one of the main goal of our Hybrid approach [figure V.18]. Nevertheless, observing the results of case 3 where Hybrid approach is applied with the same criteria of transformation on a simulation performed with volume restriction [bottom figure V.10] shows that almost no droplets have been transformed into particles for this configuration. We understand this difference by the wide presence of *VoF* in the dispersed area. When the algorithm determines if a droplet can be transformed, we check that there are no other interfaces, because the update could erase them. If we find some *VoF* structure, we cancel the transformation which restrains the transformations for this configuration.

Also, we consider that if the simulation is performed from the start with Hybrid approach and without volume restriction, we must ensure more transformation into particles. This strategy might be use for future simulation. For our analysis, it was more convenient to use an already converged simulation even though our study is limited by our choice.

To improve the treatment of the Hybrid approach without volume restriction, an equilibrium must be found. We commented from the distance of transformation analysis that early transformations occur even though restrictive morphological criteria are implemented [figure V.12]. The conclusions from these results would be to increase the distance of transformation in order to ensure that transformations only occur far from the breakup area. On the other hand, the evolution of the droplets' distribution for case 2 shows that the more we wait before transformation, the more small structures are dispersed in the secondary atomization area. Then, we suppose that in dense jet no transformations occur because of too restrictive criteria. It shows that our study is totally modified by the change of interface's transport and that the criteria are sensitive to the method.

To solve it, a new scale of transformation can be proposed. Its objective would be to allow transformations without respect to the distance criteria for structures below a threshold. However, these transformed structures have a high probability to be transformed back due to the small distance from the possible other interface. Even though interface reconstruction has been improved [section III.5], these reconstructions would be impossible to perform and the droplets would simply vanish at *Level-set* update. In future works, it is conceivable to introduce a class of particles that do not validate distance criterion and are no longer transformed into droplets.



Figure V.17: Side view snapshots of crossflow simulation without volume restriction Hybrid (case 5).

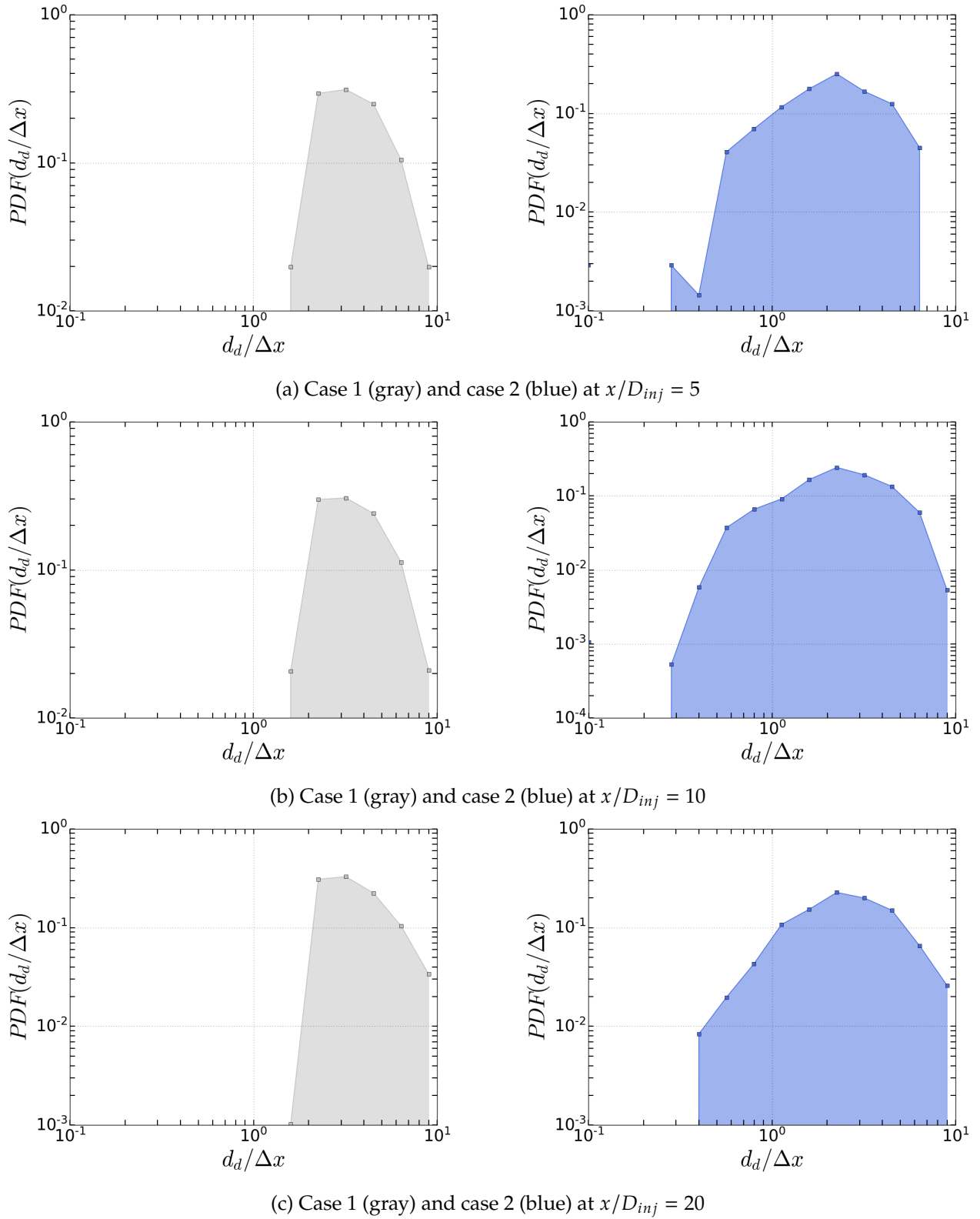


Figure V.18: Probability density function of diameter distribution scaled by mesh size. Results showed are for the case 1 (gray) against case 2 (navy blue) at  $x/D_{inj} = [5, 10, 20]$  [figures V.15a, V.15b and V.15c].

## Influence of the Lagrangian tracking

Using Hybrid approach to transport small droplets can have an influence on the droplets size distribution, but also on the velocity distribution of the droplets. Moreover, two Hybrid coupling are used, Hybrid One-way and Two-way approaches (cases 3 and 6). Due to the wide number of droplets and the complexity to select exactly the same droplet, two droplets/particles trajectories per method are randomly extracted, their trajectories are showed on 3D axis [figure V.19].

First, all droplets/particles are going out of the domain through the  $x+$  boundary, it shows that whatever the method, the crossflow speed gives the direction of propagation. From the reference, we expect to observe a convergence toward  $u_p/U_c = 1$  downstream to the jet [Herrmann, 2010b]. For case 1 and case 3, it appears that two droplets/particles are located in the recirculation area since a *loop* is observed in their trajectories before to reach crossflow velocity, following already commented observations.

Next the velocity evolution of each droplets/particles for the three configurations are plotted (since we aim to follow droplets/particles identification, we plot only droplets/particles velocity evolution when more than 10 events are obtained, even though we have more droplets in case 1 than case 3 and 6, it is easier to follow particles since we treat interactions as collisions, i.e. no breakup and coalescence appears that modifies the id), giving a noisy graph that exhibits some clear tendencies [figure V.20]. On this graph, we do not differentiate between droplets and particles for Hybrid configurations, moreover, we also observe that some droplets/particles are sharing the same id which creates some discontinuities. They are minor and do not modify the analysis.

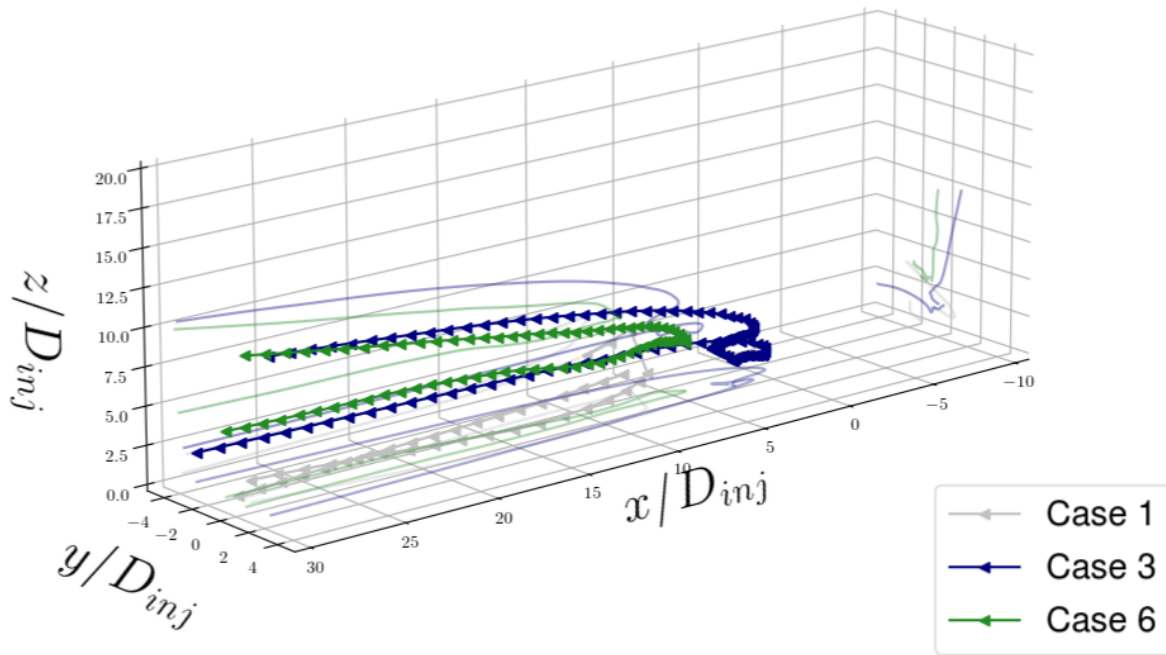


Figure V.19: Droplets/Particles 3D trajectory within the domain for three configurations, full ICM simulation (gray case 1), Hybrid One-way simulation (navy blue case 3) and Hybrid Two-way simulation (green case 6).

We commented that the physic of the crossflow leads to a creation of two breakup area, one on its top and one behind it. It is complex to determine a clear tendency for the droplets detached from the top of the crossflow, however, droplets detached from the main liquid core are trapped in the recirculation area. It explains why negative velocities are observed near the injection area. Later, droplets' velocity converges toward crossflow velocity. This pattern is easier to observed for Hybrids' simulations since we have more data. From these results, we do not observe differences between these two configurations. The joined PDF is constructed to go further on this analysis, adding the reference simulations' results, similarly to the ICM analysis [figure V.4].

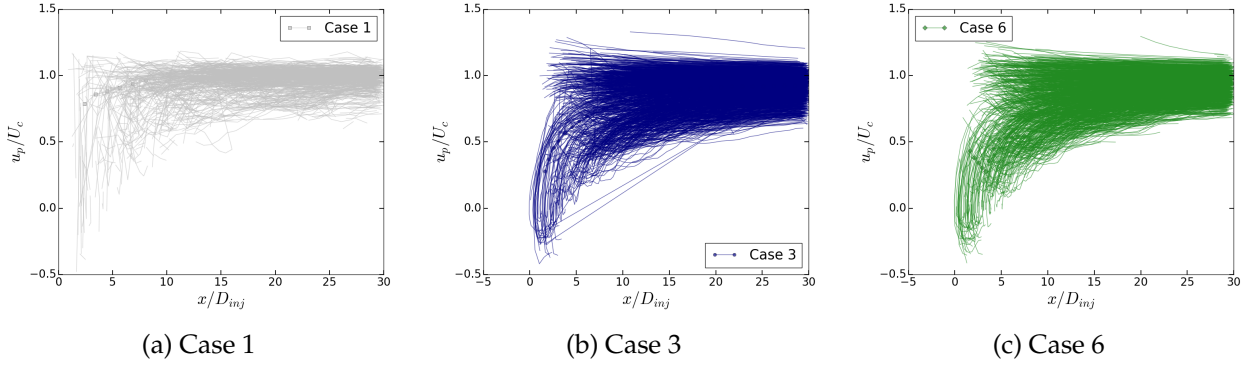


Figure V.20: Droplets/Particles velocity evolution scaled by crossflow velocity,  $u_p/U_c$ , against the distance to the injector  $x/D_{inj}$  for cases 1,3 and 6, respectively figures V.20a, V.20b and V.20c.

The two classes of droplets are used, small and medium and results are respectively showed on figures V.21a and V.21b. Hybrid approaches (cases 3 and 6), are slightly underestimating the highest probability found for the ICM results (case 1), we consider that it is observed because the range of velocities is higher.

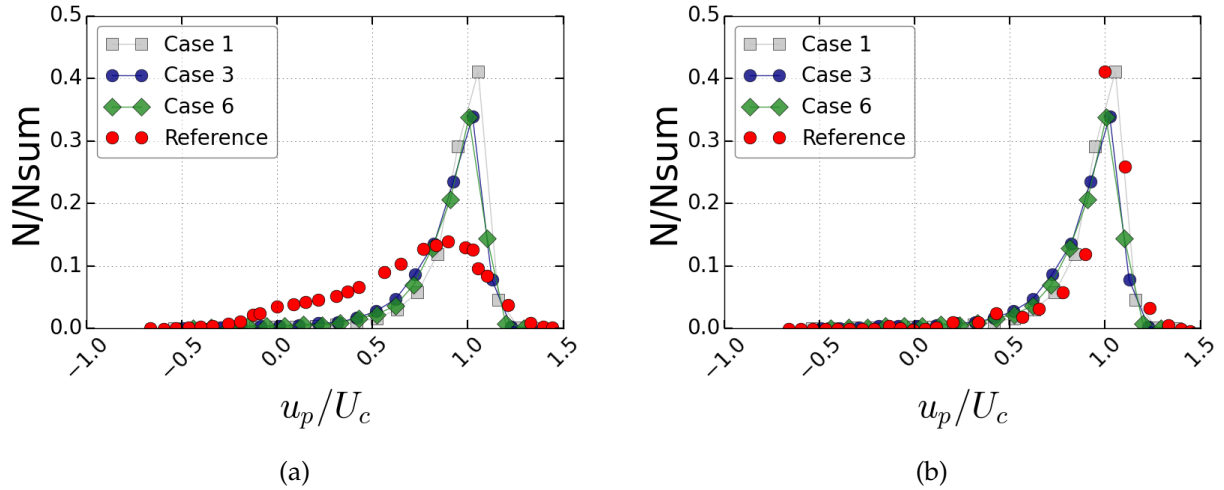


Figure V.21: Velocity distribution in the direction of the crossflow scaled by crossflow injection velocity for smallest class of droplets  $d_0$  [figure V.21a], and medium droplets  $d_4$  [figure V.21b] compared to reference's results [Herrmann, 2010b].

We now study droplets/particles velocity evolution scaled by the turbulent jet injection velocity in  $y$ -direction. Near injection and for all methods, the dispersion of velocity is wide and downstream to the jet we converge toward  $v_p/U_j = 0$ . It can be surprising to observe few negative velocities, we understand these evolutions by droplets ejected at the top of the liquid jet that evolve along  $y$ -direction. For this configuration, we do not observe a clear difference between all results.

Again, the two classes of droplets are used, and we plot the joined PDF [figure V.23]. For small droplets [figure V.23a], it is observed that we overestimate the probability that a droplet/particle evolve with a velocity  $v_p/U_j < 0$  compared to reference results. The dispersion are relatively close in all our configurations, it appears that the Hybrid Two-way and full ICM simulations tend to have the higher over estimation of droplets with negative values. The wideness of the distribution is underestimated on the range  $v_p/U_j > 0$  for all configurations. For medium droplets, we recover the reference's maximum, centered on  $v_p/U_j = 0$ . Again, we do not observe clear differences between the three configurations.

Finally, we study the transverse velocity evolution,  $z$ -direction, scaled by the crossflow velocity. The figure displaying droplets/particles trajectories [figure V.19] showed that near injector (some evolution were observed along the transverse direction that decreased downstream to the jet). Then,

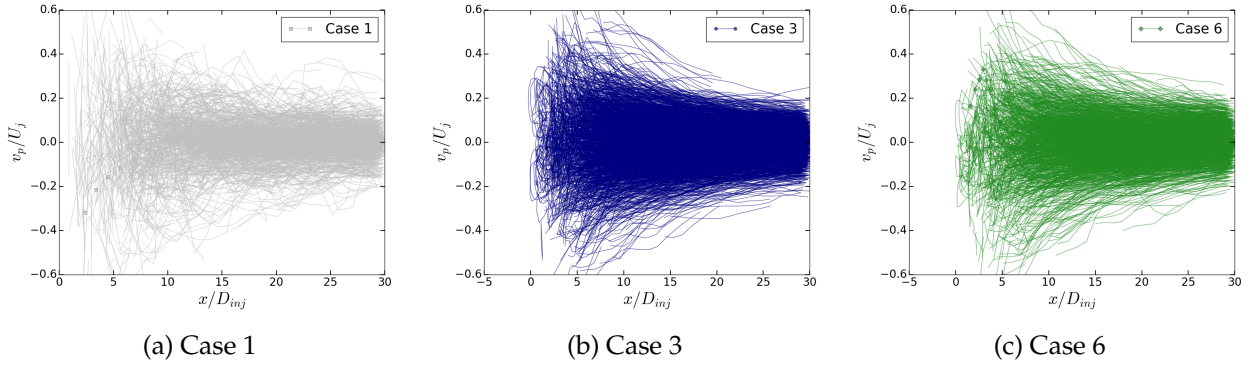


Figure V.22: Droplets/Particles velocity evolution scaled by liquid jet velocity,  $v_p/U_j$ , against the distance to the injector  $x/D_{inj}$  for cases 1,3 and 6, respectively figures V.22a, V.22b and V.22c.

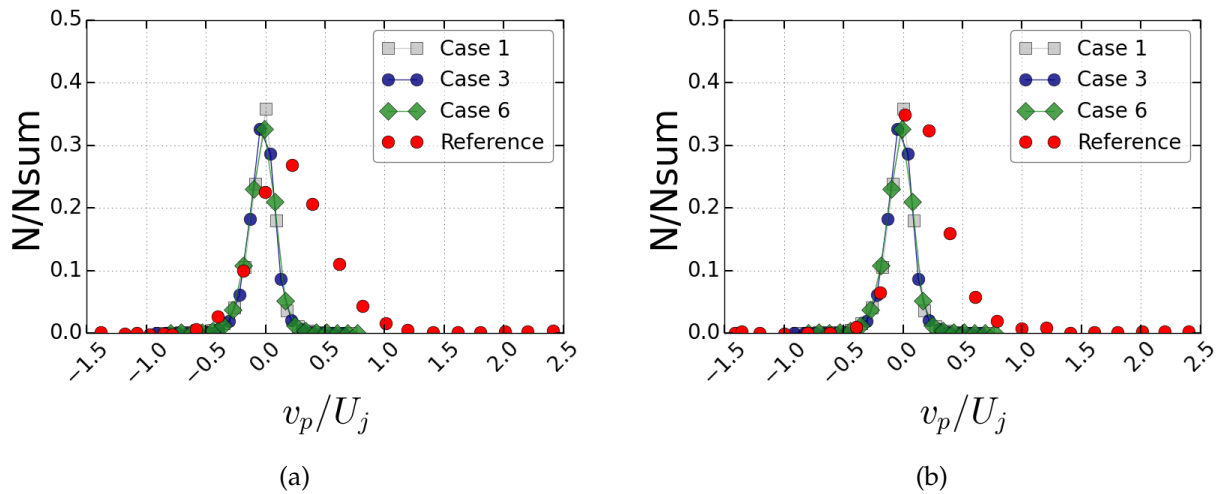


Figure V.23: Velocity distribution in the jet injection direction scaled by liquid jet injection velocity for smallest class of droplets  $d_0$  [figure V.23a], and medium droplets  $d_3$  [figure V.23b] compared to reference's results [Herrmann, 2010b].

the convergence toward  $w_p/U_c = 0$  observed for all configurations is recovered [figure V.24]. A difference of transverse velocity evolution is observed between ICM and Hybrids results, a lot of oscillations are observed for the ICM meanwhile we do not observe strong change in case 3 and 6 evolutions. Near the injector, it is noted that Hybrid Two-way approach has a wider transverse velocity dispersion than Hybrid One-way approach, we suppose that these events are not representative of the global statistics but are worth being commented since we expect to improve the physic of the dispersed zone through the consideration of particles' momentum.

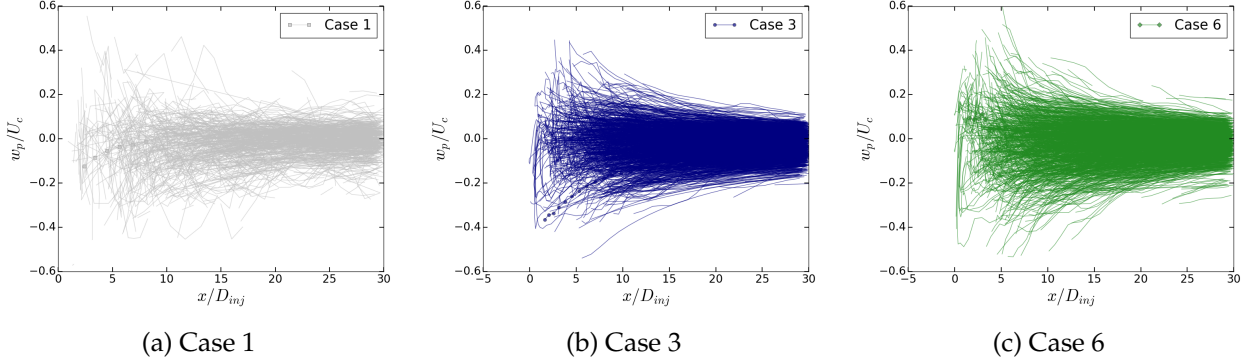


Figure V.24: Droplets/Particles velocity evolution scaled by crossflow velocity,  $w_p/U_c$ , against the distance to the injector  $x/D_{inj}$  for cases 1,3 and 6, respectively figures V.24a, V.24b and V.24c.

The joined PDF for the two classes of droplets, small and mediums are plotted considering  $w_p/U_c$  [figure V.25]. For this configuration, we recover the higher frequency obtained for the reference simulation even though we underestimate its dispersion. Again, results obtained for the three configurations are similar, a notable difference is that the highest probability to find  $w_p/U_c = 0$  is smaller for the Hybrid Two-way approach for both droplets' size.

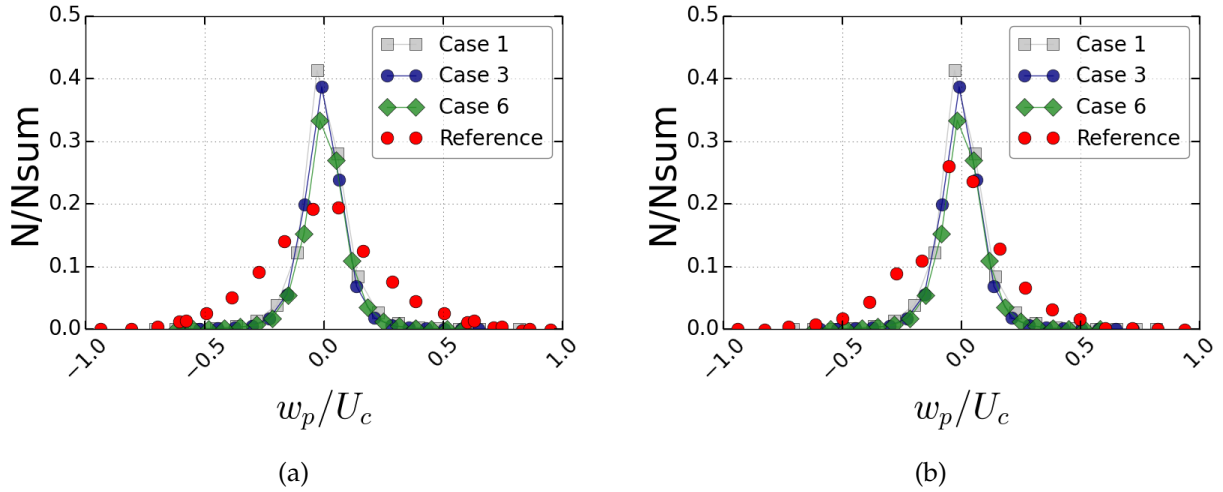


Figure V.25: Transverse velocity distribution scaled by crossflow injection velocity for smallest class of droplets  $d_0$  [figure V.25a], and medium droplets  $d_3$  [figure V.25b] compared to reference's results [Herrmann, 2010b].

A strong assumption that we tried to study in this manuscript is to know if the droplets transformed into Lagrangian particles are stable and have a small probability to break. Some physical criteria have been developed and implemented to characterize the physic of the interface. When the droplets are transformed, an indication to determine if further evolution can occur is the droplets/particles Weber number. In this manuscript, several strategies to define it are introduced to be as accurate as possible on the studied phenomenon. In the present analysis, we have to consider a Weber number that can be used respectively for droplets and particles to determine if the structure will further break. Ideally, the slip velocity might be considered but for droplets/particles, it involves length scales that



we cannot access in our configuration [Cisse et al., 2013]. A simple numerical definition is to scale the droplets/particles' velocity in the direction of the crossflow with the crossflow injection's velocity:  $|u_p - U_c|$ . From this simple definition of the Weber number, a threshold below the which no breakup are observed is estimated,  $We < 12$  [Pilch and Erdman, 1987, Wierzbna, 1990] (below this range, only vibrationnal breakup is considered). We define it as follows:

$$We = \frac{\rho_g d_p (|u_p - U_c|)^2}{\sigma}.$$

This Weber number is computed for each droplets/particles, to differentiate them, four categories are created; droplets that can be transformed with  $d_d/\Delta x < 4$  (in red), that cannot be transformed with  $d_d/\Delta x > 4$  (in black), and the two kinds of particles, respectively One-way and Two-way (blue and green). A filter is applied for droplets with a *Flattening* smaller than 0.25 to discriminate structure far from sphericity. The results are showed for the three configurations [figure V.26], for all configurations the closer to the injector the higher is the Weber number. Most of the droplets with  $d_d/\Delta x > 4$  have a low Weber number at several radii of the injector, we suppose that these droplets reached a stable shape and the probability to observe a breakup is low. For the Hybrid results, droplets with  $d_d/\Delta x < 4$  have a low Weber number, we suppose that these droplets are not transformed due to the high restriction on the distance criteria. At several radii from the injector, one can assume that these droplets would be better transformed.

Near injector, a wider dispersion is observed for transformed particles in both Hybrid approaches [figures V.26b and V.26c]. Therefore, we assume that some droplets are transformed into particles too early since a high probability to break is observed,  $We > 12$ . Downstream to the jet, it appears that the Weber number of these particles decrease, it is coherent with the observations of particles reaching the crossflow velocity reducing the slip velocity.

From this analysis, one can consider that a secondary breakup model is required to further break particles with a high Weber number, however, their Weber number decrease downstream to the jet and these early transformations are not so irrelevant. The strategy to compute the Weber number, scaled by the crossflow velocity can also modify our conclusions. A better strategy would be to compute the Weber number of particles/droplets with a slip velocity based on the carrier velocity on the vicinity of the droplets/particles, but it is complex to achieve due to the proximity with other structures. This is the reason our entire strategy to determine a physical criterion is based on the information that the droplets can collect inside/at its interface.

### V.2.3 Configuration comparisons

To conclude on the influence of criteria on the simulation results, the diameter frequency distributions for all configurations is commented considering droplets and particles [table V.3]. This distribution is constructed following the methodology presented before [figure V.3], using the same bins for all distributions. Here, we consider the smallest diameter equal to  $d_d/\Delta x = 1.5$ , it corresponds to the area where morphological criteria are no longer validated in configuration 7 which is the most restrictive. Since the configuration using Hybrid approach without volume restriction is relatively close to case 2, we do not show the results [figure V.27]. Similar observations for case 6 that is relatively close to case 3.

For the full ICM configuration (cases 1 and 2), differences are observed below  $d_d/D_{inj} < 0.2$ . Due to the use of the volume restriction, configuration 1 filters some of the small droplets. However, some structures are not removed which yields to a non-zero probability to find droplets below this threshold, similarly to what was observed in the ICM volume restriction comparison [figures V.18]. Thus, we decide to truncate case 1's distribution. Above this threshold, the tendency is similar since we observed that same maximums are obtained, near  $d_d/\Delta x = 2.5$ , for both configurations [figure V.18]. The lower probability to find bigger droplets in the ICM without volume restriction simulation is the result of an accumulation of small droplets since the ratio liquid core/dispersed phase are similar [table V.5].

Using Hybrid approach that transforms under resolved droplets below the numerical resolution  $d_d/\Delta x < 4$  modifies the droplets' size distribution. Below  $d_d/\Delta < 4$ , it is observed that with Hybrid



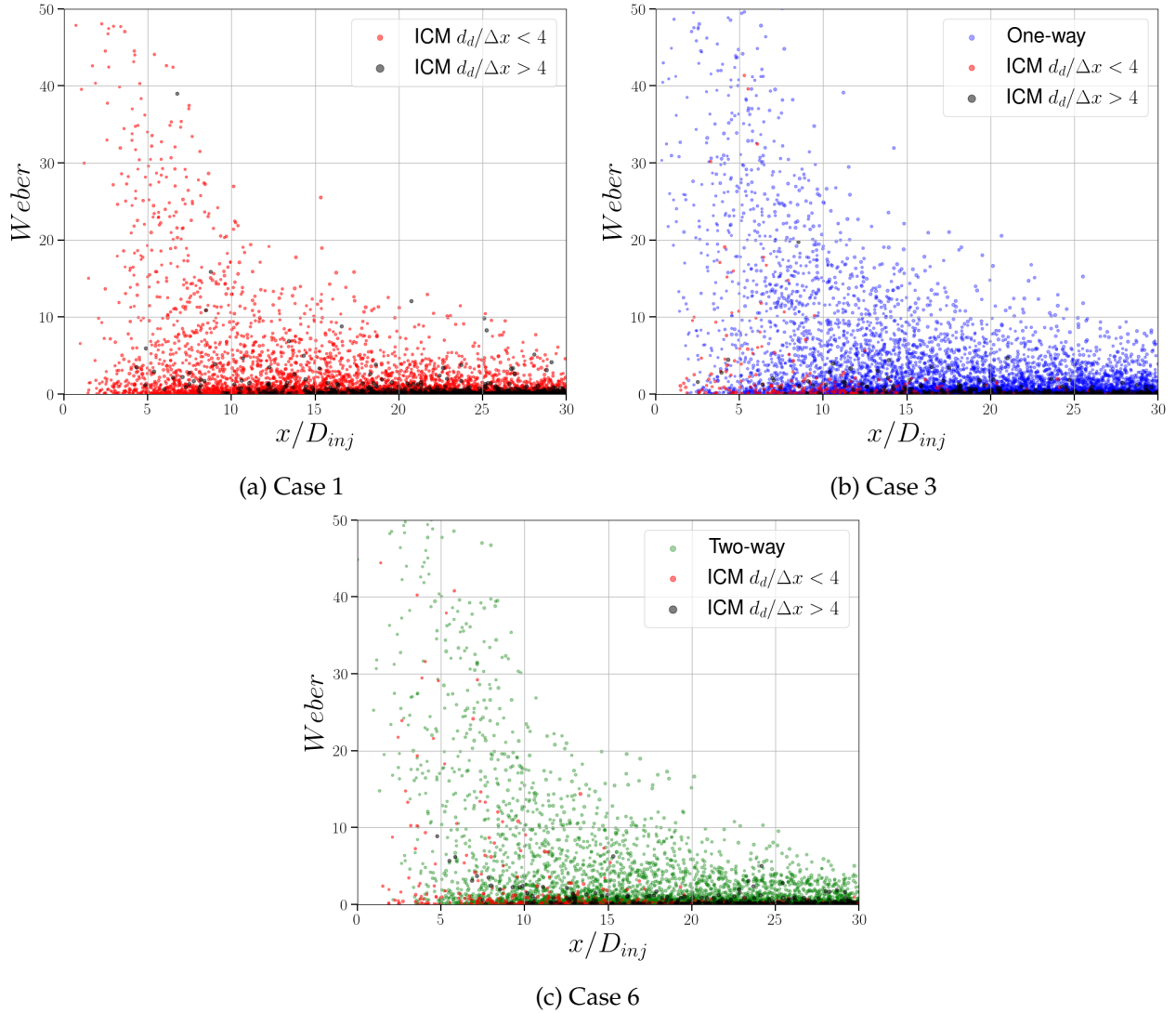


Figure V.26: Droplets/Particles Weber number evolution against the distance to the injector  $x/D_{inj}$  for cases 1, 3 and 6, respectively figures V.26a, V.26b and V.26c. In red ICM droplets size below  $d_d/\Delta x < 4$ , in black ICM droplets size above  $d_d/\Delta x > 4$ , in blue One-way method particles transport, in green Two-way method particles transport.

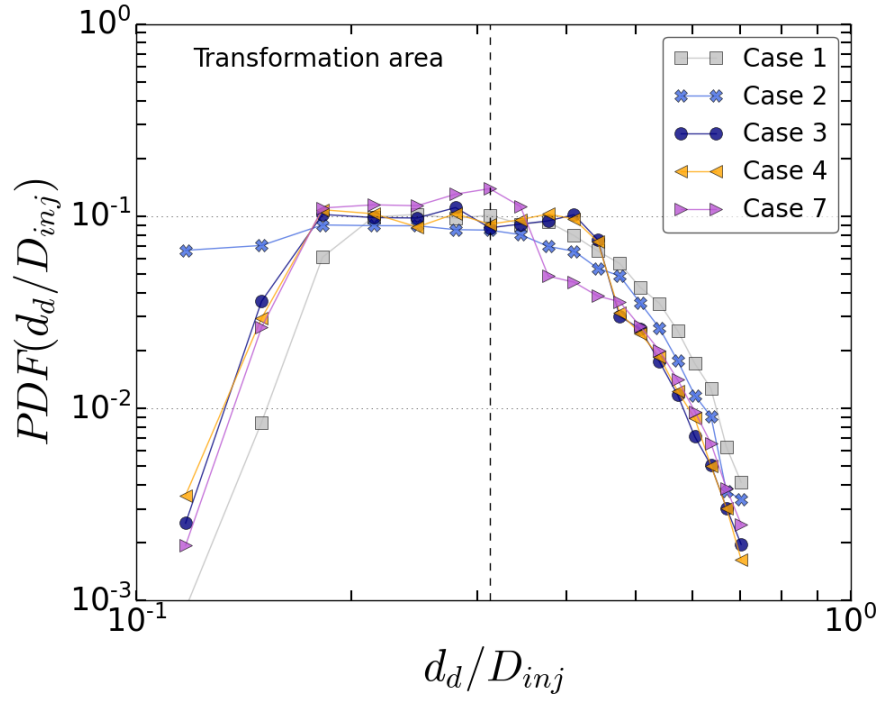


Figure V.27: Diameter scaled by liquid jet injection diameter probability density function for all configurations [table V.3] considering droplets and particles (only for Hybrid approaches).

approaches, cases 3, 4 and 7, the probability to find small droplets is higher than for the ICM simulation, case 1. However, this probability remains below the results observed without volume restriction, case 2, since we no longer filter structures. As a consequence, the probability to find bigger droplets in the Hybrid approach is lower than for ICM methods. Following our understanding, the reason why lies in the range  $0.2 < d_d/D_{inj} < 0.4$ . When a droplet evolves within the domain breakup events can occur, thus, the transformation from droplet toward particle stops this phenomenon [figure V.26]. Due to transformation events, we observe a discontinuity of droplets/particles distributions at  $d_d/D_{inj} \approx 0.45$  and  $d_d/D_{inj} \approx 0.33$ , respectively for the configurations where the threshold of direct transformation is set to  $d_d/\Delta x = 2$  and  $d_d/\Delta x = 1.5$ , see case 3 and 7. We are not able to identify the origin of the discontinuities on the PDF that occurs for droplets larger than the diameter used as criteria to transform droplets to particles. We suppose that the difference in the droplets/particles accumulation area are caused by this criterion since it is the only difference between the simulations even if it remains a zone of shadow in our study.

From this analysis it appears that the morphological criteria are useful since they modified the droplet's size distributions (case 3 vs case 7). However, the variation of the criteria must be relatively high in order to observe differences (case 3 vs case 4).

### V.3 Computational cost of simulation

From the comparison of simulations [section V.1 table V.2], four configurations are selected to study the computational cost of the simulation: case 1, case 2, case 3 and case 6. These configurations are selected to study:

- the influence of the transport of the small structures that are not removed in case 2,
- the influence of the use of Hybrid method with respect to full ICM,
- the influence of a most sophisticated particles transport algorithm with Hyb. Two-way vs Hyb. One-way approaches.

We recall that the load per processor is  $32^3$  cells since the domain is meshed with  $N_x \times N_y \times N_z = 512 \times 128 \times 256$  with 512 processors split in  $16 \times 4 \times 8$ .

The procedure to determine the time spent in each subroutine is to use a timer function that is swiped when the category of interest is changed, for example going from Eulerian solver to Lagrangian solver. The advantage of this strategy is to recover exactly the total time spent in the simulation and to split it into our categories of interest: the Lagrangian transport function, transformation functions, *CLSVoF* transport and flux transport [Vaudor et al., 2017], Poisson solver and other Eulerian functions. All categories are split in two parts: the time spent in the sequential algorithm (Sequential) and the time spent in MPI exchanges (MPI).

The simulations are performed for  $0.2t^*$  [s] of an already converged crossflow simulation, for the Hybrid approaches, droplets were already transformed in particle, and we ensured that the time steps selected to relaunch the simulation were coherent with the volume ratio 1/3 liquid core, 1/3 dispersed droplets and 1/3 particles. We compare the results for full ICM configurations [figure V.28], it is recalled that the main difference is the quantity of small droplets involved in configuration 2.

The results are described using case 1 [figure V.28a] because the distribution of time spent in each subroutine is similar. The three main categories where efforts are concentrated are in interface transport, other Eulerian functions and Poisson solver, respectively 740, 800 and 546 *seconds*. For the two first categories, it appears that approximately 65% of the time is spent in MPI exchanges. For Poisson solver, the tendency is inverted since *only* 40% of the computational time is spent in this subroutine. It is noted that the time spent in the post treatment category considers the time spent to identify droplets in our simulation, small with respect to other categories.

To compute the same time without volume restriction, the solver takes 1.26 more time. First, the time spent in post treatment, mainly droplets identification, is ten times higher since we have more isolated small structures in this configuration [figure V.17]. It represents almost 10% of the computational cost and must be considered when droplets statistics are computed. The time spent in Eulerian others and *CLSVoF* is increased of 1.2, it seems that this increase is related to the volume variation between both simulations. In both categories, the strong increase is located in the MPI functions since the serial part of the computation remains constant. We observe that another influence of the volume restriction on the simulation is then to reduce the CPU time of the simulation.

The results for the Hybrid methods are showed using the same categories [figure V.29]. At the end of the restart for Hybrid One-way approach, around 1000 particles were identified in the domain, and around 600 were identified for the Hybrid Two-way approach meaning that efforts spent to transport particles are not equivalent. We observe that considering Two-way approach drastically increases the time spent in Lagrangian transport since it increased from less than 0.1 [s] for  $0.2t^*$  [s] of simulation in Hyb. One-way simulation to 336 [s] for the Hybrid Two-way simulation. The reason is in the interpolation/redistribution of the particles' momentum. Using the Hyb. One-way approach drastically decreases the computational cost and is worth using to treat two-phase flow atomization.

The strategy to redistribute particles' momentum is to send the particles' to all neighboring processors and to update an Eulerian field where the particles' momentum is added through volume force. This field is then added to Navier-Stokes equations to consider particles' momentum. The drawback of our implementation is that all particles are sent to the neighbors even if it is not required since it facilitates MPI exchanges. A filter on the list of particles to share with neighbors can be considered to reduce this computational cost. This has to be considered in future developments.

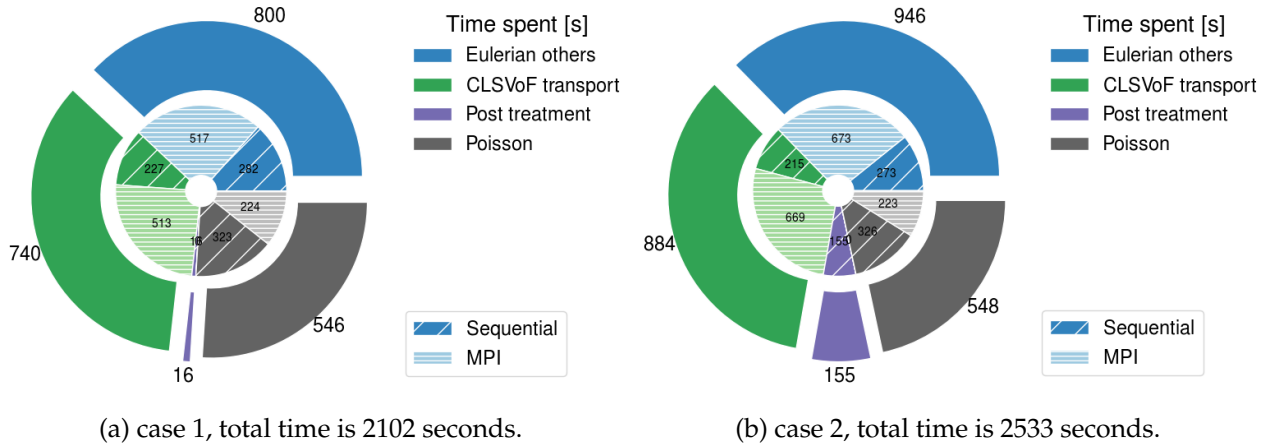


Figure V.28: Computational cost of configurations full ICM with [figure V.28a] and without volume restriction [figure V.28b] for crossflow application. Simulations are performed during  $0.2t^*$  [s] from an already converged simulation.

Comparing figures V.28a and V.29a, we observe that the time spent in the Eulerian subroutines is slightly decreased, approximately 4%. For these configurations, we observe that the volume transported with *CLSVoF* is reduced of approximately 30% in Hybrid One-way approach and the gain in total computational time is of 5%. Transformation toward One-way approach is a relative gain in terms of computational time.

The results displayed for the Two-way approach are showing a different behavior. Even though the volume transported with *CLSVoF* has been reduced of 20%, the time spent in the overall code is increased. More tests are required to fully understand these results on a configuration with total control of all parameters involved.

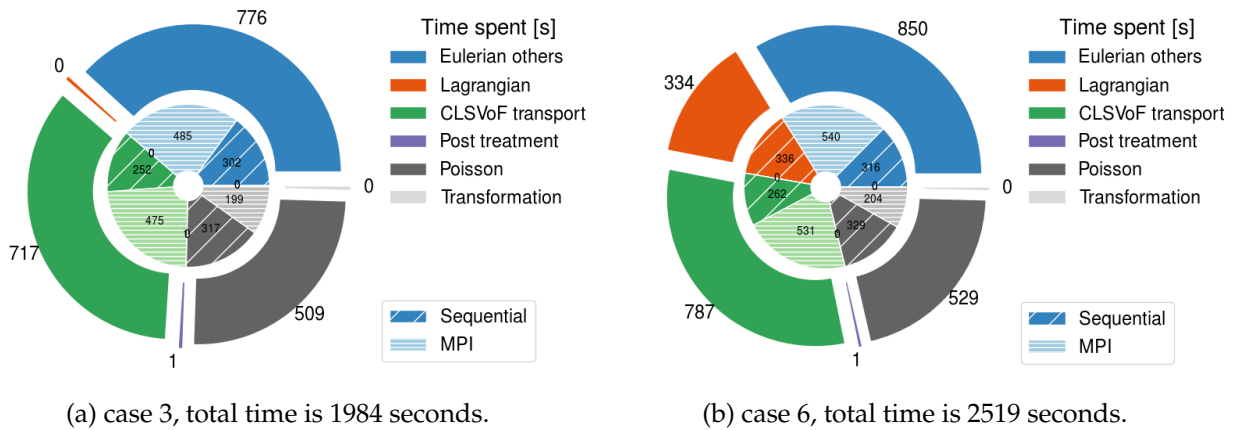


Figure V.29: Computational cost of configurations Hybrid approaches with volume restriction, respectively One-way [figure V.29a] and Two-way [figure V.29b] for crossflow application. Simulations are performed during  $0.2t^*$  [s] from an already converged simulation.

---

## Perspectives

---

The work presented in this manuscript is focused on the direct numerical simulation of two-phase flow atomization. The numerical solver *Archer* has been used, developed in CORIA laboratory [Ménard et al., 2007, Aniszewski et al., 2014, Vaudor et al., 2017]. In the first chapter, we briefly introduced the general concept of atomization, the numerical methods to transport interface focusing on *Archer* (CLSVoF method), giving us the opportunity to introduce our objectives.

Our main goal was to improve the treatment of the small droplets through a Lagrangian transport. It has been done in three main stages. First, the development of a MPI Lagrangian solver able to treat several Lagrangian tracking approaches. It is in this part that most of the efforts have been concentrated in this PhD since we wanted to build an efficient, robust and adaptable Lagrangian solver that can handle several particles of different kinds with a dynamic allocation. Then, this solver has been coupled with the already implemented Interface Capturing Method in *Archer* to enhance the treatment of small structures. The goal is to avoid volume restriction using a Lagrangian description of the smallest structures, introducing criteria of transformation from Eulerian toward Lagrangian. Finally, developing these criteria introduced some questions on droplets morphological analysis. Our conclusions are summarized and perspectives resulting from our analysis are listed.

The Lagrangian tracking implemented methods are based on spherical sphere assumption, detailed in the second chapter. Two main families are used, Full Resolved Particle method that considers particles' interface and a Dispersed Particle method that does not represent the interface of the particle. In our implementation, the IBM (FRP) [Uhlmann, 2005, Breugem, 2012] method consists in considering a Lagrangian grid representing the particles' interface where velocities are interpolated and redistributed. The second method consists in the use of a fictitious particle on the Eulerian grid. We use a fluid's velocity interpolation to transport it. The assumption to use this method is to consider the influence of the particle as relatively small with respect to other physical phenomena. However, this assumption is less accurate when droplets of the size of the mesh are considered, then a particle momentum's redistribution is implemented. In this study, we observed that this redistribution modifies particles evolution because of the flow disturbance. A strategy has been implemented to filter it, showing great improvements on particles transport [Evrard et al., 2020].

The second goal of this manuscript is to transport under resolved droplets with particles tracking algorithm. One of the objective of our investigation was to consider several methods to ensure an accurate treatment of all droplets' size. All transformations from droplets toward particles and vice versa have been implemented, and validated ensuring mass and momentum conservation. We observed that the IBM method was less accurate than the CLSVoF method to transport medium droplets, thus we did not use this method in the Hybrid approach applied to more realistic applications. In future developments, this method can be coupled as a step toward One-way or Two-way considering the use of Adaptive Mesh Refinement, following [Zuzio et al., 2018]. Thus, only One-way and Two-way tracking are considered to transport particles. A remaining question is the influence of the momentum's redistribution near liquid interface, no clear conclusions are observed since we did not observe discrepancies. In future works, if the Two-way method modifies the behavior of the simulation, it could be interesting to use an improved version considering its volume fraction [Evrard et al., 2019]. So far, this method is able to simulate highly refined simulation and the study of two-phase flow atomization might be enhanced improving statistics in dispersed zone [figure V.30].

We noted that several assumptions are required to ensure a transformation of a droplet into particle such as its distance to other structures and its sphericity. We observed that these assumptions have a



Figure V.30: Crossflow atomization simulation using Hybrid approach in *Archer* solver.

strong influence on the droplets' size distribution at the end of the simulation.

When volume restriction is considered, the smaller scales of the simulation are removed to avoid numerical discrepancies. The challenge is to transform the droplet into particle before. The structure must be far from other interfaces in order to avoid a numerical modification of the simulation at transformation since the *Level-set* can be perturbed. After few iterations, the conservation of the *Level-set* distance property updates the entire Eulerian field. Then, the balance between distance of transformation and under resolved structure might be found. Recent developments have been done on interface transport [Mukundan et al., 2019b], however, this method remains costly, and we are currently coupling it with the Hybrid approach. It will benefit us since the method might be less dependent on the distance of transformation.

The other main criterion of transformation is the sphericity of the droplet that we aim to transport. We defined our strategy with two classes of transformation, a class where the morphology of the droplet can be studied and a class below a resolution where computation of morphological information is no longer accurate and structures are directly transformed. We observed that the influence of morphological criteria variation does not have a strong influence on the final droplets' size distribution, however, the threshold to go from one class of transformation to the other influences this distribution :an accumulation of droplets/particles is observed below this threshold. A solution to avoid this accumulation could be to implement a secondary breakup model (SBM).

We suppose that this SBM must be developed based on the droplets/particles physical properties. Several factors can modify the shape of the droplet, and break it resulting in smaller droplets. Coupling all these factors yield to complex models [Chen et al., 1998].

We decided to isolate physical phenomenon to characterize droplets evolution, based on a brief literature review we implemented a criteria based on capillary breakup and turbulent breakup. The capillary breakup criterion showed good results, more tests are required to extract information from our analysis and use these results to define an accurate SBM model based on the criterion [Lalanne et al., 2015].

The second criterion based on turbulent breakup came from the idea that the dissipation at droplets' interface can lead to strong shape variation, considered first through restrictive assumptions [Hinze, 1955] and later on analyzed through experimental and numerical analysis [Galinat et al., 2007, Aly et al., 2010, Perlekar et al., 2012, Dodd and Ferrante, 2016]. The fluctuation of velocity at interface has been used in this manuscript. In future developments, we consider that the local dissipation at droplets interface must be used to improve turbulent breakage mechanisms. In *Archer* solver, we have to account for the dissipation jump at the interface, recent works have to be followed to implement it in our analysis [Chen et al., 2019b].

We hope that future models to characterize droplets' breakup might be considered in a future PhD. From morphological droplets' information, we can imagine that non-spherical droplets might be transformed and transport adapting drag force computation since their breakage will be considered

through SBM modeling.

Beyond the results presented in this manuscript, our study has allowed us to develop transversal studies within the laboratory and international collaborations:

- to develop a methodology to analyze the loss of information for morphological analysis of projected droplets [Chéron et al., 2020],
- to conduct an internship on the droplets experimental collisions and expose our results at regional scale,
- a three months internship in SUSTECH University based in Shenzhen, mainland China has been done to benchmark two-phase flow interface treatment between *Archer* and a novel strategy [Chen et al., 2019a].

Other academical simulations have been performed such as the study of an airblast atomizer presented in national conference [Chéron et al., 2019]. All these developments open new horizons for future works.

- Il doit être terriblement imposant.  
Voilà ce que je veux être quand je  
serai grand.  
- Imposant ?  
- Hum...  
- Il ne faut pas viser aussi bas.  
- Que voulez-vous dire ?  
- Regarde le mont Fuji.  
- Je ne serai jamais comme le mont  
Fuji.  
- Au lieu de vouloir être comme ci ou  
comme ça, transforme-toi en un géant  
silencieux et immuable. Telle est la  
montagne, ne perds pas ton temps à  
essayer d'impressionner les autres. Si  
tu deviens le genre d'homme que les  
gens peuvent respecter, ils te  
respecteront sans que tu aies à lever  
le petit doigt.

Extrait des paroles de  
Myaomoto Musashi à  
son disciple.

*La pierre et le sabre,*  
Eiji Yoshikawa



---

# Appendix

---

## Richardson extrapolation algorithm

The Richardson extrapolation algorithm is used when a physical analysis does not have an analytical solution [Christiansen and Petersen, 1989]. It is based on the assumption that the convergence regime has been reached. That means that the errors are reduced in a regular manner by the algorithm when increasing the accuracy, refining the mesh. In this case, the value obtained from this algorithm is the theoretical value that is obtained at infinite mesh resolution (similar conclusions can be done for time resolution).

In most of the configurations studied in this manuscript, this algorithm is used to provide a value of convergence. We used it for a classical convergence study through mesh convergence, and also with CFL variation [section II.3].

The main assumption is that numerical error (i.e. the difference between the Richardson solution  $u_\infty$  and the solution for a given mesh resolution  $h$  is given by:

$$u_h - u_\infty = \alpha h^k. \quad (\text{A.1})$$

In this formula, there are three unknowns:  $u_\infty$ ,  $\alpha$  and the order of the method  $k$ . Using three numerical resolutions,  $h_1, h_2, h_3$ , the order of convergence of the method and the Richardson extrapolation solution can be obtained when the three meshes are given by:

$$h_1 = \beta h_2 = \beta^2 h_3, \quad (\text{A.2})$$

these solutions are given by:

$$k = \ln \left( \frac{h_3 - h_2}{h_2 - h_1} \right) / \ln(\beta), \quad (\text{A.3})$$

$$u_\infty = u_{h_1} + \frac{u_{h_1} - u_{h_2}}{\beta^k - 1}. \quad (\text{A.4})$$

In our case, sometimes we use a non regular convergence study and an iterative solver is used to recover these quantities [algorithm A.1]. It is important to recall that the Richardson extrapolation algorithm can be only used if the assumption [equation A.1] is verified. Otherwise, this algorithm can not provide the solution.

```
1 from scipy.optimize import fsolve
2 def Richardson(x,*data):# ,u1,u2,u3,h1,h2,h3):
3     u1,u2,u3,h1,h2,h3 = data
4     out = [u1-(x[0] + x[1]*h1**x[2])]
5     out.append(u2-(x[0] + x[1]*h2**x[2]))
6     out.append(((u1-u2)/(u1-u3)) - ((h1**x[2]-h2**x[2])/(h1**x[2]-h3**x[2])))
7     return out
8 def VRichardson(dic):
9     data = min(dic[str(Case[-1])]),min(dic[str(Case[-2])]),min(dic[str(Case[-3])]),Case
10    [-1],Case[-2],Case[-3]
11    print('Convergence order',fsolve(Richardson,[min(dic[str(Case[-1])]),1.,1.9],data)[:])
12    return fsolve(Richardson,[min(dic[str(Case[-1])]),1.,1.9],data)[0]
```

Algorithm A.1: Recovering Richardson terminal solution and method convergence order for three discontinuous points

---

## List of Figures

---

1	Energy consumption per inhabitant and sector. . . . .	15
2	Number of death from outdoor air pollution from <i>Our world in data</i> . . . . .	16
3	Atomization of a liquid jet in a combustion chamber [Dumouchel and Grout, 2009]. . .	17
I.1	Natural atomization illustration. . . . .	20
I.2	Discharge coefficient influence on liquid instability. . . . .	22
I.3	Industrial atomizers design illustrations. . . . .	22
I.4	Jet in crossflow for two density ratio, left: $\rho^* = 10$ , right: $\rho^* = 100$ , from [Herrmann, 2010b].	24
I.5	Representation of a spray with angle measurements. . . . .	25
I.6	Droplets distribution description. . . . .	27
I.7	Plateau-Rayleigh Instability on a cylindrical atomized liquid jet. . . . .	28
I.8	Ligament erosive breakup illustration. . . . .	28
I.9	Kelvin-Helmholtz natural and industrial examples. . . . .	29
I.10	Coaxial atomization from [Marmottant and Villermaux, 2004b]. . . . .	30
I.11	Breakup regimes map for capillary number against viscous ratio. . . . .	31
I.12	Mother droplet breakup scheme. . . . .	33
I.13	Droplet-Eddy interaction scheme. . . . .	34
I.14	Staggered and collocated grid description. . . . .	38
I.15	Interface length scale illustration to compare sharp interface, in blue, and diffuse interface, in red, modelling. . . . .	39
I.16	Description of reconstruction and advection of interface from [Tryggvason et al., 2011].	41
I.17	Initialization of the <i>Level-set</i> field around a circular droplet, from [Tanguy, 2004]. . . . .	42
I.18	CLSVOF reconstruction scheme. . . . .	44
I.19	Eulerian temporal scheme in <i>Archer</i> . . . . .	45
I.20	Mass flux decomposition for consistent computation. . . . .	46
I.21	Ghost fluid implementation illustration. . . . .	47
I.22	Comparison of experimental atomization results [Marmottant and Villermaux, 2004b] against <i>Archer</i> results [Vaudor et al., 2017] . . . . .	48
I.23	Frozen liquid parcel in <i>Archer</i> . . . . .	49
I.24	Volume restriction in <i>Archer</i> for an under resolved droplet. . . . .	50
I.25	Illustration of Hybrid method use on a splash configuration. . . . .	50
II.1	One-way and Two-way coupling illustration. . . . .	54
II.2	Steps to advect particle with Two-way coupling in <i>Archer</i> . . . . .	57
II.3	Eulerian and Lagrangian grid representing the surface of the yellow particle [Breugem, 2012].	58
II.4	Steps to advect IBM particle in <i>Archer</i> . . . . .	59
II.5	Illustration of eulerian domain splitting to store particles over one processor. . . . .	63
II.6	Memory storage implementation illustration for particles' information. . . . .	64
II.7	Illustration of research of particles collision algorithm. . . . .	66
II.8	<i>Archer</i> Eulerian/Lagrangian temporal scheme for Euler Explicit and Runge-Kutta 2 method. . . . .	69
II.9	One-way free-falling particle velocity evolution results. . . . .	71
II.10	Presentation of array of particles simulation. . . . .	72

II.11	Array of particles reference's simulation mean and three nodes velocity evolution. . . .	72
II.12	Comparison <i>Archer</i> /Analytical solution of free-falling particle's velocity against characteristic time for granular, $V_{Sto.}$ and $V_{Sto.,\eta}$ . . . . .	73
II.13	Redistribution of the momentum of the particle for various filter's size $\delta = [3., 5., 7.] \cdot R_p$ using the Gaussian filter function. . . . .	74
II.14	Two-way free-falling particle velocity evolution results. . . . .	76
II.15	Two-way free-falling particle terminal velocity results. . . . .	77
II.16	Two-way free-falling particle maximal velocity interpolation analysis. . . . .	78
II.17	Convergence study of <i>Archer</i> Lagrangian model using EE and RK2 against CFL. . . . .	80
II.18	Influence of the density ratio on added mass and buoyancy forces. . . . .	80
II.19	Temporal convergence study for added mass, buoyancy and drag force implementation in <i>Archer</i> . . . . .	82
II.20	Euler Explicit and Runge-Kutta 2 temporal scheme results for Two-way method. . . .	84
II.21	Euler Explicit and Runge-Kutta 2 temporal scheme convergence study for Two-way method. . . . .	84
II.22	IBM free-falling particle velocity evolution results without radius retraction. . . . .	86
II.23	IBM free-falling particle velocity evolution results with radius retraction. . . . .	88
II.24	Speed up study of IBM simulation comparing two mesh generation methodologies. . .	89
II.25	IBM arrays of particles mean velocity evolution results. . . . .	90
II.26	IBM arrays of particles velocity evolution at three nodes results. . . . .	91
II.27	Streamflows around droplets/particles in free-falling droplet/particle simulation. . . .	93
II.28	Free-falling droplet velocity evolution results and comparison against particles' one. .	94
III.1	Illustration of structures detection algorithm using <i>CLFVoF</i> information. . . . .	98
III.2	Results showing tagging correction based on <i>Level-set</i> information. . . . .	99
III.3	Reconstruction of the center of gravity of a structure to conserve identity during time evolution. . . . .	99
III.4	Conservation of droplets' history after breakup. . . . .	101
III.5	Conservation of droplets' history after coalescence. . . . .	101
III.6	Speedup results for detection and transformations functions implementation in <i>Archer</i> . .	103
III.7	Illustration of the distance criterion to validate droplet toward particle transformation. .	104
III.8	Illustration of the distance criterion to validate particle toward droplet transformation. .	105
III.9	(a) Information from <i>CLSVoF</i> Method, top-left: sphericity, top-right: distance, down-left: geometric information, down-right: <i>VoF</i> . (b) evolution of the accuracy for each geometrical parameter increasing number of mesh in the droplet. . . . .	108
III.10	Evolution of deformation criteria for Lamb oscillation. . . . .	110
III.11	From left to right, initialization ( $t^* = 0$ ), step 1 ( $t^* = 0.0005$ ), step 2 ( $t^* = 0.0015$ ), and step 3 ( $t^* = 0.0035$ ). . . . .	112
III.12	Evolution of deformation criteria with respect to the dimensionless time for a droplet immersed in a HIT . . . . .	112
III.13	(a) Airblast atomizer snapshot. (b) Scatter of structures in terms of <i>Flattening</i> , $\Delta S_{VoF}$ and $\Delta \tilde{\kappa}_\phi$ . . . . .	114
III.14	Illustration of the reconstruction of the Eulerian field after transformation from droplet toward particle and vice versa. . . . .	116
III.15	Convergence study of the mass variation after transformation from particle toward droplet. .	119
III.16	Accuracy evolution of the minimization algorithm for droplet's reconstruction after transformation. . . . .	120
III.17	Scheme of reconstruction of the unperturbed velocity when resolved droplet is transformed toward Two-way particle on collocated grid, inspired from [Ling et al., 2015]. .	121
III.18	Hybrid approach applied to the free-falling droplet/particle test case to study momentum's conservation after transformation. . . . .	123
III.19	Collision Weber number against impact parameter. . . . .	125
III.20	Head-on binary collision comparison for experimental and numerical results. . . . .	127

III.21	Maximal velocity evolution comparison for ICM and Hybrid results for the head-on binary collision simulation. . . . .	128
IV.1	Snapshots from 2D ICM reference splash simulation. . . . .	132
IV.2	Liquid kinetic and interface top/bottom position evolution for 2D splash reference results. . . . .	133
IV.3	Qualitative interface evolution of the 2D splash for ICM and Hybrid approach. . . . .	138
IV.4	Hybrid One-way 2D splash results. . . . .	140
IV.5	Hybrid Two-way 2D splash results. . . . .	141
IV.6	Hybrid IBM 2D splash results. . . . .	143
IV.7	Hybrid IBM 2D top/bottom interface evolution against characteristic time. . . . .	144
IV.8	Qualitative interface evolution of the 3D splash for ICM and Hybrid approach. . . . .	145
IV.9	Influence of distance criterion in Hybrid approach on 3D splash simulation results. . . . .	146
IV.10	Qualitative interface evolution of the 3D splash for the same Hybrid approach with a variation of distance criterion. . . . .	147
IV.11	Liquid kinetic energy/interface top/bottom evolution for ICM vs all Hybrid approaches on the 3D splash. . . . .	148
IV.12	Time step evolution against characteristic time for reference simulation listed in table IV.7. . . . .	149
IV.13	Liquid kinetic energy evolution for Hybrid approach on the 3D splash with filter length variation. . . . .	149
IV.14	Illustration of the Plateau-Rayleigh atomization breakup and morphological evolution of the droplet. . . . .	150
IV.15	Computational domain, velocity profile and boundary conditions of the Plateau-Rayleigh atomization configuration. . . . .	151
IV.16	Droplets morphological evolution against the distance to the injector in Plateau-Rayleigh simulation. . . . .	154
IV.17	2D velocity field with interface representation of Plateau-Rayleigh simulation. . . . .	155
IV.18	Velocity histograms among x-y-z components for five droplets representing oscillatory regime of Plateau-Rayleigh simulation. . . . .	158
IV.19	Droplets standard deviation magnitude evolution against distance to the injector in Plateau-Rayleigh simulation. . . . .	159
IV.20	Droplets morphological evolution against the distance to the injector in Plateau-Rayleigh simulation (bis). . . . .	160
IV.21	ICM and Hybrid approaches velocity fields snapshots with interface representation in Plateau-Rayleigh simulation. . . . .	162
IV.22	Successive snapshots from coarse ICM simulation showing coalescence event downstream to the jet, image centered on $x/D_{inj} \approx 45$ . . . . .	163
IV.23	Successive snapshots from coarse ICM simulation showing volume restriction on under resolved droplet downstream to the jet, image center is approximately $x/D_{inj} = 45$ . . . . .	164
IV.24	Map of droplets transformed into particles, represented along x-y axis. . . . .	164
IV.25	Droplets/particles x-y position evolution scaled by injector diameter. . . . .	165
IV.26	Droplets/particles velocity evolution scaled by injection velocity against distance to injector along x-component. . . . .	165
IV.27	Analysis of velocity update after transformation in Plateau-Rayleigh Hybrid approach simulation. . . . .	166
IV.28	HIT flow generation illustration. . . . .	168
IV.29	Morphological droplets analysis in D-HIT simulation. . . . .	170
IV.30	Two droplets extracted from ICM simulation when released in the D-HIT with low and high <i>Flattening</i> value. . . . .	171
IV.31	Turbulent spectra comparison for ICM and Hybrid approaches in D-HIT study. . . . .	172
IV.32	ICM vs Hybrid approaches $V_{RMS}$ and position dispersion evolution against characteristic time in D-HIT simulation. . . . .	173
IV.33	ICM vs Hybrid approaches 3D position evolution in D-HIT simulation. . . . .	174
V.1	Crossflow physical configuration description. . . . .	178

V.2	Side/top snapshots ICM crossflow simulation. . . . .	179
V.3	Comparison of log-log droplets' diameter probability density function for <i>Archer</i> and reference results in crossflow simulation. . . . .	180
V.4	Velocity distribution in the direction of the crossflow scaled by crossflow injection velocity.	181
V.5	Velocity distribution in the jet injection direction scaled by liquid jet injection velocity.	181
V.6	Transverse velocity distribution scaled by crossflow injection velocity. . . . .	182
V.7	Droplets 3D trajectory in the domain. . . . .	183
V.8	Morphological atomized droplets from crossflow simulation analysis. . . . .	184
V.9	Dispersion of the velocity field inside droplets and surface criterion against distance of injector analysis in crossflow simulation. . . . .	185
V.10	Side snapshots of crossflow simulation with ICM/Hybrid approaches. . . . .	187
V.11	Transformation from droplets to particle location in crossflow with morphological criteria variation. . . . .	188
V.12	Crossflow liquid core and dispersed phase identification from the 3D <i>VoF</i> field. . . . .	188
V.13	Slice along x-z directions of the 3D crossflow entroy map. . . . .	189
V.14	3D crossflow entroy map. . . . .	189
V.15	Probability density function of diameter distribution scaled by mesh size for morphological criteria influence study. . . . .	192
V.16	Side snapshots of crossflow ICM simulation without volume restriction. . . . .	193
V.17	Side snapshots of crossflow Hybrid simulation without volume restriction. . . . .	195
V.18	Probability density function of diameter distribution scaled by mesh size for volume restriction study. . . . .	196
V.19	Droplets/Particles 3D trajectories for transport method comparison in the domain described on figure V.1. . . . .	197
V.20	Droplets/Particles velocity evolution in crossflow direction scaled by crossflow velocity against distance to injector for transport method comparison. . . . .	198
V.21	Droplets/Particles PDF of velocities in crossflow direction scaled by crossflow velocity for transport method comparison. . . . .	198
V.22	Droplets/Particles velocity evolution in jet direction scaled by jet velocity against distance to injector for transport method comparison. . . . .	199
V.23	Droplets/Particles PDF of velocities in jet direction scaled by jet velocity for transport method comparison. . . . .	199
V.24	Droplets/Particles velocity evolution in transverse direction scaled by crossflow velocity against distance to injector for transport method comparison. . . . .	200
V.25	Droplets/Particles PDF of velocities in transverse direction scaled by crossflow velocity for transport method comparison. . . . .	200
V.26	Droplets/Particles Weber number evolution against the distance to the injector for transport method comparison. . . . .	202
V.27	Diameter scaled by liquid jet injection diameter probability density function for all configurations [table V.3] considering droplets and particles (only for Hybrid approaches).	203
V.28	Computational cost of configurations full ICM with and without volume restriction for crossflow application. . . . .	205
V.29	Computational cost of configurations Hybrid approaches with volume restriction for crossflow application. . . . .	205
V.30	Crossflow atomization simulation using Hybrid approach in <i>Archer</i> solver. . . . .	207

---

## List of Tables

---

II.1	Physical parameter of the falling droplet simulation from [Ling et al., 2015] . . . . .	70
II.2	Physical parameter of the single fixed particle . . . . .	71
II.3	Parameter variation for the Two-way temporal scheme analysis . . . . .	83
II.4	Order of convergence and Richardson velocity extracted of figure II.21. . . . .	84
II.5	Richardson terminal velocities and convergence order for each IBM free-falling particle simulations. . . . .	87
III.1	List of simulations performed for the weak/strong speed up analysis in <i>Archer</i> . The same symbol represents the strong scaling: the load is modified at constant cells. The same color represents the weak scaling: the load is conserved and the resolution is modified. Those colors/symbols are listed in this table to simplify the analysis of figure III.6. . . .	102
III.2	Physical properties of head on binary collision from [Tanguy and Berlemont, 2005] to recover experiments [Ashgriz and Poo, 1990] . . . . .	126
III.3	Numerical configuration of head on binary collision from [Tanguy and Berlemont, 2005] to recover experiments [Ashgriz and Poo, 1990] . . . . .	126
IV.1	Simulation domain 3D splash, remove Z direction for 2D configuration. . . . .	132
IV.2	Parametrization of the 3D splash, remove Z direction for 2D configuration. . . . .	132
IV.3	List of simulation run with the One-way method for 2D/3D Splash. . . . .	134
IV.4	List of simulation run with Two-way approach, Splash 2D and 3D. . . . .	135
IV.5	List of simulation run with the IBM, Splash 2D and 3D. . . . .	136
IV.6	Detailed analysis on the mass conservation, crater depth and first liquid kinetic energy peak ponderated by own mesh resolution and reference for the 2D splash. The red color indicates a deviation of more than 10% and the green color a deviation of less than 3%. . . .	142
IV.7	Detailed analysis on the first liquid kinetic energy peak, the crater depth, and CPU time ponderated by own mesh resolution and reference for the 3D splash. The red color indicates a deviation of more than 10% and the green color a deviation of less than 3%. . . .	146
IV.8	Plateau-Rayleigh atomization's computational domain initialization. . . . .	151
IV.9	Plateau-Rayleigh atomization's physical properties. . . . .	151
IV.10	Simulations performed for Plateau-Rayleigh instability study, in red reference from refined ICM. . . . .	152
IV.11	Droplets morphological evolution on the range $x/D_{inj} = 36$ to $43$ [–] for <i>Flattening</i> and $\Delta\tilde{S}$ morphological criteria. . . . .	155
IV.12	<i>Flattening</i> , $\Delta\tilde{S}$ , <i>Archer</i> velocity, histogram's mean, standard deviation and skewness [figure IV.18] from the five successive droplets [figure IV.17]. . . . .	156
IV.13	Droplets standard deviation, $ \sigma(v_{Drop}) $ , evolution on the range $x/D_{inj} = 36$ to $43$ . . . .	157
IV.14	Breakup length, averaged droplet size and averaged velocity magnitude of the droplets/-particles for the ICM refined, coarse, Hybrid Two-way and Hybrid One-way simulations. . . .	163
IV.15	Physical phases configuration for D-HIT study. . . . .	168
IV.16	Characteristic number for D-HIT study. . . . .	168
V.1	Crossflow atomization's physical properties. . . . .	177
V.2	Crossflow atomization's characteristic dimensionless numbers. . . . .	177

V.3	Crossflow atomization's numerical simulation configurations. . . . .	178
V.4	Crossflow atomization's numerical liquid core/droplets/particles distribution. . . . .	180
V.5	Crossflow atomization's numerical liquid core/droplets/particles distribution performed with <i>Archer</i> at same mesh resolution: $512 \times 128 \times 256\Delta x$ . . . . .	186

---

# Bibliography

---

- [Aalburg et al., 2005] Aalburg, C., Van Leer, B., Faeth, G., and Sallam, K. A. (2005). Properties of nonturbulent round liquid jets in uniform gaseous cross flows. *Atomization and Sprays*, 15(3).
- [Ahn and Shashkov, 2009] Ahn, H. T. and Shashkov, M. (2009). Adaptive moment-of-fluid method. *J. Comput. Phys.*, 228(8):2792–2821.
- [Aly et al., 2010] Aly, H. S., Eldrainy, Y. A., Saqr, K. M., Lazim, T. M., and Jaafar, M. N. M. (2010). A mathematical model for predicting spray atomization characteristics in an Eulerian-Eulerian framework. *Int. Commun. Heat Mass Transf.*, 37(6):618–623.
- [Anderson and Jackson, 1967] Anderson, T. B. and Jackson, R. (1967). Fluid mechanical description of fluidized beds: Equations of Motion. *Ind. Eng. Chem. Fundam.*, 6(4):527–539.
- [Andersson and Andersson, 2006] Andersson, R. and Andersson, B. (2006). Modeling the breakup of fluid particles in turbulent flows. *AIChE J.*, 52(6):2031–2038.
- [Aniszewski et al., 2014] Aniszewski, W., Ménard, T., and Marek, M. (2014). Volume of Fluid (VoF) type advection methods in two-phase flow: A comparative study. *Computers & Fluids*, 97:52–73.
- [Ashgriz and Poo, 1990] Ashgriz, N. and Poo, J. Y. (1990). Coalescence and separation in binary collisions of liquid drops. *J. Fluid Mech.*, 221:183–204.
- [Auton et al., 1988] Auton, T. R., Hunt, J. C. R., and Prud’Homme, M. (1988). The force exerted on a body in inviscid unsteady non-uniform rotational flow. *J. Fluid Mech.*, 197:241–257.
- [Babu et al., 1990] Babu, K. R., Narasimhan, M. V., and Narayanaswamy, K. (1990). Correlations for Prediction of Discharge Rate, Cone Angle and Air Core Diameter of Swirl Spray Atomizers. *Int. J. Turbo Jet Engines*, 243:235–243.
- [Bachalo and Houser, 1984] Bachalo, W. D. and Houser, M. J. (1984). Phase/Doppler Spray Analyzer For Simultaneous Measurements Of Drop Size And Velocity Distributions. *Opt. Eng.*, 23(5):583–590.
- [Balachandar et al., 2019] Balachandar, S., Liu, K., and Lakhote, M. (2019). Self-induced velocity correction for improved drag estimation in Euler–Lagrange point-particle simulations. *J. Comput. Phys.*, 376:160–185.
- [Bałdyga et al., 2001] Bałdyga, J., Bourne, J., Pacek, A., Amanullah, A., and Nienow, A. (2001). Effects of agitation and scale-up on drop size in turbulent dispersions: allowance for intermittency. *Chemical Engineering Science*, 56(11):3377–3385.
- [Basset, 1888] Basset, A. B. (1888). *A treatise on hydrodynamics: with numerous examples*, volume 2. Deighton, Bell and Company.
- [Batchelor, 2019] Batchelor, B. G. K. (2019). Pressure fluctuations in isotropic turbulence. *Math. Proc. Cambridge Philos. Soc.*, (July 1950):359–374.
- [Batteen and Han, 1981] Batteen, M. L. and Han, Y. J. (1981). On the computational noise of finite-difference schemes used in ocean models. *Tellus*, 33(4):387–396.



- [Beard, 1976] Beard, K. V. (1976). Terminal Velocity and Shape of Cloud and Precipitation Drops Aloft. *J. Atmos. Sci.*, 33(5):851–864.
- [Beau et al., 2005] Beau, P. A., Lebas, R., Funk, M., and Demoulin, F. X. (2005). A multiphase flow approach and a single-phase flow approach in the context of a Euler model for primary break-up. *SAE World Congr. Exhib.*, 33(0).
- [Berger and Colella, 1989] Berger, M. J. and Colella, P. (1989). Local adaptive mesh refinement for shock hydrodynamics. *J. Comput. Phys.*, 82(1):64–84.
- [Berlemont et al., 1990] Berlemont, A., Desjonqueres, P., and Gouesbet, G. (1990). Particle Lagrangian simulation in turbulent flows. *Int. J. Multiph. Flow*, 16(1):19–34.
- [Bhatnagar et al., 1954] Bhatnagar, P. L., Gross, E. P., and Krook, M. (1954). A Model for Collision Processes in Gases. I. Small Amplitude Processes in Charged and Neutral One-Component Systems. *Phys. Rev.*, 94(3).
- [Blaisot and Yon, 2004] Blaisot, J. and Yon, J. (2004). Entropy based image analysis for the near field of direct injection diesel jet.
- [Blaisot et al., 2019] Blaisot, J.-B., Abuzahra, F., Sou, A., and Dumouchel, C. (2019). Entropy-based cavitation and primary atomization analysis with a 2D transparent injector. *ILASS - Eur. 2019, 29th Conf. Liq. At. Spray Syst.*, (September).
- [Bnà et al., 2013] Bnà, S., Cervone, A., Le Chenadec, V., Manservigi, S., and Scardovelli, R. (2013). Review of split and unsplit geometric advection algorithms. *AIP Conf. Proc.*, 1558(October):875–878.
- [Bothell et al., 2020] Bothell, J. K., Machicoane, N., Li, D., Morgan, T. B., Aliseda, A., Kastengren, A. L., and Heindel, T. J. (2020). Comparison of X-ray and optical measurements in the near-field of an optically dense coaxial air-assisted atomizer. *Int. J. Multiph. Flow*, 125.
- [Brändle De Motta, 2013] Brändle De Motta, J. C. (2013). *Simulation des écoulements turbulents avec des particules de taille finie en régime dense*. PhD thesis, Université de Toulouse.
- [Brändle de Motta et al., 2013] Brändle de Motta, J. C., Breugem, W. P., Gazanion, B., Estivalezes, J. L., Vincent, S., and Climent, E. (2013). Numerical modelling of finite-size particle collisions in a viscous fluid. *Phys. Fluids*, 25(8).
- [Brändle de Motta et al., 2019] Brändle de Motta, J. C., Costa, P., Derksen, J. J., Peng, C., Wang, L. P., Breugem, W. P., Estivalezes, J. L., Vincent, S., Climent, E., Fedde, P., Barbaresco, P., and Renon, N. (2019). Assessment of numerical methods for fully resolved simulations of particle-laden turbulent flows. *Computers & Fluids*, 179:1–14.
- [Breugem, 2012] Breugem, W. P. (2012). A second-order accurate immersed boundary method for fully resolved simulations of particle-laden flows. *J. Comput. Phys.*, 231(13):4469–4498.
- [Broumand et al., 2019] Broumand, M., Ahmed, M. M., and Birouk, M. (2019). Experimental investigation of spray characteristics of a liquid jet in a turbulent subsonic gaseous crossflow. *Proceedings of the Combustion Institute*, 37(3):3237–3244.
- [Brown and Mcdonell, 2006] Brown, C. and Mcdonell, V. G. (2006). Near Field Behavior of a Liquid Jet in a Crossflow. In *ILASS Am. 19th Annu. Conf. Liq. At. Spray Syst. Toronto, Canada, May 2006*.
- [Burluka et al., 2001] Burluka, A., Borghi, R., et al. (2001). Development of a eulerian model for the “atomization” of a liquid jet. *Atomization and sprays*, 11(6).
- [Canu et al., 2018] Canu, R., Puggelli, S., Essadki, M., Duret, B., Menard, T., Massot, M., Reveillon, J., and Demoulin, F. X. (2018). Where does the droplet size distribution come from? *Int. J. Multiph. Flow*, 107:230–245.

- [Capecelatro and Desjardins, 2013] Capecelatro, J. and Desjardins, O. (2013). An Euler-Lagrange strategy for simulating particle-laden flows. *J. Comput. Phys.*, 238:1–31.
- [Chadil et al., 2019] Chadil, M.-A., Vincent, S., and Estivalezes, J.-L. (2019). Accurate estimate of drag forces using particle-resolved direct numerical simulations. *Acta Mechanica*, 230(2):569–595.
- [Charalampous et al., 2009] Charalampous, G., Hardalupas, Y., and Taylor, A. M. (2009). Novel technique for measurements of continuous liquid jet core in an atomizer. *AIAA J.*, 47(11):2605–2615.
- [Chen et al., 1992a] Chen, S., Wang, Z., Shan, X., and Doolen, G. D. (1992a). Lattice Boltzmann computational fluid dynamics in three dimensions. *J. Stat. Phys.*, 68(3-4):379–400.
- [Chen et al., 1992b] Chen, S. K., Lefebvre, A. H., and Rollbuhler, J. (1992b). Factors influencing the effective spray cone angle of pressure-swirl atomizers. *J. Eng. Gas Turbines Power*, 114(1):97–103.
- [Chen et al., 2019a] Chen, T., Chéron, V., Guo, Z., Brändle De Motta, J. C., Ménard, T., and Wang, L.-P. (2019a). Simulation of immiscible two-phase flows based on a kinetic diffuse interface approach. *10th Int. Conf. Multiph. Flow*, (2019).
- [Chen et al., 2019b] Chen, T., Liu, T., Wang, L.-P., and Chen, S. (2019b). Relations between skin friction and other surface quantities in viscous flows. *Physics of Fluids*, 31(10):107101.
- [Chen et al., 1998] Chen, Z., Prüss, J., and Warnecke, H.-J. (1998). A population balance model for disperse systems: Drop size distribution in emulsion. *Chem. Eng. Sci.*, 53(5):1059–1066.
- [Chéron et al., 2020] Chéron, V., Brändle de Motta, J. C., Blaisot, J.-B., and Ménard, T. (2020). How to reconstruct 3D morphological information of a droplet from 2D measurements? *manuscript under submission*.
- [Chéron et al., 2019] Chéron, V., Brändle De Motta, J. C., Ménard, T., and Berlemont, A. (2019). Hybrid treatment of small droplets in atomized jet. In *Congrès Français de Mécanique*, Brest, France.
- [Christiansen and Petersen, 1989] Christiansen, E. and Petersen, H. (1989). Estimation of convergence orders in repeated richardson extrapolation. *BIT*, 29:48–59.
- [Cisse et al., 2013] Cisse, M., Homann, H., and Bec, J. (2013). Slipping motion of large neutrally buoyant particles in turbulence. *Journal of Fluid Mechanics*, 735.
- [Clay, 1940] Clay, P. H. (1940). The mechanism of emulsion formation in turbulent flow. Technical report.
- [Clift, 1978] Clift, R. (1978). *Bubbles, Drops, and Particles*. CRC press.
- [Climent and Magnaudet, 2006] Climent, E. and Magnaudet, J. (2006). Dynamics of a two-dimensional upflowing mixing layer seeded with bubbles: Bubble dispersion and effect of two-way coupling. *Phys. Fluids*, 18(10).
- [Crapper et al., 1975] Crapper, G., Dombrowski, N., and Pyott, G. (1975). Large amplitude kelvin-helmholtz waves on thin liquid sheets. *Proceedings of the Royal Society of London. A. Mathematical and Physical Sciences*, 342(1629):209–224.
- [Crowe et al., 2011] Crowe, C. T., Schwarzkopf, J. D., Sommerfeld, M., and Tsuji, Y. (2011). *Multiphase flows with droplets and particles*. CRC press.
- [Crua et al., 2015] Crua, C., Heikal, M. R., and Gold, M. R. (2015). Microscopic imaging of the initial stage of diesel spray formation. *Fuel*, 157:140–150.
- [Curtis and Hocking, 1970] Curtis, A. and Hocking, L. (1970). Collision efficiency of equal spherical particles in a shear flow. the influence of london-van der waals forces. *Transactions of the Faraday Society*, 66:1381–1390.

- [Deike et al., 2016] Deike, L., Melville, W. K., and Popinet, S. (2016). Air entrainment and bubble statistics in breaking waves. *J. Fluid Mech.*, 801:91–129.
- [Denner et al., 2017] Denner, F., Evrard, F., Serfaty, R., and van Wachem, B. G. (2017). Artificial viscosity model to mitigate numerical artefacts at fluid interfaces with surface tension. *Computers & Fluids*, 143:59–72.
- [Desjardins et al., 2008] Desjardins, O., Moureau, V., and Pitsch, H. (2008). An accurate conservative Level-set/ghost fluid method for simulating turbulent atomization. *J. Comput. Phys.*, 227(18):8395–8416.
- [Di Felice, 1996] Di Felice, R. (1996). A relationship for the wall effect on the settling velocity of a sphere at any flow regime. *Int. J. Multiph. Flow*, 22(3):527–533.
- [Di Felice and Parodi, 1996] Di Felice, R. and Parodi, E. (1996). Wall Effects on the Sedimentation Velocity of Suspensions in Viscous Flow. *AIChE J.*, 42(4):927–931.
- [Dodd and Ferrante, 2016] Dodd, M. S. and Ferrante, A. (2016). On the interaction of Taylor length scale size droplets and isotropic turbulence. *J. Fluid Mech.*, 806:356–412.
- [Dukowicz, 1980] Dukowicz, J. K. (1980). A particle-fluid numerical model for liquid sprays. *J. Comput. Phys.*, 35(2):229–253.
- [Dumouchel, 2008] Dumouchel, C. (2008). On the experimental investigation on primary atomization of liquid streams. *Exp. Fluids*, 45(3):371–422.
- [Dumouchel and Grout, 2009] Dumouchel, C. and Grout, S. (2009). Application of the scale entropy diffusion model to describe a liquid atomization process. *International journal of multiphase flow*, 35(10):952–962.
- [Duran, 2015] Duran, A. (2015). *Numerical simulation of depth-averaged flow models : a class of Finite Volume and discontinuous Galerkin approaches*. PhD thesis, Université de Montpellier 2.
- [Duret et al., 2012] Duret, B., Luret, G., Reveillon, J., Menard, T., Berlemont, A., and Demoulin, F. X. (2012). DNS analysis of turbulent mixing in two-phase flows. *Int. J. Multiph. Flow*, 40:93–105.
- [Duret et al., 2013] Duret, B., Reveillon, J., Menard, T., and Demoulin, F. X. (2013). Improving primary atomization modeling through DNS of two-phase flows. *Int. J. Multiph. Flow*, 55:130–137.
- [Elghobashi and Truesdell, 1992] Elghobashi, S. and Truesdell, G. C. (1992). On the two-way interaction between homogeneous turbulence and dispersed solid particles. I: Turbulence modification. *Phys. Fluids A*, 5(7):1790–1801.
- [ELShamy, 2007] ELShamy, O. M. (2007). *Experimental investigations of steady and dynamic behavior of transverse liquid jets*. PhD thesis, University of Cincinnati.
- [Evrard et al., 2019] Evrard, F., Denner, F., and van Wachem, B. (2019). A multi-scale approach to simulate atomisation processes. *Int. J. Multiph. Flow*, 119:194–216.
- [Evrard et al., 2020] Evrard, F., Denner, F., and van Wachem, B. (2020). Euler-Lagrange modelling of dilute particle-laden flows with arbitrary particle-size to mesh-spacing ratio. *manuscript under review*.
- [Fedkiw et al., 1999] Fedkiw, R. P., Aslam, T., Merriman, B., and Osher, S. (1999). A Non-oscillatory Eulerian Approach to Interfaces in Multimaterial Flows (the Ghost Fluid Method). *J. Comput. Phys.*, 152(2):457–492.
- [Galinat et al., 2007] Galinat, S., Risso, F., Masbernat, O., and Guiraud, P. (2007). Dynamics of drop breakup in inhomogeneous turbulence at various volume fractions. *J. Fluid Mech.*, 578:85–94.

- [Glimm et al., 1998] Glimm, J., Grove, J. W., Li, X. L., Shyue, K.-m., Zeng, Y., and Zhang, Q. (1998). Three-dimensional front tracking. *SIAM Journal on Scientific Computing*, 19(3):703–727.
- [Gorokhovski and Herrmann, 2008] Gorokhovski, M. and Herrmann, M. (2008). Modeling primary atomization. *Annu. Rev. Fluid Mech.*, 40:343–366.
- [Grace, 1982] Grace, J. R. (1982). Dispersion phenomena in high viscosity immiscible fluid systems and application of static mixers as dispersion devices in such systems. *Chem. Eng. Commun.*, 14(3-6):225–277.
- [Grace et al., 1978] Grace, J. R., Wairegi, T., and Brophy, J. (1978). Break up of drops and bubbles in stagnant media. *Can. J. Chem. Eng.*, 56(1):3–8.
- [Grant et al., 2000] Grant, G., Brenton, J., and Drysdale, D. (2000). Fire suppression by water sprays. *Prog. Energy Combust. Sci.*, 26(2):79–130.
- [Gualtieri et al., 2015] Gualtieri, P., Picano, F., Sardina, G., and Casciola, C. (2015). Exact regularized point particle method for multiphase flows in the two-way coupling regime. *Journal of Fluid Mechanics*, 773:520–561.
- [Guildenbecher et al., 2009] Guildenbecher, D. R., López-Rivera, C., and Sojka, P. E. (2009). Secondary atomization. *Exp. Fluids*, 46(3):371–402.
- [Guo et al., 2015] Guo, Y., Wu, C., and Thornton, C. (2015). Pyrolysis of Heavy Oil in the Presence of Supercritical Water: The Reaction Kinetics in Different Phases. *AIChE J.*, 61(3):857–866.
- [Håkansson et al., 2009] Håkansson, A., Trägårdh, C., and Bergenståhl, B. (2009). Dynamic simulation of emulsion formation in a high pressure homogenizer. *Chem. Eng. Sci.*, 64(12):2915–2925.
- [Han et al., 2011] Han, L., Luo, H., and Liu, Y. (2011). A theoretical model for droplet breakup in turbulent dispersions. *Chem. Eng. Sci.*, 66(4):766–776.
- [Hansen, 2013] Hansen, H. (2013). Method for spray-coating medical devices. Technical Report 12.
- [Hendrickson, ] Hendrickson, K. E. I. *The encyclopedia of the industrial revolution in world history*.
- [Herrmann, 2010a] Herrmann, M. (2010a). A parallel Eulerian interface tracking/Lagrangian point particle multi-scale coupling procedure. *J. Comput. Phys.*, 229(3):745–759.
- [Herrmann, 2010b] Herrmann, M. (2010b). The influence of density ratio on the primary atomization of a turbulent liquid jet in crossflow. *West. States Sect. Combust. Inst. Spring Tech. Meet. 2010*, 33(2):191–205.
- [Hinze, 1955] Hinze, J. (1955). Fundamentals of the hydrodynamic mechanism of splitting in dispersion processes. *AIChE journal*, 1(3):289–295.
- [Hirt and Nichols, 1981] Hirt, C. W. and Nichols, B. D. (1981). Volume of Fluid method for the dynamics of free boundaries. *J. Comput. Phys.*, 42(3):357–366.
- [Horwitz and Mani, 2016] Horwitz, J. and Mani, A. (2016). Accurate calculation of stokes drag for point-particle tracking in two-way coupled flows. *Journal of Computational Physics*, 318:85–109.
- [Ireland and Desjardins, 2017] Ireland, P. J. and Desjardins, O. (2017). Improving particle drag predictions in Euler-Lagrange simulations with two-way coupling. *J. Comput. Phys.*, 338:405–430.
- [Janssen and Meijer, 1993] Janssen, J. M. H. and Meijer, H. E. H. (1993). Droplet breakup mechanisms: Stepwise equilibrium versus transient dispersion. *J. Rheol.*, 37(4):597–608.
- [Jazi, 2014] Jazi, M. B. (2014). *Surface breakup of a liquid jet injected into a gaseous crossflow*. PhD thesis.

- [Jiang et al., 2010] Jiang, X., Siamas, G. A., Jagus, K., and Karayiannis, T. G. (2010). Physical modelling and advanced simulations of gas-liquid two-phase jet flows in atomization and sprays. *Prog. Energy Combust. Sci.*, 36(2):131–167.
- [Jun, 1996] Jun, Z. (1996). Acceleration of five-point red-black Gauss-Seidel in multigrid for Poisson equation. *Appl. Math. Comput.*, 80(1):73–93.
- [Kang et al., 2000] Kang, M., Fedkiw, R. P., and Liu, X. D. (2000). A boundary condition capturing method for multiphase flow with phase change. *J. Sci. Comput.*, 15.
- [Karagozian, 2010] Karagozian, A. R. (2010). Transverse jets and their control. *Progress in energy and combustion science*, 36(5):531–553.
- [Karimi and Andersson, 2018] Karimi, M. and Andersson, R. (2018). An exploratory study on fluid particles breakup rate models for the entire spectrum of turbulent energy. *Chem. Eng. Sci.*, 192:850–863.
- [Karimi and Andersson, 2020] Karimi, M. and Andersson, R. (2020). Stochastic simulation of droplet breakup in turbulence. *Chem. Eng. J.*, 380(August 2019):122502.
- [Kedelty et al., 2019] Kedelty, D., Uglietta, J., and Herrmann, M. (2019). A dual-scale approach for modeling turbulent liquid/gas phase interfaces. In *Turbulent Cascades II*, pages 257–264. Springer.
- [Kempe et al., 2009] Kempe, T., Schwarz, S., and Frohlich, J. (2009). Modelling of spheroidal particles in viscous flow. In *Acad. Colloq. Immersed Bound. Methods*.
- [Kindlmann et al., 2003] Kindlmann, G., Whitaker, R., Tasdizen, T., and Möller, T. (2003). Curvature-Based Transfer Functions for Direct Volume Rendering: Methods and Applications. *Proc. IEEE Vis. Conf.*, d:513–520.
- [Kitagawa et al., 2001] Kitagawa, A., Murai, Y., and Yamamoto, F. (2001). Two-way coupling of Eulerian-Lagrangian model for dispersed multiphase flows using filtering functions. *Int. J. Multiph. Flow*, 27(12):2129–2153.
- [Klein et al., 2003] Klein, M., Sadiki, A., and Janicka, J. (2003). A digital filter based generation of inflow data for spatially developing direct numerical or large eddy simulations. *Journal of computational Physics*, 186(2):652–665.
- [Kocamustafaogullari and Ishii, 1995] Kocamustafaogullari, G. and Ishii, M. (1995). Foundation of the interfacial area transport equation and its closure relations. *Int. J. Heat Mass Transf.*, 38(3):481–493.
- [Kolev, 2015] Kolev, N. I. (2015). *Multiphase flow dynamics 1: Fundamentals*. Springer Berlin Heidelberg.
- [Lalanne et al., 2015] Lalanne, B., Abi Chebel, N., Vejražka, J., Tanguy, S., Masbernat, O., and Risso, F. (2015). Non-linear shape oscillations of rising drops and bubbles: Experiments and simulations. *Physics of Fluids*, 27(12):123305.
- [Lasheras et al., 2002] Lasheras, J. C., Eastwood, C., Martínez-Bazán, C., and Montaes, J. L. (2002). A review of statistical models for the break-up an immiscible fluid immersed into a fully developed turbulent flow. *Int. J. Multiph. Flow*, 28(2):247–278.
- [Lasheras et al., 1998] Lasheras, J. C., Villermaux, E., and Hopfinger, E. J. (1998). Breakup and atomization of a round coal water slurry jet by an annular air jet. *J. Fluid Mech.*, 357:351–379.
- [Lawson et al., 1988] Lawson, J., Walton, W. D., and Evans, D. D. (1988). *Measurement of droplet size in sprinkler sprays*. Center for Fire Research.
- [Lefebvre and McDonell, 2017] Lefebvre, A. H. and McDonell, V. G. (2017). *Atomization and sprays*. CRC press.

- [Lemoine et al., 2017] Lemoine, A., Glockner, S., and Breil, J. (2017). Moment-of-fluid analytic reconstruction on 2D Cartesian grids. *J. Comput. Phys.*, 328:131–139.
- [Lévy, 1983] Lévy, T. (1983). Fluid flow through an array of fixed particles. *Int. J. Eng. Sci.*, 21(1):11–23.
- [Li et al., 2013] Li, Z., Wu, Y., Yang, H., Cai, C., Zhang, H., Hashiguchi, K., Takeno, K., and Lu, J. (2013). Effect of liquid viscosity on atomization in an internal-mixing twin-fluid atomizer. *Fuel*, 103:486–494.
- [Liao and Lucas, 2009] Liao, Y. and Lucas, D. (2009). A literature review of theoretical models for drop and bubble breakup in turbulent dispersions. *Chemical Engineering Science*, 64(15):3389–3406.
- [Ling et al., 2013] Ling, Y., Parmar, M., and Balachandar, S. (2013). A scaling analysis of added-mass and history forces and their coupling in dispersed multiphase flows. *Int. J. Multiph. Flow*, 57:102–114.
- [Ling et al., 2015] Ling, Y., Zaleski, S., and Scardovelli, R. (2015). Multiscale simulation of atomization with small droplets represented by a Lagrangian point-particle model. *Int. J. Multiph. Flow*, 76:122–143.
- [Liu et al., 2000] Liu, X. D., Fedkiw, R. P., and Kang, M. (2000). A boundary condition capturing method for Poisson’s equation on irregular domains. *J. Comput. Phys.*, 160(1):151–178.
- [López and Hernández, 2008] López, J. and Hernández, J. (2008). Analytical and geometrical tools for 3D volume of fluid methods in general grids. *J. Comput. Phys.*, 227(12):5939–5948.
- [Lord, 1900] Lord, R. (1900). Investigation of the character of the equilibrium of an incompressible heavy fluid of variable density. *Scientific papers*, pages 200–207.
- [Luo et al., 2007] Luo, K., Wang, Z., Fan, J., and Cen, K. (2007). Full-scale solutions to particle-laden flows: Multidirect forcing and immersed boundary method. *Phys. Rev. E - Stat. Nonlinear, Soft Matter Phys.*, 76(6):1–9.
- [Maaß et al., 2012] Maaß, S., Paul, N., and Kraume, M. (2012). Influence of the dispersed phase fraction on experimental and predicted drop size distributions in breakage dominated stirred systems. *Chem. Eng. Sci.*, 76:140–153.
- [Malot and Blaisot, 2000] Malot, H. and Blaisot, J. B. (2000). Droplet size distribution and sphericity measurements of low-density sprays through image analysis. *Part. Part. Syst. Charact.*, 17(4):146–158.
- [Marella et al., 2005] Marella, S., Krishnan, S., Liu, H., and Udaykumar, H. S. (2005). Sharp interface Cartesian grid method I: An easily implemented technique for 3D moving boundary computations. *J. Comput. Phys.*, 210(1):1–31.
- [Mark and van Wachem, 2008] Mark, A. and van Wachem, B. G. (2008). Derivation and validation of a novel implicit second-order accurate immersed boundary method. *J. Comput. Phys.*, 227(13):6660–6680.
- [Marmottant and Villermaux, 2004a] Marmottant, P. and Villermaux, E. (2004a). Fragmentation of stretched liquid ligaments. *Physics of fluids*, 16(8):2732–2741.
- [Marmottant and Villermaux, 2004b] Marmottant, P. H. and Villermaux, E. (2004b). On spray formation. *J. Fluid Mech.*, 498(498):73–111.
- [Martinez-Bazan et al., 1999] Martinez-Bazan, C., Montanes, J., and Lasheras, J. (1999). On the breakup of an air bubble injected into a fully developed turbulent flow. part 2. size pdf of the resulting daughter bubbles. *Journal of Fluid Mechanics*, 401:183–207.
- [Maxey et al., 1997] Maxey, M. R., Patel, B. K., Chang, E. J., and Wang, L. P. (1997). Simulations of dispersed turbulent multiphase flow. *Fluid Dyn. Res.*, 20(1-6):143–156.

- [Maxey and Riley, 1983] Maxey, M. R. and Riley, J. J. (1983). Equation of motion for a small rigid sphere in a nonuniform flow. *The Physics of Fluids*, 26(4):883–889.
- [Ménard et al., 2007] Ménard, T., Tanguy, S., and Berlemont, A. (2007). Coupling level set/VOF/ghost fluid methods: Validation and application to 3D simulation of the primary break-up of a liquid jet. *Int. J. Multiph. Flow*, 33(5):510–524.
- [Merrington and Richardson, 1947] Merrington, A. C. and Richardson, E. G. (1947). The break-up of liquid jets. *Proc. Phys. Soc.*, 59(1):1–13.
- [Moallemi et al., 2016] Moallemi, N., Li, R., and Mehravaran, K. (2016). Breakup of capillary jets with different disturbances. *Phys. Fluids*, 28(1).
- [Mukundan et al., 2019a] Mukundan, A. A., Ménard, T., Berlemont, A., and Brändle De Motta, J. C. (2019a). A comparative study of DNS of airblast atomization using CLSMOF and CLSVOF methods. In *ILASS - Eur. 2019, 29th Conf. Liq. At. Spray Syst.*
- [Mukundan et al., 2019b] Mukundan, A. A., Ménard, T., Brändle de Motta, J. C., and Berlemont, A. (2019b). A 3D Moment of Fluid method for simulating complex turbulent multiphase flows. *Computers & Fluids*, 198.
- [Mukundan et al., 2020] Mukundan, A. A., Tretola, G., Ménard, T., Herrmann, M., Navarro-Martinez, S., Vogiatzaki, K., de Motta, J. C. B., and Berlemont, A. (2020). Dns and les of primary atomization of turbulent liquid jet injection into a gaseous crossflow environment. *Proceedings of the Combustion Institute*.
- [Müller et al., 2017] Müller, B., Krämer-Eis, S., Kummer, F., and Oberlack, M. (2017). A high-order discontinuous Galerkin method for compressible flows with immersed boundaries. *Int. J. Numer. Methods Eng.*, 110(1):3–30.
- [Nasr et al., 2002] Nasr, G. G., Yule, A. J., and Bendig, L. (2002). *Industrial Sprays and Atomization*.
- [Ng et al., 2008] Ng, C.-L., Sankarakrishnan, R., and Sallam, K. (2008). Bag breakup of nonturbulent liquid jets in crossflow. *International Journal of Multiphase Flow*, 34(3):241–259.
- [Noh and Woodward, 1976] Noh, W. F. and Woodward, P. (1976). Slic (simple line interface calculation). In *Proceedings of the fifth international conference on numerical methods in fluid dynamics June 28–July 2, 1976 Twente University, Enschede*, pages 330–340. Springer.
- [Osmar et al., 2014] Osmar, L., Vincent, S., Caltagirone, J. P., Estivalezes, J. L., Auguste, F., Magnaudet, J., Menard, T., Berlemont, A., Aniszewski, W., Ling, Y., and Zaleski, S. (2014). Interface tracking methods applied to phase separation. In *Am. Soc. Mech. Eng. Fluids Eng. Div. FEDSM*, volume 1B.
- [Patankar, 2018] Patankar, S. (2018). *Numerical heat transfer and fluid flow*. Crc press edition.
- [Payri et al., 2019] Payri, R., Salvador, F. J., Gimeno, J., and Crialesi, M. (2019). Comparison of mapped and synthetic inflow boundary conditions in Direct Numerical Simulation of sprays. *ILASS2019 Paris,FR*, (September).
- [Peng et al., 2019] Peng, C., Ayala, O. M., and Wang, L. P. (2019). A comparative study of immersed boundary method and interpolated bounce-back scheme for no-slip boundary treatment in the lattice Boltzmann method: Part I, laminar flows. *Computers & Fluids*, 192(000):104233.
- [Peng and Wang, 2020] Peng, C. and Wang, L. P. (2020). Force-amplified, single-sided diffused-interface immersed boundary kernel for correct local velocity gradient computation and accurate no-slip boundary enforcement. *Phys. Rev. E*, 101(5):53305.
- [Perlekar et al., 2012] Perlekar, P., Biferale, L., Sbragaglia, M., Srivastava, S., and Toschi, F. (2012). Droplet size distribution in homogeneous isotropic turbulence. *Phys. Fluids*, 24(6).

- [Peskin, 1972] Peskin, C. S. (1972). Flow patterns around heart valves: A numerical method. *J. Comput. Phys.*, 10(2):252–271.
- [Peskin and McQueen, 1989] Peskin, C. S. and McQueen, D. M. (1989). A three-dimensional computational method for blood flow in the heart I. Immersed elastic fibers in a viscous incompressible fluid. *J. Comput. Phys.*, 81(2):372–405.
- [Pilch and Erdman, 1987] Pilch, M. and Erdman, C. (1987). Use of breakup time data and velocity history data to predict the maximum size of stable fragments for acceleration-induced breakup of a liquid drop. *International journal of multiphase flow*, 13(6):741–757.
- [Rabe et al., 2010] Rabe, C., Malet, J., and Feuillebois, F. (2010). Experimental investigation of water droplet binary collisions and description of outcomes with a symmetric Weber number. *Phys. Fluids*, 22(4):1–11.
- [Renardy, 2008] Renardy, Y. (2008). Effect of startup conditions on drop breakup under shear with inertia. *Int. J. Multiph. Flow*, 34(12):1185–1189.
- [Richardson and Zaki, 1954] Richardson, J. F. and Zaki, W. N. (1954). The sedimentation of a suspension of uniform spheres under conditions of viscous flow. *Chem. Eng. Sci.*, 3(2):65–73.
- [Richardson, 2007] Richardson, L. F. (2007). *Weather prediction by numerical process*. Cambridge university press.
- [Ritz and Caltagirone, 1999] Ritz, J. B. and Caltagirone, J. P. (1999). A numerical continuous model for the hydrodynamics of fluid particle systems. *Int. J. Numer. Methods Fluids*, 30(8):1067–1090.
- [Roma et al., 1999] Roma, A. M., Peskin, C. S., and Berger, M. J. (1999). An Adaptive Version of the Immersed Boundary Method. *J. Comput. Phys.*, 153(2):509–534.
- [Rosa et al., 2020] Rosa, B., Pozorski, J., and Wang, L.-P. (2020). Effects of turbulence modulation and gravity on particle collision statistics. *International Journal of Multiphase Flow*, page 103334.
- [Rosales and Meneveau, 2005] Rosales, C. and Meneveau, C. (2005). Linear forcing in numerical simulations of isotropic turbulence: Physical space Implementations and convergence properties. *Phys. Fluids*, 17(9):1–8.
- [Rudman, 1997] Rudman, M. (1997). Volume-tracking methods for interfacial flow calculations. *Int. J. Numer. Methods Fluids*, 24:671–691.
- [Rudman, 1998] Rudman, M. (1998). A volume-tracking method for incompressible multifluid flows with large density variations. *International Journal for numerical methods in fluids*, 28(2):357–378.
- [Saff and Kuijlaars, 1997] Saff, E. B. and Kuijlaars, A. B. (1997). Distributing many points on a sphere. *Math. Intell.*, 19(1):5–11.
- [Schober et al., 2002] Schober, P., Meier, R., Schäfer, O., and Wittig, S. (2002). Visualization and phase doppler particle analysis measurements of oscillating spray propagation of an airblast atomizer under typical engine conditions. *Ann. N. Y. Acad. Sci.*, 972:277–284.
- [Shinjo, 2018] Shinjo, J. (2018). Recent advances in computational modeling of primary atomization of liquid fuel sprays. *Energies*, 11(11):2971.
- [Shinjo and Umemura, 2010] Shinjo, J. and Umemura, A. (2010). Simulation of liquid jet primary breakup: Dynamics of ligament and droplet formation. *Int. J. Multiph. Flow*, 36(7):513–532.
- [Simonin et al., 2016] Simonin, O., Chevrier, S., Audard, F., and Fede, P. (2016). Drag force modelling in dilute to dense particle-laden flows with mono-disperse or binary mixture of solid particles.



- [Simonin and Squires, 2003] Simonin, O. and Squires, K. D. (2003). On Two-way coupling in gas-solid turbulent flows. *Proc. ASME FEDSM'03*, pages 1–18.
- [Sirignano, 2010] Sirignano, A. W. (2010). *Fluid dynamics and transport of droplets and sprays*. Cambridge University Press.
- [Sleicher Jr., 1962] Sleicher Jr., C. A. (1962). Maximum stable drop size in turbulent flow. *AIChE J.*, 8(4):471–477.
- [Smagorinsky, 1963] Smagorinsky, J. (1963). General circulation experiments with the primitive equations: I. the basic experiment. *Monthly weather review*, 91(3):99–164.
- [Solsvik et al., 2016] Solsvik, J., Skjervold, V. T., Han, L., Luo, H., and Jakobsen, H. A. (2016). A theoretical study on drop breakup modeling in turbulent flows: The inertial subrange versus the entire spectrum of isotropic turbulence. *Chem. Eng. Sci.*, 149:249–265.
- [Song et al., 2014] Song, J., Cary Cain, C., and Guen Lee, J. (2014). Liquid Jets in Subsonic Air Crossflow at Elevated Pressure. *Journal of Engineering for Gas Turbines and Power*, 137(4). 041502.
- [Squires and Eaton, 1990] Squires, K. D. and Eaton, J. K. (1990). Particle response and turbulence modification in isotropic turbulence. *Phys. Fluids A*, 2(7):1191–1203.
- [Stenzler et al., 2006] Stenzler, J. N., Lee, J. G., Santavicca, D. A., and Lee, W. (2006). Penetration of liquid jets in a cross-flow. *Atomization and Sprays*, 16(8).
- [Stephen B. Pope, 2000] Stephen B. Pope (2000). *Turbulent Flows*. Cornell University.
- [Sussman et al., 1998] Sussman, M., Fatemi, E., Smereka, P., and Osher, S. (1998). An improved Level-set method for incompressible two-phase flows. *Computers & Fluids*, 27(5-6):663–680.
- [Sussman and Puckett, 2000] Sussman, M. and Puckett, E. G. (2000). A coupled Level-set and Volume-of-Fluid method for computing 3D and axisymmetric incompressible two-phase flows. *J. Comput. Phys.*, 162(2):301–337.
- [Tanguy, 2004] Tanguy, S. (2004). *Développement d’une méthode de suivi d’interface. Applications aux écoulements diphasiques*. PhD thesis, Université de Rouen.
- [Tanguy and Berlemont, 2005] Tanguy, S. and Berlemont, A. (2005). Application of a Level-set method for simulation of droplet collisions. *Int. J. Multiph. Flow*, 31(9):1015–1035.
- [Tomar et al., 2010] Tomar, G., Fuster, D., Zaleski, S., and Popinet, S. (2010). Multiscale simulations of primary atomization. *Computers & Fluids*, 39(10):1864–1874.
- [Trontin, 2009] Trontin, P. (2009). *Développement d’une approche de type LES pour la simulation d’écoulements diphasiques avec interface . Application à l’atomisation primaire*. PhD thesis, Université de Toulouse.
- [Trontin et al., 2010] Trontin, P., Vincent, S., Estivalezes, J. L., and Caltagirone, J. P. (2010). Direct numerical simulation of a freely decaying turbulent interfacial flow. *Int. J. Multiph. Flow*, 36(11-12):891–907.
- [Tryggvason et al., 2001] Tryggvason, G., Bunner, B., Esmaeeli, A., Juric, D., Al-Rawahi, N., Tauber, W., Han, J., Nas, S., and Jan, Y. J. (2001). A Front-tracking method for the computations of multiphase flow. *J. Comput. Phys.*, 169(2):708–759.
- [Tryggvason et al., 2011] Tryggvason, G., Scardovelli, R., and Zaleski, S. (2011). *Direct numerical simulations of gas–liquid multiphase flows*. Cambridge University Press.
- [Uhlmann, 2005] Uhlmann, M. (2005). An improved immersed boundary method with direct forcing for the simulation of particle laden flows. *J. Comput. Phys.*, 209(9):448–476.

- [Uhlmann and Chouippe, 2017] Uhlmann, M. and Chouippe, A. (2017). Clustering and preferential concentration of finite-size particles in forced homogeneous-isotropic turbulence. *J. Fluid Mech.*, 812:991–1023.
- [van Beeck and Riethmuller, 1996] van Beeck, J. P. A. J. and Riethmuller, M. L. (1996). Rainbow phenomena applied to the measurement of droplet size and velocity and to the detection of nonsphericity. *Appl. Opt.*, 35(13):2259.
- [Vaudor, 2015] Vaudor, G. (2015). *Atomisation assistée par un cisaillement de l'écoulement gazeux Développement et validation*. PhD thesis, Université de Rouen.
- [Vaudor et al., 2017] Vaudor, G., Ménard, T., Aniszewski, W., Doring, M., and Berlemont, A. (2017). A consistent mass and momentum flux computation method for two phase flows. Application to atomization process. *Computers & Fluids*, 152:204–216.
- [Vowinckel et al., 2012] Vowinckel, B., Kempe, T., Fröhlich, J., and Nikora, V. I. (2012). Numerical simulation of sediment transport in open channel flow. *River Flow 2012 - Proc. Int. Conf. Fluv. Hydraul.*, 1:507–514.
- [Walter and Blanch, 1986] Walter, J. F. and Blanch, H. W. (1986). Bubble break-up in gas-liquid bioreactors: Break-up in turbulent flows. *Chem. Eng. J.*, 32(1).
- [Wang et al., 2014] Wang, L. P., Ayala, O., Gao, H., Andersen, C., and Mathews, K. L. (2014). Study of forced turbulence and its modulation by finite-size solid particles using the lattice Boltzmann approach. *Comput. Math. with Appl.*, 67(2):363–380.
- [Wendland, 1995] Wendland, H. (1995). Piecewise polynomial, positive definite and compactly supported radial functions of minimal degree. *Adv. Comput. Math.*, 4(1):389–396.
- [Weymouth and Yue, 2010] Weymouth, G. D. and Yue, D. K.-P. (2010). Conservative volume-of-fluid method for free-surface simulations on cartesian-grids. *Journal of Computational Physics*, 229(8):2853–2865.
- [Wierzba, 1990] Wierzba, A. (1990). Deformation and breakup of liquid drops in a gas stream at nearly critical Weber numbers. *Exp. Fluids*, 9(1-2):59–64.
- [Wu et al., 1997] Wu, P.-K., Kirkendall, K. A., Fuller, R. P., and Nejad, A. S. (1997). Breakup processes of liquid jets in subsonic crossflows. *Journal of Propulsion and power*, 13(1):64–73.
- [Xiao et al., 2016] Xiao, F., Wang, Z., Sun, M., Liang, J., and Liu, N. (2016). Large eddy simulation of liquid jet primary breakup in supersonic air crossflow. *International Journal of Multiphase Flow*, 87:229–240.
- [Yon and Blaisot, 2004] Yon, J. and Blaisot, J. (2004). Spray sizing by imaging: Focusing and droplet image superposition. In *ILASS - Eur. 2004, Conf. Liq. At. Spray Syst.*
- [Zaccone et al., 2007] Zaccone, A., Gäbler, A., Maaß, S., Marchisio, D., and Kraume, M. (2007). Drop breakage in liquid-liquid stirred dispersions: Modelling of single drop breakage. *Chem. Eng. Sci.*, 62(22):6297–6307.
- [Zhang and Prosperetti, 1997] Zhang, D. Z. and Prosperetti, A. (1997). Momentum and energy equations for disperse two-phase flows and their closure for dilute suspensions. *Int. J. Multiph. Flow*, 23(3):425–453.
- [Zuzio et al., 2018] Zuzio, D., Estivalèzes, J.-L., and DiPierro, B. (2018). An improved multiscale eulerian-lagrangian method for simulation of atomization process. *Computers & Fluids*, 176:285–301.

## Résumé

**Mot-clef :Simulation Numérique Directe, Level-Set, VOF, Lagrangien, Couplage, Atomisation**

L'étude de l'atomisation d'un jet liquide constitué de deux phases non miscibles est un sujet de recherche fondamental. Les motivations principales liées à l'étude de ces phénomènes sont les nombreuses applications en découlant. Par exemple, dans l'étude de propagation d'un spray au sein d'une chambre de combustion ou pour des applications pharmaceutiques. Leur étude s'effectue par une approche théorique, expérimentale, et numérique. Chacune de ces techniques fait face à des limites qui lui sont propres : dans le cadre de l'étude numérique, le traitement des gouttelettes résultantes de la cassure de jet est un facteur limitant de par le rapport de taille introduit. Ce manuscrit de thèse présente le couplage entre une méthode de traitement d'interface Eulerienne et une méthode de transport de particule Lagrangienne, proposant une approche multi échelle de l'atomisation.

Le code de calcul numérique *Archer* est utilisé dans le but de transporter un écoulement diphasique et d'en étudier son évolution, résolvant les équations incompressibles de Navier Stokes. L'interface séparant les deux phases est représentée par une méthode alliant précision et robustesse, le couplage Volume of Fluid/Level-Set. La discrétisation des équations de Navier Stokes et le transport de l'interface est présenté dans la première partie de ce manuscrit. Cela introduit les faiblesses de cette méthode due à l'aspect multi échelle des jets atomisés : la faible précision du transport des gouttes résultantes de l'atomisation secondaire. La seconde section de ce manuscrit se consacre à l'introduction du transport Lagrangien de gouttes, différentes approches sont implémentées et validées au sein du code de calcul *Archer*. Puis, le couplage entre le solveur Eulerien et Lagrangien, validé par des expériences numériques, est introduit. Ces dernières ont pour but de présenter la méthodologie implémentée pour valider le couplage en respectant la conservation du moment et de la masse. Cette méthode est par la suite appliquée à des cas académiques permettant d'introduire la paramétrisation permettant la jonction entre les solveurs Eulerien et Lagrangien. Finalement, la méthode développée est appliquée à l'étude d'un jet atomisé de configuration crossflow, utilisé au sein de turbine à gaz ou statoréacteur. Les résultats obtenus démontrent les possibilités liées au couplage Eulerien/Lagrangien, tant sur l'aspect physique que numérique, ouvrant sur un modèle de breakup de goutte sous transport Lagrangien.

## Abstract

**Keyword: MotsDirect Numerical Simulation, Level-Set, VOF, Lagrangian, Coupling, Atomization**

The study of the liquid jet's atomization consisting of two immiscible phases is a fundamental research subject. The main motivations linked to the study of these phenomena are the numerous applications resulting from them. For example, in the study of the propagation of a spray within a combustion chamber or for pharmaceutical applications. Their study is carried out by a theoretical, experimental and numerical approach. Each of these techniques faces its own limitations: in the numerical study, the treatment of the droplets resulting from the jet break is a limiting factor due to the size ratio introduced. This thesis manuscript presents the coupling between an Eulerian interface treatment method and a Lagrangian particle transport method, proposing a multi-scale approach to atomization.

The numerical solver *Archer* is used to transport a two-phase flow and to study its evolution, solving the incompressible Navier Stokes equations. The interface separating the two phases is represented by a method combining precision and robustness, the Volume of Fluid/Level-Set coupling. The discretization of the Navier Stokes equations and the transport of the interface is presented in the first part of this manuscript. This introduces the weaknesses of this method due to the multi-scale aspect of the atomized jets: the low precision of the transport of the drops resulting from the secondary atomization. The second section of this manuscript is dedicated to the introduction of Lagrangian drop transport, different approaches are implemented and validated within the computational code *Archer*. Then, the coupling between the Eulerien and Lagrangian solver, validated from numerical experiments, is introduced. The latter aim to present the methodology implemented to validate the coupling while respecting the conservation of time and mass. This method is then applied to academic cases to introduce the parameterization allowing the junction between the Eulerien and Lagrangien solvers. Finally, the developed method is applied to the study of an atomized jet of crossflow configuration, used in gas turbine or ramjet. The results obtained demonstrate the possibilities related to the Eulerien/Lagrangien coupling, both on the physical and numerical aspects, opening up a model of drop breakup under Lagrangien transport.